

8-2019

MODELING CANCER USING LI-FRAUMENI SYNDROME PATIENT-DERIVED INDUCED PLURIPOTENT STEM CELLS

Ruoji Zhou

Follow this and additional works at: https://digitalcommons.library.tmc.edu/utgsbs_dissertations



Part of the [Cancer Biology Commons](#), [Cell Biology Commons](#), [Genomics Commons](#), and the [Medicine and Health Sciences Commons](#)

Recommended Citation

Zhou, Ruoji, "MODELING CANCER USING LI-FRAUMENI SYNDROME PATIENT-DERIVED INDUCED PLURIPOTENT STEM CELLS" (2019). *UT GSBS Dissertations and Theses (Open Access)*. 963.
https://digitalcommons.library.tmc.edu/utgsbs_dissertations/963

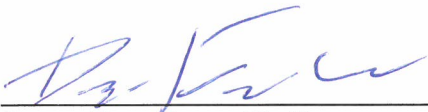
This Dissertation (PhD) is brought to you for free and open access by the Graduate School of Biomedical Sciences at DigitalCommons@TMC. It has been accepted for inclusion in UT GSBS Dissertations and Theses (Open Access) by an authorized administrator of DigitalCommons@TMC. For more information, please contact nha.huynh@library.tmc.edu.

**MODELING CANCER USING LI-FRAUMENI SYNDROME PATIENT-DERIVED
INDUCED PLURIPOTENT STEM CELLS**

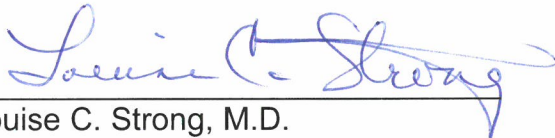
by

Ruoji Zhou, M.D., M.S.

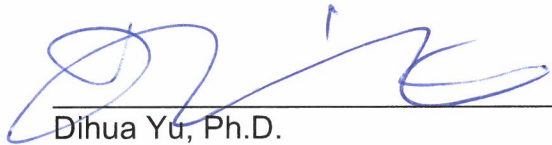
APPROVED:



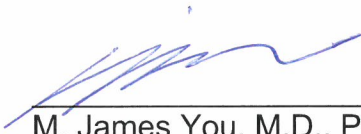
Dung-Fang Lee, Ph.D.
Advisory Professor



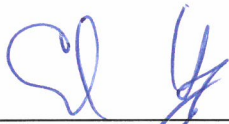
Louise C. Strong, M.D.



Dihua Yu, Ph.D.



M. James You, M.D., Ph.D.



Chad Huff, Ph.D.

APPROVED:

Dean, The University of Texas
MD Anderson Cancer Center UTHealth Graduate School of Biomedical Sciences

**MODELING CANCER USING LI-FRAUMENI SYNDROME PATIENT-DERIVED
INDUCED PLURIPOTENT STEM CELLS**

A

DISSERTATION

Presented to the Faculty of

The University of Texas

MD Anderson Cancer Center UTHealth

Graduate School of Biomedical Sciences

in Partial Fulfillment

of the Requirements

for the Degree of

DOCTOR OF PHILOSOPHY

by

Ruoji Zhou, M.D., M.S.

Houston, Texas, August, 2019

Dedication

To my mom Xiaoling Ma
And my husband Jiun-sheng Chen
For their love and support

Acknowledgment

First and foremost, I must thank my advisor, Dr. Dung-fang Lee for accepting me into Lee lab family and supporting me every step of the way. Dr. Lee is the person who led me into the field of stem cell and cancer research. Over the past three years, he spent countless hours training me, from bench skill, experimental design to scientific writing and critical thinking. He also provided guidance as well as flexibility in my research project. Under his encouragement and support, I was able to apply for different fellowship and scholarship. Dr. Lee is one of the most dedicated and hardworking scientists I have ever seen, regardless of where life takes me, I will always be inspired by his passion and persistence for science.

Second, I would like to express my most sincere appreciation for my advisory committee members. I would like to thank Dr. Louis Strong for her support for my application for fellowship and scholarship and her invaluable suggestions for our review paper, my thesis project and my career plan. I would also like to thank Dr. James You, who has been my committee member the longest time. Dr. You provided me strongest support during my most difficult time in graduate school and I gained a lot from his suggestions in both science and in life. Dr. Chad Huff, as both my advisory member and collaborator, offered great support and help in data analysis in my research project and provided lots of constructive suggestions for my project. I would also like to thank Dr. Dihua Yu, who was also Dr. Lee's advisor committee member during his Ph.D. study. Although she is very busy, she was also responsive whenever I have questions and met with me individually. I really

appreciated her suggestions and questions during committee meetings, which helped me improving my critical thinking and promoted my project.

Third, I have to acknowledge the support given to me by lab members from both Lee lab and Dr. Ruiying Zhao's lab, especially Dr. Jian Tu who helped me with the mouse work in my project, and previous lab member Yu-Hsuan Lin who helped me when I just started in Lee lab. I would like to thank Dr. An Xu for his generous help, and we had great time working collaboratively in the lab. Many thanks to other lab members who are always willing to help me when I have difficulties with my work. In addition, I must thank my collaborator outside of the laboratory. I had a chance to be involved in research project led by Dr. Huensuk Kim from Dr. Ihor R. Lemischka's and Dr. Christoph Schaniel Lab. This collaborative project provided me with solid bases for my project, supported my research hypothesis and promoted the progress of the project. I also want to thank Dr. Yao Yu and Jiunsheng Chen from Dr. Chad Huff's lab in helping me with sequencing data analyses. Their intelligence and diligence ensured the progress of my project.

I also want to acknowledge all faculty members and students from Human Molecular Genetics program, for their help, support, caring and encouragement during the past several years.

Last but not least, I want to express my deep appreciation to my families, especially my mother, for her unconditional love and support. I would like to thank my beloved husband, who is always by my side, taking caring of me, supporting and encouraging me during my difficult time. I am really grateful that we met each other in GSBS; without him, I would not be able to make through my graduate study.

MODELING CANCER USING LI-FRAUMENI SYNDROME PATIENT-DERIVED INDUCED PLURIPOTENT STEM CELLS

Ruoji Zhou, M.D., M.S.

Advisory Professor: Dung-Fang Lee, Ph.D.

Li-Fraumeni syndrome (LFS) is an autosomal dominant disease caused by germline mutations in the gene *TP53*, which predispose individuals to a wide range of malignancies, including osteosarcoma and breast cancer. In the previous study, our group developed a novel disease model platform by reprogramming LFS patients' fibroblasts to induced pluripotent stem cells (iPSCs), and further differentiate these iPSCs into mesenchymal stem cells (MSCs) then to osteoblasts (OBs), the cells from which osteosarcomas originate. Interestingly, LFS iPSC-derived osteoblasts recapitulated the osteosarcoma phenotype, creating “a bone tumor in a dish”. This “tumor in a dish” platform proved that LFS is an ideal model system to study and modeling LFS associated malignancies.

In this study, we applied whole exome deep sequencing in LFS iPSCs derived samples carrying different tumorigenic potential (MSCs, OBs, OB derived tumors) to identify cancer drivers that contribute to LFS associated osteosarcomagenesis. We found that LFS patient derived OBs exhibit both *in vitro* and *in vivo* oncogenic properties. We also observed increased somatic mutation prevalence in LFS OBs derived tumors compare to LFS OBs. Genes that are commonly mutated between LFS OBs derived tumors and genes carrying truncating or frameshift mutations in LFS OBs derived tumors were identified, including *USP34*, *ANAPC1*, *ESPL1*,

MYLK, *SLC35G2*, *FAM160A2*, *SLC25A32*, *SYNE2*, *RPL8*, and *FAM20A*. These genes are potential candidate driver genes during early osteosarcoma development.

Breast cancer is the most common tumor among women with germline *TP53* mutations. In this study, we also generated iPSC lines from LFS breast cancer patient and healthy family member. Using precise genome editing tools, we created *TP53* mutation (delG) in unaffected relative derived the iPSCs, generating isogenic controls to facilitate studying of mutant p53 related phenotypic differences. We also demonstrated differentiation of LFS iPSCs to non-neural ectoderm using a chemical based protocol. Further establishment of mammary organoids differentiation protocol will provide *in vitro* platform in modeling LFS associated breast cancer.

In addition, we successfully corrected *TP53* mutation (Y205C) in LFS patient derived iPSCs using TALEN-mediated precise gene editing. Similar approach was used to generate two H1 human embryonic stem cells (hESCs) carrying homozygous *TP53* R282W and *TP53* R248W mutation. These engineered iPSCs/hESCs offers exciting opportunities for studying mechanisms of mutant p53 associated malignancies and testing existing or potential compounds targeting mutant p53-associated pathway.

In summary, our studies demonstrated the potential of LFS patient derived iPSCs in cancer modeling.

Table of Contents

Approval Sheet.....	i
Title Page	i
Dedication	iii
Acknowledgment	iv
Abstract	vi
Table of Contents	viii
List of Figures	xii
List of Tables	xvi
Chapter 1 Introduction.....	1
1.1 Discovery of Li-Fraumeni syndrome (LFS) and identification of <i>TP53</i> as a crucial gene for tumorigenesis	1
1.2 Biological functions of p53: ever-growing complexity	4
1.3 Mutant p53 gain-of-function: more than merely a loss.....	7
1.4 Current LFS disease models	14
1.5 Modeling disease with pluripotent stem cells.....	19
1.6 Modeling cancer with pluripotent stem cells	21
1.7 Personalizing cancer therapy through precise genome editing	27
Chapter 2 Materials and Methods	29
2.1 Generation of LFS iPSCs	29
2.2 iPSC/hESC culture in feeder culture condition (on mouse embryonic fibroblast)	29

2.3 iPSC/hESC culture in feeder-free culture condition (iPS-Brew XF medium)	30
2.4 Immunofluorescent staining	33
2.5 SeV genome and transgenes detection	34
2.6 Alkaline phosphatase staining (AP staining)	34
2.7 Quantitative real-time PCR	34
2.8 Karyotype analysis	36
2.9 <i>In vivo</i> teratoma formation assay	36
2.10 Mycoplasma detection	36
2.11 Short tandem repeat (STR) analysis	36
2.12 Differentiation of iPSCs to mesenchymal stem cells (MSCs)	37
2.13 Differentiation of mesenchymal stem cells (MSCs) to osteoblasts (OBs)	37
2.14 Alizarin Red S (ARS) staining	38
2.15 <i>In vitro</i> soft agar assay (anchorage independent assay)	38
2.16 <i>In vivo</i> xenograft tumor model of LFS MSC-derived osteoblasts	40
2.17 <i>In vitro</i> culture of LFS osteoblast derived tumors	41
2.18 Generation of TALEN and CRISPR/Cas9 guides and WT/mutant p53 donor vector	41
2.19 T7 Endonuclease I assay	45
2.20 Generation of engineered iPSC and hESC line by precise genome editing	45
2.21 Western blot	46
2.22 Southern blot	47

2.23 Culture of embryoid bodies (EB) and MammoCult-derived embryoid bodies (mEBs)	48
2.24 Chemical based differentiation of non-neural ectoderm	49
2.25 Mammary-like organoid differentiation.....	50
2.26 Whole exome sequence and analysis	51
Chapter 3 Identification of bone cancer driver genes using Li-Fraumeni syndrome iPSCs.....	53
3.1 Introduction	53
3.2 Hypothesis and experimental design.....	55
3.3 Generation and characterization of iPSCs from LFS patients with heterozygous <i>TP53</i> mutation.....	57
3.4 Differentiation of LFS iPSCs to mesenchymal stem cells (MSCs).....	62
3.5 Differentiation of LFS MSCs to osteoblasts	65
3.6 LFS derived osteoblasts (OBs) exhibit <i>in vitro</i> oncogenic properties	68
3.7 Continuous cultured LFS derived osteoblasts (OBs) exhibit increased <i>in vitro</i> oncogenic properties.....	75
3.8 Establishment of xenograft model to study <i>in vivo</i> tumorigenesis of LFS MSC-derived osteoblasts.....	79
3.9 Establishment of LFS OB derived tumor cell lines.....	80
3.10 Whole exome sequencing of LFS OB derived tumor cell lines.....	85
3.11 Discussion	102
Chapter 4 Potential of Li-Fraumeni syndrome iPSCs platform in modeling breast cancer.....	106

4.1 Introduction	106
4.2 Generation and characterization of iPSCs from LFS patients with breast cancer	108
4.3 Generation of isogenic control by creating <i>TP53</i> mutation in WT iPSCs using TALEN mediated genome editing	115
4.4 Differentiation of LFS iPSC into mammary-like organoid	123
4.5 Discussion	134
Chapter 5 Potential of modeling mutant p53 associated malignancies using engineered iPSCs and hESCs	137
5.1 Correction of mutant p53 iPSC using precise gene editing	137
5.2 Generation of homozygous p53 R282W mutant human embryonic stem cell line using TALEN-mediated precise gene editing	144
5.3 Establishment of a human embryonic stem cell line with homozygous <i>TP53</i> R248W mutant by TALEN mediated gene editing	148
5.5 Discussion	153
Chapter 6 Future Directions	156
6.1 Identification of osteosarcoma driver genes using LFS patient derived iPSCs-MSCs-OBs platform.....	156
6.2 Intersection of the LFS iPSC model with new methodologies: organoids and organs-on-chip.....	160
6.3 LFS iPSC Model: New Opportunities for Screening Compounds.....	165
Reference	169

List of Figures

Figure 1. Milestones of Li–Fraumeni syndrome (LFS) and p53 Research.....	6
Figure 2. Mutational landscape of <i>TP53</i> germline and somatic mutations in human cancer.....	8
Figure 3. Mutant p53 gain-of-Function cancer driver mutations and hallmarks of cancer.....	13
Figure 4. Illustration of <i>in vitro</i> soft agar assay.....	39
Figure 5. Schematic of non-neural ectoderm differentiation and mammary-like organoid differentiation.....	50
Figure 6. LFS iPSC-derived osteoblasts recapitulate osteosarcoma features and represent osteosarcoma signatures.	54
Figure 7. Schematic graph of experiment setup to identify cancer drivers during LFS-associated osteosarcomagenesis.	56
Figure 8. The LFS pedigree used in modeling LFS-osteosarcoma.....	57
Figure 9. Generation of additional LFS iPSC from LFS patient carrying heterozygous <i>TP53</i> mutation.	59
Figure 10. Characterization of LFS iPSCs carrying heterozygous <i>TP53</i> mutation (Y205C).	60
Figure 11. Differentiation of LFS iPSCs to MSCs.....	64
Figure 12. Differentiation of MSCs to osteoblasts.....	64
Figure 13. Differentiation of WT and LFS MSCs to osteoblasts.....	66
Figure 14. Soft agar assay confirmed <i>in vitro</i> tumorigenic ability of LFS derived osteoblasts.	68

Figure 15. <i>In vitro</i> tumorigenic ability recapitulated in a different LFS patient derived osteoblasts.	71
Figure 16*. Overexpression of sFRP2 in LFS associated osteosarcoma model (figures and legends used with permission).	74
Figure 17. LFS derived osteoblasts exhibit increased <i>in vitro</i> oncogenic properties when culture continuously.	77
Figure 18. <i>In vivo</i> tumorigenesis of LFS MSC-derived osteoblasts.	81
Figure 19. Xenograft model to study <i>in vivo</i> tumorigenesis of LFS MSC-derived osteoblasts	82
Figure 20. <i>In vitro</i> expansion of LFS patient osteoblasts derived tumor.	84
Figure 21. Workflow of sequencing analysis and quality control.	88
Figure 22. Summary of sequencing results highlighting commonly mutated genes in LFS OB derived tumors.	90
Figure 23. Summary of commonly mutated gene in LFS OB derived tumors.	91
Figure 24. Analysis of identified variants in LFS OB and OB derived tumors.	92
Figure 25. Mutational signature of LFS OBs and OB-derived tumors.	94
Figure 26. Characterization of mutated genes identified in LFS OBs derived tumors.	96
Figure 27. Tumor distribution with <i>TP53</i> germline mutations.	106
Figure 28. Generation of iPSC from LFS patient with breast cancer.	110
Figure 29. Characterization of iPSC from LFS patient with breast cancer.	112
Figure 30. Characterization of iPSC from LFS patient with breast cancer (continued).	114

Figure 31. Schematic diagram of the strategy for correcting mutant p53 (delG) and creating mutant p53 (delG) using precise genome editing tools.	119
Figure 32. Generation of isogenic controls by correcting <i>TP53</i> mutation (delG) using precise genome editing tools.	120
Figure 34. Generation of mEBs and EBs from hESCs.	127
Figure 35. Generation of m EBs and EBs from LFS derived iPSCs.	128
Figure 36. Immunostaining of AP-2 γ during 12-day mEB formation.	129
Figure 37. Immunostaining of CK18 during 12-day mEB formation.	130
Figure 38. Two step differentiation of mammary-like organoids from LFS iPSCs.	131
Figure 39. Chemical based non-neural ectoderm differentiation and 3D mixed floating gel culture for mammary lineages differentiation.	133
Figure 40. Correction of mutant p53 (G245D) iPSC using precise gene editing.	140
Figure 41. Correction of mutant p53 (Y205C) iPSC using TALENs-mediated precise gene editing.	141
Figure 42. Correction of mutant p53 (Y205C) iPSC using TALENs-mediated precise gene editing (continued).	142
Figure 43. Establishment and characterization of the homozygous p53 R282W mutant human embryonic stem cell line H1-p53(R282W/R282W).	147
Figure 44 Generation and characterization of the homozygous p53 R248W mutant human embryonic stem cell line H1-p53(R248W/R248W).	152
Figure 45. Mutation landscape of <i>TP53</i> in human cancers.	153

Figure 46. Application of LFS iPSC models to drug development for LFS and p53 mutation-associated tumors. 163

List of Tables

Table 1. Current LFS Disease Models	19
Table 2. Established PSCs models of cancer or diseases that predispose to cancer.	26
Table 3. Compositions of culture medium and solution used in this study.	31
Table 3. Compositions of culture medium and solution used in this study (continued).	32
Table 4. Antibodies used in immunofluorescent staining.	33
Table 5. PCR reaction and primers used in SeV genome and transgenes detection.	34
Table 6. RT-PCR primers used in this study.	35
Table 7. Seeding density of MSCs for osteoblastic differentiation.	38
Table 8. Summary of the TALEN and CRISPR/Cas9 guides targeting different <i>TP53</i> genomic region.	43
Table 9. Primers used to generate WT and p53 mutant donor vector.	45
Table 10. PCR primers used to identify correctly inserted colonies.	46
Table 11. Antibodies used in western blot in this study.....	47
Table 12. Potential candidate genes driving LFS-associated osteosarcoma development.....	101
Table 13. Potential candidate genes driving LFS-associated osteosarcoma and their reported biological functions.....	159
Table 14. Compounds targeting WT and mutant p53.	167

Chapter 1 Introduction

Copyright information:

Contents of Chapter 1.1-1.4 and 1.7 are based my review article: Zhou R*, Xu A*, Gingold J, Strong LC, Zhao R, Lee DF. Li–Fraumeni Syndrome Disease Model: A Platform to Develop Precision Cancer Therapy Targeting Oncogenic p53. Trends Pharmacol. Sci. (2017), 10.1016/j.tips.2017.07.004. (*: First authors). I am the first author of the review. Permission to reuse the whole article for thesis was obtained from www.copyright.com with license number: 4598280693164.

Contents of Chapter 1.5 and 1.6 are based my review article: Gingold J, Zhou R*, Lemischka IR, Lee DF. Modeling Cancer with Pluripotent Stem Cells. Trends cancer (2016), 10.1016/j.trecan.2016.07.007. (*: Second author). I am the primary author of the review. Permission to reuse the whole article for thesis was obtained from www.copyright.com with license number: 4598280931533.

1.1 Discovery of Li-Fraumeni syndrome (LFS) and identification of *TP53* as a crucial gene for tumorigenesis

Li-Fraumeni Syndrome (LFS) [Online Mendelian Inheritance in Man (OMIM) 151623; <https://www.omim.org/entry/151623>] is a rare familial autosomal dominant cancer syndrome characterized by early onset of multiple tumors, particularly soft-tissue sarcomas, osteosarcomas, breast cancers, brain tumors, adrenocortical carcinomas, and leukemia. LFS was first described in 1969 by Li and Fraumeni (1, 2) (**Figure 1**). In reviewing 280 medical charts and 418 death certificates of 648 childhood rhabdomyosarcoma patients in the USA from 1960 to 1964, they

identified four families in whom a second child had developed a soft tissue sarcoma. These four families also had striking histories of breast cancer and other neoplasms, suggesting a previously undescribed familial cancer syndrome.

The classic LFS pedigree was defined in the proband as a patient with sarcoma diagnosed before age 45 years, plus a first-degree relative with any cancer before age 45 and another first or second-degree relative with any cancer before age 45 or a sarcoma at any age. This definition was based on 24 kindreds with the syndrome of sarcoma, breast carcinoma, and other neoplasms in young patients (3). The defined criteria for this syndrome gradually evolved to include not only classic LFS but also LFS-like syndrome (LFL), which shares features of LFS but does not conform to the strict definition (4).

While the six core cancers mentioned above account for the majority of LFS-associated tumors, the remaining cancers include diverse carcinomas of the lung, stomach, ovary, and colon/rectum, as well as lymphoma, melanoma, and other neoplasms (5). One half of patients with LFS develop at least one LFS-associated cancer before age 30, compared to a 1% incidence of cancer before age 30 in the general population (6). The lifetime risk of cancer in LFS is estimated to be 73% for males and almost 100% for females, with the increased risk of breast cancer accounting for the difference (7, 8).

LFS patients are also at a remarkably increased risk of developing a second malignancy (9, 10). A study of 200 LFS patients from 24 kindreds showed that 57% of patients developed a second malignancy within 30 years after diagnosis of the first cancer (10). LFS patients also are at increased risk of developing treatment-

related secondary malignancies. Several case reports suggested that ionizing radiation-induced cancers are more common in LFS patients (11-13), and research studies also support this relationship (14, 15). Therefore, radiation therapy is generally avoided in the management of these patients if possible. A stringent surveillance strategy is one of the key components of LFS patient management. A prospective clinical trial aimed at improving cancer screening for LFS patients showed that a surveillance strategy including whole-body magnetic resonance imaging (MRI) and other biochemical tests was able to detect tumors earlier, and this was associated with improved long-term survival (16).

In 1990, Malkin et al. used a candidate gene approach to first link a *TP53* germline mutation to LFS (17). Srivastava *et al.* later analyzed *TP53* mutations in a LFS family, identifying the same point mutation in codon 245 of the *TP53* gene in different generations of this pedigree (18). Together with the previous observations that p53 is also inactivated in the sporadic (nonfamilial) forms of cancers, these studies suggested that loss of p53 is a rate-limiting step for tumorigenesis (17), and implied that inherited *TP53* mutations could be responsible for the increased susceptibility to cancer.

The initial detection of a *TP53* heterozygous point mutation was only in five LFS families (17). Numerous subsequent studies have shown that ~70% of LFS families harbor detectable germline *TP53* mutations (4, 19-22). These mutations are also highly associated with a significant increase in DNA copy-number variations (CNVs) (23). For those patients without detectable *TP53* mutations, a complete heterozygous germline deletion of *TP53* was reported (24), indicating

that rearrangements affecting *TP53* occur rarely, but should be considered in LFS families. According to the National Comprehensive Cancer Network (NCCN) guidelines (<https://www.nccn.org/>), *TP53* genetic testing is recommended for individuals from a family with a known *TP53* mutation, or for individuals who meet either the classic LFS criteria, the Chompret criteria (25), or who were diagnosed with breast cancer before age 31. To date, *TP53* germline variants from more than 700 LFS pedigrees have been reported and integrated into the International Agency for Research on Cancer (IARC) TP53 Database (<http://p53.iarc.fr/>) that provides updated resources of hereditary *TP53* variants, including the distribution of mutations over the *TP53* gene and the influence of different types of mutations on the tumor spectrum (26).

1.2 Biological functions of p53: ever-growing complexity

As a central regulator within an extremely complex biological network, p53 plays a much broader role in many normal cellular and developmental processes in addition to its well-known tumor-suppressor function. The most extensively studied mechanism by which wild-type (WT) p53 functions is as a transcription factor, regulating the expression of a set of target genes involved in cell-cycle arrest, senescence, apoptosis, and DNA damage repair (27-29). Beyond these classic functions, p53 also plays roles in regulating glucose metabolism (30, 31), antioxidant activity (31-33), autophagy (34, 35), motility and invasion (36), angiogenesis (37), bone remodeling (38, 39), stem cell self-renewal (40, 41), differentiation (42-49), and somatic cell reprogramming (50-52). Most of these biological processes regulated by p53 have also been proved to contribute to its

tumor-suppressive effect (29), although there is emerging evidence of a 'dark side' of p53 in which WT function can prevent cell death or even promote cancer development and progression (53-55).

Although much still needs to be understood about this ever-growing p53-associated network, it is clear that restoration of functional WT p53 leads to tumor growth suppression (56-58). Therapeutic manipulation of p53 is an ongoing hot research field, and more than 100 related clinical trials have been conducted (59). Translation of our current knowledge of p53 into the clinic has been challenging and is often complicated by the interplay between WT and mutant p53, mutant p53 gain-of-function, inconsistent findings from different study systems, and the versatility of p53 in distinct microenvironments. Even so, novel and creative approaches to treat p53-associated diseases are in high demand.

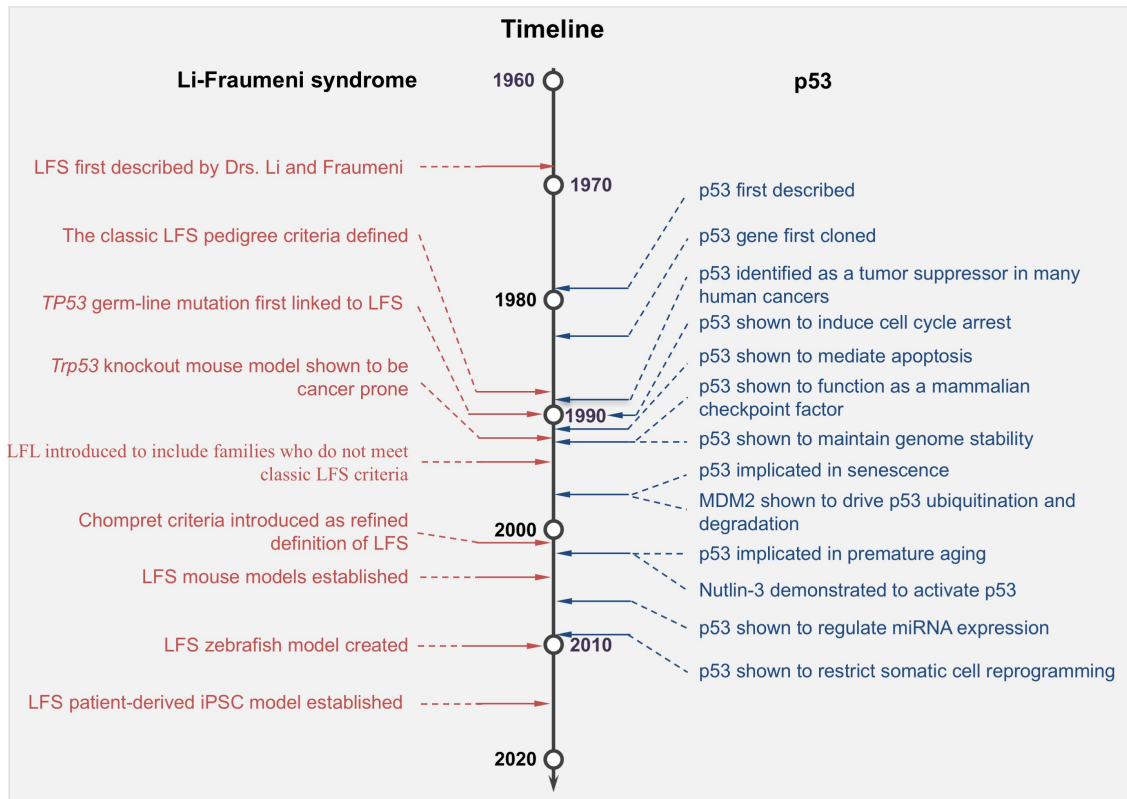


Figure 1. Milestones of Li–Fraumeni syndrome (LFS) and p53 Research.

The left column timeline shows important research developments in LFS, including discovery of the disease, identification of the underlying genetic cause, and establishment of a disease model. The right column timeline lists the equivalent key findings during 38 years of research on p53. Abbreviations: iPSC, induced pluripotent stem cell.

1.3 Mutant p53 gain-of-function: more than merely a loss

TP53 is the most frequently mutated gene in human cancers (60, 61). Deletion or truncation mutations in p53 abrogate its normal function by attenuating p53-responsive cellular activities; when both alleles become mutated, the anticancer protection of p53 is shut down. Although p53 loss of function is a common feature of cancer, p53 does not fully follow the classic Knudson's two-hit theory during carcinogenesis or cancer progression (62). It is not simply the loss of WT p53 that drives cells to cancer. The majority of the p53 mutations found in tumors are missense mutations, resulting in production of full-length protein with only a single amino acid change (63). Many of these mutant proteins exhibit a mutant p53 dominant negative effect over WT p53, mostly by forming mixed tetramers with diminished DNA-binding and transactivation activity (64). In this way, mutation of only one copy of p53 can lead to many of the downstream effects that would otherwise require loss of both copies.

Probably the most striking fact about the p53 mutation landscape in cancer is the high prevalence of missense substitutions at particular locations, mainly in the DNA-binding domain (DBD) (63) (**Figure 2**). These 'hotspot' mutations indicate selective advantages during cancer development and progression. Indeed, many hotspot mutations arm the mutant p53 with new weapons to promote cancer. Such activities, known as mutant p53 gain-of-function, are involved in the regulation of various cancer hallmarks (**Figure 3**), including genomic instability (65-69), anti-apoptotic activities(70-79), replicative mortality (69, 80), invasion and metastasis (63, 64, 66, 67, 71, 81-91), angiogenesis (92-95), dysregulated metabolism (96-

99), and tumor related inflammation (100-103). Mutant p53 gain-of-function can drive cancer through several potential mechanisms (104, 105): (i) binding to structure-specific DNA to subsequently exert transcriptional regulation, (ii) interacting with transcription factors or cofactors to enhance or decrease the transcription of their targeted genes, (iii) associating with chromatin or the chromatin regulatory complex, and (iv) directly interacting with and influencing other proteins and their functions.

Several excellent reviews (64, 104-113) have addressed p53 gain-of-function from various aspects. We highlight here some of the most recent discoveries on mutant p53 gain-of-function and address their therapeutic potential in cancer treatment.

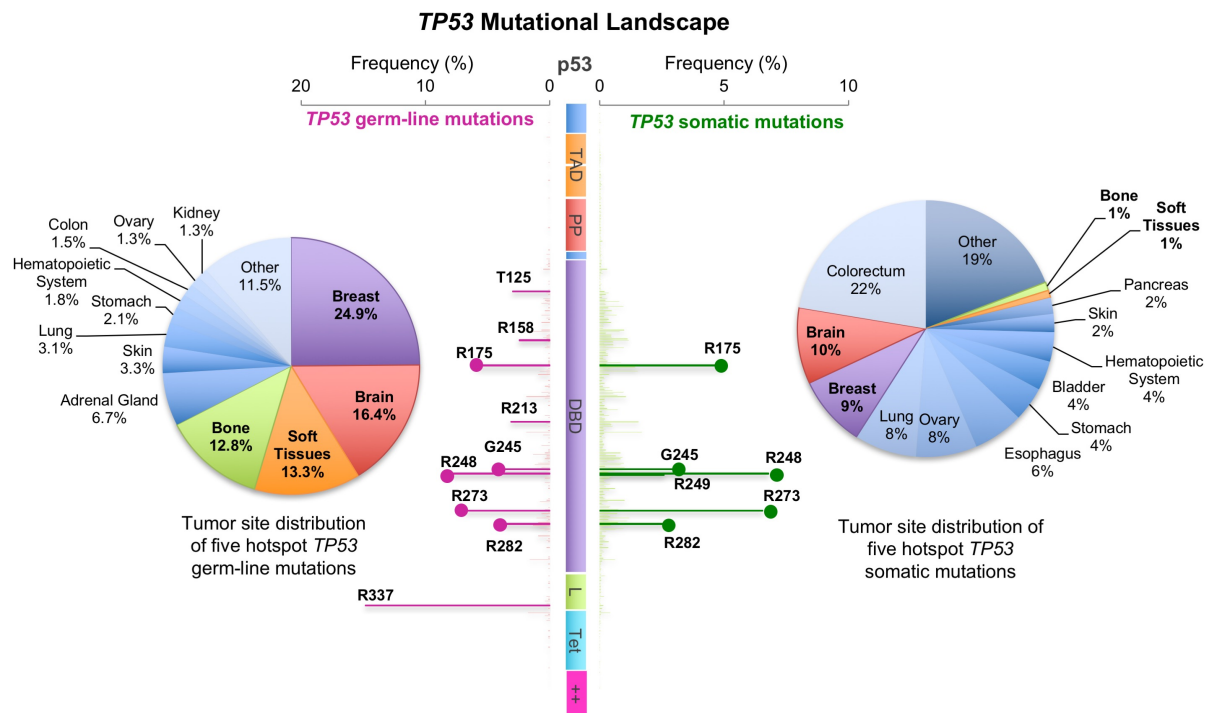


Figure 2. Mutational landscape of TP53 germline and somatic mutations in human cancer.

TP53 missense mutation data are obtained from the International Agency for Research on Cancer (IARC) *TP53* database (<http://p53.iarc.fr/>). The distribution of *p53* mutations is plotted over the function of amino acid position; the left side indicates germline mutations and the right side indicates somatic mutations. The horizontal axis shows the frequency of any mutation at the indicated residues. The vertical axis represents *p53* protein starting with the N-terminus at the top. *p53* protein contains transcriptional activation domains I and II (TAD 1, 20–40; TAD II, 40–60), the proline domain (PP, 60–90), the sequence-specific core DNA-binding domain (DNA-binding core, DBD; residues 100–300), the linker region (L, 301–324), the tetramerization domain (Tet, 325–356), and the lysine-rich basic C-terminal domain (++, 363–393). The most common mutations or hotspots are indicated in bold; residues R175, G245, R248, R273, and R282 are the five common hotspots for both germline and somatic mutations (indicated as a lollipop). Pie charts illustrate the tumor site distribution of five hotspot *TP53* mutations (left, germline; right, somatic). Malignancies of breast, brain, soft tissues, and bone are the most commonly seen for the five hotspot germline mutations; malignancies from these tumor sites are also distributed in the same five hotspots of *TP53* somatic mutations (indicated in bold).

Regulating imprinted genes

Aberrant imprinting or dysregulation of imprinted genes is associated with developmental disorders and an increased risk of cancer (114-116). Alterations in the expression of genes in the imprinted *H19-IGF2* locus have been described in Beckwith–Wiedemann syndrome (BWS) (117) and Russell–Silver syndrome (RSS) (118), which are associated with risk for Wilms tumor, hepatoblastoma, and rhabdomyosarcoma. Bidirectional links between WT p53 and imprinted genes in the *H19-IGF2* locus have been demonstrated in several studies (119-121). Loss of imprinting of IGF2 accelerates tumor formation by inactivating WT p53 (119). Maternally imprinted H19, which encodes a long noncoding RNA, has been shown to be negatively regulated by p53 (120). In 2015, this link was extended to the mutant p53. A study by Lee *et al.* revealed that numerous p53 mutants exhibit gain of function and can inhibit H19 expression (122). Using LFS patient-derived induced pluripotent stem cells (iPSCs) to model osteosarcoma, this study found that the p53 (G245D) mutant represses H19 expression during osteoblastic differentiation. Moreover, many hotspot p53 mutants including R175H, G245S, R248W, and R280K also showed strong inhibition of H19 expression compared to WT p53, indicating that mutant p53 gain-of-function in regulating imprinted gene expression is a general mechanism in LFS-associated osteosarcoma across distinct p53 mutations.

Driving cancer through interplay with chromatin

One of the features of gain-of-function mutant p53 is the ability to associate with chromatin and other transcriptional factors to globally influence the gene

expression profile (76, 96, 101, 123, 124). Recently, it was shown that multiple mutant p53 forms bind to the SWI/SNF chromatin remodeling complex (92). This interaction with the SWI/SNF complex mediates up to 40% of the mutant p53 regulated genes, including the angiogenesis-promoting gene *VEGFR2*, further suggesting that repressing the SWI/SNF complex or its downstream targets (e.g., by anti-VEGF) may help to reverse the changes caused by mutant p53 in cancer. A proteome-wide analysis found that the p53 R273H mutant is tightly associated with chromatin and can modulate the protein levels of PARP, PCNA, and MCM4 in a transcription-independent manner (125). Inhibition of PARP activity showed efficacy in treating these mutant p53 expressing cancer cells. Another mutant p53 gain of function causes mutant p53 to interact specifically with transcription factor ETS2 and leads to upregulation of chromatin regulatory genes, including *MLL1*, *MLL2*, and *KAT6A*, resulting in a global increase of histone modifications (methylation and acetylation) and tumor progression (126). This suggests the possibility that therapeutic inhibition of the MLL1 methyltransferase complex might decrease cancer cell proliferation.

Driving oncogene expression by repressing transcription factors

Mutant p53 can exert its pro-oncogenic properties by physically interacting with the p53 family members, p63 and p73, and altering their transcriptional activity (72, 81, 127, 128). Mutant p53 promotes pancreatic cancer invasion and metastasis by upregulating the cancer driver *PDGFRB* (129). p53 mutants at the hotspot sites R175H and R273H were shown to bind to the p73/NF-Y complex. This interaction impairs the repressive transcriptional regulation of p73 at the *PDGFRB* promoter

region. The study also showed that inhibition of PDGFRB using RNAi or small molecules is effective in attenuating metastasis *in vivo*, suggesting a possible target in controlling metastasis in p53 mutant pancreatic cancer.

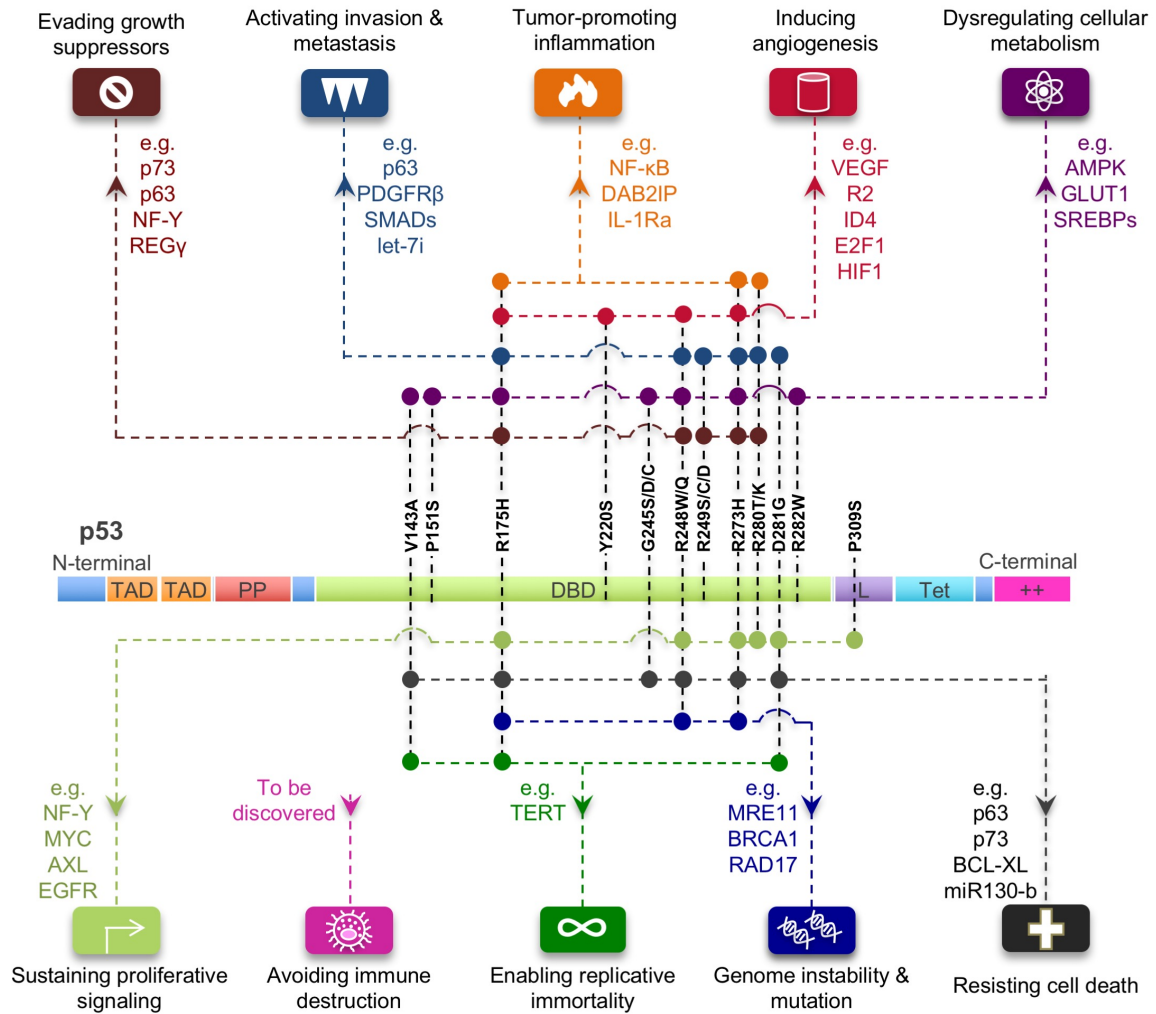


Figure 3. Mutant p53 gain-of-Function cancer driver mutations and hallmarks of cancer.

Different mutations in p53 protein (structural domains are described in Figure 2) arm p53 with new weapons (downstream targets indicated in the figure) to drive cancer development and progression. Each color-coded node indicates gain-of-function of a specific mutation in *TP53* which further drives cancer through various hallmark properties of cancer cells.

1.4 Current LFS disease models

Engineered mouse models

Engineered mouse models have been used extensively for mammalian *in vivo* and *in vitro* studies of LFS. In 1992, to investigate the role of the *Tp53* gene in mammalian development and tumorigenesis, a null mutation was introduced into the gene by homologous recombination in murine embryonic stem cells (130). Mice homologous for the null allele (*Tp53*^{-/-}) appear to be developmentally normal but are highly susceptible to early onset of a variety of neoplasms. Subsequent homozygous knockout mice with different deletions of *Tp53* showed similar tumorigenic phenotypes (131, 132).

However, a more appropriate genetic model for LFS with heterozygous mutations in *Tp53* is needed because LFS patients are invariably heterozygous rather than homozygous for mutant p53. With this in mind, heterozygous p53-null mice (*Tp53*^{+/-}) were generated. Nearly 50% of them developed tumors by 18 months of age, although with a comparative cancer onset delay compared to the homozygous mice. This was roughly similar to the 50% cancer incidence before age 30 in affected LFS individuals, given that C57BL/6 mice have an average lifespan of 30 to 36 months (133). The similarities between *Tp53*^{+/-} mice and LFS patients are even more striking with respect to their tumor spectrum. *Tp53*^{+/-} mice develop osteosarcomas and soft tissue sarcomas, as seen with high frequency in LFS families, while homozygous mice predominantly develop malignant lymphomas (134).

Missense mutations are the most common mutations in affected LFS individuals apart from null mutations. Mouse models of these mutations garnered significant attention in the p53 research community. In 2000 the first heterozygous mouse containing an R to H substitution at p53 amino acid 172 was generated, which corresponds to the R175H hotspot mutation in human cancers and the germline mutation in LFS kindreds (135). Although this model contained an unexpected deletion of a G nucleotide at a splice junction that attenuated levels of mutant p53 to near WT levels, mice heterozygous for the mutant allele differed from $Tp53^{+/-}$ mice because the osteosarcomas and carcinomas developed in these missense mutant mice frequently metastasized (69% and 40%, respectively). This indicated, for the first time, that a p53 missense mutation could confer a gain of function *in vivo*, even when expressed at relatively low levels.

Later in 2004, two groups independently reported knock-in mouse models of LFS expressing the p53 mutant alleles R172H and R270H ($Tp53^{M/-}$), equivalent to the codons 175 and 273 in humans (136, 137) (**Table 1**). Both studies demonstrated that $Tp53^{M/-}$ mice developed a broader tumor spectrum with a more invasive and metastatic phenotype compared to $Tp53^{+/-}$ mice, although no change in survival was observed. The broad spectrum of tumors included a variety of carcinomas, bone sarcomas, leukemias, and even a glioblastoma multiforme (GBM, the most common brain tumor in LFS), indicating that $Tp53^{M/-}$ mice better recapitulate the human LFS familial syndrome than do $Tp53^{+/-}$ mice. Interestingly, $Tp53^{M/-}$ and $Tp53^{+/-}$ mice did not develop breast cancer, one of the most common tumors in LFS patients, but increased the incidence of hematological malignancies (e.g.,

lymphomas) (136, 137), implying that either species differences or a specific susceptible genetic background influence the ability of these model models to recapitulate human LFS.

Similarly, HUPKI mouse models (humanized *TP53* knock-in models) (138) were constructed by targeting the mutant human *TP53* DNA sequence into murine embryonic stem cells (**Table 1**). HUPKI models were generated for the human mutations R175H, G245S, R248W, R248Q, and R273H (65, 139, 140). All these knock-in mice except the G245S model showed a broader tumor spectrum than *Tp53* null mice, providing strong support for the gain-of-function hypothesis of various missense p53 mutants in driving and enhancing spontaneous tumorigenesis.

Zebrafish models

Another model of LFS was created in zebrafish (**Table 1**), a powerful vertebrate system that is accessible to both large-scale screens and *in vivo* manipulation for cancer studies (141). A forward genetic screen was performed using a specific ionizing radiation (IR)-induced phenotype in zebrafish embryos, leading to the identification of the p53 I166T mutations. This mutation was shown to give rise to tumors, predominately sarcomas, with 100% penetrance in adult fish. As in humans with LFS, heterozygous *tp53*^{I166T} fish follow Knudson's two-hit hypothesis, and the tumors displayed loss of heterozygosity (LOH) at the *tp53* locus. Additionally, the data demonstrated that the p53 regulatory pathway, including Mdm2, is evolutionarily conserved in zebrafish. This work demonstrated the

potential of zebrafish models to discover novel genes and therapeutic compounds that modulate the evolutionarily conserved LFS pathway.

Primary cell line systems

Researchers have also gained insight into LFS through direct investigation of patient primary cells. A comparison of soft tissue sarcomas, including fibrosarcomas, from affected LFS patients with fibroblasts derived from skin biopsies from the same patients demonstrated chromosomal anomalies, resistance to senescence, and spontaneous immortalization in the LFS fibroblasts compared to control cultures (142, 143). Immortalization of these cells appeared to be associated with loss of the WT *TP53* allele, p16INK4A (*CDKN2A*) expression, and telomere elongation (144-146). Loss of p53 during this immortalization has been shown to cause a decrease in TSP-1 expression, a potent inhibitor of angiogenesis, and switch the LFS fibroblasts to a pro-angiogenic phenotype (147, 148). In addition, normal breast epithelial cells obtained from a patient with LFS (with a mutation at codon 133 of the *TP53* gene) spontaneously immortalized during *in vitro* culture, while breast stromal fibroblasts from this same patient did not (149). The immortalization of normal cells from LFS patients strongly indicates that transformation is characteristic of the LFS genetic background.

Patient-derived iPSCs

The motivation for use of patient-derived iPSCs stems from limitations inherent to other systems. Animal models do not fully represent human LFS disease features, while primary cells from affected patients are limited to a few cell types (150, 151).

To access a wider spectrum of cell types, iPSCs were generated from patient fibroblasts obtained from a LFS family with a heterozygous *TP53* (G245D) hotspot mutation and differentiated into targeted lineages (122) (**Table 1**). Despite their defective p53 function, LFS iPSC-derived mesenchymal stem cells (MSCs) maintained normal MSC characteristics and could be differentiated into osteoblasts. Interestingly, once turned into osteoblasts, genome-wide transcriptome analysis revealed that the cells expressed an osteosarcoma signature. LFS osteoblasts recapitulated the differentiation defects and oncogenic properties of osteosarcoma. Part of this phenotype was shown to be mediated by repression of the imprinted gene *H19* by mutant p53 gain-of-function. Furthermore, LFS osteoblasts and tumors in this model system showed a negligible number of the cytogenetic rearrangements that are commonly found in osteosarcoma, indicating the existence of a relatively intact genome in this model system and the feasibility of studying early cancer progression before the accumulation of broad genome alterations. These data show that the LFS iPSC disease model successfully transforms clinical samples into cell line models. As techniques for directed differentiation improve, this technique may be applied to study many more cancer types in affected LFS families.

Model	p53 mutation	Mutant p53 function	LOH	Tumor types	Metastasis	Model system	Reference
Zebrafish	I166T	Dominant negative	Yes	Broad spectrum	N.A.	<i>In vivo</i>	(141)
Heterozygous mouse	R172H R270H	Gain of function	Yes	Broad spectrum	Yes	<i>In vivo</i>	(135, 136)
HUPKI mouse	R175H, R245S, R248Q, R248W R273H	Gain of function	N.A.	Broad spectrum	N.A.	<i>In vivo</i>	(65, 138, 139)
Patient derived iPSCs	G245D	Gain of function	N.A.	Osteosarcoma	N.A.	<i>In vitro</i>	(122)

Table 1. Current LFS Disease Models

Abbreviations: LOH, loss of heterozygosity; N.A., not available.

1.5 Modeling disease with pluripotent stem cells

In 1998, Thomson and colleagues isolated human ESCs (see Glossary) from blastocysts and developed a defined culture system to maintain the cells *in vitro* (152), opening a new avenue for medical research. Later, in 2006–2007, a breakthrough by the laboratories of Yamanaka and Thomson heralded the development of a new kind of pluripotent cells – induced pluripotent stem cells (iPSCs) (150, 151, 153). Both groups demonstrated that somatic cells (e.g., dermal fibroblasts and peripheral blood) could be reprogrammed to an ES-like cell state using a defined transcriptional factor cocktail (Yamanaka's OCT4, SOX2, KLF4, c-MYC; or Thomson's OCT4, SOX2, NANOG, LIN28) (154). Over the past decade, subsequent advances facilitated the generation of iPSCs with chemicals, microRNA and modified RNA, or other gene delivery systems (retroviruses,

adenoviruses, Sendai virus, transposons, and plasmids) (154). Applications for iPSCs include regenerative medicine, disease modeling, drug screening, and personalized therapy.

The unique combination of pluripotency and self-renewal distinguishes PSCs, including both ESCs and iPSCs, from all other cells. The unlimited proliferative potential of these undifferentiated cells provides an arbitrarily large source of experimental material, while their pluripotency allows them to be coaxed into forming all adult tissue types. Well-defined protocols, including directed differentiation and organoid cultures have been developed to derive many major target tissues and cell types from PSCs of endodermal (liver, small intestine, stomach, thyroid, and lung), mesodermal (muscle, bone, cartilage, kidney, and blood), or ectodermal (epidermis, retinal, and cerebral tissue) lineages (155-157). PSCs provide unparalleled advantages as a model system, allowing investigators to study a cell continuously from the moment it differentiates from a multipotent progenitor into a differentiated cell type of interest. The relevant genetic background for the model system can be introduced into PSCs using two primary strategies. In one approach, somatic cells from patients with genetic disorders are used to derive iPSC lines. These patient-derived iPSCs and their derivative differentiated tissues are then used to recapitulate a disease phenotype in vitro or shed light on disease-relevant mechanisms (158). This approach has been applied successfully to study the genetic causes of neurodegeneration (159-161), mental disorder (162), heart disease (163-166), and metabolic disorders (167).

While the field of PSC-derived cancer research remains in its infancy, a number of PSC-derived cell lines have been generated to model disorders with a cancer predisposition. Several groups have applied patient-derived iPSCs and/or engineered PSCs to phenocopy cancer features, explore disease mechanisms, and screen potential therapeutic drugs (122, 168-171) (**Table 2**). Their experience highlights the potential of human PSCs in cancer studies by overcoming limitations related to availability of patient samples or translation of results from animal models or cell lines with inappropriate genetic backgrounds.

1.6 Modeling cancer with pluripotent stem cells

Over the past 40 years, researchers have used cancer cell lines, patient samples, and small organism models (e.g., fruit fly, zebrafish, and mouse) to study the molecular mechanisms of cancer initiation, progression, and metastasis, but the complexity of the cancer genome and differences among species frequently limit clinical translation. Although there are iPSC models for a number of genetic diseases that predispose to cancer, to date, relatively few of these systems have been used to explore mechanisms of oncogenesis.

Li–Fraumeni syndrome

Li–Fraumeni syndrome (LFS) is an autosomal dominant inherited cancer syndrome that is characterized by early onset of a variety of tumor types, including soft-tissue sarcoma and osteosarcoma, breast cancer, brain tumors, leukemia, and adrenocortical carcinoma (3). Our group established a model of LFS using patient-derived iPSCs to delineate mechanisms of mutant p53 in osteosarcoma

(122). In this system, osteoblasts differentiated from LFS iPSC derived mesenchymal stem cells (MSCs) recapitulate osteosarcoma features, including defective osteoblastic differentiation and tumorigenic ability. Gene expression in LFS osteoblasts is also similar to the expression profile in primary osteosarcomas, particularly the more aggressive phenotypes. LFS-derived osteoblasts are free of cytogenetic rearrangements, permitting study of early oncogenic mechanisms prior to accumulation of secondary genomic alterations. Expression of the long noncoding RNA H19 had been previously linked to p53 activity (120) and transcriptome analysis suggested impaired expression of H19 in LFS osteoblasts. Further functional studies showed that H19 is essential for normal osteogenesis and inhibition of tumorigenesis. The LFS iPSC disease model uncovered a previously unidentified role of p53 in osteogenic differentiation defects and tumorigenesis.

Noonan syndrome

Noonan syndrome (NS) is an autosomal dominant disorder characterized by a wide spectrum of congenital heart abnormalities, short stature, facial dimorphism, and predisposition to hematological malignancies. A subset of NS patients will develop juvenile myelomonocytic leukemia (JMML), an aggressive myelodysplastic and myeloproliferative neoplasm (172). Mulero-Navarro *et al.* (168) investigated the molecular mechanisms involved in NS-associated JMML harboring PTPN11 mutations using hematopoietic cells derived from NS/JMML patient-specific iPSCs. These hematopoietic cells recapitulated several JMML characteristics including hypersensitivity to granulocyte-macrophage colony-

stimulating factor and increased myeloid population. Comparison of transcriptome profiles of controls and NS/JMML-derived CD33+ myeloid cells confirmed dysregulation of extracellular signal-regulated kinase (ERK) and Janus kinase/signal transducers and activators of transcription signaling (JAK/STAT) and proliferation of NS/JMML CD33+ myeloid cells. Expression levels of miR-15a and miR-223 were also elevated in these cells. Notably, dysregulation of miR-15a and miR-223 is commonly observed in mononuclear cells isolated from JMML patients harboring PTPN11 mutations. Using the NS/JMML iPSC model, Mulero-Navarro *et al.* (168) demonstrated that inhibition of these miRNAs could restore normal myelopoiesis, providing a novel therapeutic target for PTPN11-mutated JMML.

Myelodysplastic syndrome

Myelodysplastic syndrome (MDS) is a bone marrow disorder that leads to defective hematopoiesis and a disposition to develop anemia, cytopenia, and leukemia. Sporadic loss of one copy of the long arm of chromosome 5 [del(5q)] and/or chromosome 7 [del(7q)] is a characteristic cytogenetic abnormality in MDS (173). Kotini *et al.* (169) established del(7q) MDS iPSCs from patient hematopoietic stem cells with loss of chromosome 7q and iPSCs derived from normal fibroblast isogenic controls. iPSCs with del(7q) recapitulated the phenotype of impaired myeloid lineage differentiation seen in MDS. This defective differentiation potential could be reproduced by engineering hemizyosity of definite 7q segments in normal iPSCs and could be rescued by spontaneous acquisition of an extra chromosome 7. Through phenotype-rescue screening, Kotini *et al.* (169) identified

HIPK2, ATP6V0E2, LUC7L2, and EZH2 as haploinsufficient genes involved in del(7q) MDS-associated hematopoietic defects.

Diffuse intrinsic pontine gliomas

Diffuse intrinsic pontine gliomas (DIPGs) are rare highly aggressive pediatric brain tumors that arise from glial tissue. Somatic p.Lys27Met substitution in histone 3.3 (H3.3K27M) is commonly detected in patients with DIPGs and is associated with poor survival (174, 175). Funato et al. (170) engineered human ESC-derived neural progenitor cells (NPCs) with heterozygous H3.3K27M mutations. To mimic genetic alterations found in clinical samples of H3.3K27M-mutated DIPGs, ESC-derived NPCs were transduced with lentiviruses also carrying constitutively active PDGFRA (D842V) and p53 small hairpin RNA. In this NPC model, H3.3K27M expression synergized with PDGFRA activation and p53 loss, culminating in neoplastic transformation. Genome-wide analyses of H3.3K27M-transformed NPCs revealed that they maintain both an undifferentiated epigenome structure and a primitive stem cell gene signature, enabling their tumorigenic potential. Using a small-molecule chemical library screen of compounds targeting epigenetic regulators, they identified the MEN1 inhibitor MI-2 as a potential drug for the subset of DIPGs harboring the H3.3K27M mutation. This study demonstrates the potential of PSCs for drug screening.

Glioblastoma multiforme

Glioblastoma multiforme (GBM), also known as Grade IV astrocytoma, is a highly malignant brain tumor derived from glial cells. While GBMs are genetically very

diverse, mutations in PTEN are common and correlate with increased invasion, drug resistance, and tumor recurrence (176). Duan *et al.* (171) engineered PTEN-deficient ESCs using a TALEN-based genome editing methodology and derived neural stem cells (NSCs) to model GBM. PTEN-deficient NSCs displayed the GBM-associated gene signature and formed intracranial tumors in vivo. Duan *et al.* (171) found that elevated levels of PAX7 contributed to neoplastic transformation by producing more aggressive phenotypes. Elevated PAX7 expression can be explained directly by PTEN deficiency since PTEN interacts with CREB/CBP and co-occupies the PAX7 promoter. Screening for anticancer compounds in PTEN-deficient NSCs suggested mitomycin C as a potential drug.

Disease	Inheritance	Defected Gene	Cancer Type	Key Model Findings in Cancer	Refs
Diffuse intrinsic pontine gliomas	Sporadic	<i>H3.3</i>	Brain tumor	Undifferentiated epigenome structure and a primitive stem cell gene signature in NPCs with H3.3K27M expression, PDGFRA activation and p53 loss	(170)
Glioblastoma multiform	Sporadic	<i>EGFR, PIK3CA, PTEN, and TP53</i>	Brain tumor	Elevated PAX7 and GBM-associated gene signature in PTEN-deficient NSCs	(171)
Li-Fraumeni syndrome	Autosomal dominant	<i>TP53</i> and <i>CHEK2</i>	Osteosarcoma, breast cancer, brain tumor, and soft tissue sarcoma	Impaired expression of H19 and osteosarcoma signature in LFS osteoblasts	(122)
del(7q)-Myelodysplastic syndrome	Sporadic	Chromosome 7q	Leukemia	Impaired myeloid lineage differentiation in del(7q) iPSC cells dependent on HIPK2, ATP6V0E2, LUC7L2 and EZH2	(169)
Noonan syndrome	Autosomal dominant	<i>PTPN11, BRAF, KRAS, NRAS, RAF1, and SOS1</i>	Leukemia	Proliferation of CD33+ myeloid cells and elevated miR-15a and miR-223 in NS/JMML hematopoietic cells	(168)

Table 2. Established PSCs models of cancer or diseases that predispose to cancer.

1.7 Personalizing cancer therapy through precise genome editing

Advances in genomics have led to an exponential increase in available cancer genomic data and finally directed us to the gene mutations that drive cancer. In some cases, mutations found in only a fraction of cells extracted from a single patient tumor sample can be identified. Nevertheless, translation of this knowledge into personalized therapy is far from reality. One of the biggest bottlenecks is how to convert knowledge of a specific genomic alteration into a therapeutic assay against which therapies can be targeted (177). Hundreds of *TP53* mutations have been detected in both germline (26) and sporadic tumors (61), but collecting samples from all these patients and assembling them into a biobank of LFS iPSCs would entail a substantial research endeavor.

Precise genome editing tools such as zinc-finger nuclease (ZFNs), transcription activator-like effector nucleases (TALENs), and clustered, regularly interspaced, short palindromic repeat/Cas9 (CRISPR/Cas9) present an alternative way around this bottleneck. These site-specific nucleases (SSNs) have proved their power in facilitating site-directed mutagenesis as well as in correcting mutations in PSCs, and are beginning to revolutionize fields of biomedical research (178-180). By increasing the diversity of genetic diseases available to study and model, these genome editing tools are facilitating the discovery of therapeutics.

Specific p53 mutations can be engineered into WT pluripotent stem cells (PSCs; including ESCs and iPSCs) by using genome editing tools, and can thus provide a wide and varied collection of mutant p53 PSCs against which candidate drugs can be screened and tested. Establishment of such a collection of mutant p53

PSCs will allow the testing of existing compounds that target specific p53 mutants (discussed above) on a wider range of p53 mutants (**Figure 3**). This collection will also facilitate screening and testing of novel potential therapeutics in a more targeted fashion. Finally, with preclinical data that clearly defines the p53 mutants for which a therapy would be expected to be successful, the cost of conducting clinical trials can be dramatically reduced through better patient stratification.

While iPSC technology offers unique advantages in modeling disease down to the genetic background of a particular patient, this specificity can be a double-edged sword. Genetic diversity between individuals often complicates the interpretation of findings across multiple iPSC lines. On the other hand, genome-edited PSCs, either from well-characterized ESCs or iPSCs from healthy subjects, have proved to be useful in revealing disease-relevant phenotypic differences while minimizing the variability found across patient-derived iPSC lines. For instance, introduction of *KCNH2* mutations into human ESCs (177) or integration of *KCNQ1* and *KCNH2* dominant negative mutations (181) into WT PSCs recapitulates the long-QT syndrome phenotype when the PSCs are differentiated into cardiomyocytes. Deletion of the kidney disease genes *PKD1* or *PKD2* induces cyst formation in a PSC-derived kidney organoid model, recapitulating the human disease phenotype (182). These successful research examples suggest that PSCs with various *TP53* mutations have great potential in elucidating the pathogenesis of mutant p53 associated cancers, facilitating the identification of potential drug targets for tumors with different p53 mutations.

Chapter 2 Materials and Methods

Copyright information:

Contents of Chapter 2.1, 2.14 and 2.16 are based on Zhou R, Xu A, Tu J, Liu M, Gingold JA, Zhao R, Lee DF. 2018. Modeling Osteosarcoma Using Li-Fraumeni Syndrome Patient-derived Induced Pluripotent Stem Cells. J Vis Exp. 13;(136). I am the first author of this article. According to this journal, “authors own the copyright to the written article”.

2.1 Generation of LFS iPSCs

Fibroblasts obtained from LFS patients were cultured and maintained in fibroblast culture medium (**Table 3**). Fibroblast reprogramming were performed by transducing Sendai virus expressing the four reprogramming factors OCT4, SOX2, KLF4, and c-MYC (CytoTune iPS 2.0 Sendai Reprogramming Kit, Invitrogen) according to manufacturer protocol. Inoculate the transduced cells on irradiated CF1 mouse embryonic fibroblast (MEF) and cultured with hESC medium (**Table 3**). Wait for iPSCs clones big enough to be observed by the naked eye and then pick the iPS clones into feeder-free culture condition. The reprogrammed iPSCs were cultured for at least 10 passages to be characterized.

2.2 iPSC/hESC culture in feeder culture condition (on mouse embryonic fibroblast)

iPSCs, hESCs and the engineered clones were cultured on mouse embryonic fibroblasts (MEFs) in hESC medium (**Table 3**) and maintained at 37 °C in a humidified 5% CO₂ incubator. Cells were passaged using Accutase cell

detachment solution (Corning) when reaching 85% confluence. Mouse embryonic fibroblast (MEF) culture dishes were prepared one day before cell passaging. Tissue culture dishes were coated with 0.1% gelatin at room temperature for 30 min. The gelatin was aspirated after coating. 6.7×10^5 irradiated CF1 MEFs (Thermo Fisher) were seeded per 100 mm dish using MEF culture medium hESC medium with 2 μ M ROCK inhibitor Thiazovivin (Calbiochem) to improve survival of dissociated cells. Culture medium was then changed to hESC medium the following day. hESC medium was changed every other day. Cells were passaged every 5–7 days at a 1:10 ratio.

2.3 iPSC/hESC culture in feeder-free culture condition (iPS-Brew XF medium)

iPSCs, hESCs and the engineered clones were cultured on Matrigel (Corning)-coated plates in StemMACS™ iPS-Brew XF medium (Miltenyi Biotec) and maintained at 37 °C in a humidified 5% CO₂ incubator. Cells were passaged using StemMACS™ Passaging Solution XF (Miltenyi Biotec) when reaching 85% confluence. The plates were pre-coated with basement membrane matrix coating solution (**Table 3**) for 1 hour at room temperature. hESC medium with 2 μ M ROCK inhibitor Thiazovivin (Calbiochem) was used to improve survival of dissociated cells. Culture medium was then changed to StemMACS™ iPS-Brew XF medium the following day. StemMACS™ iPS-Brew XF medium was changed every other day. Cells were passaged every 5–7 days at a 1:10 ratio.

Name of medium/solution	Volume
Fibroblast Medium (500 mL)	
DMEM	440 mL
Heat-inactivated FBS	50 mL
Antibiotics(Pen/Strep) (100x)	5 mL
Nonessential Amino Acid (100x)	5 mL
2-Mercaptoethanol	3.5 μ L
MEF/MSC Culture Medium (500 mL)	
DMEM	440 mL
Heat-inactivated FBS	50 mL
Antibiotics(Pen/Strep) (100x)	5 mL
L-Glutamine (100x)	5 mL
hESC medium (500 mL)	
DMEM/F-12	384.5 mL
KnockOut Serum Replacement	100 mL (total: 20%)
Nonessential Amino Acid (100x)	5 mL
Antibiotics (Pen/Strep) (100x)	5 mL
L-Glutamine (100x)	5 mL
bFGF (10 μ g/mL)	500 μ L
2-Mercaptoethanol	3.5 μ L
MSC Differentiation Medium (500 mL)	
KnockOut DMEM/F-12 or DMEM/F-12	445 mL
KnockOut Serum Replacement	50 mL
bFGF (10 μ g/mL)	500 μ L (10 ng/mL)
PDGF-AB (25 μ g/mL)	200 μ L (10 ng/mL)
Nonessential Amino Acid (100x)	5 mL
2-Mercaptoethanol	3.5 μ L
Osteoblast Differentiation Medium (ODM) (500 mL)	
α MEM	395 mL
Heat-inactivated FBS	50 mL
10 mM β -Glycerophosphate	50 mL (1.08 g in 50 mL α MEM)
0.1 μ M Dexamethasone (Light Sensitive)	10 μ L of 5 mM dexamethasone
200 μ M Ascorbic Acid (Light Sensitive)	100 μ L of 1 mM ascorbic acid
Antibiotics (Pen/Strep) (100x)	5 mL

Table 3. Compositions of culture medium and solution used in this study.

Name of medium/solution	Volume
Matrigel coating solution (50 mL)	
Basement Membrane Matrix	2 mL
DMEM/F-12 (pre-cold 4 °C)	48 mL
Osteoblast Detachment Solution (50 mL)	
0.25% Trypsin-EDTA	25 mL
Collagenase II Solution (1 mg/mL)	25 mL
Embryoid body medium (EB medium) (500 mL)	
IMDM	390 mL
KnockOut Serum Replacement	100 mL
Nonessential Amino Acid (100x)	5 mL
2-Mercaptoethanol	3.5 µL
Antibiotics (Pen/Strep) (100x)	5 mL
MammoCult based embryoid body medium (mEB medium) (500 mL)	
MammoCult medium (StemCell Technologies)	500 mL
Heparin (2 mg/mL, StemCell Technologies)	1mL
Hydrocortisone Stock Solution (StemCell Technologies)	2.5 mL
EDTA dissociation solution (50 mL)	
5M EDTA	50 µL
DPBS	50mL

Note: Prepare osteoblast detachment solution fresh right before use.
Collagenase II solution is stored at -20 °C for up to 6 months.

Table 3. Compositions of culture medium and solution used in this study

(continued).

2.4 Immunofluorescent staining

Cells were fixed with 4% paraformaldehyde for 15 minutes at room temperature, blocked with 10% serum in Dulbecco's phosphate-buffered saline (DPBS) supplemented with 0.01% Tween-20 (Sigma) (DPBST) at room temperature for 1 hour. After blocking, cells were incubated with the indicated primary antibodies (**Table 4**) at 4 °C overnight. Cells were then washed with DPBST 3 times at room temperature, and incubated with corresponding secondary antibodies at room temperature for 1 hour. DAPI counterstaining was performed by incubating cells with 3 µM DAPI (Thermo Fisher) diluted in DPBS at room temperature for 5 minutes. The results were visualized by Leica DMI8.

Antibody Name	Vender	Catalog #	Dilution
NANOG	R&D System	AF1997	1:500
OCT4	Santa Cruz	sc-9081	1:300
SSEA-4 PE-conjugated	R&D System	FAB1435P	1:600
TRI-1-81	DB Biosciences	560123	1:600
Donkey Anti-Goat IgG	Jackson ImmunoResearch	705-545-003	1:500
Goat Anti-Rabbit IgG	Jackson ImmunoResearch	111-545-144	1:500
CD105	eBioscience	12-1057-42	1:500
CD44	DB Biosciences	555478	1:500
CD73	DB Biosciences	550257	1:500
CD166	DB Biosciences	560903	1:500
CD24	DB Biosciences	555427	1:500
AP-2α (3B5)	Santa Cruz	sc-12726	1:500
AP2 gamma	Abcam	ab76007	1:500
Cytokeratin 18	Abcam	ab133263	1:500
Anti-HLA-ABC-PE	Miltenyl Biotec (MACS)	130-101-446	1:300

Table 4. Antibodies used in immunofluorescent staining.

2.5 SeV genome and transgenes detection

Total mRNA was isolated using TRIzol (Invitrogen) following the manufacturer's instruction. Reverse transcription reaction using 1 µg of RNA were performed using an iScript reverse transcription kit (Bio-Rad). PCR reaction (condition indicated in **Table 3**) were performed using the primers listed in **Table 5**.

Step	Temperature	Time	Cycle
Denaturation	95 °C	30 seconds	
Annealing	55 °C	30 seconds	35
Elongation	72 °C	30 seconds	

Target	Primer Sets
SeV	Forward: GGATCACTAGGTGATATCGAGC Reverse: ACCAGACAAGAGTTTAAGAGATATGTATC
<i>KOS</i> (<i>KLF4/OCT4/SOX2</i>)	Forward: ATGCACCGCTACGACGTGAGCGC Reverse: ACCTTGACAATCCTGATGTGG
<i>KLF4</i>	Forward: TTCCTGCATGCCAGAGGAGCCC Reverse: AATGTATCGAAGGTGCTCAA
<i>c-MYC</i>	Forward: TAACTGACTAGCAGGCTTGTCG Reverse: TCCACATACAGTCCTGGATGATGATG

Table 5. PCR reaction and primers used in SeV genome and transgenes detection.

2.6 Alkaline phosphatase staining (AP staining)

Alkaline phosphatase activity of generated iPSCs, hESCs or differentiated MSCs were examined using Alkaline Phosphatase Staining Kit II (Stemgent) following the manufacturer protocol.

2.7 Quantitative real-time PCR

Total mRNA was isolated using TRIzol (Invitrogen) following the manufacturer's instruction. 1 µg of RNA was used for cDNA synthesis using the iScript cDNA synthesis kit (Bio-Rad). Real-time PCR analysis was performed on a CFX96 machine (Bio-Rad) using the SYBR Green PCR Master Mix (Bio-Rad). The PCR reaction consisted of 10 µl SYBR Green PCR Master Mix, 1 µl of 10 µM forward and reverse primers, and 1 µl of diluted template cDNA (1:3 dilution in water). The RT-PCR reaction was performed using the following protocol: 50 °C for 10 min, 95 °C for 5 min, 40 cycle of 95 °C for 10 s and 60 °C for 30 s, respectively, and 95 °C for 10 s. Samples were analyzed in triplicate and normalized to GAPDH expression. The primer sequences are shown in **Table 6**.

Target	Primer Sets
<i>NANOG</i>	Forward: TTTGTGGGCCTGAAGAAACT Reverse: AGGGCTGTCCTGAATAAGCAG
<i>SOX2</i>	Forward: AGAAGAGGAGAGAGAAAGAAAGGGAGAGA Reverse: GAGAGAGGCAAACCTGGAATCAGGATCAAA
<i>OCT4</i>	Forward: AACCTGGAGTTTGTGCCAGGGTTT Reverse: TGAACCTCACCTTCCCTCCAACCA
<i>DPPA4</i>	Forward: GACCTCCACAGAGAAGTCGAG Reverse: TGCCTTTTTCTTAGGGCAGAG
<i>REX1</i>	Forward: GCCTTATGTGATGGCTATGTGT Reverse: ACCCCTTATGACGCATTCTATGT
<i>ALPL</i>	Forward: GGGACTGGTACTCAGACAACG Reverse: GTAGGCGATGTCCTTACAGCC
<i>COL1A1</i>	Forward: GTGCGATGACGTGATCTGTGA Reverse: CGGTGGTTTCTTGGTCGGT
<i>PTH1R</i>	Forward: AGTGCGAAAAACGGCTCAAG Reverse: GATGCCTTATCTTTCCTGGGC
<i>BGLAP</i>	Forward: GCGCTACCTGTATCAATGG Reverse: GCGCTACCTGTATCAATGG
<i>SFRP2</i>	Forward: AACCTACATCAACCGAGATACCA Reverse: CTTCAGGTCCCTTTCGGACAC

Table 6. RT-PCR primers used in this study.

2.8 Karyotype analysis

iPSC, hESCs and the generated clones of 65% confluency were treated with KaryoMAX Colcemid Solution (Gibco) for 3 hours. Cell pellets were then carefully resuspended in hypotonic KCl solution (7.5 mM) for 8 minutes and fixed in Carnoy's fixative (3:1 methanol to glacial acetic acid). The G-banding karyotype was performed in Department of Pediatrics, Baylor College of Medicine, Texas Children's Cancer and Hematology Centers. Twenty metaphase chromosome spreads were classified according to the standard G-banding technique (450–500 nucleotide resolution).

2.9 *In vivo* teratoma formation assay

2×10^7 iPSCs, hESCs or engineered hESCs were resuspended in 100 μ l of ice cold $1 \times$ DPBS and then mixed with 100 μ l of phenol red-free Matrigel (Corning). The Matrigel-mixed cells were injected subcutaneously into both sides of flanks of immunocompromised nude mice (Charles River/Jackson Laboratory). Teratomas were excised 6 to 8 weeks after injection and fixed in 10% neutral buffer formalin. Tissue embedding and H&E staining were performed by HistoWiz (Brooklyn, NY).

2.10 Mycoplasma detection

Mycoplasma detection was performed using PCR Mycoplasma Detection Kit (Applied Biological Materials Inc) according to the manufacturer's protocol.

2.11 Short tandem repeat (STR) analysis

STR analysis was performed by Characterized Cell Line Core Facility at The University of Texas M.D. Anderson Cancer Center. The number of STRs at 14 loci,

namely AMEL, CSF1PO, D13S317, D16S539, D18S51, D21S11, D3S1358, D5S818, D7S820, D8S1179, FGA, TH01, TPOX and vWA were assessed.

2.12 Differentiation of iPSCs to mesenchymal stem cells (MSCs)

iPSC clones were mainlined in feeder culture condition for at least 2 weeks. Cultured iPSCs in 100 mm tissue culture dishes with 80 - 90% confluence were dissociated with Accutase cell detachment solution (Corning). MEF culture medium were added to neutralize the detachment solution and transfer cells in a new 100 mm dish. Incubate the cells at room temperature for 30 min to allow the MEFs to attach to the plate. After MEF removal, iPSCs were seed with MSC differentiation medium (**Table 3**) on 0.1% gelatin-coated plate to initiate MSC differentiation (Day 0). Change the MSC differentiation medium every two days to remove unattached and/or dead cells (Day 1-28).

Trypsinize differentiated MSCs with 0.25% Trypsin-EDTA and seed the cells on 0.1% gelatin-coated plate for MSC maturation (Day 28-45). When the MSCs display a fibroblast-like morphology, immunofluorescent staining of MSC surface markers CD44, CD73, CD105, and CD166 were performed to confirm success of MSC differentiation. Expand MSCs at a 1:3 ratio. Freeze MSCs from an early passage number after confirming MSC characteristics

2.13 Differentiation of mesenchymal stem cells (MSCs) to osteoblasts (OBs)

Begin osteogenic differentiation with MSCs cultured in 100 mm tissue culture dish to 95% confluency. Trypsinize MSCs with 0.25% trypsin-EDTA and plate proper number of MSCs on a culture plate in MSC culture medium (Day -1) (**Table 7**).

Change MSC culture to osteogenic differentiation medium (ODM) (Day 0) and change medium every two days during osteogenic differentiation process (Day 0 - Day 24).

Culture Plate	Seeding Density	Assay
12-well Plate	0.67x10 ⁴ cells per well	Alkaline phosphatase staining (AP staining)
6-well Plate	2x10 ⁴ cells per well	Alizarin red S staining (ARS staining) RT-PCR detection Preosteoblast markers: ALPL, COL1A1 Mature osteoblast markers: PTH1R, BGLAP
100 mm Dish	3-4.5x10 ⁵ cells per plate	<i>In vivo</i> tumorigenesis

Table 7. Seeding density of MSCs for osteoblastic differentiation.

2.14 Alizarin Red S (ARS) staining

Remove culture medium from each well and gently wash cells with 1 × DPBS, and fix cells in 4% paraformaldehyde for 15 minutes at room temperature. After three-time wash with ddH₂O, 1 mL of 40mM ARS were added for each well. Incubate at room temperature for 30 minutes with gentle shaking and visualize the staining results after ddH₂O wash with scanner or microscope.

2.15 *In vitro* soft agar assay (anchorage independent assay)

LFS and WT MSCs were cultured and passaged in 100 mm dish at a density 1.5 x 10⁵. Osteogenic differentiation was initiated for 7 days, and cells were lifted using 0.25% Trypsin-EDTA. 1 × 10⁴ cells or osteoblast detachment solution contacting collagenase II if cells are hard to dissociated into single cells (**Table 3**). Cells were then passed through 40 μm cell strainer to remove aggregated cells and

resuspended in osteoblast differentiation medium (ODM) with 0.5% low melting point agarose (Lonza). The cell suspensions were then plated in 12-well plates containing solidified 1% agarose in ODM. Control experiments were performed in parallel with MSCs in the same manner: cells were maintained in MSC culture medium throughout the experimental course. Cells were maintained in half-solidified condition for 35 days with medium changed every 3 days. Colony with diameter $\geq 50 \mu\text{m}$ was counted positive under a microscope. **Figure 4** illustrate the experiment setting of soft agar assay.

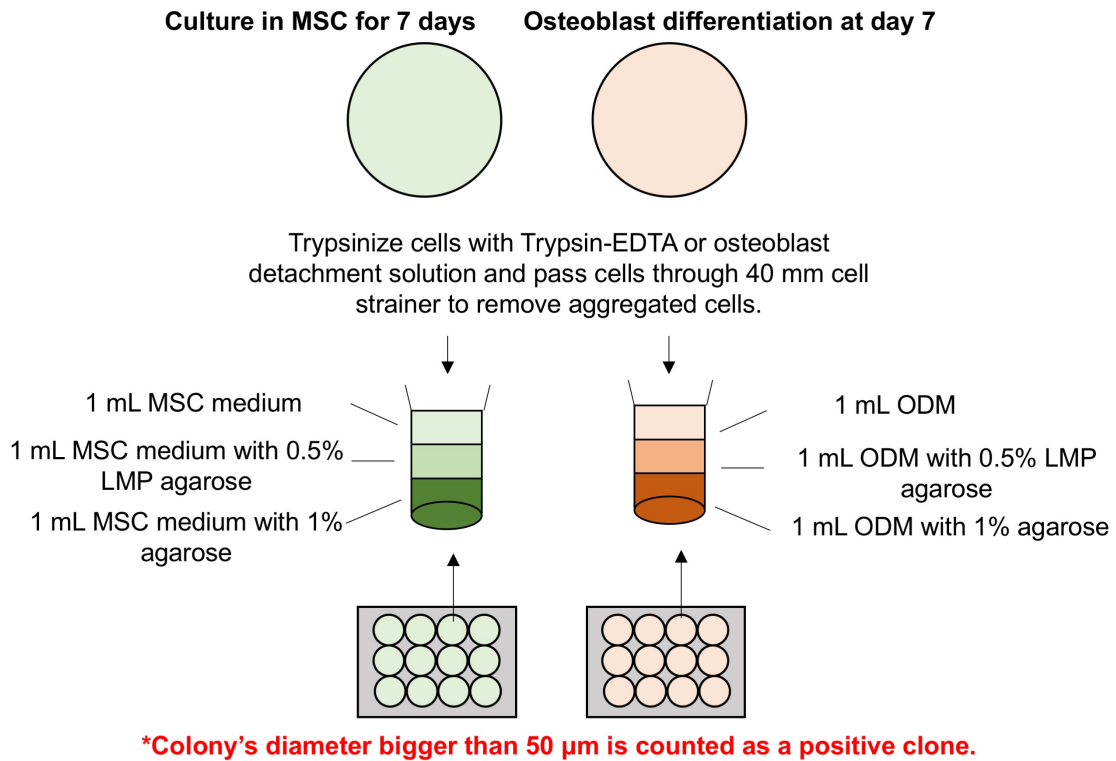


Figure 4. Illustration of *in vitro* soft agar assay.

2.16 *In vivo* xenograft tumor model of LFS MSC-derived osteoblasts

Seed 3 - 4.5 x 10⁵ MSCs in 100 mm tissue culture dish. Prepare five dishes for one subcutaneous injection (**Table 7**). Culture MSCs in ODM to differentiate MSCs to osteoblasts to Day 7 or Day 14. Trypsinize the cells with osteoblast detachment solution (**Table 3**) and pass the cells through a 70 µm cell strainer to remove aggregated cells.

For subcutaneous injection, resuspend the 1 x 10⁷ osteoblasts in 50 µL ice-cold 1x DPBS. Mix differentiated osteoblasts with 50 µL of phenol-red free basement membrane matrix (osteoblasts suspension and basement membrane matrix were mixed at a 1:1 ratio). For intratibial injection, resuspend the 2 x 10⁶ osteoblasts in 20 µL ice-cold 1x DPBS. Mix differentiated osteoblasts with 20 µL of phenol-red free basement membrane matrix (osteoblasts suspension and basement membrane matrix were mixed at a 1:1 ratio).

Anesthetize 8-week-old female immunocompromised NU/NU mice or 8-week-old female immunocompromised SCID mice in a chamber supplying 5% (v/v) inhaled isoflurane in 1 L/min of oxygen. After the animal becomes recumbent, switch the anesthetic delivery system to the nose cone, supplying 2% (v/v) inhaled isoflurane in 200mL/min of oxygen. Use 26 G needle to perform subcutaneous injection of basement membrane matrix-mixed LFS osteoblasts into one side of hind legs of 8-week-old immunocompromised NU/NU mice. For intratibial injection, used 26 G needle to inject basement membrane matrix-mixed LFS osteoblasts into the proximal tibial area of 8-week-old immunocompromised SCID mice.

Developed tumors were dissected around 6-8 weeks after injection. Tumor were fixed overnight in 10% neutral buffer formalin, embedded in paraffin, sectioned. Various staining methods were used to examined the tumor including Hematoxylin and Eosin (H&E) staining, Picro Sirius Red staining, and von Kossa staining.

2.17 *In vitro* culture of LFS osteoblast derived tumors

Developed tumors were dissected and chopped into pieces with autoclaved blades. Resuspend the tumor pieces in 1 x DPBS and transfer into a 15mL tube and centrifuge at 230 x g at 4 °C for 4 minutes. Digest the tumor with 1 mg/mL collagenase I (Millipore) at 37 °C for 30 minutes, and add 0.25% Trypsin-EDTA for 10 minutes to further dissociate tumors. Neutralize the digested tumor cells with ODM and seed the cells in 60 mm culture dish. LFS osteoblast derived tumor cells will proliferate around 3-4 weeks after seeding. Passage the cells at 1:3 ratio.

2.18 Generation of TALEN and CRISPR/Cas9 guides and WT/mutant p53 donor vector

The TALEN guides targeting different region of *TP53* was designed using ZiFiT Targeter Version 4.2 (<http://zifit.partners.org/>). TALEN guides targeting sites used in this study were summarized in **Table 8**, these TALEN guides were assembled using REAL Assembly TALEN kit (Addgene) and inserted into JDS vectors according to protocol (183).

The CRISPR/Cas9 guided RNA (double nickase design) targeting different region of *TP53* were designed using Guide Design Resources (<https://zlab.bio/guide-design-resources>). CRISPR/Cas9 guides targeting sites used in study were

summarized **Table 8**. The designed guides were then constructed into pX335-U6-Chimeric_BB-CBh-hSpCas9n(D10A) following Zhang Lab General Cloning Protocol available at Addgene (<https://www.addgene.org/crispr/zhang/>).

Homologous arms were amplified using H1 hESC genomic DNA isolated by the PureLink Genomic DNA Mini Kit (Thermo Fisher). The primers used to amplify the left and the right homologous arms of different donors used in this study are shown in **Table 9**. PCR products were run on 0.8% agarose gel, purified and ligated into pGEM-T Easy vector.

To generate R248W mutant donor arm, site-directed mutagenesis was performed on left homologous. Homologous arms were then digested with EcoRI (left homologous arm) and BamHI and NotI (right homologous arm), respectively, and ligated into the pFNF (Frt-EM7-NeoR-Frt) vector. To generate R282W mutant donor arm, site-directed mutagenesis was performed on right homologous. Homologous arms were then digested with Sall and EcoRI (left homologous arm) and BamHI and NotI (right homologous arm), respectively, and ligated into the pFNF (Frt-EM7-NeoR-Frt) vector. To generate delG mutant donor arm, site-directed mutagenesis was performed on left homologous. Homologous arms were then digested with HindIII and EcoRI (left homologous arm) and BamHI and NotI (right homologous arm), respectively, and ligated into the pFNF (Frt-EM7-NeoR-Frt) vector. The primers used for mutagenesis in study were summarized in **Table 9**.

Guides	Targeting site of <i>TP53</i>
Targeting intron 5	Correction of mutant p53 (Y205C)
TALEN pair	Upstream: Downstream:
Targeting intron 7	Correction of mutant p53 (G245D) Generation of homozygous p53 R248W mutant
TALEN pair	Upstream: 5'-TCCAGGTCAGGAGCCAC-3' Downstream: 5'-GGCCTGCTGTGCCCA-3'
CRISPR/Cas9 Pair	Upstream: 5'-TGGCCACCTCTTACCGAT-3' Downstream: 5'- CCTCTCATCATCCCCGGCGGC-3'
Targeting intron 8	Generation of homozygous p53 R282W mutant
TALEN pair	Upstream: 5'-TTTCCTTACTGCCTCT-3' Downstream: 5'-CTATCCTGAGTAGTGGTA-3'
Targeting intron 9	Create or correct mutant p53 (delG) in LFS iPSCs
TALENs Pair 1	Upstream: 5'-TTTCCAGTCTAACACTCA-3' Downstream: 5'-TTGACTGTTTTACCTGCA-3'
TALENs Pair 2	Upstream: 5'-TGGAAAGTTTCCAGTCTA-3' Downstream: 5'-TTCTTCTTGACTGTTTTA-3'
CRISPR/Cas9 Pair 1	Upstream: 5'-GTCTAACACTCAAATGCCG-3' Downstream: 5'-CAATTGGGGCATTGCCATC-3'
CRISPR/Cas9 Pair 2	Upstream: 5'-GTCTAACACTCAAATGCCG-3' Downstream: 5'-GACTGTTTTACCTGCAATTG-3'

Table 8. Summary of the TALEN and CRISPR/Cas9 guides targeting different *TP53* genomic region.

Primer	Forward/Reverse primer (5'–3')
Correction of mutant p53 (Y205C)	
5p53-L002-1 kb/ for left homologous arm	GTCGACGGGACAGCCAAGTCTGTGACTTGCAC GGTC
3p53-L002-1 kb/ for left homologous arm	GAATTCGCCCTGTTCGTCTCTCCAGCCCCAGCT GCTC
5p53-R002-1 kb/ for right homologous arm	GGATCCTGGTTGCCAGGGTCCCCAGGCCTCT GATTCCTC
3p53-R00-1 kb/ for right homologous arm	GCGGCCGCACTGAGTGGGAGCAGTAAGGAGA TTCCCCGCC
Correction of mutant p53 (G245D)	
Generation of homozygous p53 R248W mutant	
5p53-L001-1 kb/EcoRI for left homologous arm	GAATTCGCGTCCGCGCCATGGCCATCTACAA GCAGTCACAG
3p53-L001-1 kb/EcoRI for left homologous arm	GAATTCAGGCCAGTGTGCAGGGTGGCAAGTG GCTCCTGACCT
5p53-R001-1 kb/BamHI for right homologous arm	GGATCCGCTGTGCCCCAGCCTCTGCTTGCCTC TGACCCCTGG
3p53-R001-1 kb/NotI for right homologous arm	GCGGCCGCCAGGCTAGGCTAAGCTATGATGTT CCTTAGATTAGG
5p53-R248W for R248W mutagenesis	TGCATGGGCGGCATGAACTGGAGGCCCATCCT CACCATC
3p53-R248W for R248W mutagenesis	GATGGTGAGGATGGGCCTCCAGTTCATGCCGC CCATGCA
Generation of homozygous p53 R282W mutant	
5p53-L003-1 kb/Sall for left arm	GTCGACCCTATGAGCCGCCTGAGGTCTGGTTT GCAA
3p53-L003-1 kb/EcoRI for left arm	GAATTCGAAATCAGGTCCTACCTGTCCCATTTA AAAAACCAGGCTC
5p53-R003-1 kb/BamHI for right arm	GGATCCCTTACTGCCTCTTGCTTCTTTTTCT ATCCTGAGTAGTG
3p53-R003-1 kb/NotI for right arm	GCGGCCGCCAAGGCAGGCAGATCACAAGGTC AGGAGTTCGAGAC
5p53-R282W for mutagenesis	GCCTGTCCTGGGAGAGACTGGCGCACAGAGG AAGAGAAT
3p53-R282W for mutagenesis	ATTCTTTCCTCTGTGCGCCAGTCTCTCCCAG GACAGGC
Create or correct mutant p53 (delG) in LFS iPSCs	
5p53-L008-1 kb/HindIII for left arm	AAGCTTCAGGAGCCACTTGCCACCCTGCACAC TGGC

3p53-L008-1 kb/EcoRI for left arm	GAATTCTTTTGAGTGTTAGACTGGAAACTTTCC ACTTGATAAGAGG
5p53-R008-1 kb/BamHI for right arm	GGATCCTGCCGTTTTCTTCTTGACTGTTTTACC TGC
3p53-R008-1 kb/NotI for right arm	GCGGCCGCGCTGAGCTGGGAGGATGGATGGA GCCTGGG
5p53-delG for mutagenesis	GAATATTTACCCTTCAGTACTAAGTCTTGGGA CCTC
3p53-delG for mutagenesis	GAGGTCCCAAGACTTAGTACTGAAGGGTGAAA TATTC

Table 9. Primers used to generate WT and p53 mutant donor vector.

2.19 T7 Endonuclease I assay

H1 hESC genomic DNA were isolated by the PureLink Genomic DNA Mini Kit (Thermo Fisher). PCR amplicons including nuclease (TALENs or CRISPR/Cas9 guides) target sites were generated using the forward primer: 5'-CGCTTCGAGATGTTCCGAGA-3' and reverse primer: 5'-AACTGAGTTTGACGGGGGTC-3'. PCR amplicons were then denatured by heating and annealed to form heteroduplex DNA using a thermocycler and then digested with T7 endonuclease 1 (New England Biolabs) for 15 minutes at 37°C and then analyzed using agarose gel electrophoresis.

2.20 Generation of engineered iPSC and hESC line by precise genome editing

To generate engineered iPSC or hESC line, 10^7 H1 iPSCs/hESCs were re-suspended with 0.6 ml Embryo Max Electroporation Buffer (Millipore), mixed with 50 µg of donor vector and 5 µg (10 µg) of each TALEN or CRISPR/Cas9 encoding plasmid and electroporated at 300V/500uF in BIO-RAD Gene Pulser Xcell System.

The electroporated cells were immediately dispensed into 100 mm MEF plates in hESC medium (**Table 1**) supplemented with 2 μ M ROCK inhibitor Thiazovivin. Cells were then selected with 50 μ g/ml G418 for 2-3 weeks and medium was changed every two days until colonies emerged. Individual clones were then picked and expanded. The correctly inserted colonies were identified by PCR using specific primer sets shown in **Table 10**.

Primer	Sequence
3FNF-N1	TCCAGACTGCCTTGGGAAA
5FNF-C1	GGGGAGGATTGGGAAGACAA
p53_4FM13	TGTAAAACGACGGCCAGTCTTCCTGAAAACAA CGTTCTG
p53_5FM13	TGTAAAACGACGGCCAGTCTAGCTCGCTAGTG GGTTGC
p53_6FM13	TGTAAAACGACGGCCAGTCCACCATGAGCGCT GCTCAG
3p53_7FM13	TGTAAAACGACGGCCAGTGCCTCCCCTGCTTG CCACAG
5p53_7RM13	CAGGAAACAGCTATGACCGGGAGCAGTAAGG AGATTCC
3p53_8/9FM13	TGTAAAACGACGGCCAGTACCTCTTAACCTGT GGCTTC
5p53_8/9RM13	CAGGAAACAGCTATGACCTACAACCAGGAGCC ATTGTC
3p53_16821_RM13	CAGGAAACAGCTATGACCGCCCAGGAGGGTAT AATGAGCTA
3p53_17099_RM13	CAGGAAACAGCTATGACCGGTGCAGGCCTGTA GTTGAAGCAACT

Table 10. PCR primers used to identify correctly inserted colonies.

2.21 Western blot

Cells were lysed in lysis buffer (20 mM Tris-HCl, 100 mM NaCl, 1 mM EDTA, 0.5% NP-40, 0.5% Triton X-100, 1 mM phenylmethylsulfonyl fluoride, 1 mM NaF, 1 mM sodium orthovanadate, 1 μ g each of aprotinin, leupeptin, and pepstatin per ml) on

ice for 30 minutes and sonicated for 5 seconds at 20% intensity for 5-8 times. Generally, 15-30 µg protein lysate were resolved by various percentages of SDS-PAGE gels and then electrophoretically transferred (Bio-Rad) to PVDF membranes (Millipore). The membranes were then blocked by TBST buffer (150 mM NaCl, 10 mM Tris pH8.0, 0.1% Tween20) supplemented with 5% non-fat milk for 1 hour at room temperature prior to incubation with indicated primary antibodies (**Table 11**). Subsequently membranes were washed three times by TBST and incubated with secondary antibodies for 1 hour at room temperature and washed 3 times with TBST. Immunodetected bands on the membranes were recorded using film developer in darkroom after incubating with chemiluminescence (ECL) system (Roche Molecular Biochemicals).

Antibody Name	Vender	Catalog #	Dilution
p53	Santa Cruz	sc-126	1:1000
AP2 gamma	Abcam	ab76007	1:1000
Cytokeratin 18	Abcam	ab133263	1:1000

Table 11. Antibodies used in western blot in this study.

2.22 Southern blot

Total genomic DNA of picked clones were isolated by the PureLink Genomic DNA Mini Kit (Thermo Fisher). 10 µg of genomic DNA were digest with restrict enzyme BamHI in 37 °C water bath for 16 hours. BamHI digestion resulted in two cleave sites upstream and downstream of neomycin resistant cassette (NeoR). The digested fragments were resolved by electrophoresis in a 0.7% agarose gel for 1 hour at 110 V, blotted using standard methods, and covalently bound to a Nylon+ membrane by UV exposure in an automated crosslinker.

DIG-labeled hybridization probes were synthesized from pFNF (Frt-EM7-NeoR-Frt) vector using primers (forward primer: 5'-AATGGGATCGGCCATTGAACAAGAT-3' and reverse primer: 5'-TCAGAAGAAGCTCGTCAAGAAGGCG-3') according to the manufacturer's protocol (Roche PCR DIG Probe Synthesis Kit, 11636090910). Crosslinked membrane was hybridized and washed as the manufacturer recommended (Roche DIG Easy Hyb, 11796895001). Hybridized membranes were subsequently treated with an anti-DIG antibody and bands on the membranes were recorded using film developer in darkroom after incubating with chemiluminescent substrate *CDP-Star* (Roche *CDP-Star*, ready-to-use, 12041677001).

2.23 Culture of embryoid bodies (EB) and MammoCult-derived embryoid bodies (mEBs)

hESCs (RUES2) and iPSCs were maintained in feeder-free system as described in Chapter 2.3 with growth factor-reduced BD Matrigel matrix and cultured in chemically-defined mTeSR1 medium (StemCell Technologies) for at least 2 weeks before EB or mEB formation. For EB culture, hESCs and iPSCs were lifted by Accutase cell detachment solution (Corning) and suspended in EB medium (**Table 3**); for mEB culture, the lifted hESCs and iPSCs were suspended in mEB medium (**Table 3**). Embryoid bodies were subsequently formed and cultured using AggreWell™400 (Stemcell Technologies) according to the manufacturer's instruction. Medium was changed every 3 days.

2.24 Chemical based differentiation of non-neural ectoderm

Cell Adaptation before differentiation:

iPSCs and hESCs were cultured on coated plates in Essential 8 medium (Thermo Fisher) and maintained at 37 °C in a humidified 5% CO₂ incubator for 4-5 weeks (~6-8 passages) before differentiation. Cells were passaged using EDTA dissociation solution (**Table 3**) when reaching 80% confluence. The plates were pre-coated with Vitronectin (0.5ug/cm², Thermo Fisher) overnight at 4 °C. E8 medium with 2 μM ROCK inhibitor Thiazovivin (Calbiochem) was used to improve survival of dissociated cells. Culture medium was then changed to E8 medium the following day. E8 medium was changed every day. Cells were passaged every 5–7 days at a 1:10 ratio.

Day –1 of differentiation:

iPSCs and hESCs with 80% confluent were detached using Accutase cell detachment solution (Corning) and passed through a 45-micron cell strainer. 250,000-300,000 cells per cm² in E8 medium were then plated with 10μM ROCK inhibitor Thiazovivin (Calbiochem) and maintained at 37 °C in a humidified 5% CO₂ incubator overnight.

Day 0-12 of differentiation:

Wash cells with PBS or Essential 6 medium (E6, Thermo Fisher) before starting the 12-day non-neural ectoderm differentiation (**Figure 5**). Cells were maintained in E6 medium containing 10 ng/ml BMP4 (R&D), 10μM SB431542 (SB, R&D) and 10μM SU-5402 (SU, Tocris Bioscience) on Day 0 (0-24hrs). The medium was then changed to E6 medium containing 10 ng/ml BMP4, 10μM SB and 10μM SU on

Day 1 (24-48hrs). Medium were changed every other day with E6 medium containing 5 ng/ml BMP4 and 10 μ M SB from Day 2-12.

2.25 Mammary-like organoid differentiation

10-day mEBs or 500 differentiated non-neural ectoderm cells were embedded in domed-shape, mixed Matrigel (2.5 mg/mL)/Collagen I (1 mg/mL) gel on the Nunclon delta surface culture plate (Sigma) (**Figure 5**). Mixed gel was composed of 3 portions of 10.1 mg/ml Matrigel and 1 portion of 4 mg/mL Collagen I (Advanced BioMatrix). The mixed Matrigel/Collagen gel embedded with mEBs/cells were then solidified at 37 °C in a humidified 5% CO₂ incubator and culture medium were added for 3D culture.

To induce mammary commitment, 3D gels were cultured in complete EpiCult B medium supplemented with 100 ng/ml parathyroid hormone (pTHrP, Peprotech) for 5 days; to induce branch and alveolar differentiation, the gels were cultured in complete EpiCult B medium (StemCell Technologies) supplemented with 1 μ g/ml hydrocortisone (Sigma), 10 μ g/ml insulin (Sigma), 50 ng/ml FGF10 (Peprotech), and 50 ng/ml HGF (Peprotech) for 25 days.

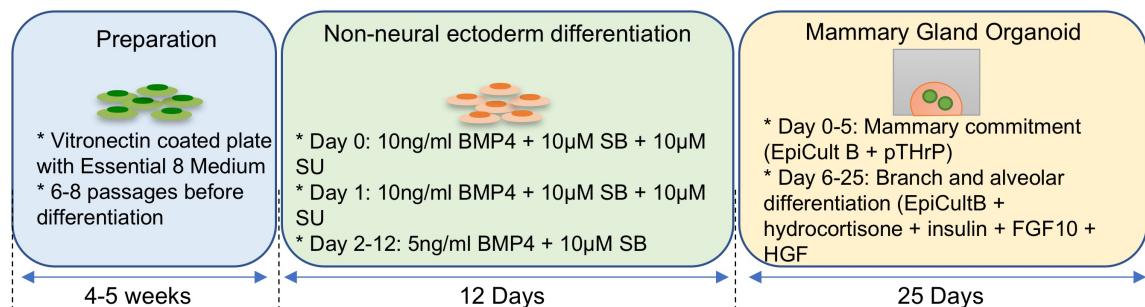


Figure 5. Schematic of non-neural ectoderm differentiation and mammary-like organoid differentiation.

2.26 Whole exome sequence and analysis

DNA isolation, library preparation, exome capture and sequencing

Total genomic DNA of MSCs, OBs and tumor derived cells were extracted using PureLink Genomic DNA Mini Kit (Thermo Fisher) according to the manufacture's instruction. Quality control, library construction, exome capture and sequencing was performed at Novogene Corporation.

For quality control, two methods were used for quality control: (1) agarose gel electrophoresis to test DNA degradation and potential contamination; (2) Qubit 2.0 were used to quantify the DNA concentration precisely.

Sequencing libraries were generated using Agilent SureSelect Human All ExonV6 kit (Agilent Technologies, CA, USA) following manufacturer's recommendations.

In brief, 1 µg genomic DNA were sheared into fragments with an average size of 180-280 base pairs (bp) using hydrodynamic shearing system (Covaris, Massachusetts, USA). Remaining overhangs were converted into blunt ends via exonuclease/polymerase activities and enzymes were removed. After adenylation of 3' ends of DNA fragments, adapter oligonucleotides were ligated. DNA fragments with ligated adapter molecules on both ends were selectively enriched in a PCR reaction. Captured libraries were enriched in a PCR reaction to add index tags to prepare for hybridization. Products were purified using AMPure XP system (Beckman Coulter, Beverly, USA) and quantified using the Agilent high sensitivity DNA assay on the Agilent Bioanalyzer 2100 system.

The qualified libraries were pooled into Illumina sequencers (Illumina HiSeq2000) and sequenced with 150-bp paired reads.

Pipeline for mapping, somatic mutation calling, and annotation

FASTQ files were mapped to the human reference genome HG19 using Burrows-Wheeler Aligner V0.7.15. Picard Tools (V2.9) were used to fix mate pairs and to compress, index, sort and generate BAM files. Local realignment around known indels identified in dbSNPv137 and the 1000 Genomes Project was performed using Indel Realigner (GATK v.3.3-0). 3 base quality was recalibrated with GATK Base Recalibrator (GATK v.3.3-0) to generate analysis-ready reads. Somatic variant calls were carried out using MuTect 2, comparing sequencing data by pairing MSCs with OBs and tumor derived cells respectively (**Figure 21A**). MuTect 2 was run with default parameters to generate analysis-ready variant, and functional annotation of somatic variant were carried out using ANNOVAR (184).

Network2Canvas, mutational signature analyses and Venn diagram

Pathway analysis and mutational signature analysis were performed using Network2Canvas (<http://www.maayanlab.net/N2C/>) (185) and web-based application MusiCa (<http://bioinfo.ciberehd.org/GPtoCRC/en/tools.html>) (186). Venn diagram was plotted using VENNY 2.1 (<http://bioinfogp.cnb.csic.es/tools/venny/>).

Chapter 3 Identification of bone cancer driver genes using Li-Fraumeni syndrome iPSCs

Copyright information:

Contents of Chapter 3.3-3.5 and 3.8 are based on Zhou R, Xu A, Tu J, Liu M, Gingold JA, Zhao R, Lee DF. 2018. Modeling Osteosarcoma Using Li-Fraumeni Syndrome Patient-derived Induced Pluripotent Stem Cells. *J Vis Exp.* 13;(136). I am the first author of this article. According to this journal, “authors own the copyright to the written article.”

3.1 Introduction

Recent advance in methodologies have made the modeling of human genetic diseases with patient derived induce pluripotent stem cells (iPSCs) feasible (122, 169, 187-190). Taking advantage of LFS patient iPSCs, our group have successfully delineated the fundamental pathological mechanism caused by mutant p53 in osteosarcoma (122) (**Figure 6**). This novel disease model platform is established by differentiating LFS iPSCs into MSCs then to osteoblasts (OBs), the cells from which osteosarcomas originate from. These LFS osteoblasts recapitulated the differentiation defects and oncogenic properties of osteosarcoma, creating “a bone tumor in a dish” (**Figure 6**). Interestingly, once differentiated into osteoblasts, genome-wide transcriptome analysis revealed that LFS osteoblasts expressed an osteosarcoma signature, resembling tumor samples obtained from osteosarcoma patients. These data show that the LFS iPSC disease model

successfully transforms clinical samples into cell line models, permitting studying early oncogenic mechanisms.

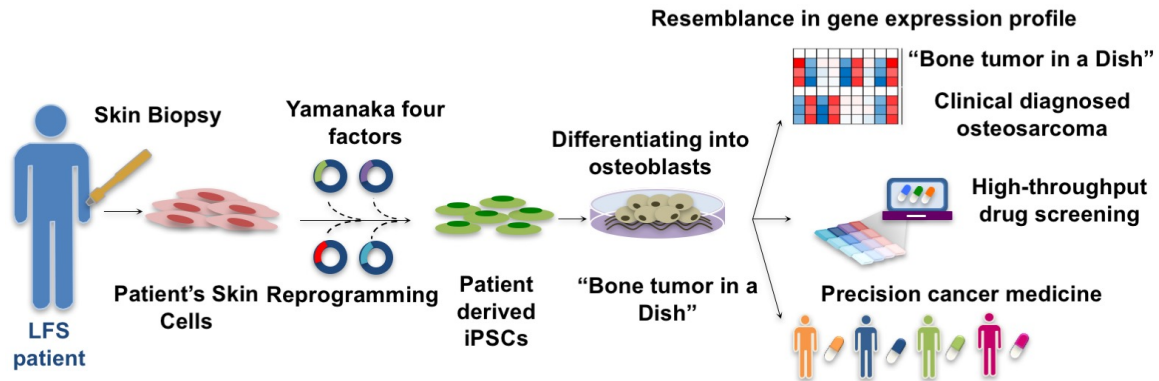


Figure 6. LFS iPSC-derived osteoblasts recapitulate osteosarcoma features and represent osteosarcoma signatures.

LFS iPSCs can be generated by somatic reprogramming of patient fibroblasts using Yamanaka four factors (OCT4, SOX2, KLF4, and c-MYC). Further differentiation of LFS iPSCs into mesenchymal stem cells then to osteoblasts can create “a bone tumor in a dish”. The differentiated LFS osteoblasts represent clinical diagnosed osteosarcoma gene signatures and recapitulate oncogenic properties of osteosarcoma. This novel disease model platform can be used for therapeutic screening and may facilitate identification of potential biomarker or therapeutic targets regarding clinical management of osteosarcoma

3.2 Hypothesis and experimental design

Based on previous studies, I hypothesize that genetic and epigenetic driver events accumulate during the LFS iPSC-derived MSCs to osteoblasts differentiation process and contribute to the LFS-associated osteosarcoma development. By differentiating LFS patient derived iPSCs to MSCs then to osteoblasts, it is hypothesized that LFS derived osteoblasts (sample B) will start to gain tumorigenic ability (**Figure 7**). Xenograft tumor model can be established from subcutaneous injection of LFS derived osteoblasts into immunocompromised mice. LFS osteoblast derived *in vivo* tumor (sample C) will acquire increased tumorigenic ability, and serial transplantation of the first-round tumor enable collection of tumor samples (sample D) with aggregating tumorigenic ability. LFS samples with different tumorigenic potentials, including MSCs (no tumorigenic ability), osteoblasts (gaining tumorigenic ability), and osteosarcoma grown in subcutaneous transplantation (retaining *in vivo* tumorigenic ability), and osteosarcoma grown in serial transplantation (aggregating *in vivo* tumorigenic ability) can be collected and genomic DNA will be isolated for whole exome sequence (WES).

WGS analysis will be applied to determine osteosarcomagenesis associated gene mutations, structural variations, and copy number alterations by comparing the genome alterations found across different tumorigenic LFS samples. Potential genetic driver events thus, can be examined along distinct osteosarcoma developmental stages (from sample A to sample D), providing insights for early oncogenic mechanisms during LFS-associated osteosarcomagenesis.

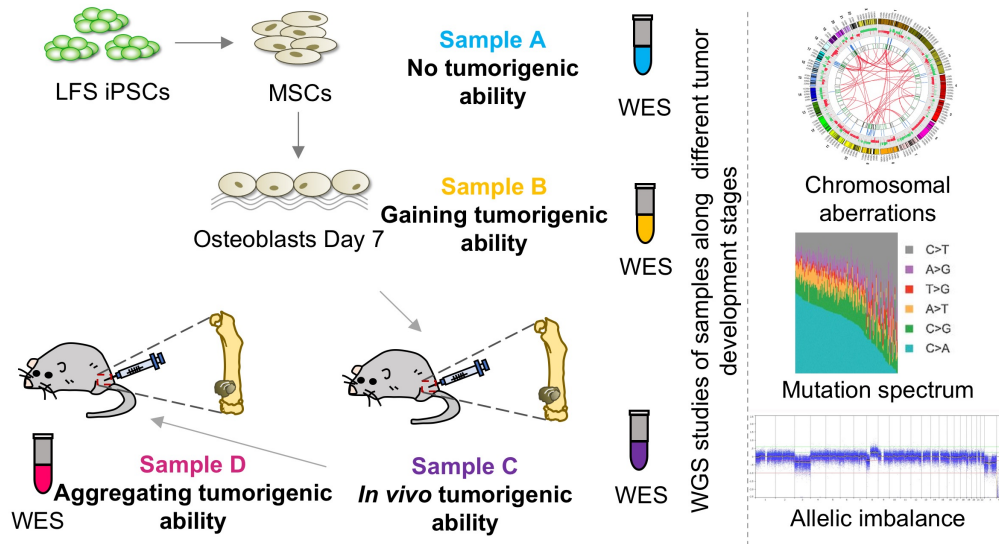


Figure 7. Schematic graph of experiment setup to identify cancer drivers during LFS-associated osteosarcomagenesis.

3.3 Generation and characterization of iPSCs from LFS patients with heterozygous *TP53* mutation.

In order to understand LFS-associated osteosarcoma pathogenesis, iPSCs generated from a LFS family and two unaffected individuals were used in this study. These iPSC lines were generated from our previous studies(122), three LFS affected individuals were diagnosed with various malignancies, including osteosarcoma (**Figure 8**).

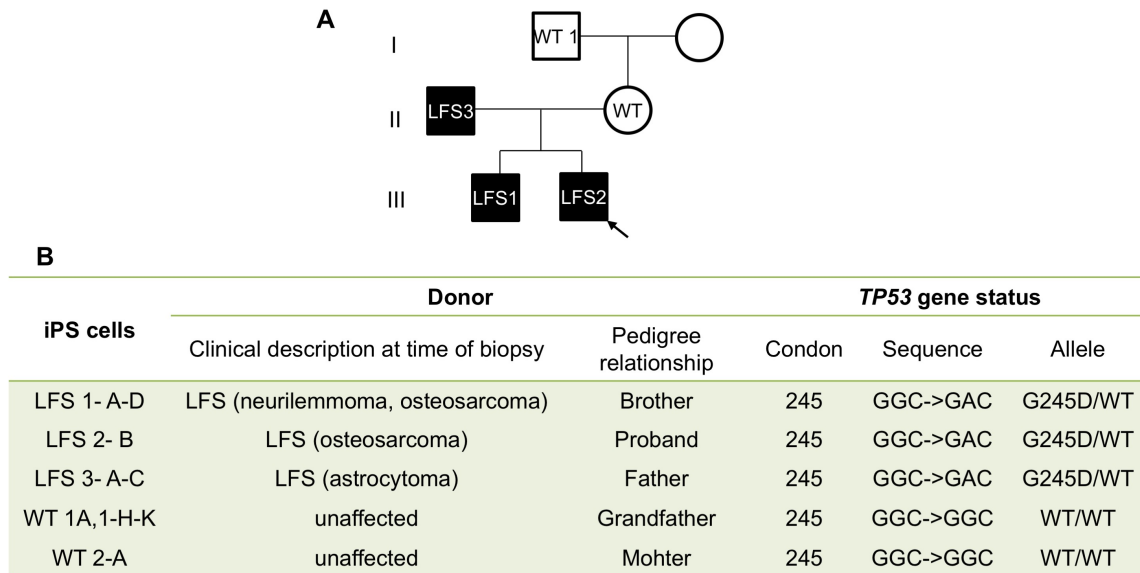


Figure 8. The LFS pedigree used in modeling LFS-osteosarcoma.

(A) LFS family tree (arrow: proband). c.734G>A mutation in *TP53* gene causing the G245D mutation is found on LFS patient fibroblasts. (B) The LFS family pedigree contains three LFS patients with a heterogeneous *TP53* (G245D) mutation and two unaffected relatives.

In addition to the already established LFS iPSCs line carrying heterozygous G245D mutation, LFS iPSC bank were expanded by generating iPSC lines from affected LFS patient carrying a different heterozygous *TP53* mutation, Y205C (TAT>TGT) (**Figure 9A**). The ability of these patient-derived iPSCs in differentiating into osteoblasts will provide platform for modeling osteosarcoma. Three iPSC clones were generated from this LFS patient fibroblasts, named LFS A8, A10, A19 respectively. Three clones carry a heterozygous substitution of A to G at positions 614, resulting a Y to C change at codon position 205 (**Figure 9B**). Generated LFS iPSC clones exhibit the typical hESC morphology and show the positive AP activity (**Figure 9C**).

Sendai virus-based delivery of the Yamanaka four factors is a non-integrating reprogramming method. Generated LFS iPSC clones were maintained in feeder free condition for 10 to 15 passages to become stable and free of Sendai virus genome and loss of exogenous OCT4, SOX2, KLF4, and c-MYC transgenes. LFS iPSC clones examined by RT-PCR using specific primers were all free of SeV genome and four transgenes (**Figure 10A**). The LFS clones also maintained a normal karyotype (**Figure 10C**).

LFS iPSCs highly express pluripotency factors (NANOG, OCT4) and hESC markers (SSEA4 and TRA-1-81) (**Figure 10D**). LFS iPSCs also highly express pluripotency factor mRNAs (NANOG, OCT4, SOX2, DPPA4, and REX1), comparable to hESC H1 line and much higher than parental fibroblasts (**Figure 10B**).

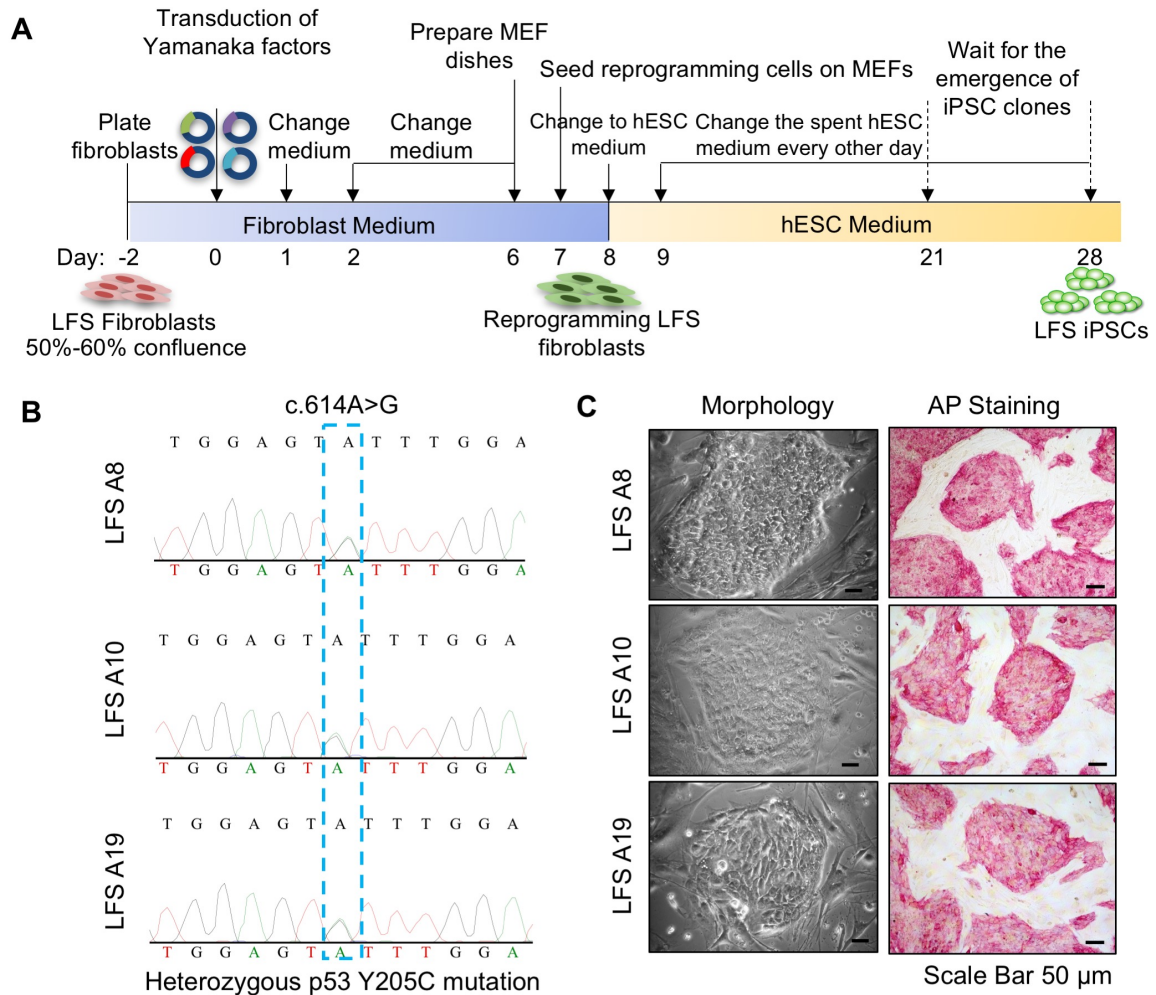


Figure 9. Generation of additional LFS iPSC from LFS patient carrying heterozygous *TP53* mutation.

(A) Schematic diagram of iPSC generation. LFS patient's fibroblast carrying carry heterozygous Y205C p53 mutation were reprogrammed using Yamanaka four factors. (B) Three iPSC clones were generated from this LFS patient fibroblasts carry heterozygous *TP53* mutation, Y205C (TAT>TGT). (C) Cell morphology of LFS iPSCs and AP staining. Scale bar, 50 μ m.

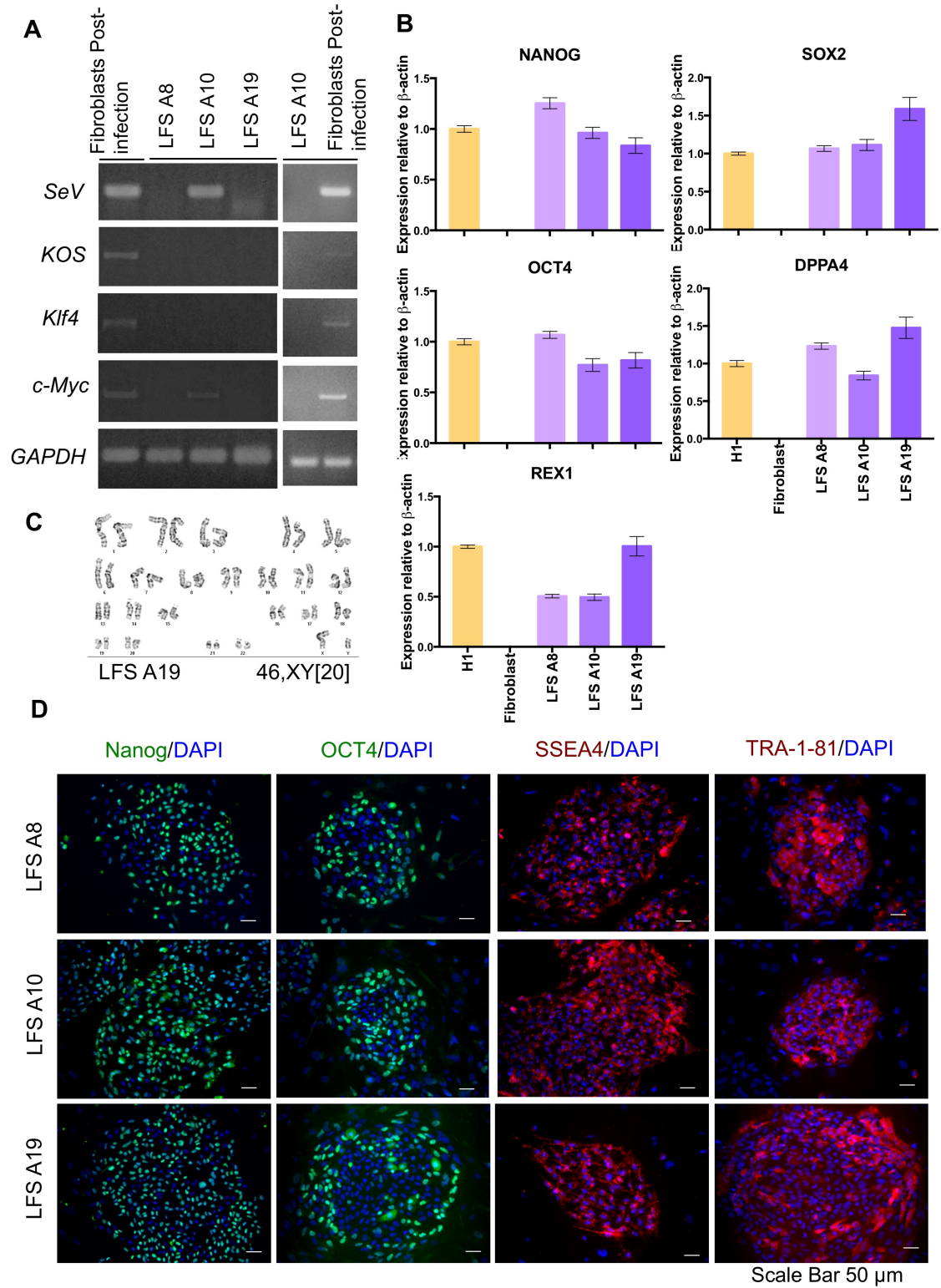


Figure 10. Characterization of LFS iPSCs carrying heterozygous TP53 mutation (Y205C).

(A) RT-PCR detection of Sendai virus genome and transgenes (KOS (KLF4, OCT4, and SOX2), KLF4, and c-MYC) in the reprogrammed iPSC clones after 10 passages and fibroblasts post-infection Day 11 (left and right lane, positive control). LFS iPSC clone A8. A10, A19 are Sendai virus free after 10 passages. GAPDH is shown as internal control. (B) qRT-PCR of NANOG, SOX2, OCT4, DPPA4, and REX1 mRNA expression in LFS iPSCs. hESC H1 line and parental LFS fibroblasts are used as a positive and a negative control, respectively. The mRNA expression is normalized to GAPDH expression. The relative mRNA expression is adjusted to hESC H1 line as 1. (C) LFS iPSC clone maintain normal karyotype. (D) Immunostaining of hESC pluripotent transcription factors (NANOG and OCT4) and hESC surface markers (SSEA4 and TRA-1-81) in LFS iPSC Clones. Scale bar, 50 μm .

3.4 Differentiation of LFS iPSCs to mesenchymal stem cells (MSCs)

Multipotent mesenchymal stem cells (MSCs) can give rise to bone, cartilage, muscle, and adipose tissues. Human osteoblasts can be induced from MSCs. To model LFS associated osteosarcoma, LFS iPSCs were first differentiated into MSCs using PDGF-AB based differentiation protocols (191, 192).

iPSCs are maintained on MEFs for at least 14 days before initiating MSC differentiation (**Figure 11A**). Although a lot of cell death happen during MSC differentiation, masses of differentiated cells are visible on the cell culture plate and fibroblast-like MSCs at the edge of the cell masses can be observed at Day 28 (**Figure 11B**). After subculturing the differentiated cells in MEF/MSC culture medium, differentiated MSCs proliferate quickly and show fibroblast-like morphology around Day 35, and then gradually present an elongated shape and form a swirl-like pattern at Day 40 (**Figure 11B**). Differentiated LFS MSCs express MSC markers, including CD44, CD73, CD105, and CD166 by immunofluorescence staining (**Figure 11C**).

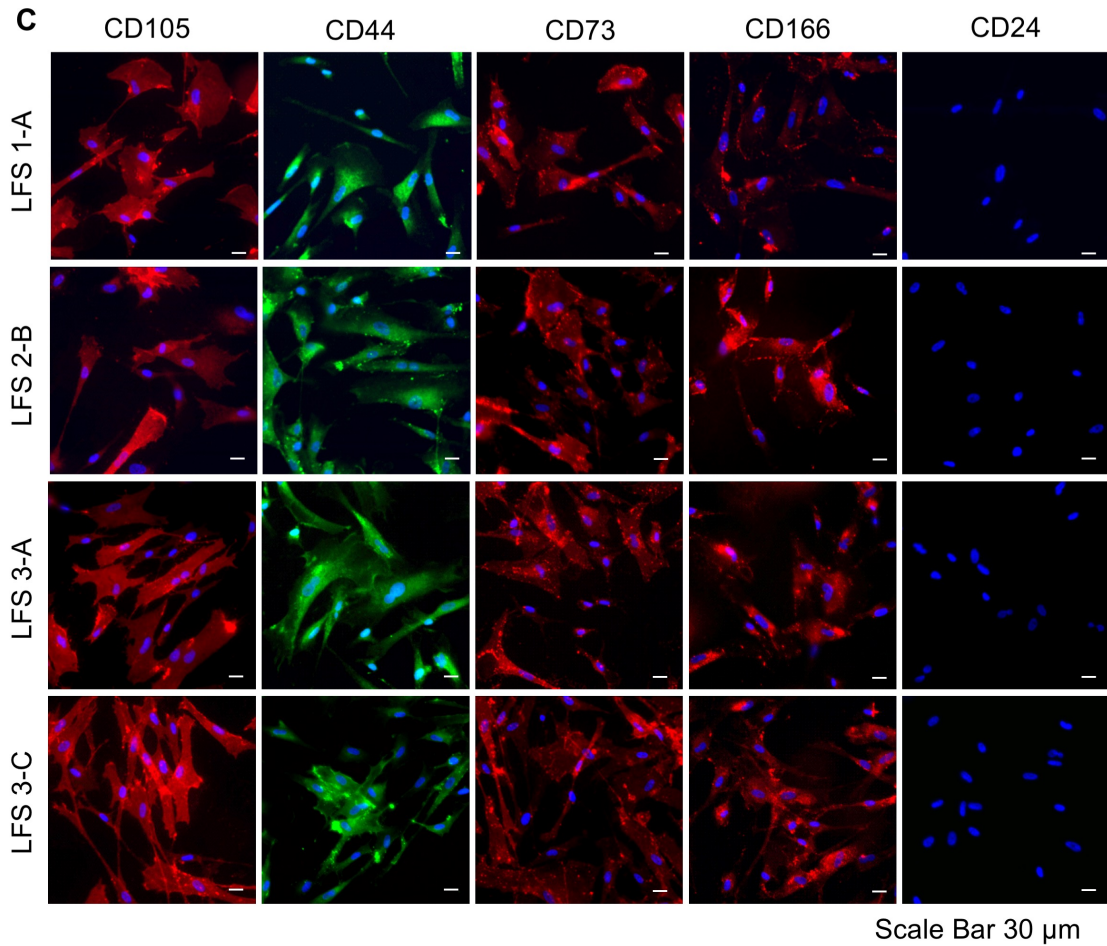
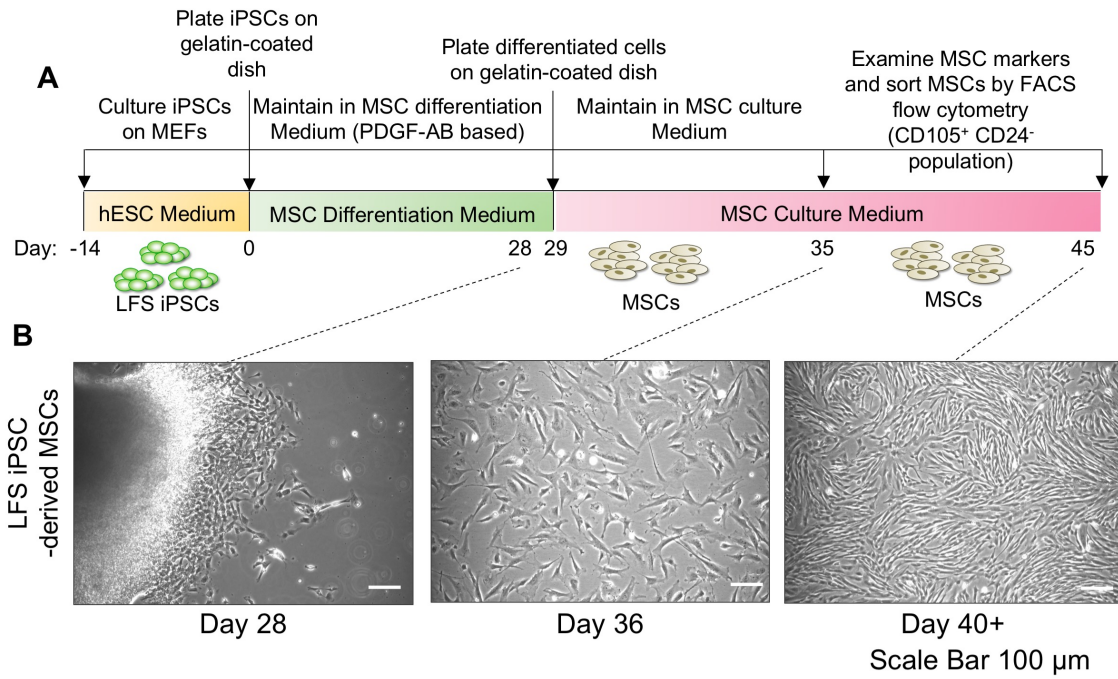


Figure 11. Differentiation of LFS iPSCs to MSCs.

(A) Schematic diagram of PDGF-AB-induced MSC differentiation. (B) Cell morphology of LFS iPSC-derived MSCs at differentiation Day 28, Day 36, and Day 40+. Scale bar, 100 μm . (C) Immunofluorescence staining demonstrates that differentiated LFS MSCs exhibit CD44+, CD73+, CD105+, CD166+, and CD24- signature. Scale bar, 30 μm .

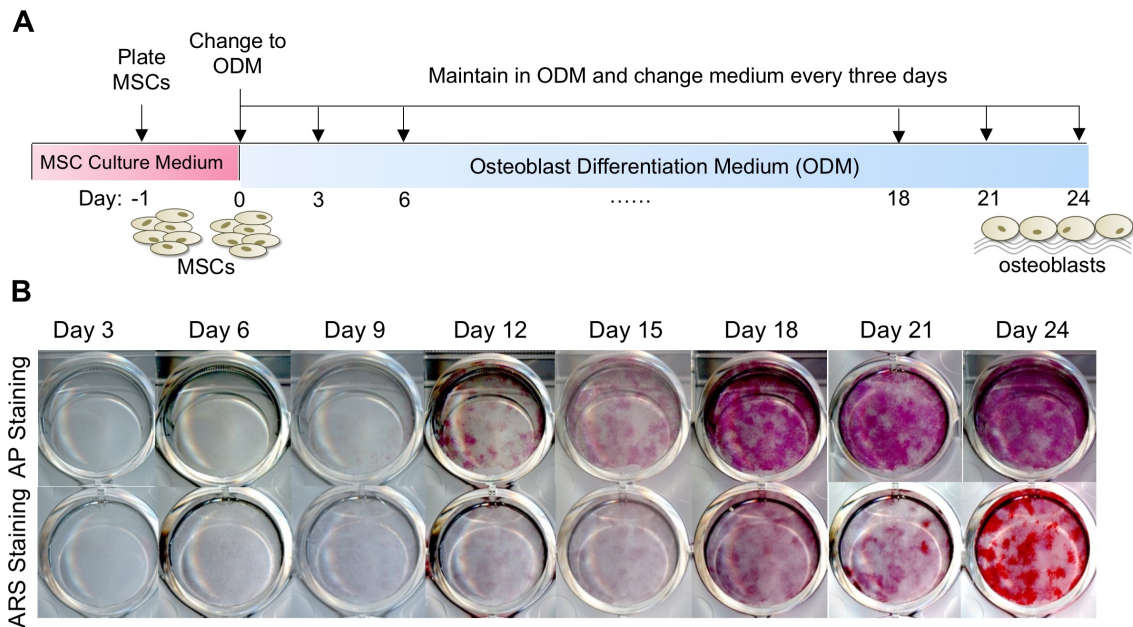


Figure 12. Differentiation of MSCs to osteoblasts.

(A) Schematic diagram of osteogenic differentiation. (B) AP and ARS staining are performed at different time points (Day 3, 6, 9, 12, 15, 18, 21, and 24). Osteogenic differentiation of LFS MSC-derived osteoblasts is expected to lead to positive AP staining around Day 9 and positive ARS staining around Day 21.

3.5 Differentiation of LFS MSCs to osteoblasts

After obtaining LFS derived MSCs, cells were further differentiated into osteoblasts following the protocol showing in **Figure 12A**. When MSCs are subjected to osteogenic differentiation signals, the differentiated cells start to show positive alkaline phosphatase activity around Day 9 (**Figure 12B**). ARS staining can be used to detect mineral deposition produced by mature osteoblasts. The bright red color staining instead of brown color staining indicates the positive result of ARS staining, which can be observed around Day 21 (**Figure 12B**).

Both WT and LFS derived MSCs can be differentiated into osteoblasts, positive alkaline phosphatase activity was detected by AP staining around Day 9 to 12 (**Figure 13A**). ARS staining were positive during differentiation process around Day 21 (**Figure 13A**). In addition, expression of pre-osteoblast (ALPL and COL1A1) and mature osteoblast (PTH1R and BGLAP) genes were all increased during osteogenic differentiation (**Figure 13B**). These results indicated successful differentiation from MSCs to osteoblasts from both WT and LFS iPSCs.

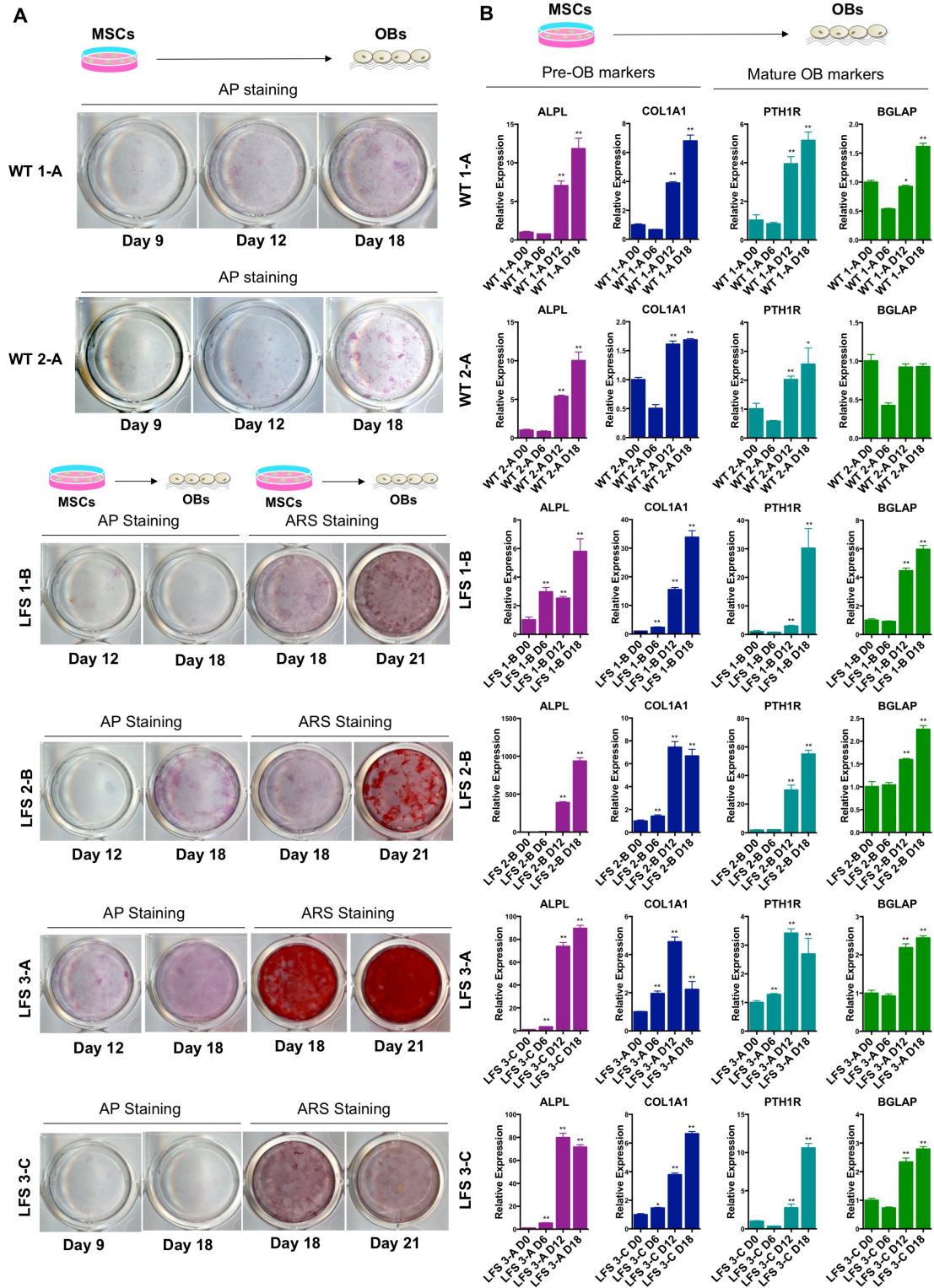


Figure 13. Differentiation of WT and LFS MSCs to osteoblasts.

(A) AP and ARS staining are performed at different time points during osteogenic differentiation for both WT and LFS MSC-derived osteoblasts. (B) The qRT-PCR analysis demonstrates the increased expression of pre-osteoblast (ALPL and COL1A1) and mature osteoblast (PTH1R and BGLAP) genes during osteogenic differentiation. The mRNA expression is normalized to GAPDH expression. Expression levels were relative to cells at differentiation Day 0.

3.6 LFS derived osteoblasts (OBs) exhibit *in vitro* oncogenic properties

To further investigate whether LFS OBs start to gain tumorigenic potential, *in vitro* soft agar assays were performed. *In vitro* tumorigenic ability of LFS OBs was confirmed by soft agar assay: both WT iPSC derived MSCs and OBs cannot form colonies, while LFS (P53 p.G245D) iPSC derived OBs can form numerous colonies larger than 50 μm (Figure 14).

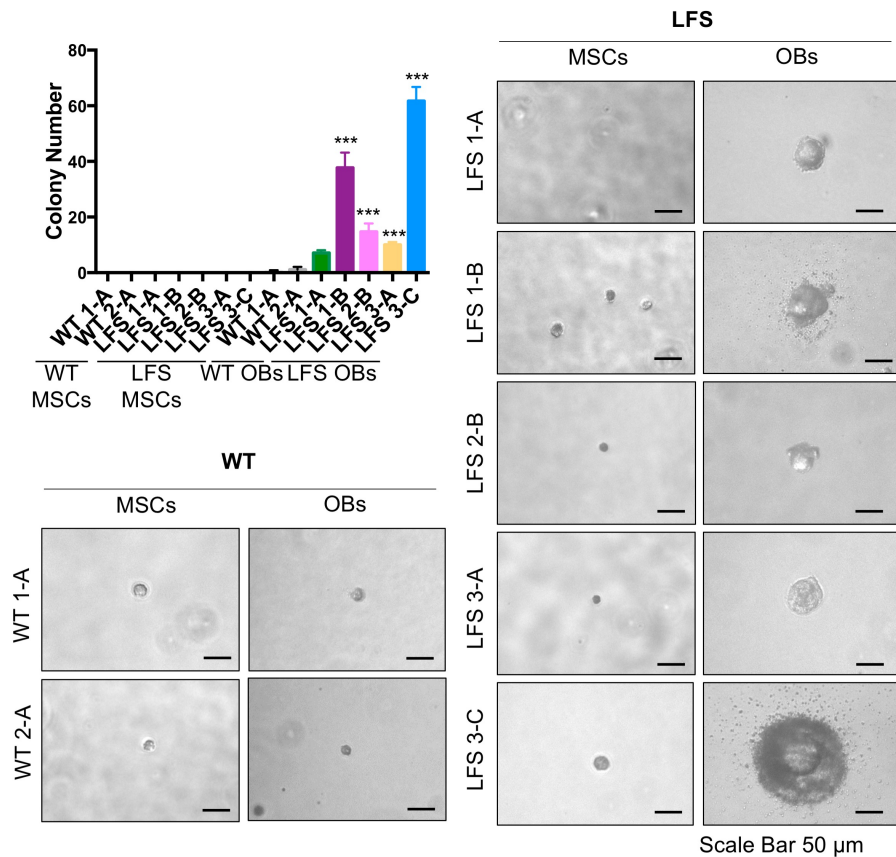


Figure 14. Soft agar assay confirmed *in vitro* tumorigenic ability of LFS derived osteoblasts.

In vitro soft agar assay demonstrates colonies formed in LFS OBs but not in WT OBs. Colony larger than 50 μm was determined under microscope as positive colony (scale bar, 50 μm).

In addition to LFS family that carry heterozygous G245D p53 mutation, another LFS patient iPSCs that carries Y205C p53 mutation were also differentiated into OBs. This LFS patient derived OBs exhibit strong positive staining for Alizarin Red S; similar to in parallel differentiated WT OBs (**Figure 15A**). *In vitro* tumorigenic ability was also confirmed in this LFS patient derived OBs: after culturing in half-solidified soft agar for 35 days, LFS derived OBs (culture in ODM) formed much more colonies larger than 50 μm compared to WT derive OBs (**Figure 15C, 15D**). In our collaborative study (193), genome-wide transcription analysis revealed differentially expressed genes pattern during MSCs to OBs differentiation between WT and LFS patient groups (**Figure 16A***). Secreted frizzled-related protein 2 (sFRP2) showed the greatest fold change (>30), and was identified as overexpressed gene with potential implication in osteosarcoma development (**Figure 16A***). sFRP2 is also enriched in the signature gene list of an osteosarcoma tumor initiating cell data set (GSE33458). RT-PCR analysis confirmed that SFRP2 expression is significantly elevated during MSCs to OBs differentiation in LFS family lines carrying germline G245D mutation (**Figure 16B***) and Y205C mutation of *TP53* (**Figure 15B**). SFRP2 expression is also significantly elevated in during MSCs to OBs differentiation of hESCs carrying heterozygous *TP53* mutation (hotspot mutation G245D, G245S, R248W).

In ovo chick chorioallantoic membrane (CAM) assays provides a convenient way to check the oncogenic ability of tumor cells (194) including sarcoma cells (195, 196). Wild type osteoblasts overexpressing SFRP2 showed increased tumor formation and cell numbers in CAM assay when compared with WT osteoblasts

(**Figure 16D***). Knocking down of SFRP2 in LFS derived osteoblasts, on the other hand, suppressed tumor formation (**Figure 16D***). In p53 mutant osteosarcoma cell line HOS, neutralizing secretory protein SFRP2 with a monoclonal anti-SFRP2 antibody significantly reduced tumorigenesis as demonstrated in the CAM assay (**Figure 16D***). These results demonstrate that overexpression of SFRP2 contributes to LFS-associated tumorigenesis and osteosarcoma development. High expression of SFRP2 in human osteosarcoma samples correlated with poor survival (**Figure 16E***). Further study demonstrated sFRP2 overexpression suppresses normal osteoblast differentiation, promotes osteosarcoma features and facilitates neoangiogenesis via autocrine and paracrine mechanism in LFS induced pluripotent stem cell disease model (193). These data demonstrated the potential of LFS iPSC-MS-C-OB platform in identifying potential therapeutic targets for osteosarcoma.

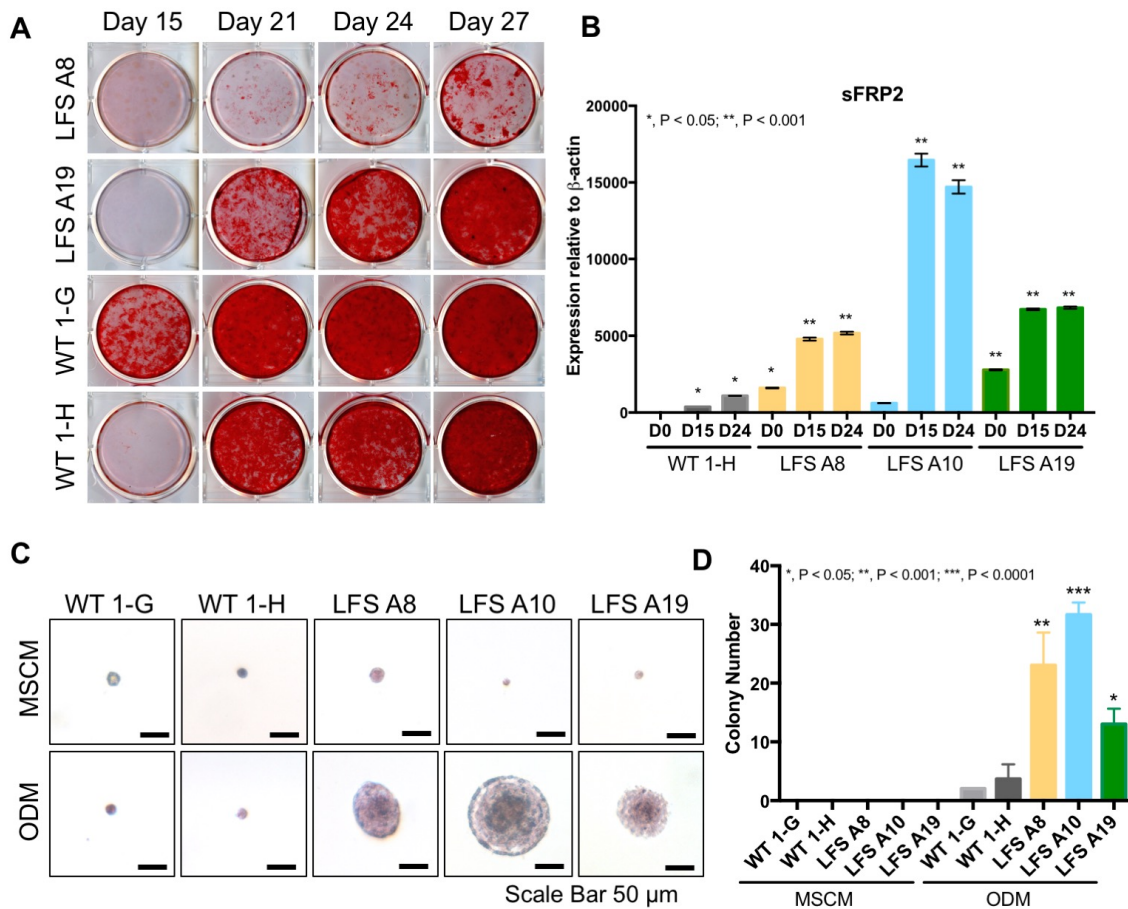


Figure 15. *In vitro* tumorigenic ability recapitulated in a different LFS patient derived osteoblasts.

(A) Alizarin Red S staining of WT and LFS (P53 p.Y205C) derived osteoblasts at indicated time points of OB differentiation. (B) Relative expression of sFRP2 in MSCs and OBs derived from LFS iPSCs carrying a heterozygous P53p.Y205C mutation compared to WT. Note that The LFS iPSCs are generated from a separate patient who is distinct from the family members corresponding to LFS (P53 p.Y205C) iPSCs. (C) Soft agar colony formation of LFS (P53p.Y205C) MSCs and OBs (scale bar, 50 μ m). (D) Quantification of colony numbers obtained with

WT and LFS (P53p.Y205C) MSCs and OBs. Colonies over 50 μm were determined under microscope as positive colonies.

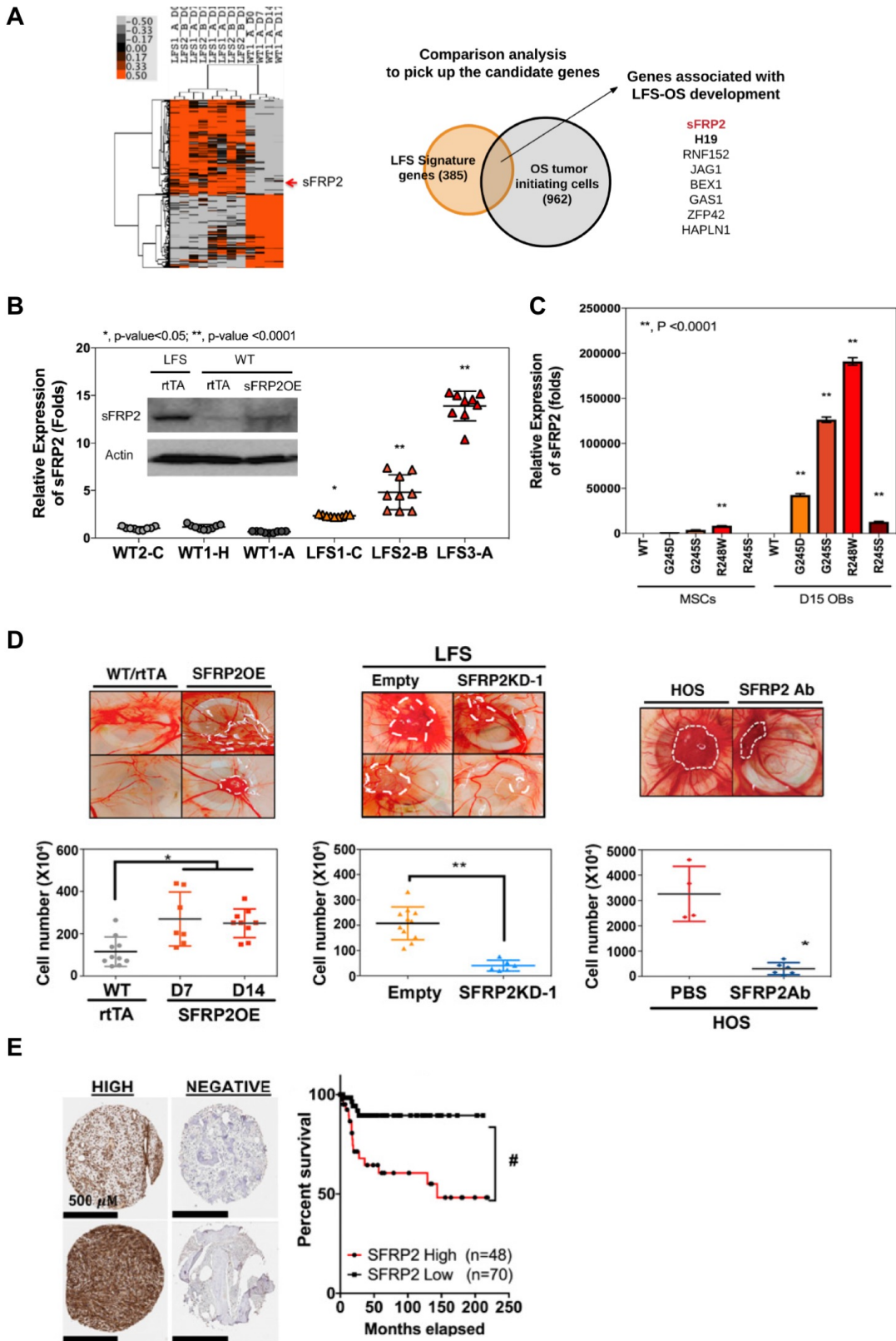


Figure 16*. Overexpression of sFRP2 in LFS associated osteosarcoma model (figures and legends used with permission).

(A) Global transcriptome analysis of LFS (P53p.G245D) and WT iPSCs-derived MSCs differentiated to OBs. Differentially expressed genes (DEGs) between LFS and WT were sorted by paired t-test ($p < 0.01$) with a fold change > 2 . SFRP2 is an overexpressed gene that is also enriched in the signature gene list of an osteosarcoma gene set (GSE33458). (B) Quantitative PCR analysis and western blotting of SFRP2 expression in LFS and WT MSCs (*, p -value < 0.05 ; **, p -value < 0.0001). Mouse monoclonal anti-SFRP2 antibody (Santa Cruz Biotechnology, Cat# sc-365524) was used in the western blot. (C) SFRP2 expression in TALEN-engineered heterozygous P53p.G245D, G245S, R248W and R249S mutant ESC line-derived MSCs and OBs. (D) CAM assays of SFRP2 overexpressing WT OBs, SFRP2 knocking down LFS OBs and HOS cells treated with SFRP2 neutralizing antibody. (E) Survival analysis of osteosarcoma patients linked to the tissue microarray. Survival curve of SFRP2 high and low expression groups was calculated using the log-rank test (chi-square=11.13; # p -value=0.0009).

*Figure 16 (A) – (E) is adapted from Kim HS, Yoo S, Zhou R[#], Xu A, Bernitz, JM, Yuan Y, Gomes AM, Daniel MG, Su J, Demicco EG, Zhu J, Moore KA, Lee DF, Lemischka IR, Schaniel C. Oncogenic role of sFRP2 in P53-mutant osteosarcoma development via autocrine and paracrine mechanism. (2018), 10.1073/pnas.1814044115. (#: co-author). *Figure 16 and legends are used with permission of author Dr. Huen Suk Kim, Dr. An Xu and Dr. Dung-Fang Lee.

3.7 Continuous cultured LFS derived osteoblasts (OBs) exhibit increased *in vitro* oncogenic properties

Following osteogenic differentiation protocol indicated in **Figure 12A**, LFS MSCs can be differentiated into mature osteoblasts around Day 24. At this time, the cells reach full confluence on culture dish and usually marks the end of osteogenic differentiation process.

Based on the central hypothesis of this study, I proposed to test whether differentiated osteoblasts can continue proliferating by subjecting MSCs to a prolonged osteogenic differentiation course. Osteogenic differentiation was initiated as described previous (**Figure 12A**); at Day 24 cells were disassociated and replated at desired density (**Table 7**) to be further cultured in ODM. Cells were replated every 24 days in the same manner for three rounds until Day 72 (**Figure 17B**). I hypothesized that during this continuous differentiation condition, LFS derived osteoblasts will gain increased *in vitro* oncogenic ability compare to WT derived osteoblasts.

Both WT and LFS cells were able to proliferate under prolonged differentiation condition, and cells exhibited positive ARS staining at Day 24, 48 and 72 (**Figure 17A**). Cells collected at Day 24, 48 and 72 were seeded in half-solidified soft agar, and maintain in ODM culture condition for 35 days. WT OBs at different time point formed few colonies, while LFS (P53 p.G245D) OBs at different time point formed much more colonies. The number of positive colonies form from LFS OBs increased significant during prolong differentiation process (**Figure 17 C, E**)

Comparing colonies formed from cells seeded at day 48 to day 24, and day 72 to day 48, the size of positive colonies was also observed to be significantly increased (**Figure 17D, E**). These results not only demonstrate that LFS derived osteoblasts under continuous culture *in vitro* exhibit increased tumorigenic ability, but also support the hypothesis that serial transplantation of *in vivo* tumors derived from LFS osteoblasts will accumulate sustaining tumorigenic ability.

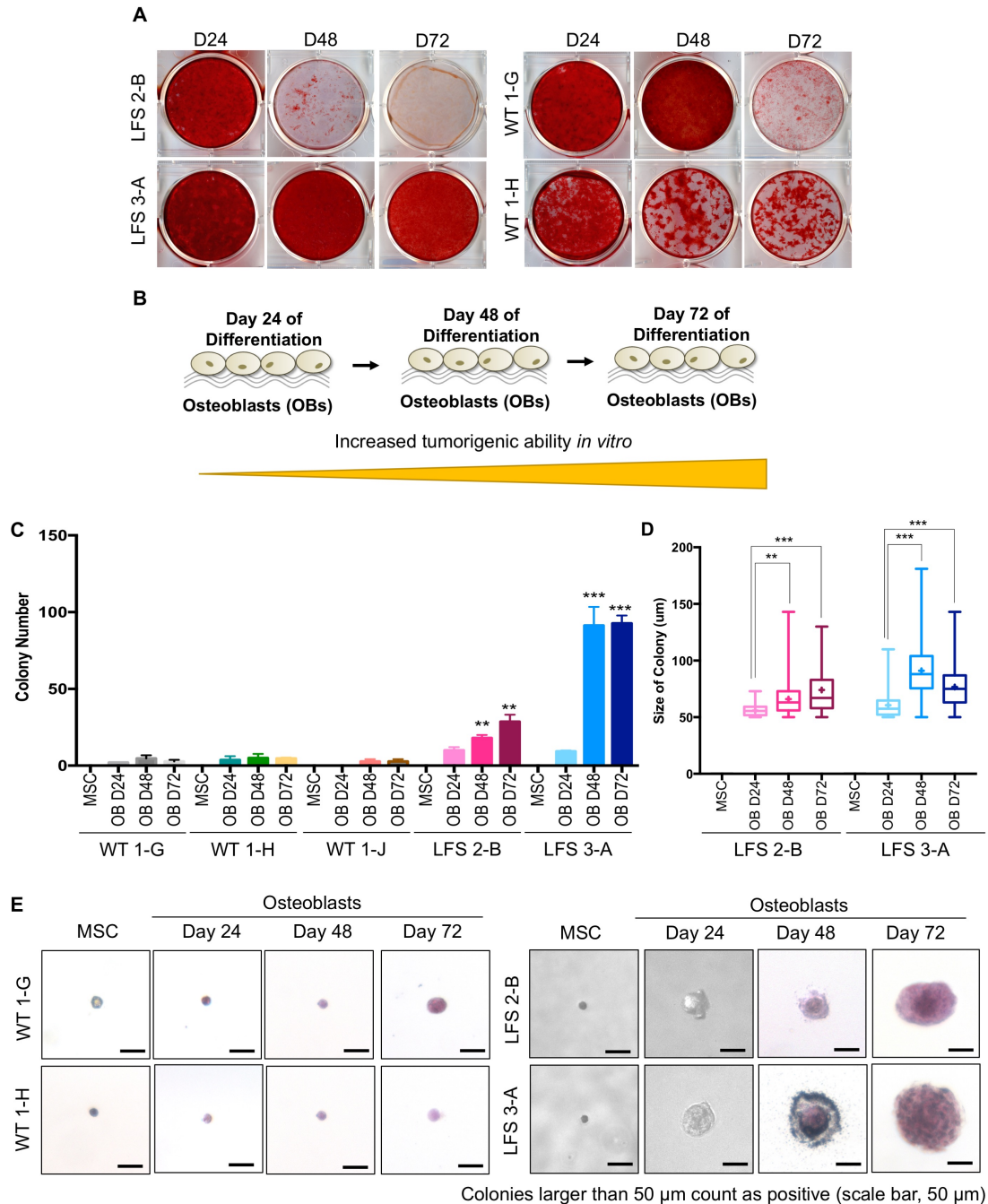


Figure 17. LFS derived osteoblasts exhibit increased *in vitro* oncogenic properties when culture continuously.

(A) Alizarin Red S staining of WT and LFS (P53p.G245D) derived osteoblasts at indicated time points during OB differentiation. (B) Differentiated osteoblasts were

replated every 24 days. Osteoblasts at Day 24, Day 48 and Day 72 were seeded for soft agar assays: cells at indicated time point were maintained in half-solidified agar to examine whether continuous cultured LFS OBs gain increased *in vitro* oncogenic ability. (C) Quantification of colony numbers obtained with WT and LFS (P53p.G245D) MSCs and OBs at indicated time points. Colonies over 50 μm were determined under microscope as positive colonies. (D) Quantification of the colony size obtained with LFS (P53p.G245D) OBs at indicated time points (**, $P < 0.001$; ***, $P < 0.0001$). (E) Representative image of soft agar colonie of WT and LFS (P53p.G245D) MSCs and OBs at indicated time point (scale bar, 50 μm).

3.8 Establishment of xenograft model to study *in vivo* tumorigenesis of LFS MSC-derived osteoblasts

To examine whether LFS OBs are able to gain *in vivo* tumorigenesis ability, subcutaneous injection of LFS derived osteoblasts into NU/NU mice were performed (**Figure 18A**). In our previous study (122), LFS OBs can form *in vivo* tumors but WT OBs cannot. Consistent with previous study, tumors can be observed 6-10 weeks after subcutaneous injection of LFS (P53 p.G245D) derived osteoblasts (**Figure 18B**). The LFS osteoblast-derived tumors demonstrated immature osteoblast characteristics, positive AP activity (AP staining), positive collagen matrix deposition (picrosirius red staining) but negative mineralization (von Kossa staining) (**Figure 18C**). The LFS xenograft tumor model demonstrates LFS MSC-derived osteoblasts recapitulate *in vivo* tumorigenic ability, which provides an alternative platform to study LFS associated osteosarcoma.

In addition to subcutaneous xenograft model, we also performed intratibial injection of LFS OBs in SCID mice in attempt to build an orthotopic xenograft model (**Figure 19A**). However, tumor formation was not observed in five LFS (P53 p.G245D) derived osteoblast lines injected intratibially (**Figure 19A**).

The osteoblasts later than differentiation Day 14 may aggregate and be difficult to dissociate due to the huge accumulations of collagens and other bone matrix materials produced by osteoblasts. To prevent the difficulty of osteoblast dissociation, LFS MSCs can be seeded in 2-3-fold higher density in the initiation step of osteogenic differentiation to facilitate osteoblast differentiation. LFS MSC-derived osteoblasts can be dissociated and collected at the Day 6-10 differentiation

time point for *in vivo* tumorigenesis assay. We also performed subcutaneous injection of LFS-derived osteoblast at differentiation Day 7 (**Figure 19B**). Out of five LFS (P53 p.G245D) derived osteoblast lines, only LFS 3-A line were able to generate grossly visible tumors: total 14 injections were performed, 5 grossly visible tumors were observed. No tumor formation was observed in other four lines. These results indicated that LFS (P53 p.G245D) derived osteoblasts around differentiation Day 10 start gaining oncogenic abilities, but are still not “malignant tumor cells”.

Subcutaneous injection of LFS-derived osteoblasts at differentiation day 72 were also performed (**Figure 19C**). Tumor formation were observed in two out of four LFS (P53 p.G245D) derived osteoblast lines, with increased tumor formation rate. For LFS 3-A line, 5 tumors were formed out of 6 injections (tumor formation rate was 83.3%, higher when compared to subcutaneous injection of LFS-derived osteoblast at differentiation Day 7, which the tumor formation was 35.7%). Tumor formation was also observed in LFS 2-B line (2 tumors formed out of 6 injections), while no tumor formation was observed in this cell line when injections were done using osteoblasts at differentiation Day 7.

3.9 Establishment of LFS OB derived tumor cell lines

Five first-round tumors successfully generated from LFS 3-A line were isolated (**Figure 20A**) and expanded in culture. Histological examination demonstrated these tumors are composed of LFS osteoblast-derived cells surrounded by collagen matrix (**Figure 20B**). Only three tumor lines (Tumor #2, #4 and #5) were successfully expanded *in vitro*. These tumor clones all express human marker HLA-

ABC (**Figure 20C**) with matched STR profile of LFS 3-A derived osteoblasts right before injections (**Figure 20D**).

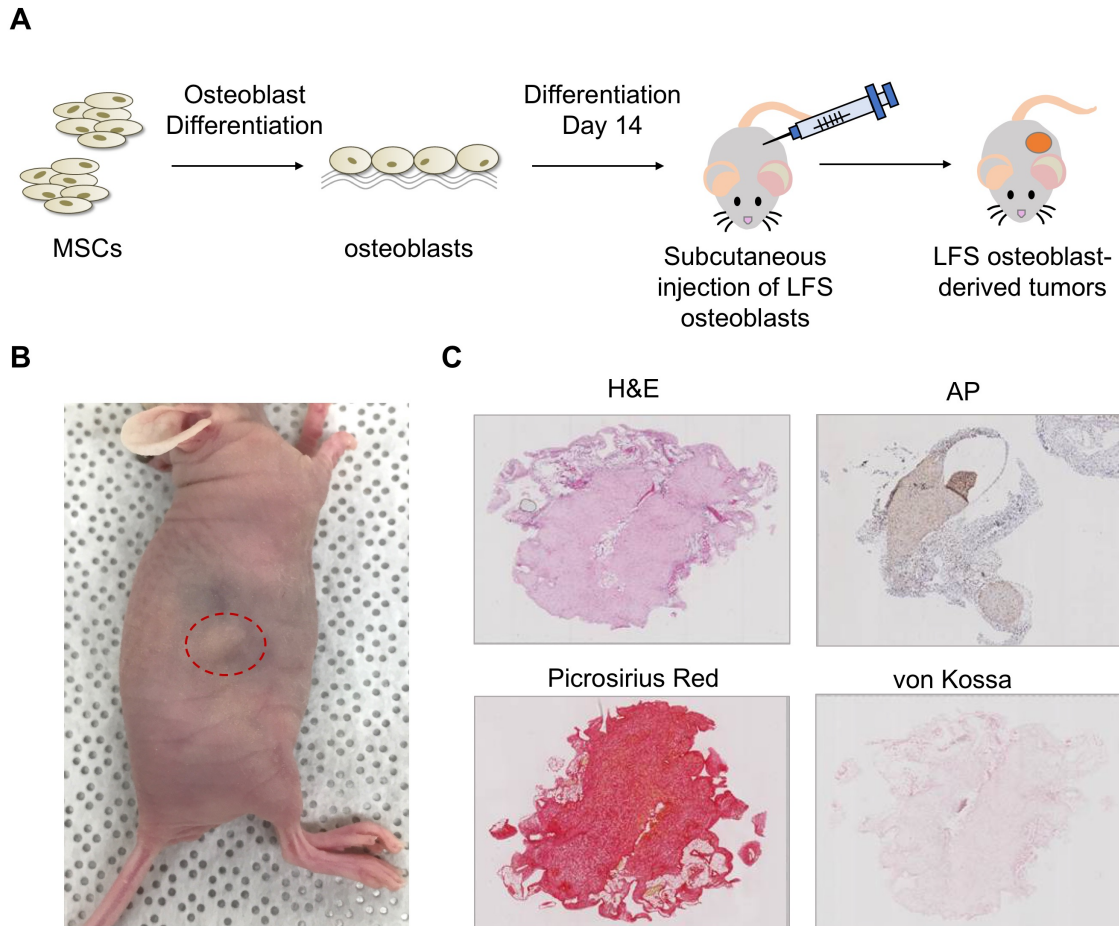
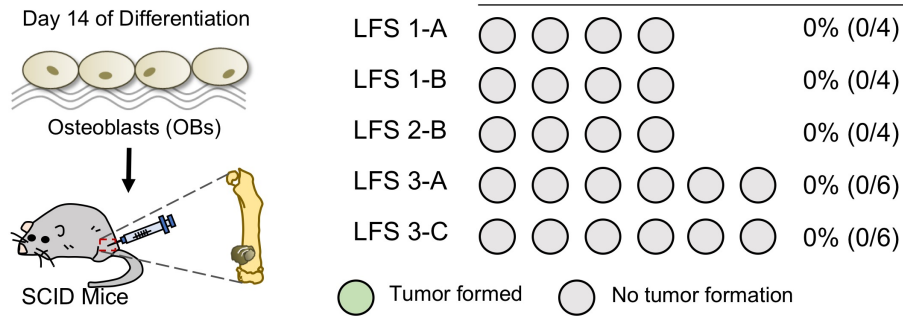


Figure 18. *In vivo* tumorigenesis of LFS MSC-derived osteoblasts.

(A) Schematic diagram of tumor xenograft of LFS osteoblasts. (B) NU/NU mice bear LFS osteoblast-derived tumors after 10 weeks of subcutaneous injection. (C) LFS osteoblast-derived tumors were examined by H&E, AP, picrosirius red, and von Kossa staining for morphology, bone-associated AP, collagen, and mineral deposits, respectively. The LFS-derived tumors represent immature osteoblast characteristics showing positive AP activity, positive collagen, and negative mineral mineralization (scale bar, 1 mm).

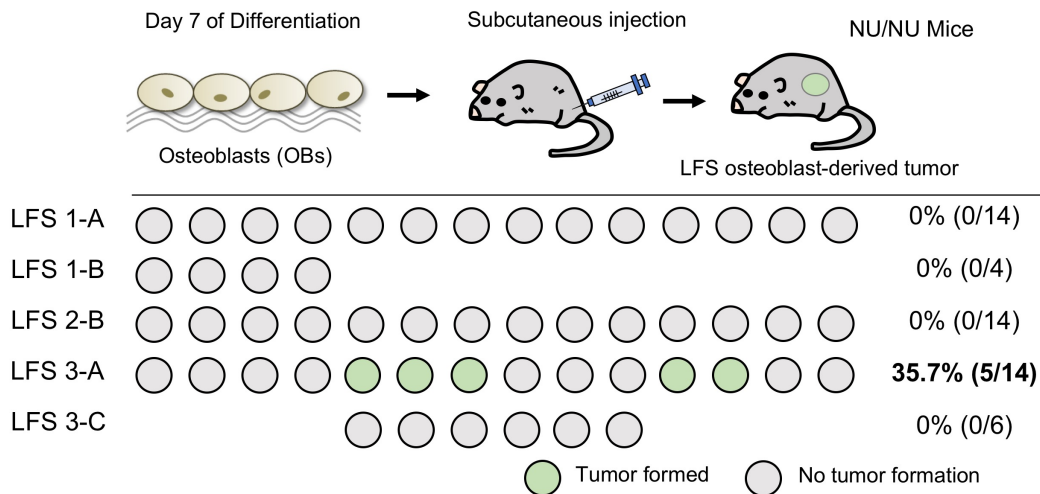
A

Intratibial injection of LFS-derived osteoblasts at Differentiation Day 14



B

Subcutaneous injection of LFS-derived osteoblasts at Differentiation Day 7



C

Subcutaneous injection of LFS-derived osteoblasts at Differentiation Day 72

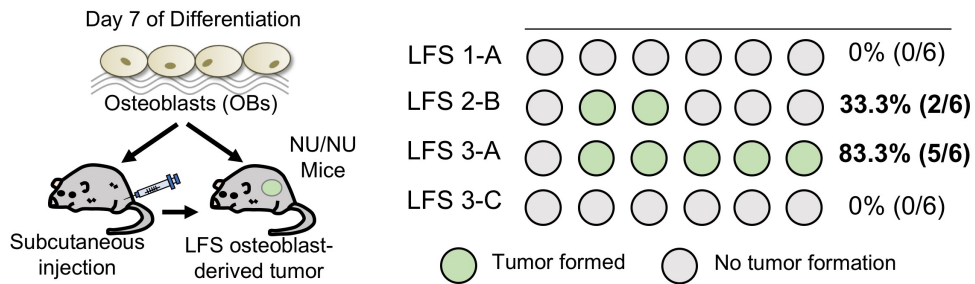


Figure 19. Xenograft model to study in vivo tumorigenesis of LFS MSC-derived osteoblasts

(A) Schematic diagram of orthotopic xenograft model by intratibial injecting of LFS OBs in SCID mice: no tumor formation was observed in five LFS (P53 p.G245D)

derived osteoblast line. (B) Schematic diagram of tumor xenograft of LFS osteoblasts at differentiation Day 7: five grossly visible tumors were observed in LFS 3-A line (35.7%, 5/14) while no tumor formation was observed in other lines. (C) Schematic diagram of tumor xenograft of LFS osteoblasts at differentiation Day 7: five tumors formed out of six injection in LFS 3-A line (83.3, 5/6); two tumors were observed in LFS 2-B line (33.3%, 2/6). No tumor formation was observed in LFS 1-A and 3-C lines.

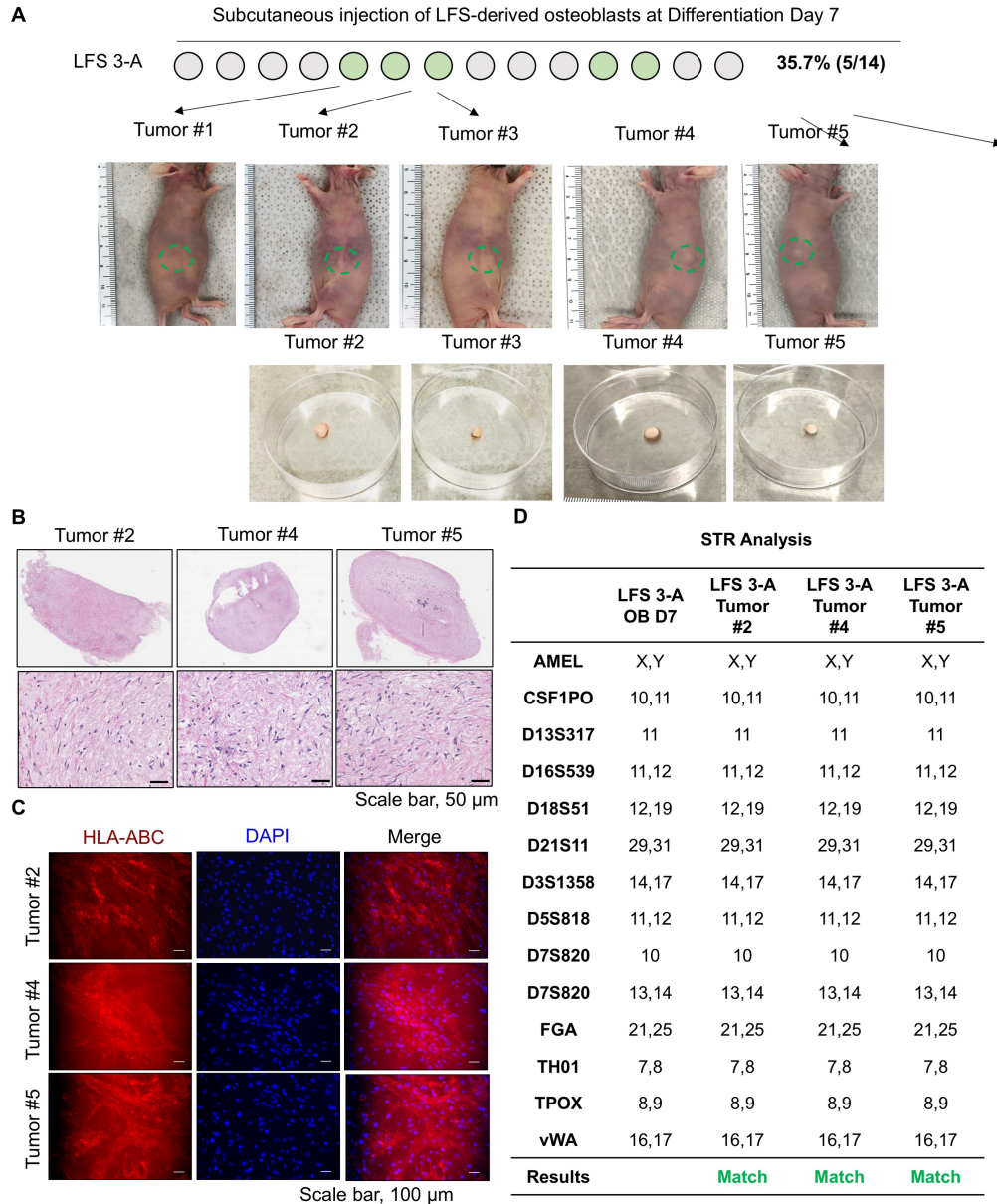


Figure 20. In vitro expansion of LFS patient osteoblasts derived tumor.

(A) Grossing of LFS 3-A osteoblasts derived tumor. (B) H&E examination of LFS osteoblast-derived tumors established from LFS 3-A line (scale bar, 50 μm). (C) Staining of human marker HLA-ABC in tumor derived cell lines (scale bar, 100 μm). (D) Short tandem repeat analysis of LFS 3-A derived osteoblasts at differentiation Day 7 and three tumors (Tumor #2, #4, #5) derived lines.

3.10 Whole exome sequencing of LFS OB derived tumor cell lines

LFS 3-A MSCs, osteoblasts at differentiation Day 7 and three OB derived tumor cell lines (Chapter 3.9) were collected and sent for whole exome sequencing. The pipeline used for mapping, somatic mutation calling, and annotation were illustrated in **Figure 21A**. The representative figure of distribution of quality score across all bases from two ends were shown and the base quality value ($Q_{\text{phred}} = -10\log_{10}(e)$, “e” represent the sequence error rate) is distributed around 36 from two ends (**Figure 21B**). The detail statistics for the quality of sequencing data are shown in **Figure 21C**. In summary, the WES data of five samples are in good quality.

Total 96 variants were called in osteoblasts at Day 7 differentiation (OB Day 7). More variants were called in tumor derived samples: 202 variants in Tumor #2, 245 variants in Tumor #4 and 751 variants in Tumor #5. The increased number of variants is as expected, suggesting more genetic events happened during LFS osteoblast-derived tumor formation process. The distribution of the variant type is shown in **Figure 22A**. Most of the variants are located at exonic and intronic region. Allele frequency distribution of these exonic variants indicate that most of the called variants are with low allele frequency. Tumor #5 present with much more exonic variants when compared to Tumor #2 and #4, and most of these exonic variants are with low allele frequency (**Figure 22B**), suggesting these variants are somatic events. The increased number of Tumor #5 might indicate this tumor derived lines are in more advanced stage in tumor development or contain sub-population of

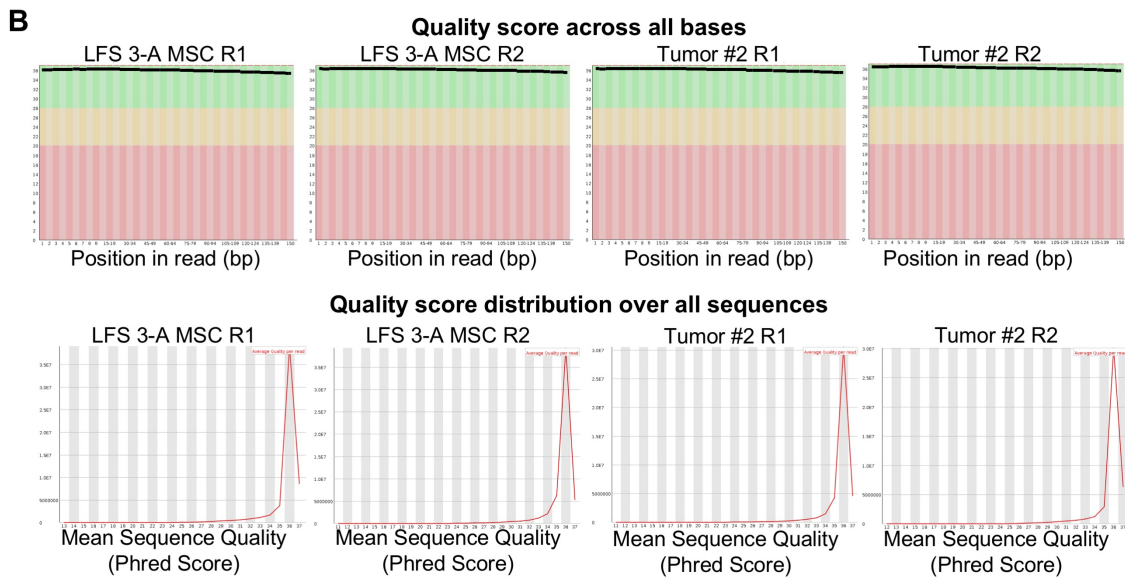
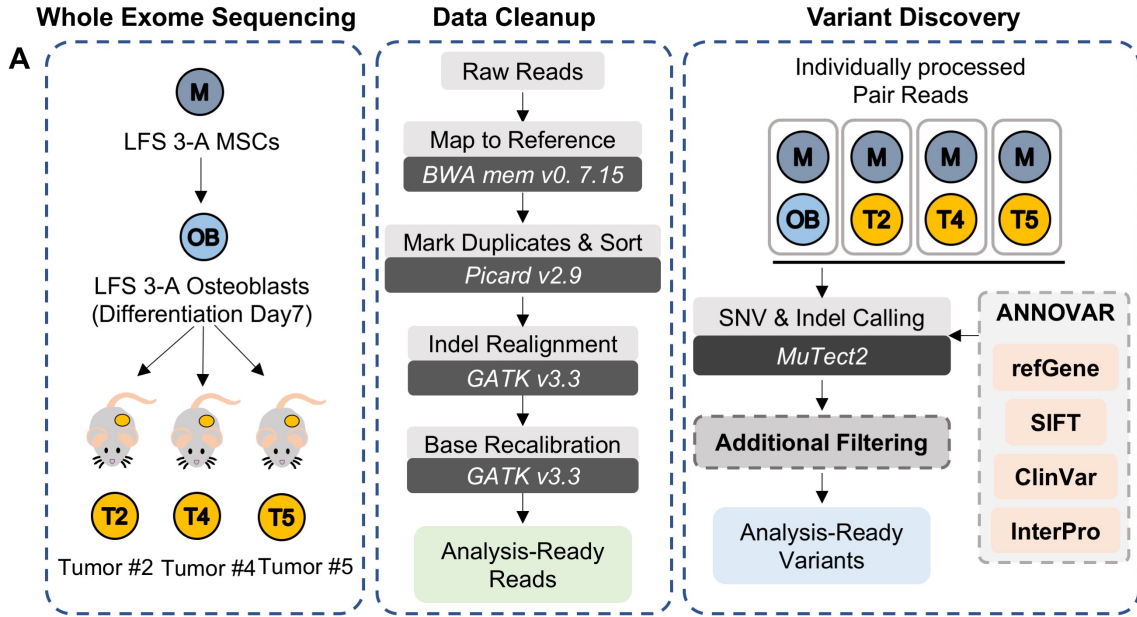
cells at different tumor initiation stage. We included all the exonic variants from three tumors for further analysis.

We next examined the commonly mutated genes between each sample. Only four genes were detected both mutated in OB Day 7 and Tumor #5, and no commonly mutated genes were found between OB Day 7 and Tumor #2, and between OB Day 7 and Tumor# 4 (**Figure 22C**). By overlapping mutated genes from three tumor cell lines, we found one gene (*GABRR2*) are commonly mutated in three tumor cell lines. Interestingly, all three tumor cells line carried same nonsynonymous mutation on *GABRR2* (c.G227T, p.A76S) (**Figure 23A**). One hypothesis is that the mutation already exists in MSCs or OB Day 7. We checked the BAM file, and no alternative reads were identified in MSCs, while very low signal of alternative read were detected in OB sample. There is an increase in allele frequency of this variant on *GABRR2* in tumor derived cell lines (**Figure 23B**). One explanation is that this mutation occurs during osteogenic differentiation, and may contribute to growth advantage during tumor formation process. *GABRR2* (gamma-aminobutyric acid type A receptor rho2 subunit) encodes a member of the rho subunit family and is a component of the GABA type A receptor complex. GABA is a well-known inhibitory neurotransmitter in the mammalian brain where it acts at GABA receptors (197). *GABRR2* are highly expressed in brain tissue, while the expression level is quite low in osteoblasts (in house database). Therefore, although commonly mutated in three tumor cells lines, *GABRR2* is not our top candidate driver gene during osteosarcomagenesis.

We also found 14 genes commonly mutated in Tumor #2 and #5, and 5 genes commonly mutated in Tumor #4 and Tumor #5 (**Figure 22C**). Genes carrying nonsynonymous mutations are bolded in the list.

Utilizing a web-based application MusiCa, which is used to characterize mutational signatures in cancer samples (186, 198), we examined somatic mutation prevalence in OB Day 7 sample and three tumor-derived cell lines. As shown in **Figure 24A**, somatic mutations are more prevalent in tumor-derived cell lines when compared to osteoblasts. **Figure 24B** are CIRCOS plots summarizing variants identified as non-frameshift substitution, frameshift substitution, nonsynonymous SNV and stopgain in each sample. We used Network2Canvas (Network Visualization on a Canvas with Enrichment Analysis) to identify signaling pathways and biological process enriched for all the genes carrying mutations (nonframeshift substitution, frameshift substitution, nonsynonymous SNV and stopgain) in three tumor samples. The top biological process includes cell adhesion and cell cycle (**Figure 23C**).

Previous study utilizing *Sleep Beauty* (SB) transposon-based forward genetic screen in mice identified new genes and pathways driving osteosarcoma (199). Common insertion site (CIS) analysis of SB induced the tumors identified 275 sites associated with osteosarcoma development and progression. We compared our mutated genes in LFS OB derived tumors with 406 CIS-associated genes identified in this study. Interestingly, there was a 20-gene overlap, including *ARID1A*, *EYA3*, *FNBP1L*, *CNOT4*, which carrying nonsynonymous mutation (**Figure 24D**).

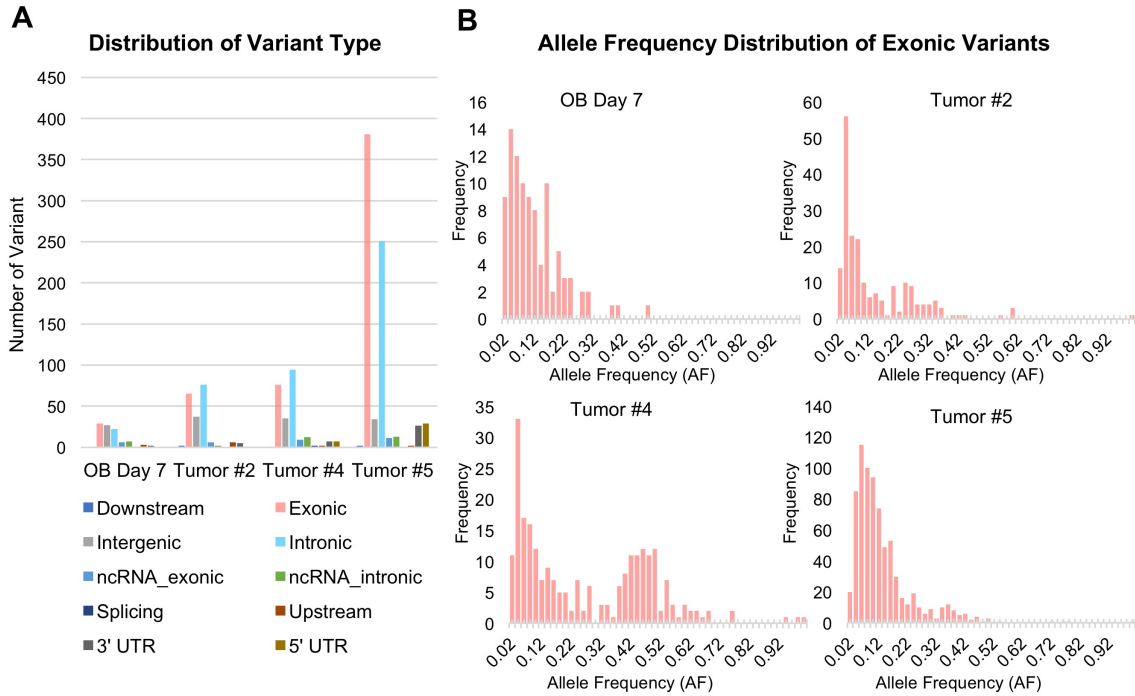


C

	Lane	Effective (%)	Error (%)	Q20 (%)	Q30 (%)	GC (%)
LFS 3-A MSC	1	98.09	0.03	97.77	94.03	52.35
LFS 3-A MSC	2	98.08	0.02	98.28	95.04	52.23
LFS 3-A OB Day 7	1	98.50	0.02	98.32	95.14	51.76
LFS 3-A OB Day 7	2	98.52	0.03	97.82	94.13	51.87
Tumor #2	1	98.21	0.03	97.83	94.14	51.80
Tumor #2	2	98.22	0.02	98.34	95.17	51.70
Tumor #4	1	97.94	0.02	98.38	95.28	51.72
Tumor #4	2	97.96	0.03	97.87	94.25	51.81
Tumor #5	1	97.62	0.03	98.20	93.78	52.08
Tumor #5	2	97.60	0.02	98.32	94.83	51.97

Figure 21. Workflow of sequencing analysis and quality control.

(A) Diagram illustrating workflow of whole exome sequencing, including data cleanup and variant discovery. (B) Representative figure showing quality score across all bases and quality score distribution over all sequences. R1 and R2 indicated reads from two ends. (C) Table summary of detail statistics for the quality of sequencing data.



C

Sample	Exonic Variant	Mutated Gene
OB Day 7	29	29
Tumor #2	65	64
Tumor #4	76	76
Tumor #5	381	342

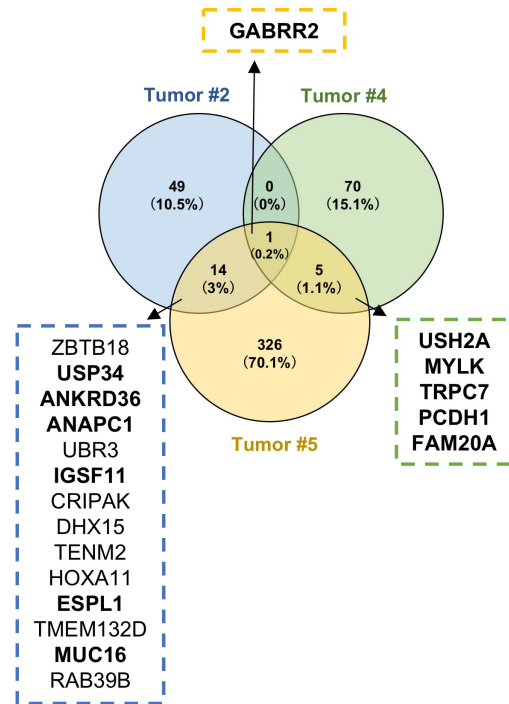
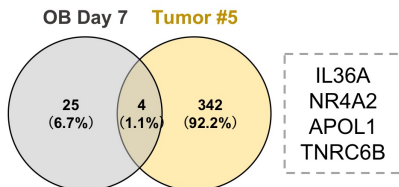
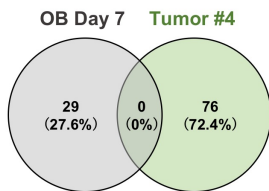
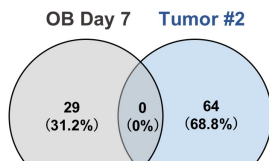


Figure 22. Summary of sequencing results highlighting commonly mutated genes in LFS OB derived tumors.

(A) Distribution of the variant type in OBs and tumor-derived cell lines. (B) Allele frequency distribution of exonic variants in OBs and tumor-derived cell lines. (C) Venn diagram depicting the overlapping mutated genes found between samples.

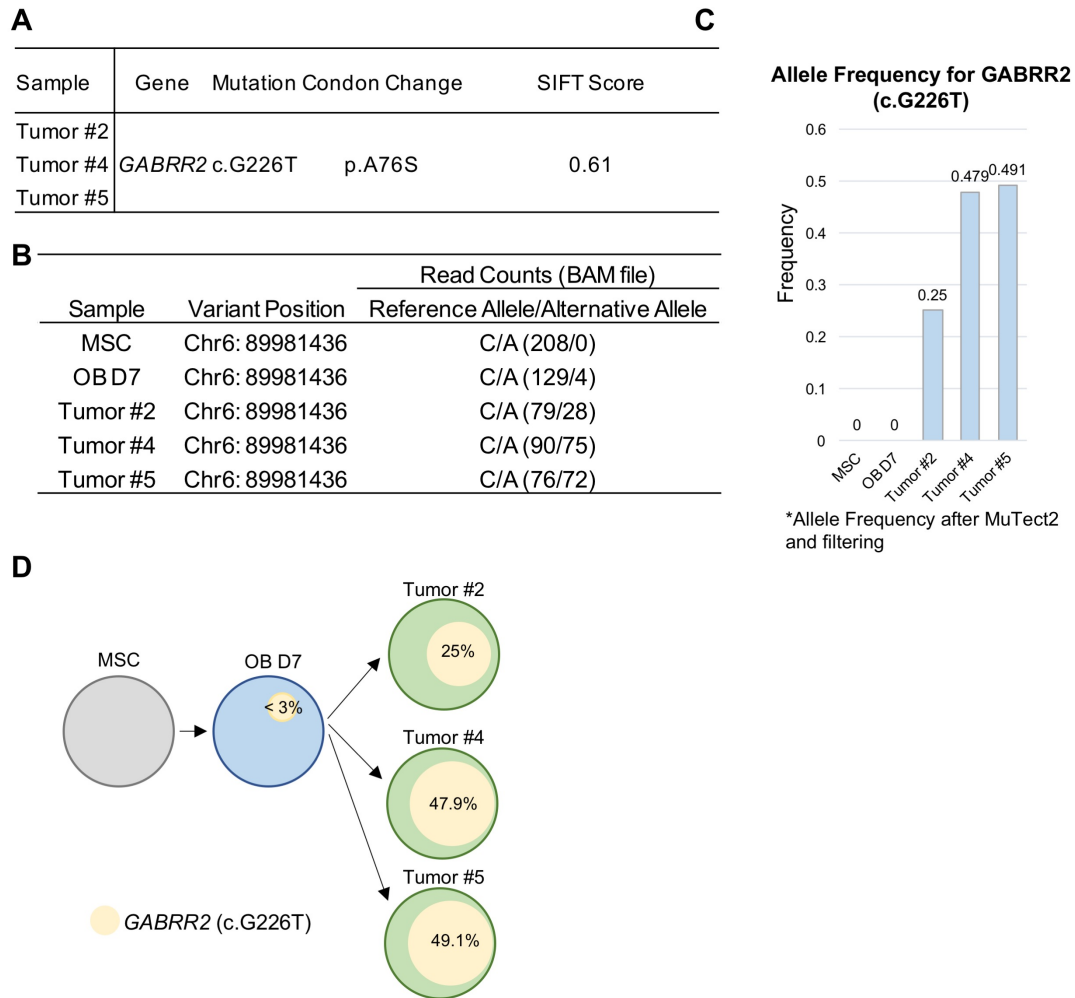


Figure 23. Summary of commonly mutated gene in LFS OB derived tumors.

(A) Table summarizing common variant in *GABRR2* found in three tumor samples. (B) Table summarizing read counts in BAM file of this variant in *GABRR2*. (C) Allele frequency of c.G226T variant of *GABRR2* in MSCs, OBs and three tumor samples. (D) Proposed the model for increased allele frequency of c.G226T variant of *GABRR2*.

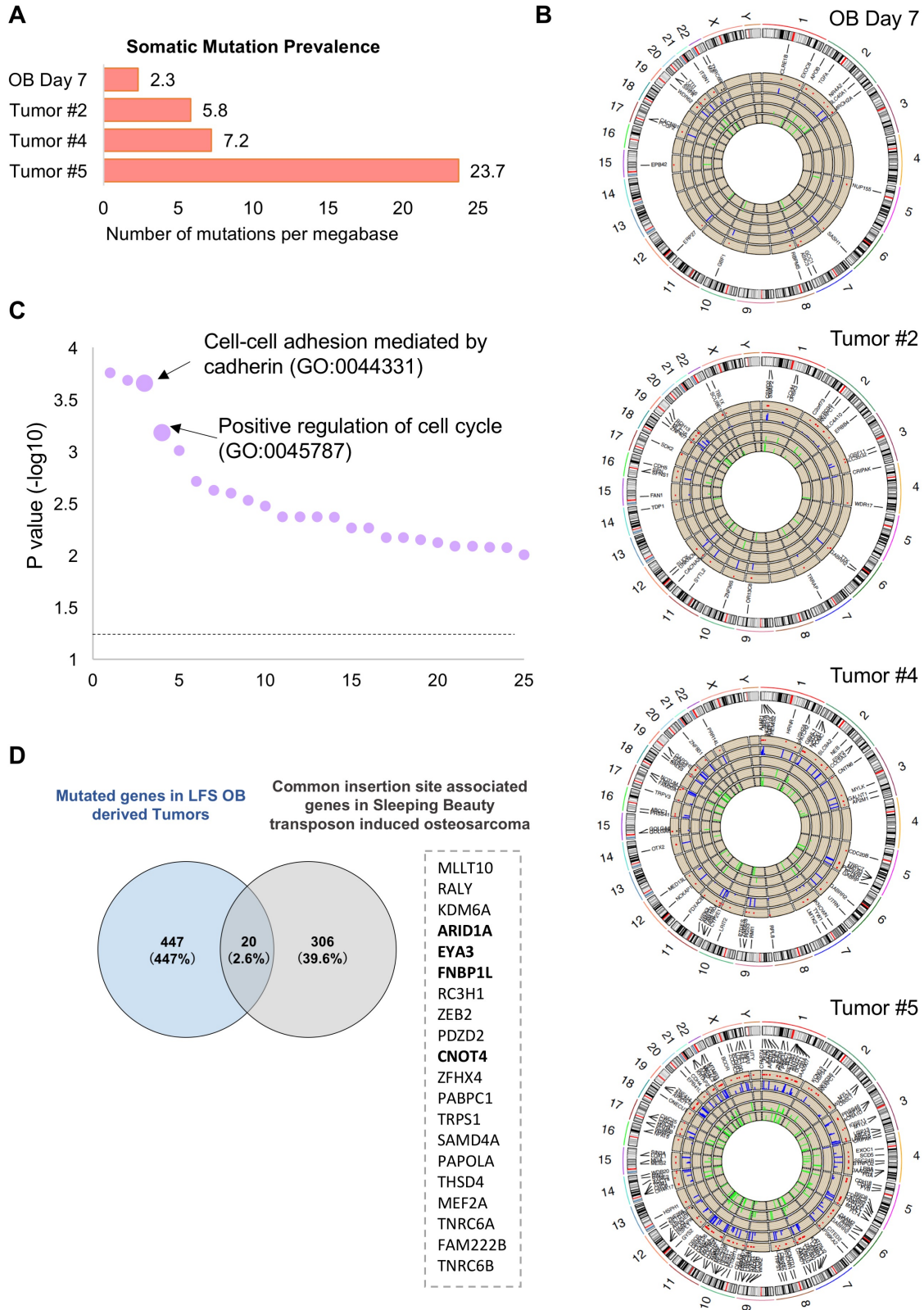
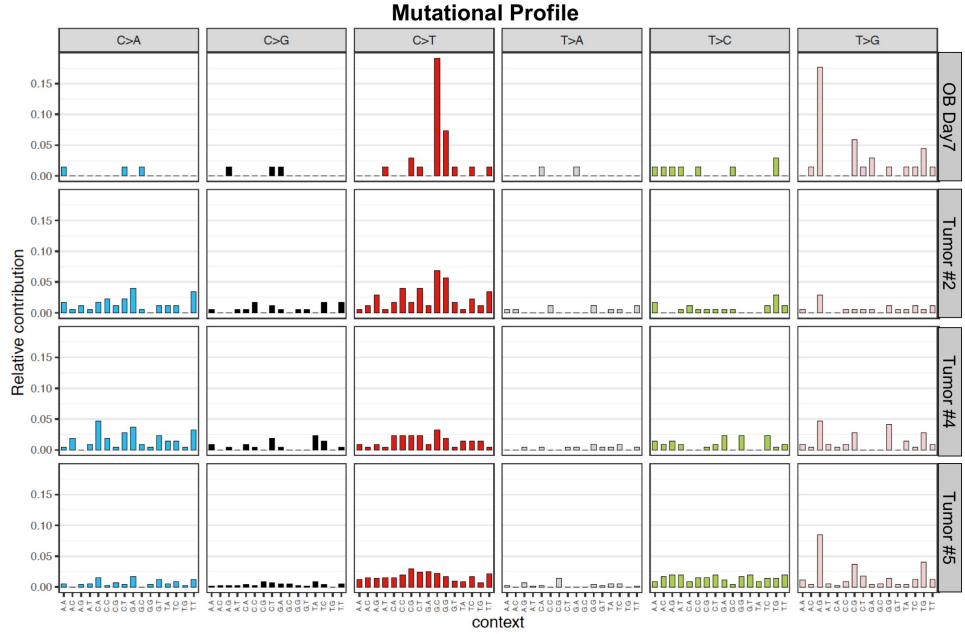


Figure 24. Analysis of identified variants in LFS OB and OB derived tumors.

(A) Somatic mutation prevalence in OBs and three tumor-derived cell lines. (B) CIRCOS plots summarizing variants identified in OBs and three tumor-derived cell lines. From outer line to inner line depicting information regarding chromosome, gene, variant type (non-frameshift substitution, nonsynonymous SNV, stopgain and frameshift substitution), alternative allele count in sample (scale from 0-30), alternative allele count in MSCs (0-30), SIFT score (0-1) and PolyPhen2 score (0-1). (C) Pathway analysis of mutated genes (non-frameshift substitution, nonsynonymous SNV, stopgain and frameshift substitution) identified in OBs and three-tumor derived cell lines. (D) Venn diagram depicting the overlapping of mutated genes in LFS OB derived tumors and CIS associated genes in SB induced osteosarcoma. Genes carrying nonsynonymous mutations are bolded in the list.

A



B

Mutational signature of LFS OB derived tumor compared with human cancer types

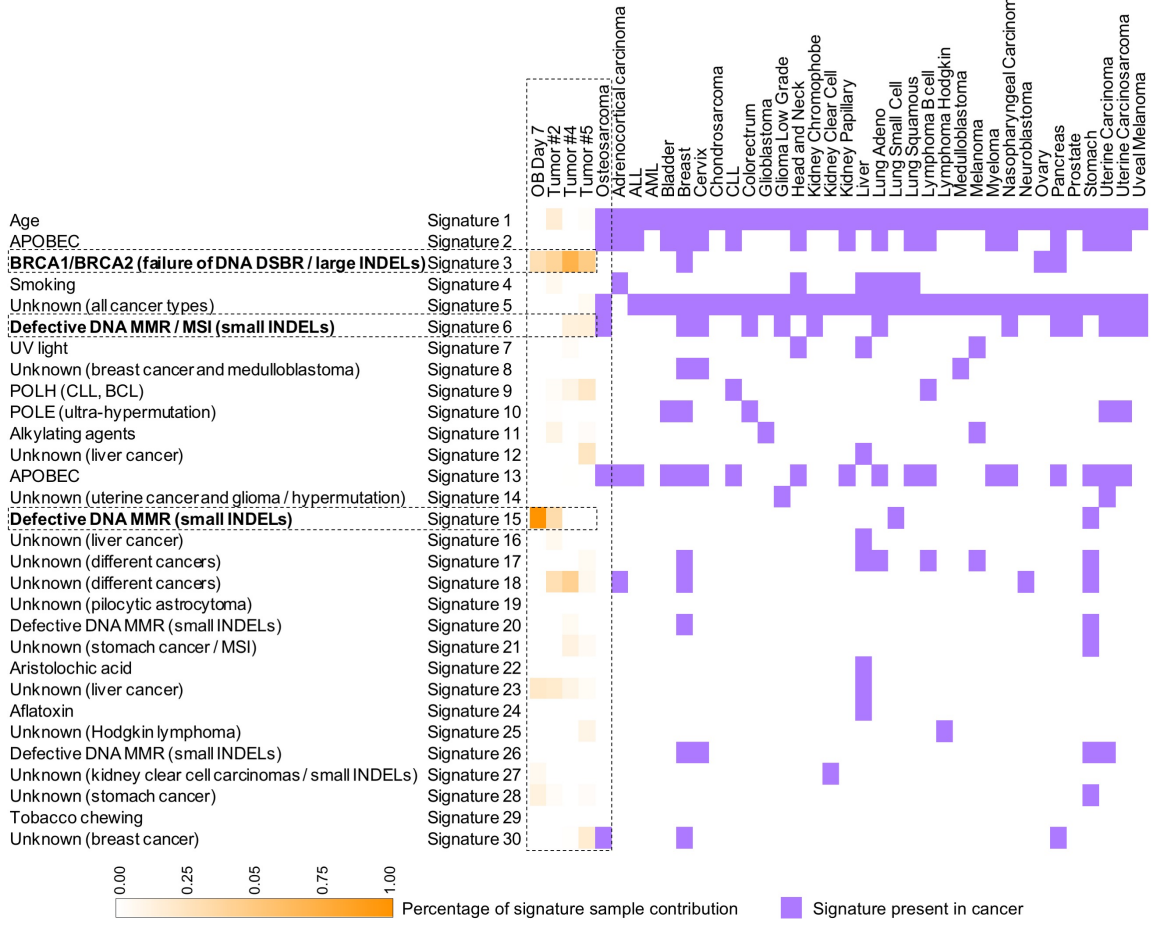


Figure 25. Mutational signature of LFS OBs and OB-derived tumors.

(A) Mutational profile of OBs and three LFS OB-derived tumor cell lines. (B) Mutational signature of OBs and three LFS OB-derived tumor cell lines compared with different human cancers.

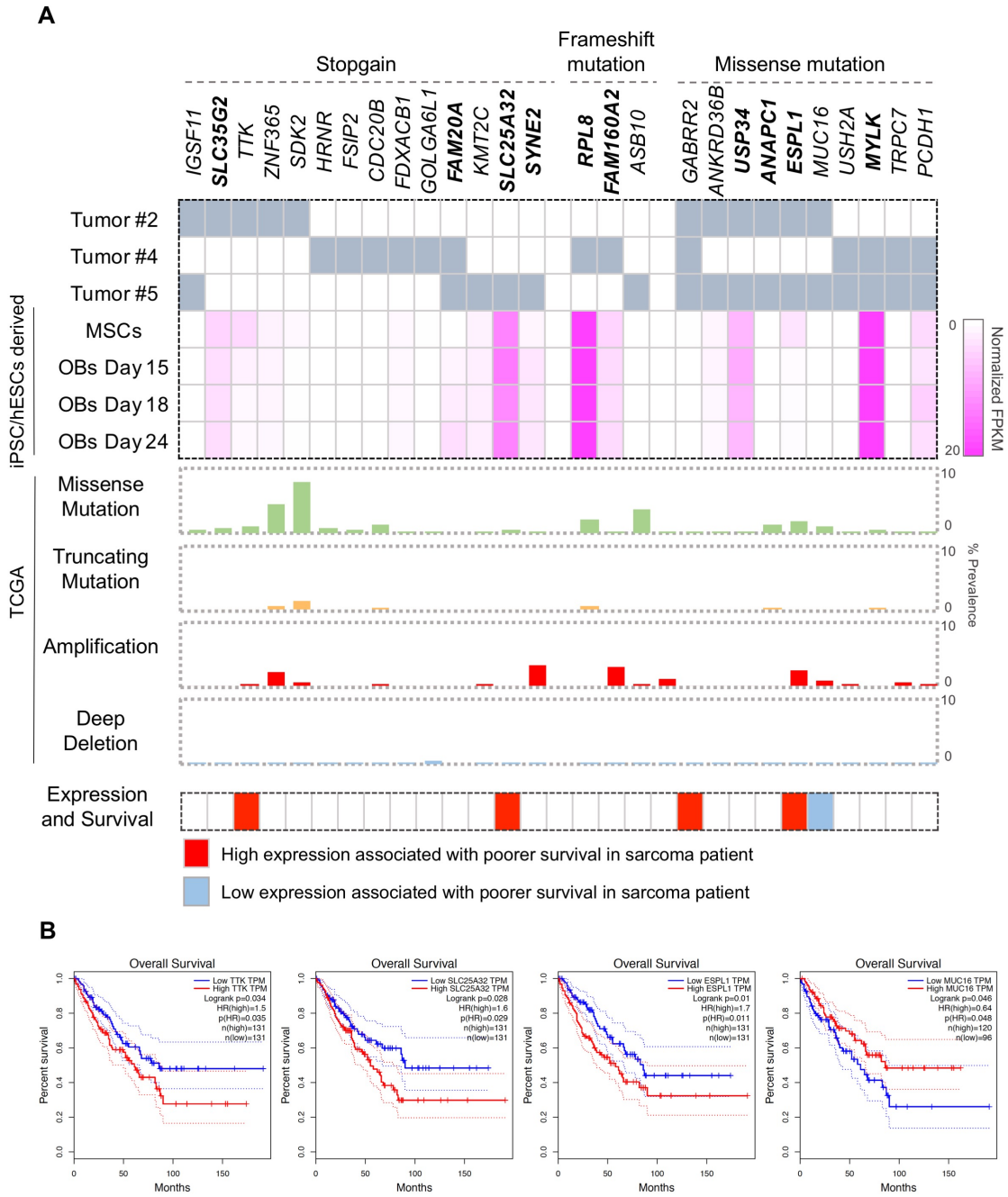


Figure 26. Characterization of mutated genes identified in LFS OBs derived tumors.

(A) Grey box indicates presence of gene mutations in each LFS OB-derived tumor. Pink heatmap indicated the overexpression level of mutated genes in iPSCs/hESCs derived MSCs and OBs at different differentiation time point. Prevalence of

missense mutation, truncating mutation, amplification and deletion of identified genes in human cancers are demonstrated in bar plot. Data were obtained from cBio Cancer Genomics Portal from 42199 tumor samples in 159 studies (<http://cbioportal.org>) (200). Red and blue box indicated whether expression level of identified genes is associated with overall survival in sarcoma patients. Potential candidate genes are bolded. (B) Kaplan–Meier plots indicate high expression level of identified genes *TTK*, *SLC25A32* and *ESPL1* are associated with poorer survival, and low expression of identified gene MUC16 is associated with poorer survival in sarcoma patients. Data were obtained using database GEPIA (<http://gepia.cancer-pku.cn/index.html>) (201).

A study carried out by Alexandrov *et al.* (198) extracted mutational signatures using base substitutions and additionally included information on the sequence context of each mutation. In addition to six classes of base substitution - C>A, C>G, C>T, T>A, T>C, T>G, the study incorporated information on the bases immediately 5' and 3' to each mutated base, creating 96 possible mutations in classification. Using this 96-substitution classification, more than 20 distinct mutational signatures are identified in human cancers. Based on this study, we also characterized mutational signatures in osteoblasts and three tumor-derived cell lines using a web-based application MusiCa (186). We observed a prevalence of C>T mutations in both OBs and tumor-derived cell lines (**Figure 25A**). When comparing mutational signature of LFS OB and OB-derived tumors with different human cancer types, we observed presence of Signature 3 and 30 both in our tumor samples and osteosarcoma (**Figure 25B**). Interestingly, we observed presence of Signature 3, 6 and 15 in LFS OB and OB-derived tumors, all of which are associated with deficiency in DNA damage repair (**Figure 25B**).

In addition to overlapped genes in LFS OB-derived tumor lines (**Figure 22C**), we also found several genes carrying stopgain or frameshift mutation in our LFS OB-derived tumors (**Figure 26A, Table 12**). We checked the expression level of these identified genes in hESCs or iPSCs derived osteoblasts (in house database), and found several genes are expressed, including *SLC35G2*, *FAM160A2*, *SLC25A32*, *SYNE2*, *RPL8*, and *FAM20A* (**Figure 26A**). As shown in **Figure 26**, these genes are also mutated, amplified or deleted in human cancers with various prevalence (data obtained from <http://cbioportal.org>) (200) and expression level of some of

these genes are associated with patient overall survival (data obtain from <http://gepia.cancer-pku.cn/index.html>) (201). We summarized the potential candidate genes that may drive LFS-associated osteosarcoma development in **Table 12**.

Gene	Sample	Mutation	Predicted effect	AA/Sequence Change	SIFT	PolyPhen2	ClinVar
IGSF11	Tumor #2, 5	chr3:118623502:C>A	stopgain	p.E283X	0.08	NA	NA
SLC35G2	Tumor #2	chr3:136573705-G-T	stopgain	p.E135X	0	NA	NA
TTK	Tumor #2	chr6:80747711:G>T	stopgain	p.E692X	0	NA	NA
ZNF365	Tumor #2	chr10:64136574:A>T	stopgain	p.K208X	1	NA	NA
SDK2	Tumor #2	chr17:71468309:G>T	stopgain	p.C91X	NA	NA	NA
HRNR	Tumor #4	chr1:152193815:G>T	stopgain	p.S97X	1	NA	NA
FSIP2	Tumor #4	chr2:186696609:G>T	stopgain	p.E6952X	0.12	NA	NA
CDC20B	Tumor #4	chr5:54439369:C>T	stopgain	p.W153X	0.2	NA	NA
FDXACB1	Tumor #4	chr11:111745843:G>A	stopgain	p.R560X	1	NA	NA
GOLGA6L1	Tumor #4	chr15:22743596:C>T	stopgain	p.Q649X	0.65	NA	NA
FAM20A	Tumor #4, 5	chr17:66536085:A>C	stopgain	p.Y276X	1	NA	NA
KMT2C	Tumor #5	chr7:151873299:G>T	stopgain	p.S3080X	1	NA	NA
SLC25A32	Tumor #5	chr8:104427097:A>C	stopgain	p.Y23X	1	NA	NA
SYNE2	Tumor #5	chr14:64691257:C>T	stopgain	p.R343X	1	NA	NA
RPL8	Tumor #4	chr8:146017298: TCCTGTGGGCAGAG GCGGCGTGAGTGCG GCGTTCCGGCCGGG CGTCCCTTCCCCTCC CGCCCCGGCCAGCG TTCCGCA>T	frameshift substitution	c.139_140A	NA	NA	NA
FAM160A2	Tumor #4	chr11:6238974: CAGCTCTT>C	frameshift substitution	c.1877_1884G	NA	NA	NA
ASB10	Tumor #5	chr7:150873754: G>GCTCCAGCA	frameshift substitution	c.1114_1114delins TGCTGGAGC	NA	NA	NA

GABRR2	Tumor #2,4,5	chr6:89981436:C>A	missense	p.A76S	NA	0.977	NA
ANKRD36B	Tumor #2, 5	chr2:97820413:T>A	missense	p.C399S	0.77	0	NA
USP34	Tumor #5	chr2:61441611:A>G	missense	p.F2756L	0.1	0.878	NA
ANAPC1	Tumor #2, 5	chr2:112615888:C>G	missense	p.Q451H	0.18	0.005	NA
ESPL1	Tumor #5	chr2:61441611:A>G	missense	p.F366L	NA	0.039	NA
MUC16	Tumor #2, 5	chr19:9059734:G>C	missense	p.P9238A	0	0.003	NA
USH2A	Tumor #4, 5	chr1:216371841:G>T	missense	p.S1299R	0.11	0.761	NA
MYLK	Tumor #4	chr3:123359161:T>G	missense	p.I1535L	0	0.378	NA
MYLK	Tumor #5	chr3:123383051:T>G	missense	p.T1227P	0.01	0.984	NA
TRPC7	Tumor #4	chr5:135692438:C>A	missense	p.S213I	0	0.995	NA
PCDH1	Tumor #4	chr5:141249168:A>C	missense	p.M1R	NA	NA	NA

Table 12. Potential candidate genes driving LFS-associated osteosarcoma development.

3.11 Discussion

We showed that LFS patient-derived iPSCs and their MSCs/OBs provide a platform for investigating the early development of LFS-associated osteosarcoma, and identified potential candidate genes in driving osteosarcoma development.

We found that LFS patient iPSCs derived osteoblasts exhibit increased *in vitro* oncogenic properties compared to WT iPSCs derived osteoblasts. The increased number of colony formation in soft agar assay were consistently observed in two LFS family carrying different *TP53* mutations. In addition, LFS derived osteoblasts under continuous culture *in vitro* exhibit increased tumorigenic ability, suggesting LFS iPSC-MSC-O platform can be further extended into *in vivo* model to facilitate driver genes identification in LFS-associated osteosarcoma development.

Interestingly, we found SFRP2 is up-regulated in patient iPSCs derived OBs and hESC-derived OBs carrying different *TP53* mutations. SFRP2 is a known WNT pathway antagonist, and it is considered to be a tumor suppressor (202, 203). In the context of LFS-associated osteosarcoma, SFRP2 functions as an oncogenic factor, and overexpression of SFRP2 exerts oncogenicity in LFS derived OBs. Further study by Kim *et al* (193) indicate SFRP2 can promote osteosarcoma phenotype by inducing angiogenesis and oncogenic molecules such as *FOXM1* and *CYR61* in a β -catenin independent. This study not only demonstrated the potential of LFS iPSC-MSC-OB platform in identifying potential therapeutic targets but also provided solid foundation for using this platform in identifying driver genes during osteosarcoma development.

Consistent with our previous study (122), we found that LFS OBs can form *in vivo* tumors while WT OBs cannot. In this study, we carried out several rounds of injection in immunocompromised mice to establish xenograft model. Generation of orthotopic xenograft model in SCID mice was unsuccessful. One of the reasons might be due to limited cell numbers (2×10^6) that can be injected intratibially as intratibial space can only fit up to 20 μ L volume of cell mix. We also found a relatively low successful rate in generating subcutaneous xenograft in NU/NU mice. In fact, on our hand, only LFS 3-A derived OBs can form visible subcutaneous tumors. The different tumor formation rate between each cell line might be due to clonal effect. Another explanation is that LFS 3-A line might already harbor some driver mutations which give cells *in vivo* growth advantage. It would be interesting to sequence other cell lines, for example LFS 3-C derived OBs, and compare the different genetic profiles between cell lines, which might also aid in osteosarcoma driver genes identification. In addition, the overall low tumor formation rate of LFS derived OBs indicates that these cells are not malignant cells yet. Therefore, sequencing the LFS OB-derived tumor cell lines can help identify driver events during osteosarcoma initiation.

Previous study (199) used *Sleeping Beauty* transposon mutagenesis to drive osteosarcomagenesis. This forward genetic screening enabled the identification of hundreds of significant CIS-associated genes that are likely to be drivers of osteosarcoma development. Here, we present a different approach in identifying driver genes during osteosarcomagenesis by sequencing LFS patient-derived cells with different oncogenic potentials, including MSCs (no tumorigenic ability),

osteoblasts (gaining tumorigenic ability), and osteoblast-derived subcutaneous xenograft (retaining *in vivo* tumorigenic ability). In pathway analysis of mutated genes of our LFS OB-derived tumors, we did not observe enrichment of PI3K/mTOR, ErbB or ERK-MAPK signaling as previous identified osteosarcomas in other studies (199, 204). In the context of LFS associated osteosarcoma, our model aims at discovering initial driver event during LFS-associated osteosarcomagenesis and the collected LFS OBs and OB-derived tumor cell lines are not really at advanced malignant stage, it is possible that the characterized pathway in osteosarcomas might not present in our samples. Interestingly, we found overlapping genes between our mutated genes in LFS OB-derived tumors and CIS-associated genes in SB induced osteosarcoma. The overlapping genes including *ARID1A*, *EYA3*, *FNBP1L*, *CNOT4*, are potential candidate drivers during osteosarcomagenesis.

Utilizing a web-based application MusiCa (186), we also characterized mutational signatures in our LFS OB-derived tumors. Interestingly, we observed a prevalence of C>T mutations in both LFS OBs and OB-derived tumors. Prevalence of localized hypermutation, in particular C>T, have also been observed in osteosarcoma samples (204). The phenomenon of localized hypermutations identified in cancer genomes termed kataegis is recently described in breast cancer (205), and later, was also described in pediatric osteosarcoma (206). In the future, it will also be interesting to figure out whether our LFS OBs and OB-derived tumors carry kataegis hypermutator features using previously described methods (205, 206).

Moreover, we found overlapping mutated genes between three independent LFS OB-derived tumors. Some of commonly mutated genes showed low expression in iPSCs or hESC derived OBs (in house database), while other genes are expressed moderately or highly in OBs, including *USP34*, *ESPL1* and *MYLK*. We also observed genes carrying stopgain or frameshift mutation in our LFS OB-derived tumors, including *SLC35G2*, *FAM160A2*, *SLC25A32*, *SYNE2*, *RPL8*, and *FAM20A*. Reported functions of these genes are summarized in **Table 13** in Chapter 6.1. These genes are potential candidate driver genes during early osteosarcoma development. In the future, functional validation of these mutated genes will provide mechanistic insight during initiation of LFS-associated osteosarcoma and also will help in developing novel therapeutic strategies in treating this disease.

Chapter 4 Potential of Li-Fraumeni syndrome iPSCs platform in modeling breast cancer

4.1 Introduction

Early onset breast cancer is one of the component tumors of Li-Fraumeni syndrome. Women with LFS are at significant high risk for breast cancer before age 40 (207). The lifetime risk of breast cancer development among women with germline *TP53* mutations is approximately 49% by age 60 and the mean age of onset is under 35 years (208-210). According to IARC *TP53* Database (<http://p53.iarc.fr/>), breast cancer is also the most common tumor among women with germline *TP53* mutations (**Figure 27**). Studies also suggest that breast cancers in women with LFS are both hormone receptor and HER2/neu-positive (209, 211, 212).

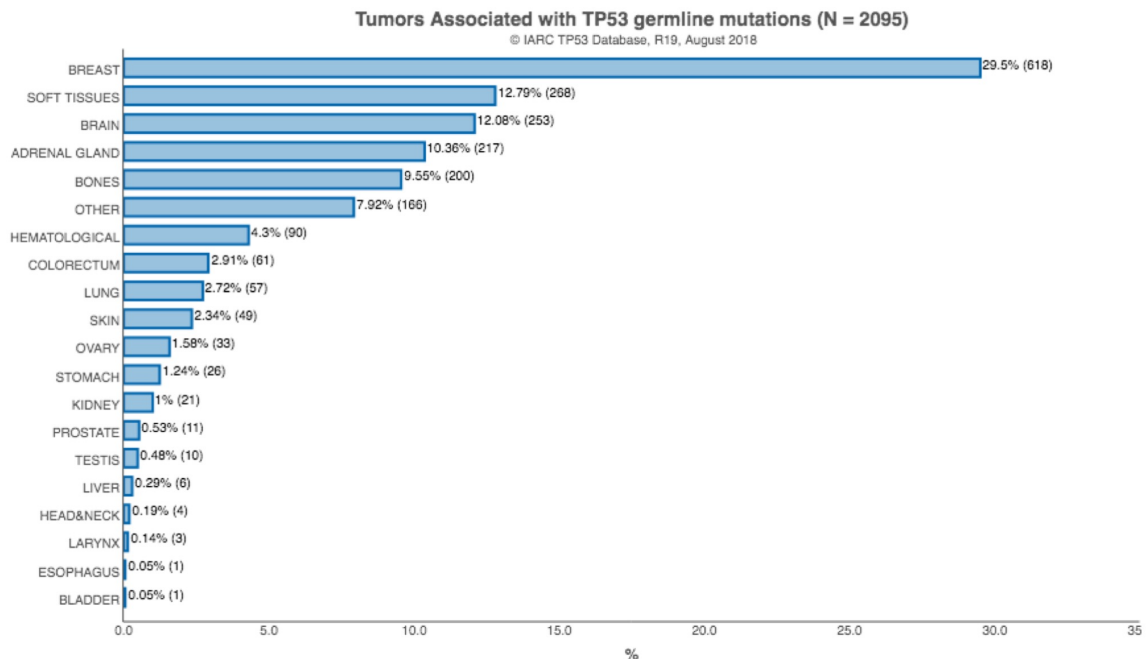


Figure 27. Tumor distribution with *TP53* germline mutations.

Human breast is an organ consists of parenchyma and stroma, originating from ectodermal and mesodermal elements, respectively (213). The branching-tree like mammary gland is composed of epithelium and surrounding stroma (214), while the bilayered mammary epithelium comprises inner layer of luminal cells and outer layer of basal or myoepithelial cells (basal/myoepithelial cells) (215).

A number of transplantation experiments (216-218) suggested the existence of mammary gland stem cells (MaSCs), in which fragments of mammary tissue could reproduce the entire epithelial ductal trees in the clear fat pad of recipient mice. Single-cell lineage-tracing experiments have also revealed the multipotency of MsSCs: a single MaSC can contribute to the formation of the ductal epithelium (during puberty) (219, 220) and of the alveolar epithelium (during lactation) (219). Several mouse model studies also suggested the potential role of MaSCs in tumorigenesis of breast cancer (221-225), supporting the hypothesis that accumulation of oncogenic events (genetically and epigenetically) can lead to the altered control of differentiation and proliferation and contribute to the development of breast cancer.

As described in Chapter 1 and Chapter 3, hereditary cancer patient derived iPSCs can be used to model and study cancer. In this chapter, I hypothesize that by differentiating LFS patient derived iPSCs into mammary gland stem cells or progenitor cells, LFS patients associated breast cancer can be modeled; recapitulating LFS associated breast cancer feature *in vitro* can help identify potential second hit required for breast tumor formation and aid the discovery of novel therapeutic targets.

4.2 Generation and characterization of iPSCs from LFS patients with breast cancer

In order to understand LFS associated breast cancer, fibroblasts were established from skin biopsy of LFS patients. Proband (3649T) of the LFS pedigree shown in **Figure 28A** were diagnosed with breast cancer and carried a heterozygous single nucleotide deletion (delG) at exon 9 and intron 9 junction of *TP53* (c.993delG). One of the proband's daughter (3648T) was also diagnosed with LFS carrying this single nucleotide deletion (delG). The other daughter (3650T) is a healthy individual with wild type *TP53* and were used as a normal control in this study (**Figure 28A, 28B**). Three fibroblasts were reprogramed using Yamanaka factors as illustrated in **Figure 9A**. The ability of these patients' derived iPSCs in differentiating into mammary stem cells (MaSCs) or mammary epithelial cells will provide platform for modeling breast cancer.

Three iPSC clones generated from proband (3649T) named C3, C14 and C17 were maintained in feeder free condition for 10 to 15 passages and further examination by RT-PCR using specific primers indicated all three clones were free of SeV genome and four transgenes (**Figure 28C**). Examination of iPSC clones generated from carrier (3648T), named B1, B2 and B3, indicated that only clone B1 is free of SeV genome and four transgenes. Clone B2 and B3 had retention of SeV genome and *c-MYC* transgene (**Figure 28C**). Four iPSC clones were generated from healthy individual (3650T), named D6, D8, D12 and D19. RT-PCR examination indicated D6, D8 and D19 clones were free of SeV genome and four transgenes, D12 clones had some retention of SeV genome (**Figure 28C**).

We further performed karyotype analysis of iPSC clones generated from proband (3649T) and carrier (3648T). Three clones (C3, C14, C17) generated from proband all maintained normal karyotype (**Figure 28D**). While B1, B2, B3 clones showed abnormal karyotype: B1 clone showed trisomy 6, B2 and B3 clones showed trisomy 5 (**Figure 28D**). Due to abnormal karyotype, iPSC clones B1, B2 and B3 generated from carrier (3648T) were not further characterized and used in this study.

Further characterization of the iPSC clones generated from LFS patient 3649T and unaffected relative 3650T indicated all seven clones exhibit the typical hESC morphology and show the positive AP activity (**Figure 29A**). LFS patient iPSC clones also highly express pluripotency factor mRNAs (NANOG, OCT4, SOX2, DPPA4, and REX1), comparable to hESC H1 line and much higher than parental fibroblasts (**Figure 30B**). Immunofluorescent staining showed these generated iPSC clones all highly express pluripotency factors (NANOG, OCT4) and hESC markers (SSEA4 and TRA-1-81) (**Figure 30A**).

Subcutaneous injection of LFS and WT iPSC clones in NU/NU mice resulted in teratoma formation. Histological analysis indicated that teratoma formed from iPSC clones contain embryonic tissues of all three germ layers (**Figure 29B**), including epithelium (endoderm); cartilage, adipose tissues (mesoderm); neural tube structure, melanin containing cells (ectoderm). These results indicate that the generated LFS (3649T) and WT (3650T) iPSC clones are truly pluripotent.

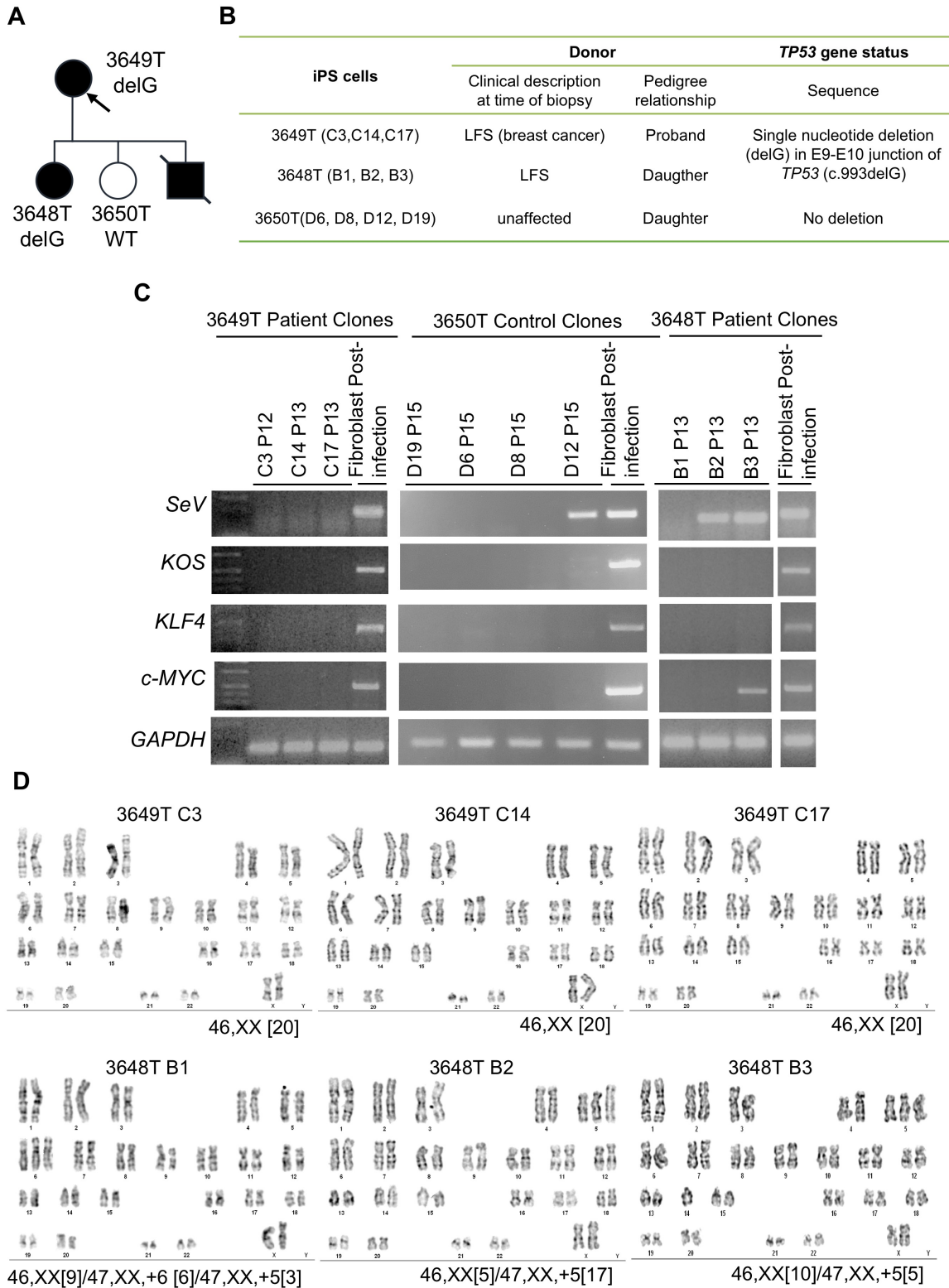


Figure 28. Generation of iPSC from LFS patient with breast cancer.

(A) LFS family tree (arrow: proband). (B) Single nucleotide deletion (delG) between exon 9 and exon 10 junction were found in LFS patient fibroblasts (3648T and 3649T). Fibroblasts were also collected from unaffected relatives carrying wild type p53. (C) RT-PCR detection of Sendai virus genome and transgenes (KOS (KLF4, OCT4, and SOX2), KLF4, and c-MYC) in the reprogrammed iPSC clones after 10 passages and fibroblasts post-infection (right lane, positive control). GAPDH is shown as internal control. LFS iPSC clone C3, C14, C17, B1, D6, D8, D19 are Sendai virus free; clone D12 showed Sendai virus genome retention; clone B2, B3 showed Sendai virus and *c-MYC* transgene retention. (C) iPSC clones generated from proband (3649T) maintain normal karyotype. iPSC clones generated from affected individual (3648T) showed abnormal karyotype: B1 clone showed trisomy 6, B2, B3 clone showed trisomy 5.

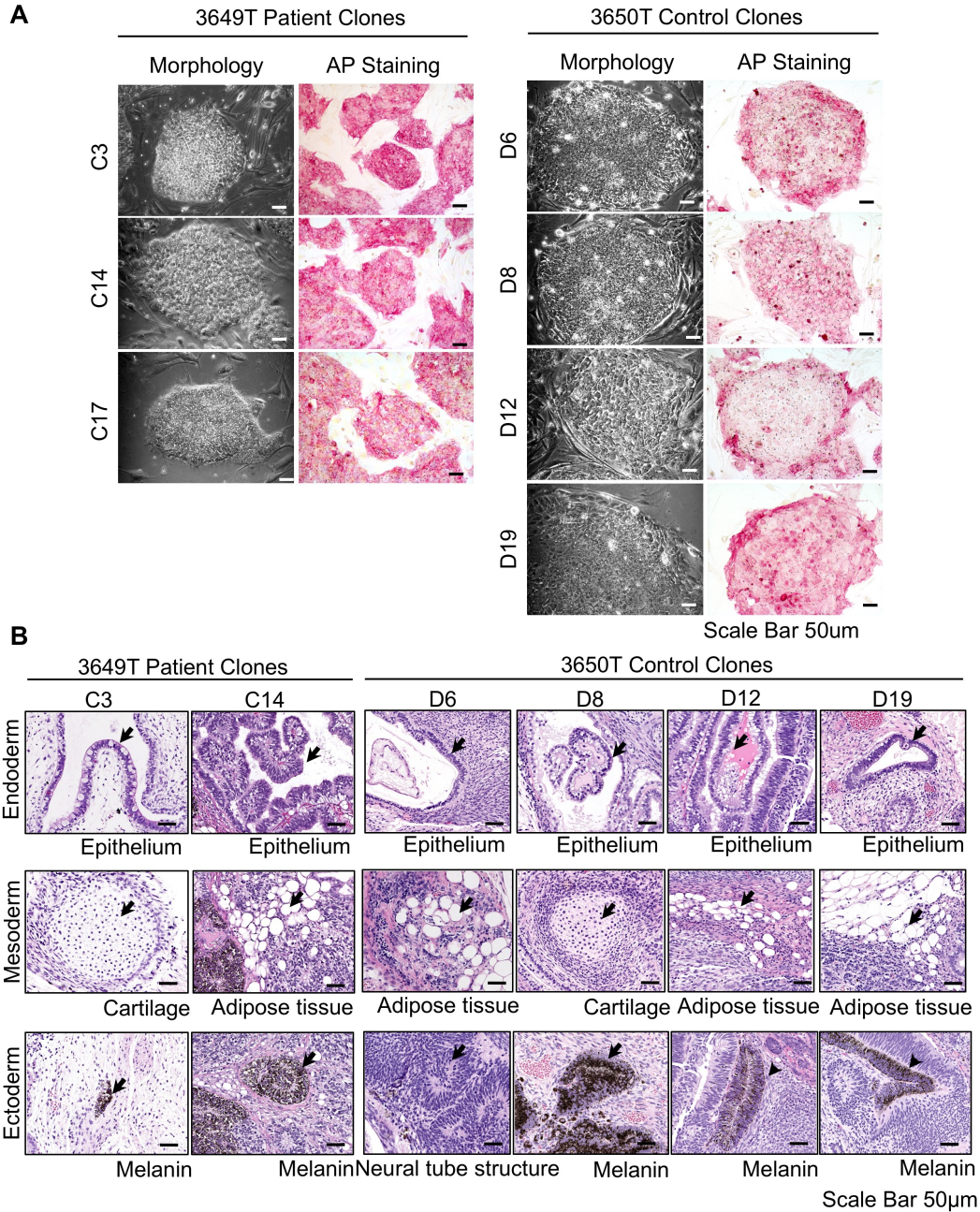


Figure 29. Characterization of iPSC from LFS patient with breast cancer.

(A) Cell morphology and AP staining of 3649T LFS patient derived iPSC clones and 3650T unaffected relative derived iPSC clones. Scale bar, 50 µm. (B) *In vitro* teratoma assay of the 3649T LFS patient derived iPSC clone C3, C14, and 3650T unaffected relative derived iPSC clone D6, D8, D12 and D19. Scale bar, 50 µm.

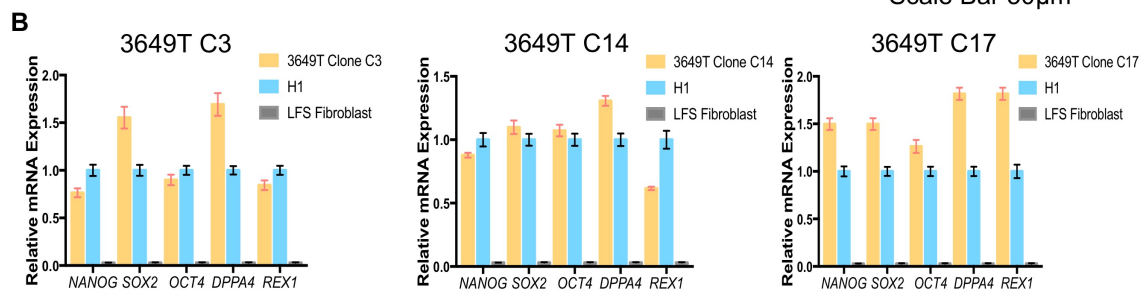
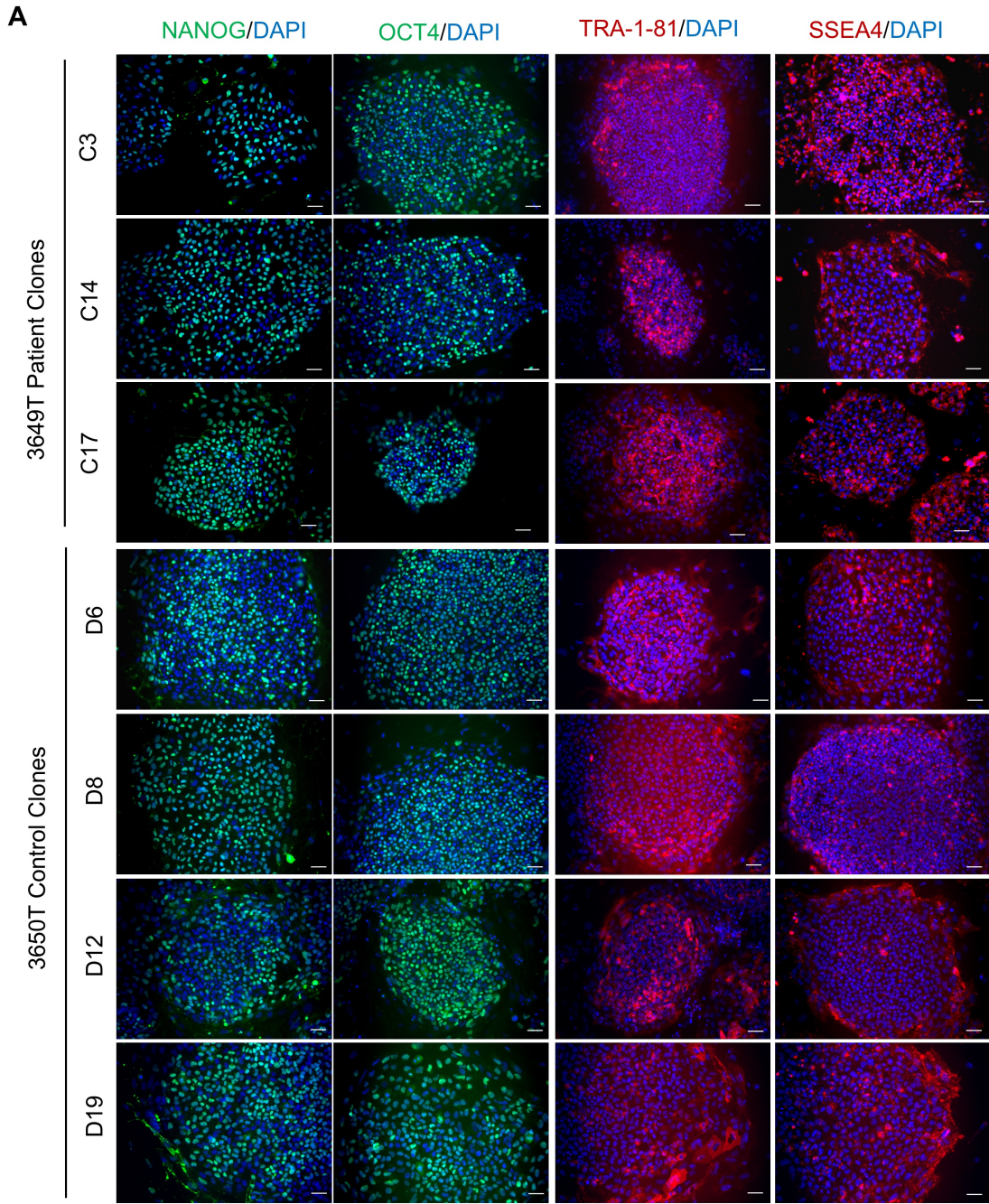


Figure 30. Characterization of iPSC from LFS patient with breast cancer (continued).

(A) Immunostaining of hESC pluripotent transcription factors (NANOG and OCT4) and hESC surface markers (SSEA4 and TRA-1-81) in 3649T LFS patient derived iPSC clones and 3650T unaffected relative derived iPSC clones. Scale bar, 50 μ m.

(B) qRT-PCR of NANOG, SOX2, OCT4, DPPA4, and REX1 mRNA expression in 3649T LFS patient derived iPSC clones. hESC H1 line and parental LFS fibroblasts are used as a positive and a negative control, respectively. The mRNA expression is normalized to GAPDH expression. The relative mRNA expression is adjusted to hESC H1 line as 1.

4.3 Generation of isogenic control by creating *TP53* mutation in WT iPSCs using TALEN mediated genome editing

iPSC clones generated from LFS patient (3649T) and unaffected relative (3650T) provide a pair of family control for this study. However, genetic diversity still exists between individuals (even between relatives). To better reveal this mutant p53 (delG) related phenotypic differences and minimize the variability between patient and healthy individual derived iPSC lines, we aimed to generate isogenic controls by either correcting *TP53* mutation (delG) using patient (3649T) derived iPSC clones or creating this single nucleotide deletion (delG) in unaffected daughter derived iPSC clones (**Figure 31A**) using TALEN-mediated or CRISPR/Cas9-mediated genome editing tools.

Two pairs of TALEN plasmids and two pairs of CRISPR/Cas9 guided plasmids targeting intron 9 of *TP53* were designed. TALEN targeted sites and CRISPR/Cas9 targeted sites are in bold red and green respectively (**Figure 31B**).

The mutant and WT donor vectors were constructed using pFNF donor vector carrying a Frt-EM7-NeoR-Frt (FNF) selection cassette flanked by 1 kb left and right homologous arms of the *TP53* genomic region and primers used to identify correctly inserted colonies are shown with arrows (**Figure 31B**).

To test the potential efficiency of designed TALEN guides and CRISPR/Cas9 guides, these vectors were transfected as pairs in to 293T cells. The transfection efficiency was satisfactory as indicated by concurrent transfection of control vector with GFP (**Figure 31C**). Targeted *TP53* sequence were amplified by PCR and

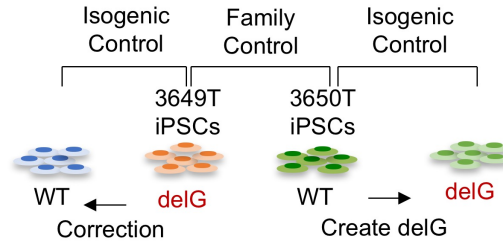
treated with T7 endonuclease I (T7E1). Compared with control, four pairs of guides showed cleaved bands.

For mutant p53 (delG) correction, iPSC clone 3649T C14 were transduced with WT donor vector and 4 pairs of guides respectively, and selected by G418. G418-resistant clones were confirmed by genomic PCR using two pairs of primers (p53_4FM13 and 3FNF-N1 for left arm, 5FNF-C1 and 3p53_17099 for right arm) (**Figure 31B**). Total 154 and 160 clones were picked for TALEN pair 1 and 2 respectively, however, none of the clones were correctly inserted (**Figure 32A**). Total 141 and 163 clones were picked from CRISPR/Cas9 pair 1 and 2 respectively, and similarly no clones were corrected inserted (**Figure 32A**). To rule out the low insertion rate was clone specific, TALENs pair 1 guides and WT donor were transduced in three patient-derived the iPSC clones (C3, C14, C17). Similar to previous results, all three clones showed low insertion rate (less than 5%) (**Figure 32B**). 4 clones were correctly inserted in 3649T C3 line, confirmed by genomic PCR using two pairs of primers (**Figure 32C**). Sanger sequence results further indicated that the correctly inserted WT donor vector in these 4 clones were all located in WT allele (**Figure 32D**). To our experience, correcting *TP53* mutation was quite difficult with low insertion rate especially low chance of WT donor vector to be inserted in mutant allele (further discussed in Chapter 5).

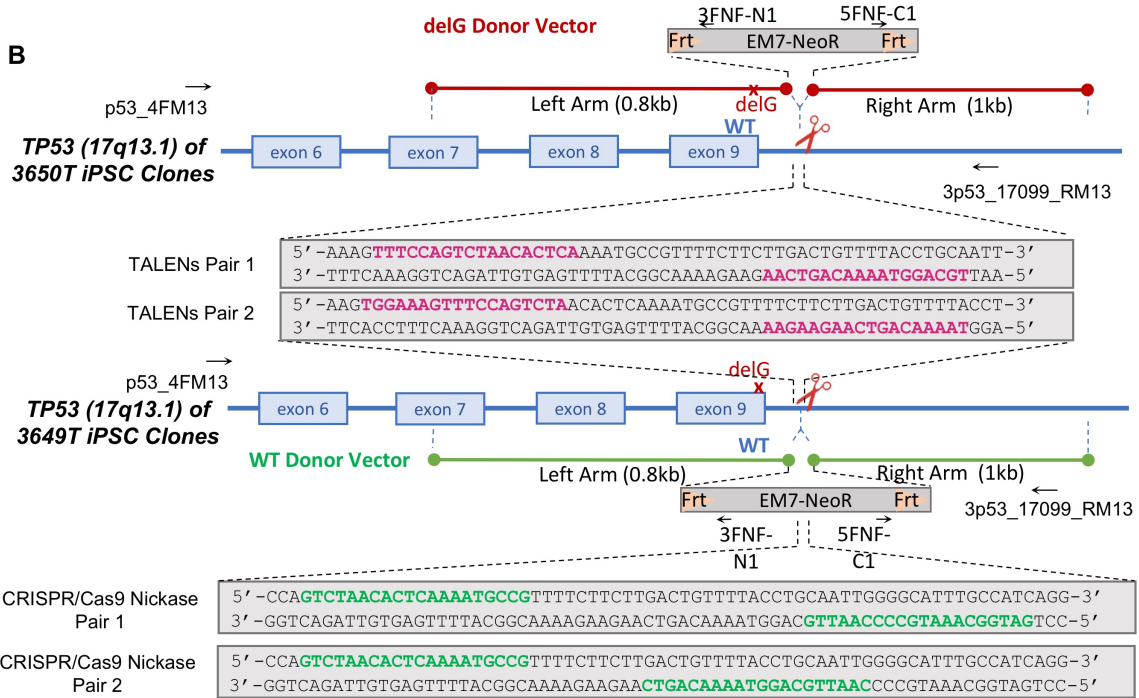
To create mutant p53 (delG), TALENs pair 1 guides and mutant donor vector were transduced in two unaffected relative derived the iPSC clones (D6, D8). Two batch of experiment were performed for each clone with different amount of TALEN guides transduced illustrated in **Figure 33A**. The overall correct insertion rates

were between 15% to 27% in both clones (**Figure 33A**). The correctly inserted clones were confirmed by genomic PCR using two pairs of primers (p53_4FM13 and 3FNF-N1 for left arm, 5FNF-C1 and 3p53_17099 for right arm), as shown in representative graph (**Figure 33B**). The correctly inserted clones were also checked by PCR amplification of exon 8 and 9 of *TP53* using primer p53_8/9FM13 and p53_8/9RM13: clones with positive band indicated that insertion was only in one allele, while absent of the band indicated that insertion was in both allele (inserted Frt-EM7-NeoR-Frt cassette was too big in size to PCR) (**Figure 33B**). Southern blot indicated, among correctly inserted clones, numerous clones carried single insertion (**Figure 33C**) located in *TP53* genomic region (shown in green and yellow arrows). Clones carried multiple bands were discarded. Sanger sequence of the single inserted clones indicated that most of clones with inserted allele carried desired *TP53* mutation (delG), while clone D6 12-1 and D8 8-4 on the other hand, the inserted allele still carried WT *TP53* (no mutation) (**Figure 33D**). Further removal of Frt-EM7-NeoR-Frt cassette by transfecting Fip recombinase in these selected clones (**Figure 32E**) will generate isogenic control for this study.

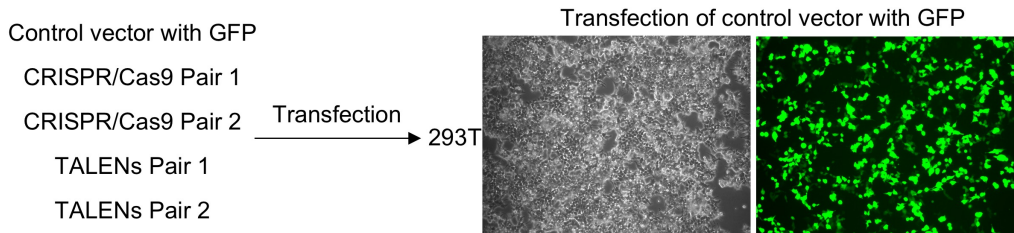
A



B



C



D

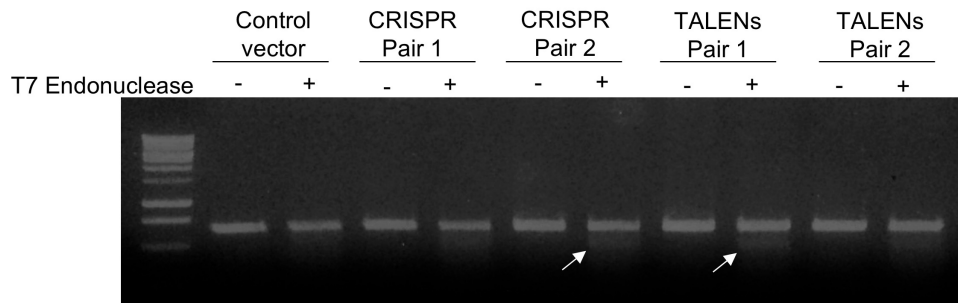


Figure 31. Schematic diagram of the strategy for correcting mutant p53 (delG) and creating mutant p53 (delG) using precise genome editing tools.

(A) Generation of isogenic controls by either correcting or creating *TP53* mutation (delG). (B) Schematic diagram of the strategy for correcting mutant p53 (delG) and creating mutant p53 (delG) using TALEN-mediated or CRISPR/Cas9-mediated genome editing tools. (C) Transfection of control GFP vector and four pairs of TALEN and CRISPR/Cas9 guides in 293T cells. (D) T7E1 assay showed cleaved bands for four pairs of guides TALENs pair 1/2 and CRPSR pair 1/2.

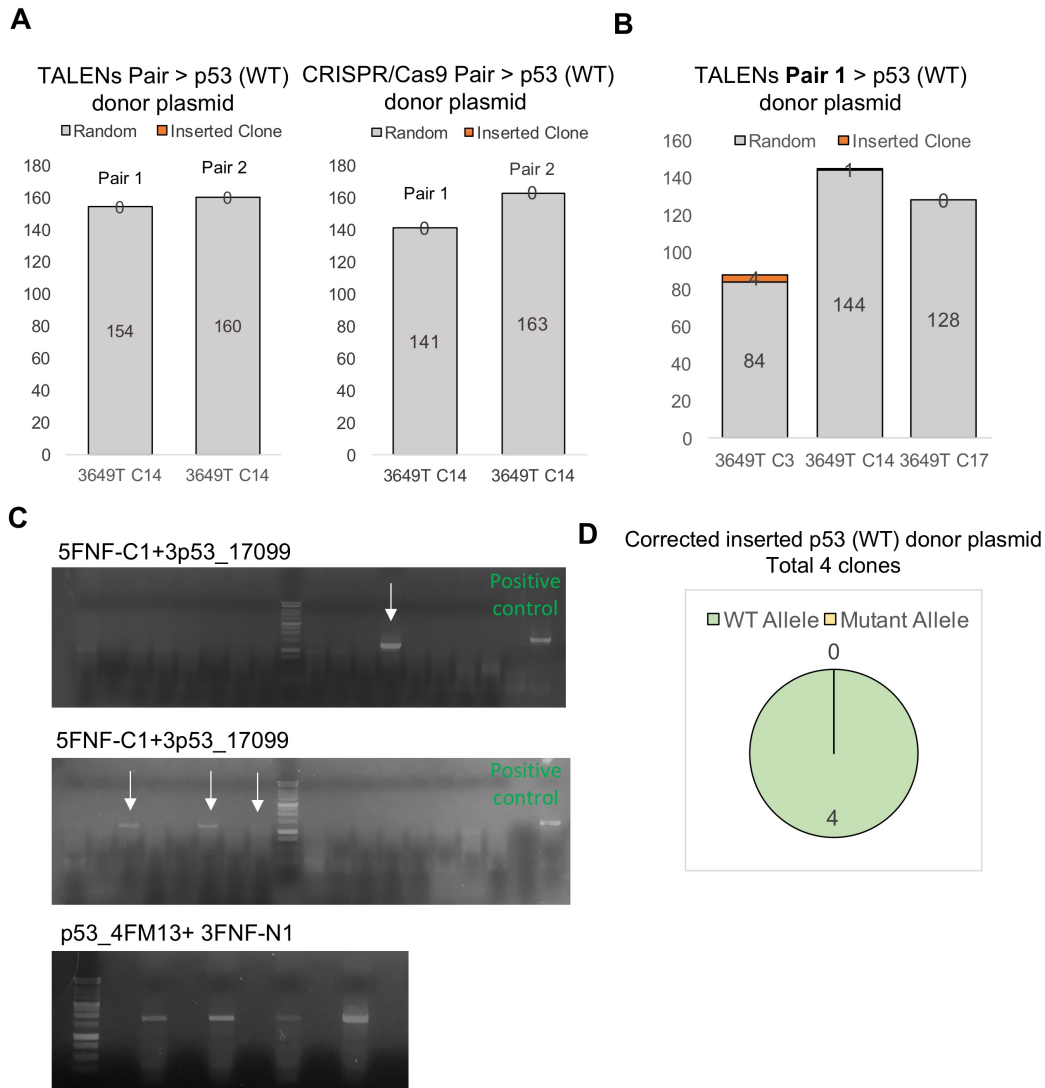
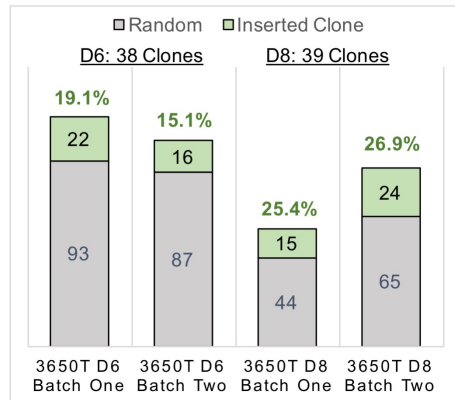


Figure 32. Generation of isogenic controls by correcting *TP53* mutation (delG) using precise genome editing tools.

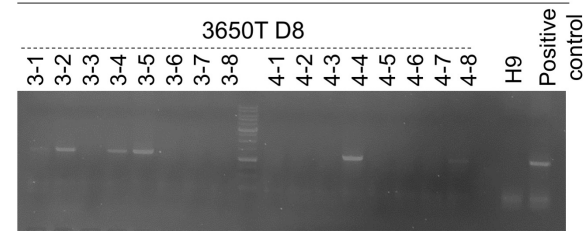
(A) Number of inserted clones picked from iPSC clone 3649T C14 transduced with WT donor vector and 4 pairs of guides respectively. (B) Number of the inserted clones picked by transducing TALENs pair 1 guides and WT donor vector in three patient-derived iPSC clones (C3, C14, C17). (C) PCR confirmation of 4 inserted clones from 3649T C3 line. (D) Correctly inserted WT donor vector in total 4 clones were all located in WT allele.

A TALENs Pair 1 > p53 (mutant) donor plasmid

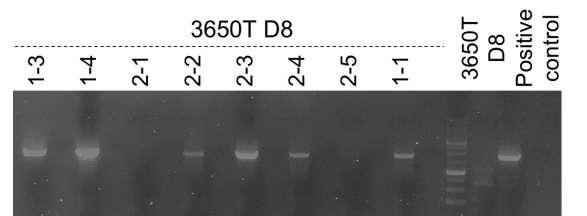


*Batch One: TALENs (5µg+5µg) > donor plasmid (50µg)
 *Batch Two: TALENs (10µg+10µg) > donor plasmid (50µg)

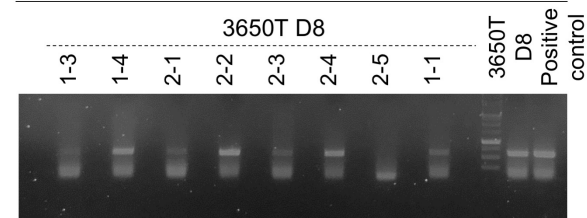
B 5NFN-C1+3p53_17099



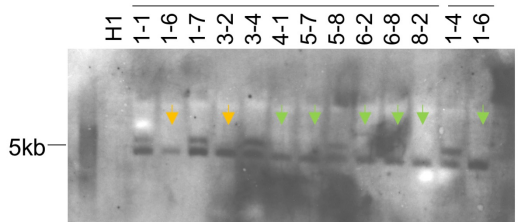
p53_4FM13+ 3FNFN-N1



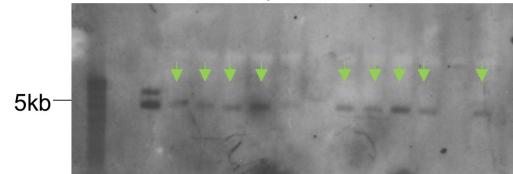
p53_8/9FM13+ p53_8/9RM13



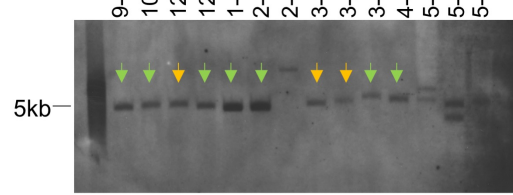
C 3650T D6 Batch One Batch Two



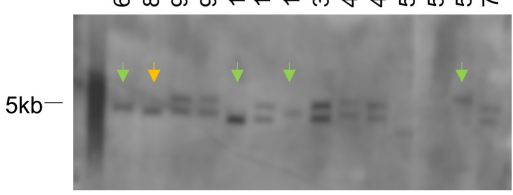
3650T D6 Batch Two



3650T D6 Batch Two 3650T D8 Batch One



3650T D8 Batch One 3650T D8 Batch Two



D

iPSCs	Clone	Sequenced Results	Single Insertion
3650T D6	1-6	delG	✓
	3-2	delG	✓
	12-2	WT	✓
3650T D8	3-1	delG	✓
	3-2	delG	✓
	8-4	WT	✓

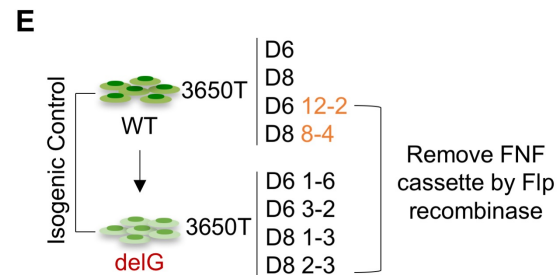


Figure 33. Generation of isogenic controls by creating *TP53* mutation (delG) using precise genome editing tools.

(A) Number of correctly inserted clones picked from iPSC 3650T D6 and D8 line transduced with mutant (delG) donor vector and TALEN pair 1 guide. Insertion rate of each experiment is shown on top of each bar. (B) Representative results of PCR confirmation of inserted clones using two pairs of primers (p53_4FM13 and 3FNF-N1 for left arm, 5FNF-C1 and 3p53_17099 for right arm). PCR amplification of exon8/9 of *TP53* using primer p53_8/9FM13 and p53_8/9RM13. (C) Southern blot of inserted clones. Numerous clones carry single insertion targeted *TP53* genomic region. Clones with multiple bands were discarded. (D) Table list out six clones with single insertion, carrying either desired *TP53* mutation or no mutation. (F) Future plan for generating isogenic control for this study: removal of Frt-EM7-NeoR-Frt cassette by transfecting Fip recombinase in selected clones.

4.4 Differentiation of LFS iPSC into mammary-like organoid

The potential of patient derived iPSCs in modeling cancer critically depend on availability of well-defined differentiation protocol. However, directed differentiation protocols of breast tissue, either for mammary stem cells (MaSCs) or mammary glands have not been sophisticatedly established so far (188). In 2017, Qu *et al.* developed a two-step wise protocol enable differentiation of human iPSCs to mammary-like organoids, providing an iPSC-based model for studying function and regulation of normal mammary cell (226). To further explore LFS-associated breast cancer using iPSC based model, we aim to induce mammary lineage differentiation following protocol described by Qu *et al.* group (226).

Formation of embryoid bodies (EBs) from iPSCs or hESCs is broadly used for direct differentiation. However, *in vitro* studies have shown that EBs formation preferentially induces neural ectoderm from iPSCs/hESCs (227). Enrichment of non-neural ectoderm cells, the origin of mammary stem cells, during initial differentiation stage is therefore critical.

The described protocol contains two steps: MammoCult medium-cultured EB (mEB) formation (step1) and 3D mixed floating gel culture (step2) (226) (**Figure 34A**). Embryoid bodies were cultured in MammoCult medium (mEB) for at least 10 days for the purpose to enrich non-neural ectoderm cells.

Instead of low attachment plates, AggreWell were used in our experiments to facilitate embryoid bodies formation (**Figure 34B, 35A**). The classic embryoid bodies formation were performed in parallel as control (**Figure 34, 35**). To test whether the first step of the protocol can be reproduced in our hand, human

embryonic stem cell line RUES2 (female derived) and LFS patient derived iPSCs (3649T C14 line) were used to form mEBs and classical EBs (**Figure 34B, 35A**). The formed mEBs and EBs were maintained for 10 days and collected, reattached overnight for immunostaining. Both 10-day mEBs and EBs express neural ectoderm marker Tuj-1 and non-neural ectoderm marker CK18. In RUES2 line, 10-day mEBs contains higher percentage of Tuj-1 positive cells when compared to cells migrate out of 10-day EBs (**Figure 34C**), which was expected to be enriched in Tuj-1 positive cells. Staining of non-neural ectoderm marker CK18 in 10-day mEBs and EBs showed expected results: 10-day mEBs contained higher percentage of CK18 positive cells (**Figure 34C**).

Immunostaining of Tuj-1 in 10-day mEBs and EBs derived from LFS iPSC (3649T C14) indicated that cells migrated out from mEBs and EBs both express high level of Tuj-1 (**Figure 35B**). Similarly, reattached 10-day mEBs and EBs derived from LFS iPSC (C14 line) expressed comparable level of CK18 (**Figure 35B**). These results indicated that neural and non-neural ectoderm cells coexist at 10-day embryoid bodies stage, both in EBs and mEBs. On our hand, MammoCult medium-cultured EBs (mEBs) expressed non-neural ectoderm marker, however, we did not observe significant enrichment of non-neural ectoderm cells when compared with classically formed EBs, as described in the protocol (226).

Qu *et al.* also indicated 10-day mEBs harbor the maximum percentage of non-neural ectoderm stem cells and have greater differentiation potential for further mammary gland lineage commitment (226). LFS iPSC (C3, C14 line) were cultured with MammoCult medium in AggreWell for 12 days, and mEBs were collected

every three days and reattached for immunostaining. For both C3 and C14 line (data of C14 line not shown here), non-neural ectoderm marker AP-2 γ and CK18 started to express in 3-day mEBs (**Figure 35, 26**). The percentage of AP-2 γ positive cells slightly increased during the 12-day mEB formation, and more than 50% of reattached cells express AP-2 γ around day 10 (**Figure 35**). More than 50% of the cells were of CK18 positive at day 3, and no significant increase of percentage of CK18 positive cells were observed during 12-day differentiation (**Figure 36**). In our experimental setting, non-neural ectoderm marker started express in early mEB formation process (day 3), and we did not observe continuous increase of the percentage of non-neural ectoderm cells during the 12-day differentiation. 10-day mEBs did not harbor the maximum percentage of non-neural ectoderm stem cells when compared to other time point (**Figure 36, 37**) as described in previous protocol (226).

Western blot results also indicated that the expression of CK18 were much higher in 10-day mEBs compared with LFS iPSCs or RUES2 (**Figure 38A**). And expression level of AP-2 γ was also elevated in C3, C17 and RUES2 derived 10-day mEBs, while C14 derived 10-day mEBs showed a slight decrease in AP-2 γ expression level compared with C14 iPSCs (**Figure 38A**).

10-day mEBs were collected and further immersed in Matrigel/Collagen matrix to induce mammary-like branching. After 25 to 30-day culture, we only observed several mEBs (3650T and 3649T iPSCs derived) be able to develop branch-like structure (**Figure 38B**). However, the overall efficiency of the step 2 in this protocol were quite low on our hand.

We further explored another published protocol seeking for better consistency and differentiation efficiency. Tchieu *et al.* (228) developed a modular platform for differentiation of human pluripotent stem cells into all major ectodermal lineages. The described non-neural ectoderm differentiation protocol is a chemical based protocol, which as stated, is much consistent and efficient.

Following their 12-day non-neural ectoderm differentiation protocol (228) (**Figure 39**), staining of non-neural ectoderm marker AP-2 α , AP-2 γ and CK18 were performed at differentiation day 12. More than 90% of the LFS iPSCs (3649T C14), WT iPSCs (3650T D6, D8) and hESCs (RUES2) derived non-neural ectoderm cells expressed AP-2 α and AP-2 γ ; percentage of CK18 positive cells was also high (>50%) in these cells (**Figure 39A**). Next we explored whether these differentiated non-neural ectoderm cells hold potential to form mammary-like organoids by embedding cells in 3D Matrigel/Collagen matrix culture system following previous used protocol (226). However, the differentiation efficiency remained low and few cells were able to form branching-like structure (**Figure 39B**).

Establishment of mammary lineages differentiation protocol with high efficiency and consistency is needed for breast cancer modeling using LFS iPSCs in this study.

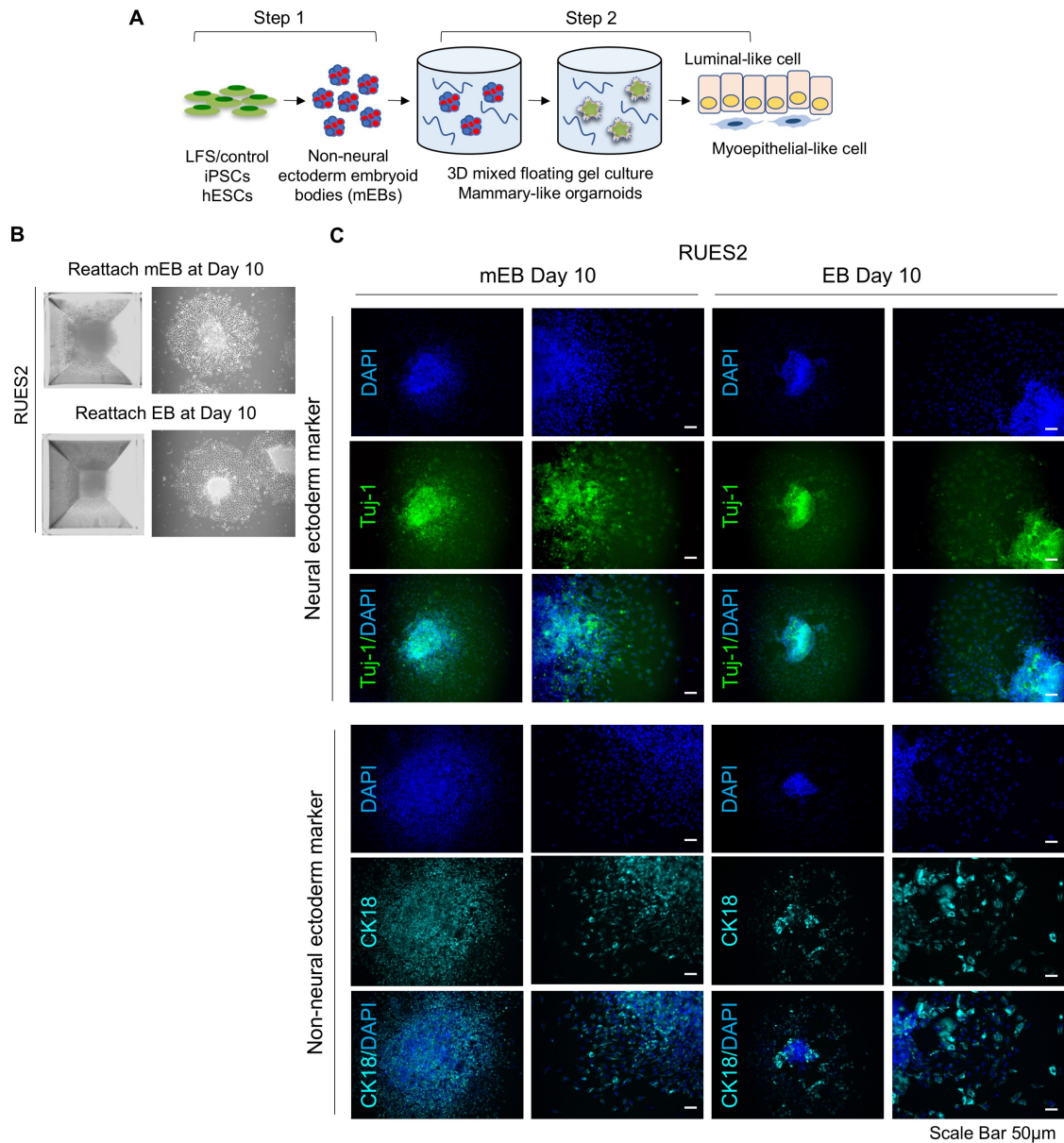


Figure 34. Generation of mEBs and EBs from hESCs.

(A) Schematic of two-step differentiation protocol for mammary-like organoid: MammoCult medium-cultured EB (mEB) formation (step1) and 3D mixed floating gel culture (step2). (B) 10-day mEBs/EBs formed in AggreWell and the morphology of reattached mEBs/EBs. (C) Immunostaining of neural ectoderm marker Tuj-1 and non-neural ectoderm marker CK18 of 10-day mEBs and EBs derived from hESCs RUES2. Scale bar, 50 μm.

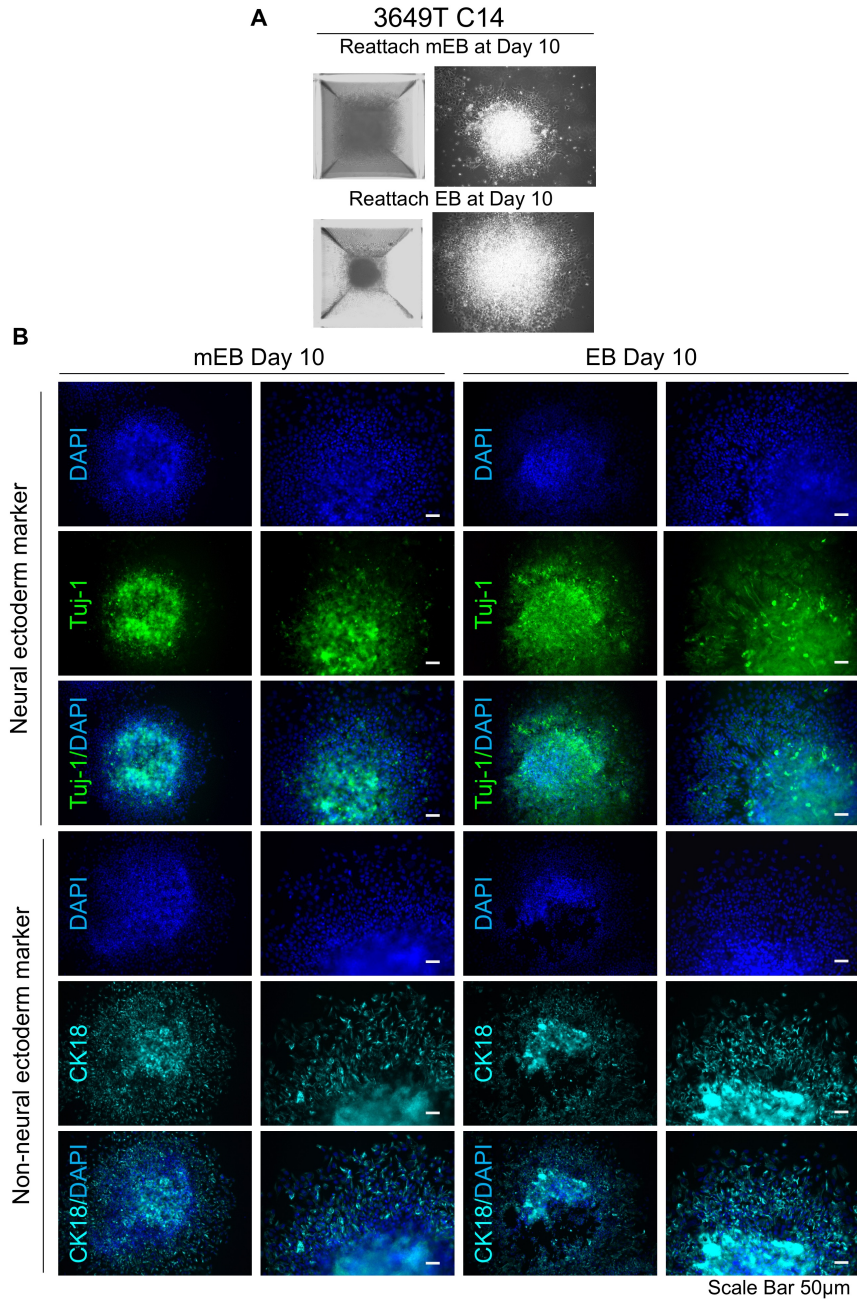


Figure 35. Generation of m EBs and EBs from LFS derived iPSCs.

(A) 10-day mEBs/EBs formed in AggreWell and the morphology of reattached mEBs/EBs. (C) Immunostaining of neural ectoderm marker Tuj-1 and non-neural ectoderm marker CK18 of 10-day mEBs and EBs derived from LFS iPSCs (3649T C14 line). Scale bar, 50 µm

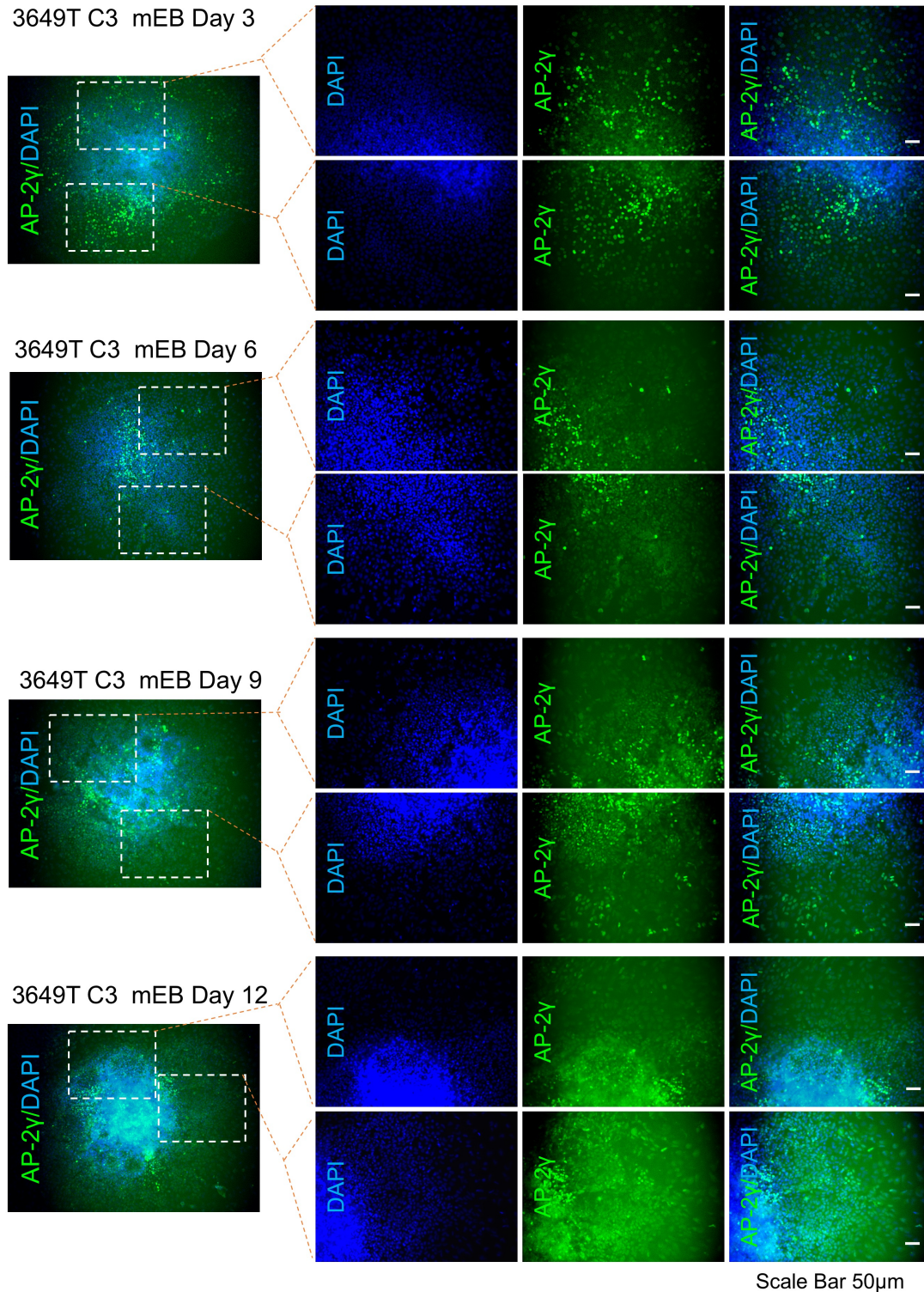


Figure 36. Immunostaining of AP-2 γ during 12-day mEB formation.

Immunostaining of non-neural ectoderm marker AP-2 γ in 3549T C3 clone derived 3-day, 6-day, 9-day and 12-day mEBs.

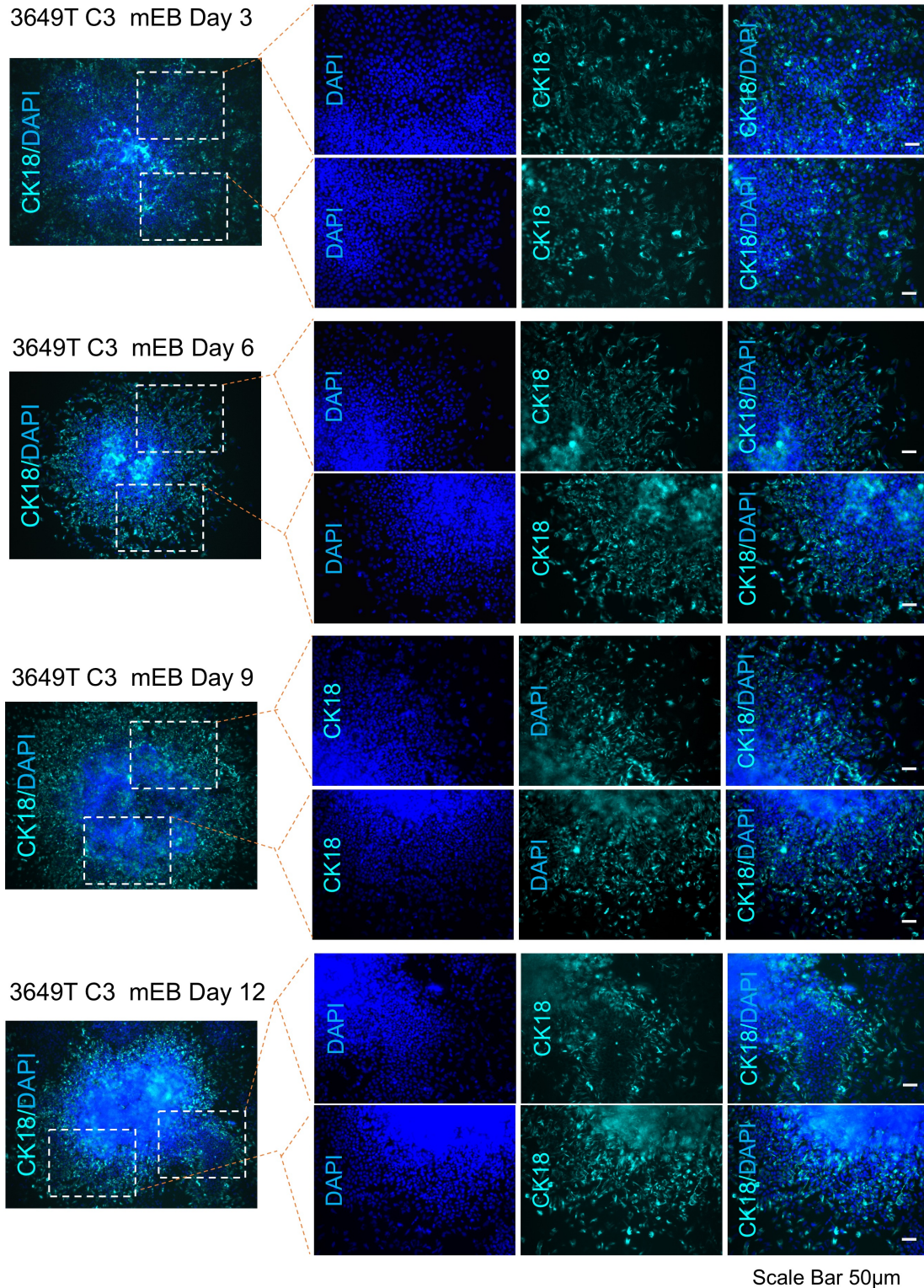


Figure 37. Immunostaining of CK18 during 12-day mEB formation.

Immunostaining of non-neural ectoderm marker CK18 of 3549T C3 clone derived 3-day, 6-day, 9-day and 12-day mEBs.

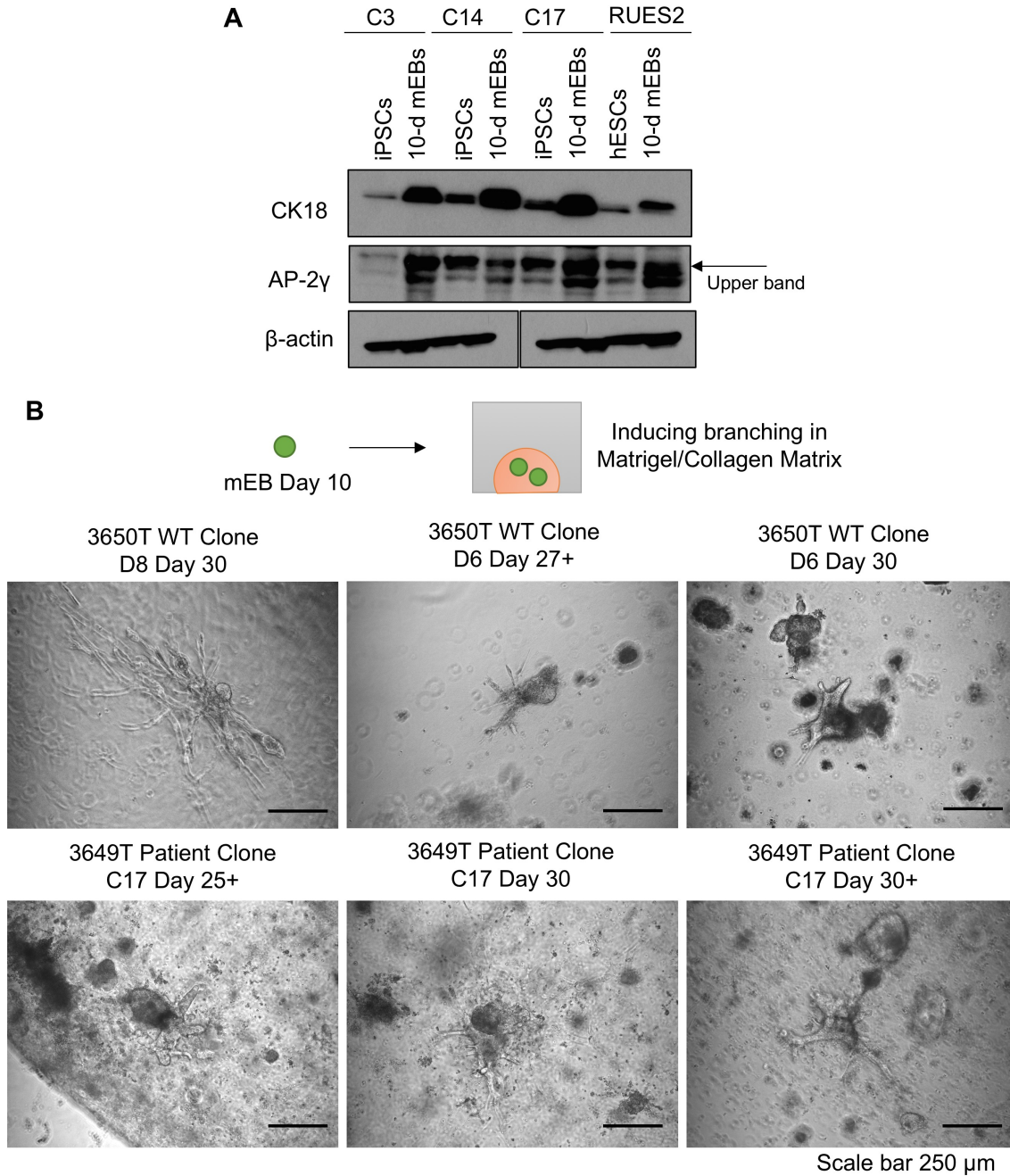


Figure 38. Two step differentiation of mammary-like organoids from LFS iPSCs.

(A) Western blot of AP-2γ and CK18 expression in LFS iPSCs and hESCs, and their derived 10-mEBs. (B) Mammary-like organoids with branching structure during 3D mixed floating gel culture.

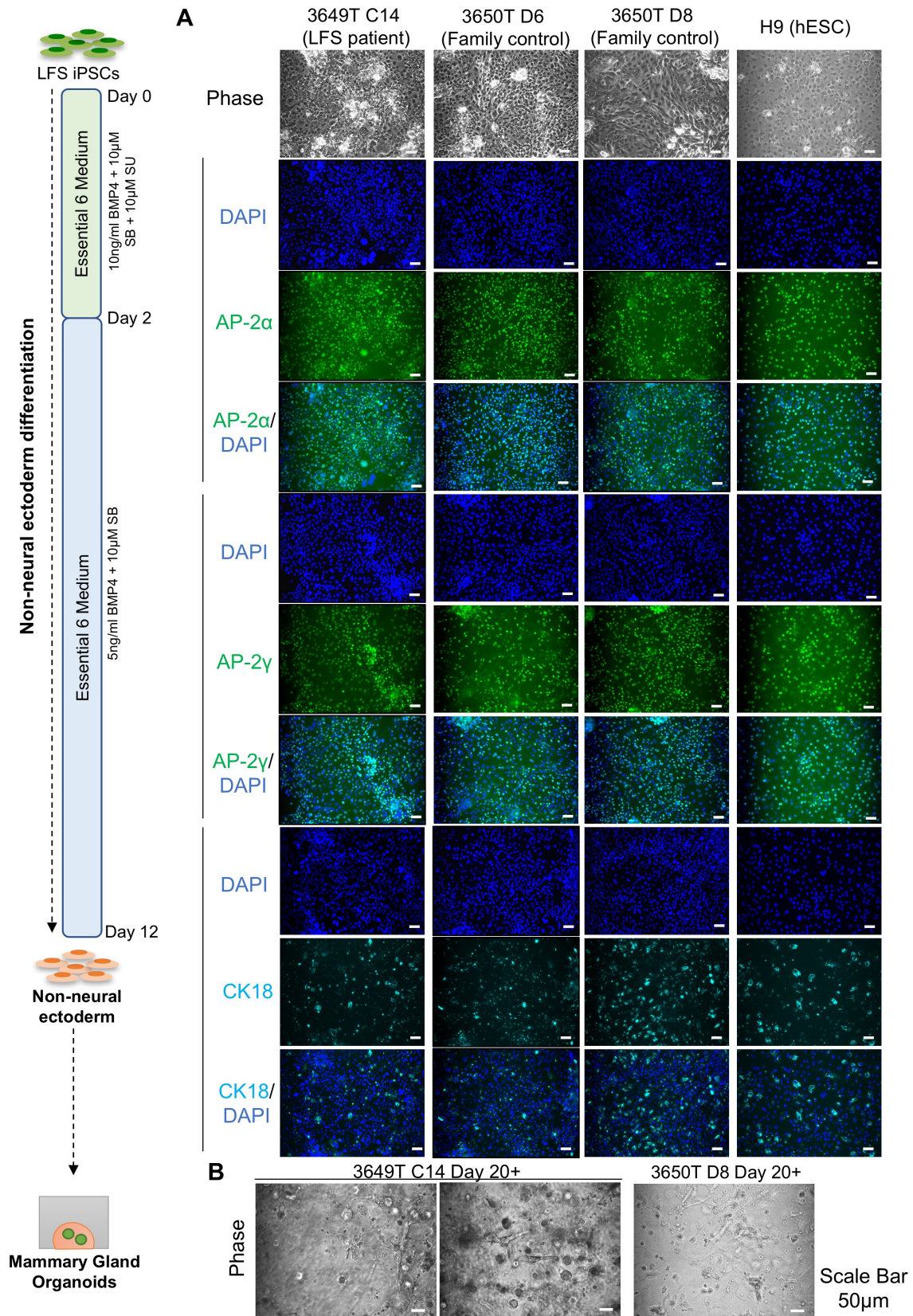


Figure 39. Chemical based non-neural ectoderm differentiation and 3D mixed floating gel culture for mammary lineages differentiation.

(A) Immunostaining of non-neural ectoderm marker AP-2 α , AP-2 γ and CK18 of the LFS iPSCs (3649T C14), WT iPSCs (3650T D6, D8) and hESCs (RUES2) derived non-neural ectoderm cells at differentiation day 12. (B) Induction of mammary-like branching during 3D mixed floating gel culture. Efficiency in forming branching-like structure were low.

4.5 Discussion

In vitro modeling of LFS associated malignancy (osteosarcoma) has been facilitated by LFS patient derived iPSCs (122, 193). “Bone tumor in a dish” model provide a proof of concept for modeling LFS associated tumor using patient derived iPSCs. Given the fact that breast cancer is also the most common tumor among women with germline *TP53* mutations and iPSCs’ ability to self-renew and differentiate into all cell lineages of an organism, LFS iPSCs holds great promise in modeling LFS associated breast cancer. However, successful recapitulation of breast cancer feature *in vitro* heavily depends on two major aspects: determination of the cell origin of breast cancer and availability of mammary lineage differentiation protocol.

In the stem cell hierarchy model, breast cancer cells are considered to originate from breast cancer stem cells (BCSCs) (229), which can maintain the feature of self-renewal and give rise to daughter neoplastic cells that form tumors (230), resembling MaSCs characteristic. Experimental data showed that both breast cancer tissue and normal human mammary gland are hierarchically organized (231), and data from hierarchy model indicates that a rare population of mammary cells is more tumorigenic than a non-stem cell population (232), supporting the hypothesis that breast cancer originates from BCSCs. However, there are still intense debates about whether BCSCs are derived from MaSCs, transformed progenitor cells (more differentiated cells) or both.

Some researchers hypothesize that accumulation of genetic mutation, either activating oncogenes or inactivating tumor suppressor during MaSCs self-renewal

and expansion can lead to unregulated differentiation and proliferation, contributing to carcinogenesis of breast tissue. Transcriptome analyses of mouse mammary cell subpopulation revealed tumors developed in MMTV-Wnt-1 and p53^{-/-} mice were enriched for MaSC-subset genes (CD29^{hi}CD24^{lo}CD61⁺) (223), suggesting the potential roles of MaSCs in tumorigenesis. By expressing Wnt-1 protooncogene in transgenic mice, another study also found that Wnt-1 induced breast tumors contained a subpopulation epithelial cells, which expressed MaSC markers (keratin 6 and Sca-1), suggesting MaSCs as a target of carcinogenesis through the ectopic Wnt pathway.

While other studies indicated that both luminal and myoepithelial progenitor cells are clonally expanding (233, 234), suggesting these more differentiated and committed progenitor cell may also be targets during carcinogenesis. Several studies implied that luminal progenitor cells might be the targets of transformation in basal-like breast cancers, specifically BRCA1-deficient (235-237) and TP53 mutated (236, 238) basal-like breast cancers. However, there is no direct evidence indicating that it is the more differentiated progenitor cells, not the MaSC are the targets during malignancy transformation in breast cancer. More precise studies are still needed in identifying the cells-of-origin of breast cancer.

Directed PSC differentiation protocols pose particular challenges to model cancer. PSCs can form teratomas, a rare tumor type from a normal genetic background. While differentiated cells derived from PSCs do not have this tumorigenic potential, even small contamination of desired differentiated cells with pluripotent cells can

give the false appearance of tumorigenic properties. An effective differentiation protocol and purification scheme is therefore essential for any cancer study.

PSC differentiation protocols have been established for generation of various type of cells, such as hepatic cells (239-241), intestinal tissue (242), neurons (171) and MSCs (192), to name a few. Despite these advances, there is still a large unmet need in directed differentiation protocols for a broader set of cancer types, including breast, ovary and prostate.

Currently, a robust and consistent directed differentiation protocols of breast tissue, either for mammary stem cells (MaSCs) or mammary glands have not been established. In this study, we tried to differentiate LFS derived iPSCs to mammary-like organoids using a two-step wise protocol developed by Qu *et al.* in 2017 (226). This protocol is primarily established using iPSCs. However, it worked in low efficiency in our hands for LFS iPSCs. Different genetic background of iPSC lines might be one reason of low successful rate in reproducing the established differentiation protocol. In addition, we also differentiated LFS iPSC to non-neural ectoderm using a chemical based protocol established by Tchieu *et al.* (228). This protocol showed consistency in pushing LFS iPSCs into non-neural ectoderm with satisfying efficiency. However, these 2D non-neural ectoderm cells showed very low efficiency in forming branching-like structured mammary organoids in 3D system described by Qu *et al.* (226). In summary, establishment of mammary lineages differentiation protocol with high efficiency and consistency is needed for breast cancer modeling using LFS iPSCs in this study.

Chapter 5 Potential of modeling mutant p53 associated malignancies using engineered iPSCs and hESCs

Copyright information:

Contents of Chapter 5.3 are based on Zhou R*, Xu A*, Wang D, Zhu D, Mata H, Huo Z, Tu J, Liu M, Mohamed AMT, Jewell BE, Gingold J, Xia W, Rao PH, Hung MC, Zhao R, Lee DF. 2018. A homozygous p53 R282W mutant human embryonic stem cell line generated using TALEN-mediated precise gene editing. *Stem Cell Res.* 27:131-135. (*: Co-first authors).

Contents of Chapter 5.4 are based on Xu A*, Zhou R*, Tu J, Huo Z, Zhu D, Wang D, Gingold JA, Mata H, Rao PH, Liu M, Mohamed AMT, Kong CSL, Jewell BE, Xia W, Zhao R, Hung MC, Lee DF. Establishment of a human embryonic stem cell line with homozygous TP53 R248W mutant by TALEN mediated gene editing. *Stem Cell Res.* 29:215-219. (*: Co-first authors).

Permission to reuse the whole articles for thesis was obtained from www.copyright.com with license number: 4598280400664.

5.1 Correction of mutant p53 iPSC using precise gene editing

As previously illustrated in Chapter 4.2, precise genome-editing tools such as TALENs and CRISPR/Cas9 can be used to generate isogenic control for LFS iPSCs. TALEN and CRISPR/Cas9 guides targeting exon 7 of *TP53* were designed (**Figure 40A**) for correcting mutant p53 (G245D) in LFS iPSCs (cell line described in Chapter 3). The overall insertion rate (correctly inserted in *TP53* locus) for designed TALEN guides were around 20% (**Figure 40B**), while CRISPR/Cas9

guided editing enabled much higher insertion rate (more than 50%) (**Figure 40C**). Experiments to correct mutant p53 (G245D) were done several times in different LFS iPSC lines, and more than a thousand clones were picked and examined. To our surprise, most of the insertion happened on WT allele in correctly inserted clones (**Figure 40B-D**). Even with luck to have picked clones with insertion located on mutant allele, as shown in **Figure 40D**, the mutant allele insertion rate is quite low (less than 20% of correctly inserted clones). Further sequence indicated all the clones with insertion located in mutant clones still carried original *TP53* mutation (G245D). These data suggested that correction of hotspot *TP53* mutation (G245D) in LFS iPSCs is quite difficult

Correction of mutant p53 was also attempted in another LFS iPSC line carrying a different heterozygous *TP53* mutation, Y205C (cell line described in Chapter 3). TALEN guides targeting intron 5 of *TP53* were designed (**Figure 41A**) for correcting mutant p53 (Y205C) in LFS iPSCs. The WT donor vectors were constructed using pFNF donor vector carrying a Frt-EM7-NeoR-Frt (FNF) selection cassette flanked by 1 kb left and right homologous arms of the *TP53* genomic region and primers used to identify correctly inserted colonies are shown with arrows; the expected size of PCR product are shown in the table (**Figure 41A**).

LFS iPSC A8 clone were used for mutant p53 (Y205C) correction. The correctly inserted clones were confirmed by genomic PCR using two sets of primers (p53_4FM13 and 3FNF-N1 for left arm, 5FNF-C1 and p53_8/9RM13 for right arm), as shown in representative graph (**Figure 41B**). Total 431 clones were picked, and 74 clones were with insertion located at *TP53* locus. Out of 74 picked clones, only

7 clones had the insertion on mutant allele (mutant allele insertion rate less than 10%) (**Figure 41C**).

Insertion in these 7 clones were re-confirmed by PCR (**Figure 42A**), and southern blot indicated that 5 clones of 7 carried single insertion (**Figure 42B**) located in *TP53* genomic region (shown in yellow arrows). Sanger sequence of the 5 single inserted clones indicated that 3 clones (A8 5-3, 15-4, 38-8) carried desired WT *TP53* sequence, while 2 clones (A8 27-6, 14-7) on the other hand, the inserted allele still carried *TP53* mutation (Y205C) (**Figure 42C, D**). Further removal of Frt-EM7-NeoR-Frt cassette by transfecting Fip recombinase into corrected clones A8 5-3, 15-4, 38-8 and mutant clone A8 27-6 was performed as indicated in **Figure 42E**, and one clone was further picked from each group (**Figure 42D**).

In summary, isogenic control of LFS iPSC A8 were successfully generated by correcting mutant p53 (Y205C) using TALENs-mediated precise genome editing.

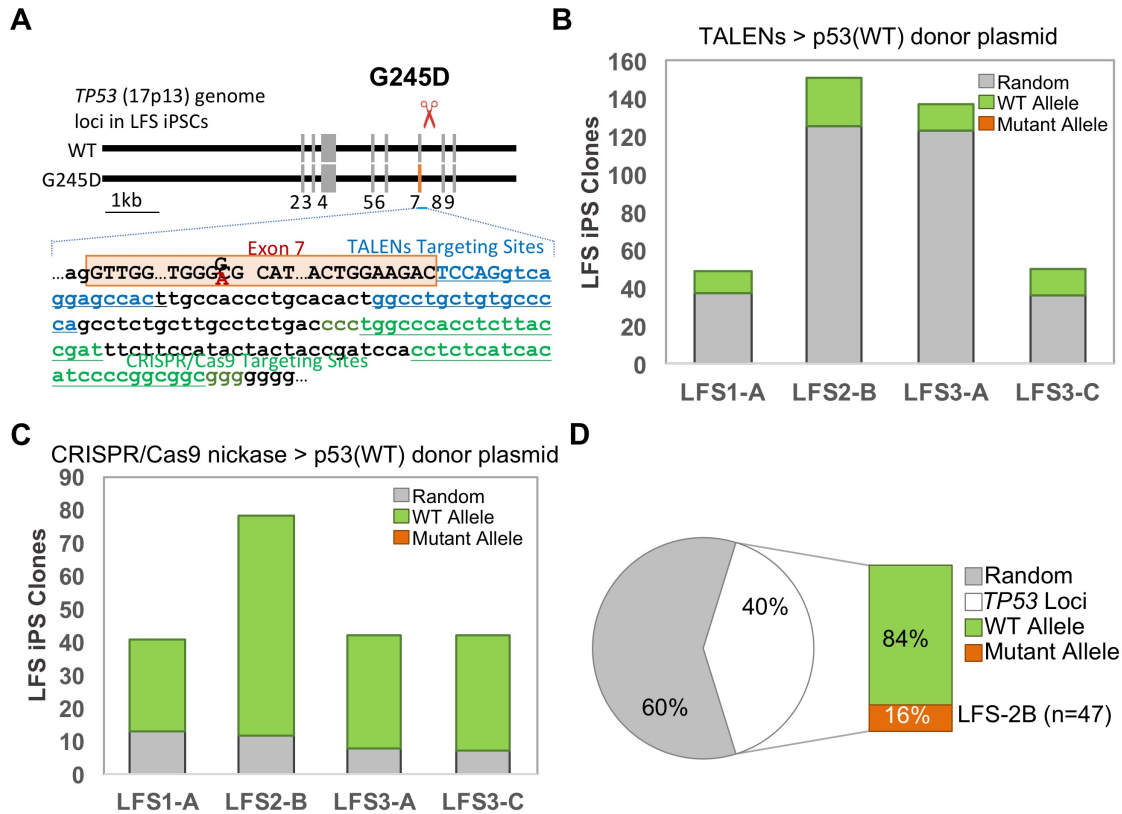


Figure 40. Correction of mutant p53 (G245D) iPSC using precise gene editing.

(A) Schematic design of TALEN and CRISPR/Cas9 guides targeting exon 7 of *TP53* locus. (B) Number of inserted clones were picked from LFS iPSC lines transduced with WT p53 donor vector and TALEN guides. (C) Number of inserted clones picked from LFS iPSC lines transduced with WT p53 donor vector and CRISPR/Cas9 guides. (D) Percentage of correctly inserted clones (insertion on *TP53* genomic region), and percentage of inserted clones with insertion located on mutant allele.

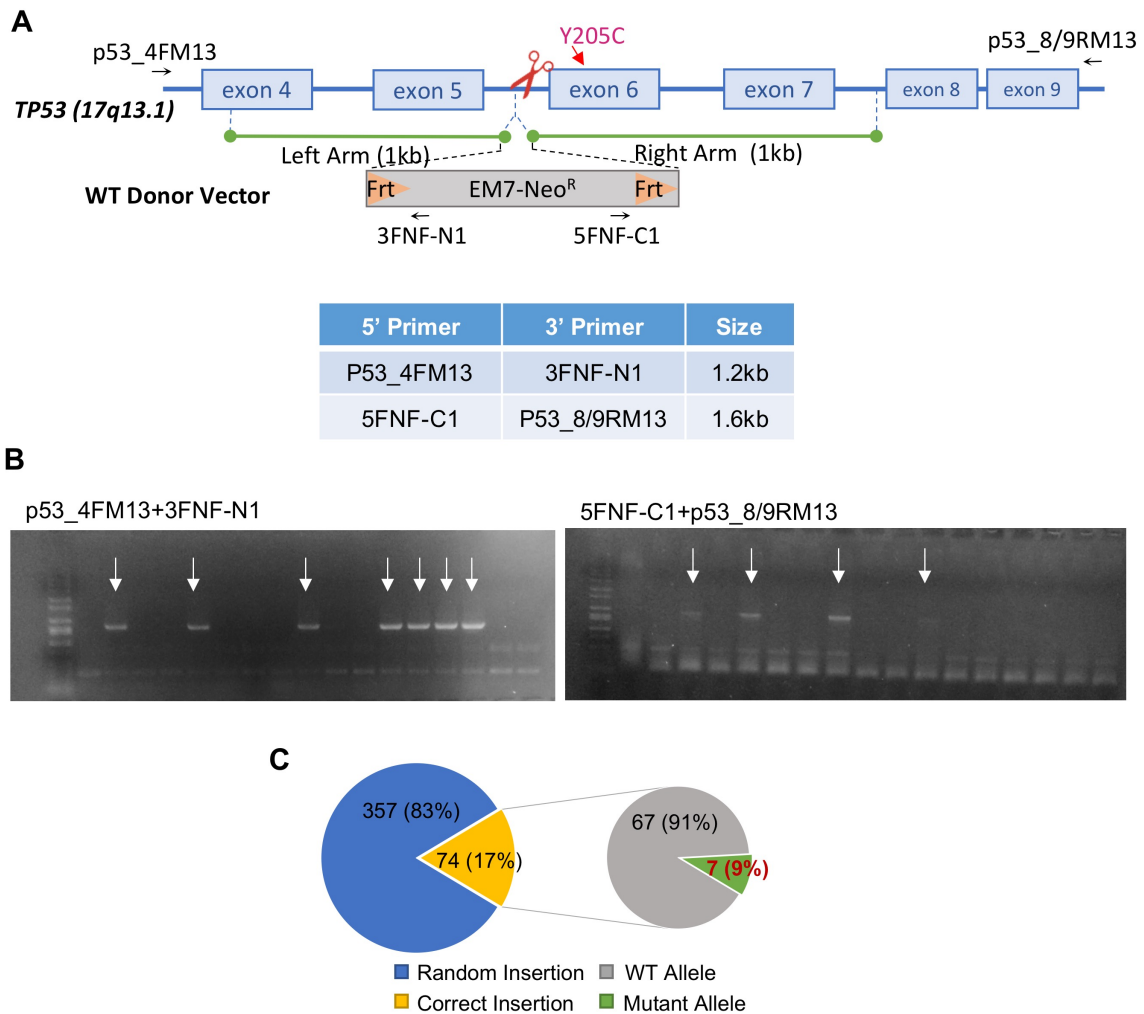


Figure 41. Correction of mutant p53 (Y205C) iPSC using TALENs-mediated precise gene editing.

(A) Schematic design of TALEN guides targeting intron 5 of *TP53* locus. Table lists two sets of primers (p53_4FM13 and 3FNF-N1 for left arm, 5FNF-C1 and p53_8/9RM13 for right arm) and expected size of PCR product used to confirmed inserted clones. (B) Representative results of PCR confirmation of inserted clones using indicated primers. (C) Percentage of correctly inserted clones (insertion on *TP53* genomic region), and percentage of inserted clones with insertion located on mutant allele.

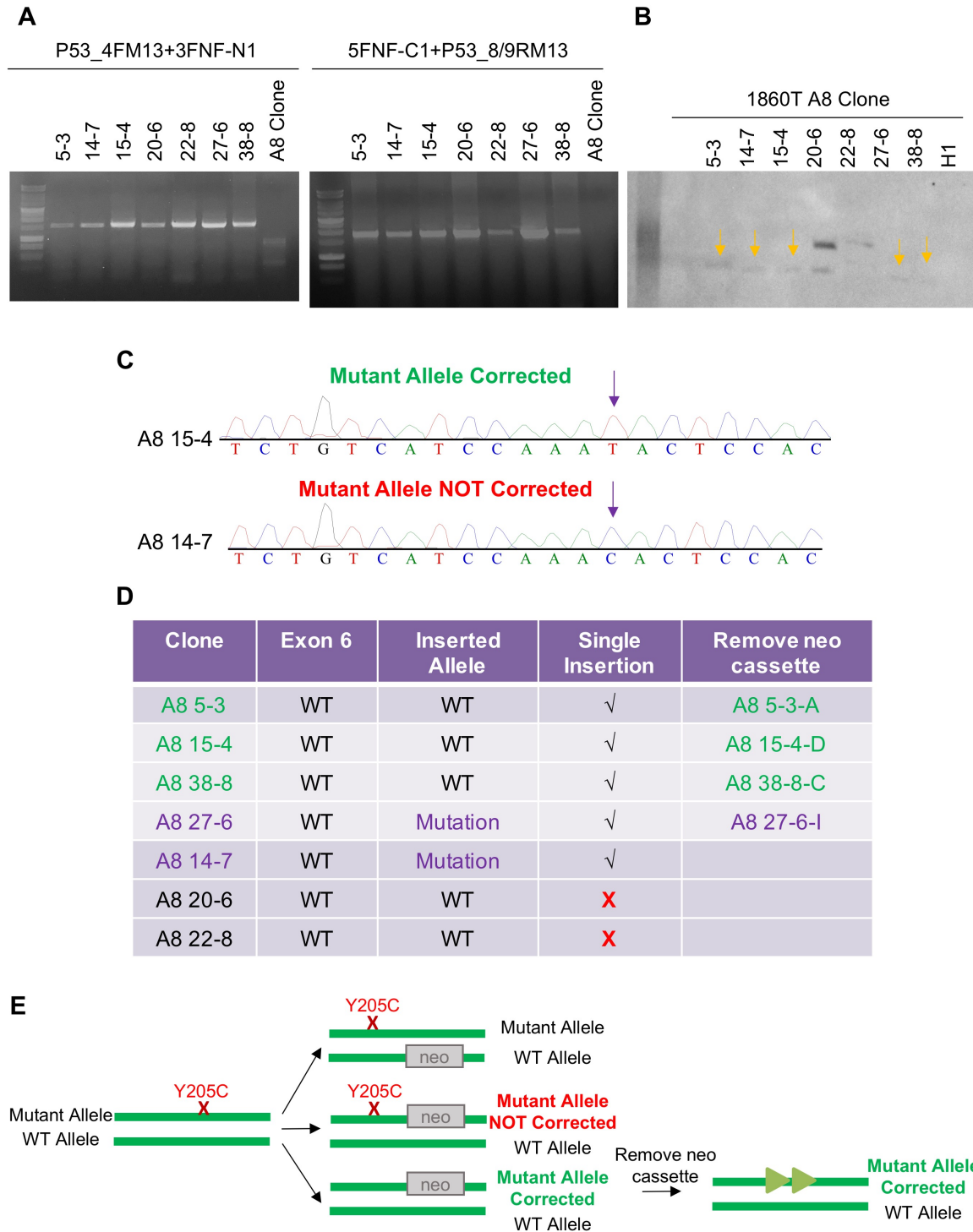


Figure 42. Correction of mutant p53 (Y205C) iPSC using TALENs-mediated precise gene editing (continued).

(A) PCR confirmation of 7 inserted clones using indicated primers. (B) Southern blot of 7 inserted clones with insertion on mutant allele. 5 clones carried single insertion targeted *TP53* genomic region, as indicated with yellow arrows. (C) Representative Sanger sequence results of inserted allele of 7 picked clones. A8 15-4 clone carried WT *TP53* sequence (mutant allele corrected), while A8 14-7 still carried original *TP53* mutation (Y205C) (mutant allele not corrected). (D) Summary table of 7 inserted clones with insertion on mutant allele. (E) Illustration of mutant p53 (Y205C) correction process in LFS iPSC A8 clone: WT p53 donor with NeoR cassette can either be inserted into WT allele or mutant allele. Only the picked clones with insertion located on mutant allele possess further chance to be corrected. Sequencing results indicated that a portion of clones with insertion in mutant allele still can carry *TP53* mutation.

5.2 Generation of homozygous p53 R282W mutant human embryonic stem cell line using TALEN-mediated precise gene editing

To provide a useful lab resource for modeling mutant p53-related cancers and diseases, we generated a H1 human embryonic stem cell line carrying a homozygous R282W mutation of *TP53* (one of the hotspot mutations) using TALEN-mediated genome editing (**Figure 43A**). TALEN target sites are in bold red. Start sites of the upstream and downstream homologous arms are underlined. The design of the mutant donor vector is also illustrated. Primers used to identify correctly inserted colonies are shown with arrows.

hESC H1 cells were transfected by electroporation with paired TALEN plasmids and a R282W donor vector containing a Frt-EM7-NeoR-Frt (FNF) selection cassette. The electroporated cells were selected by G418 (Geneticin). The G418-resistant clones were picked up, isolated, and expanded. The *TP53* targeted regions were analyzed by PCR (**Figure 43B**) using two pairs of primers (p53_6FM13 and 3FNF-N1; and 5FNF-C1 and 3p53_16821_RM13). We confirmed that the R4–18 clone underwent precise homologous recombination and FNF cassette insertion between exons 8 and 9. The presence of exon 8/9 PCR product when using exon 8/9 paired primers (p53_8/9FM13 and p53_8/9RM13) suggested that the FNF cassette was inserted into only one allele instead of two alleles (**Figure 43B**). Upon removal of the FNF cassette by Flp recombinase, PCR of the exon 8/9 region in FNF-removed clone 1R5 revealed the existence of double bands, suggesting that the lower band is the original exon 8/9 and the higher band is the TALEN-modified exon 8/9 containing a Frt fragment in between exon 8 and

9. Unexpectedly, PCR/Sanger sequencing of the exon 8/9 region revealed that clone 1R5 contains a R282W mutation in both alleles (only TGG rather than (T/C)GG in the mutated exon 8/9 region) (**Figure 43C**). The possibility of additional R282W mutation in the unengineered allele is due to spontaneous homologous recombination-mediated mutagenesis by the R282W donor vector. Immunoblotting results revealed the increased level of p53 in R4-18 and 1R5 clones in comparison with that of parental H1 cells (**Figure 43D**), suggesting mutant p53(R282W) is more stable than wild-type p53. We rename the 1R5 line to H1-p53(R282W/R282W).

The H1-p53(R282W/R282W) line displayed a typical round shape hESC-like morphology and exhibited positive alkaline phosphatase activity (**Figure 43E**). H1-p53(R282W/R282W) cells also express pluripotency transcription factors NANOG and OCT4 as well as hESC surface markers SSEA4 and TRA-1-81 (**Figure 43F**). Quantitative real-time PCR (qRT-PCR) analysis showed comparable mRNA expression of pluripotency genes (NANOG, OCT4, SOX2, DPPA4, REX1 and TERT) to parental H1 cells (**Figure 43G**). The H1-p53(R282W/R282W) line maintained a normal karyotype (**Figure 43H**) and pluripotency, namely the ability to differentiate into three germ layers in vivo (**Figure 43I**). PCR-based mycoplasma detection assay demonstrated that the cell line is free of mycoplasma (**Figure 43J**). In summary, H1-p53(R282W/R282W) cells maintain a pluripotent state with a normal karyotype. This line provides a useful resource to study p53(R282W)-associated malignancies and is of great value in exploring gain-of-function of p53(R282W) mutation.

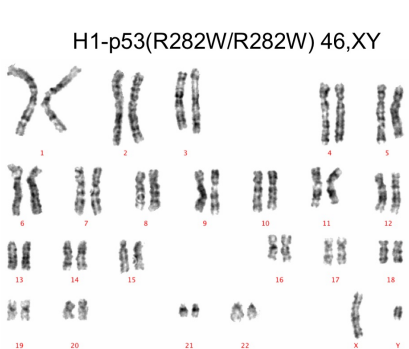
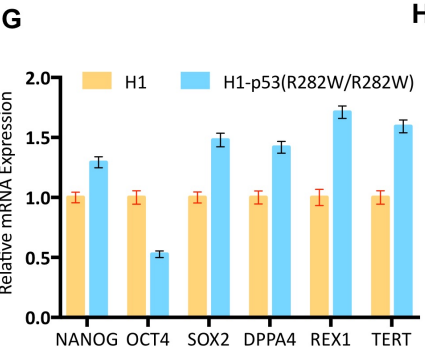
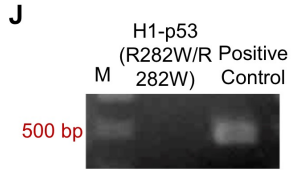
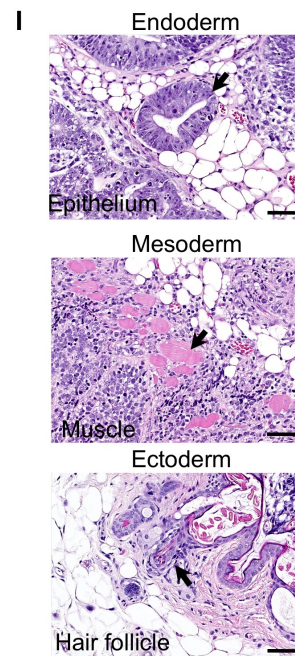
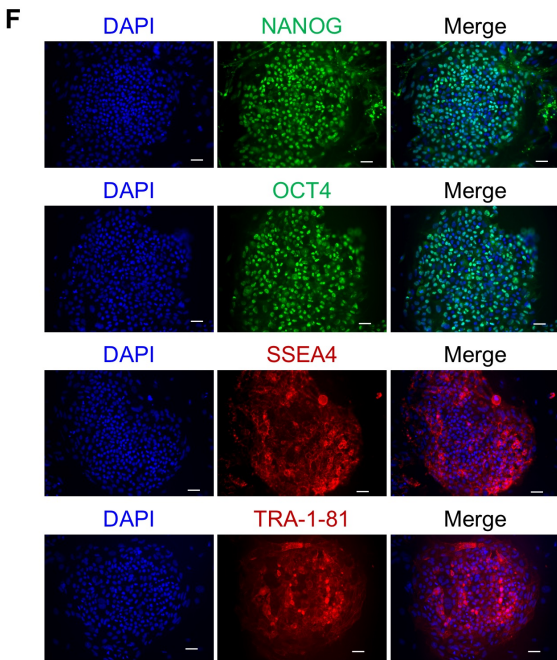
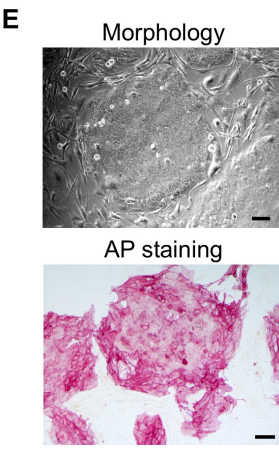
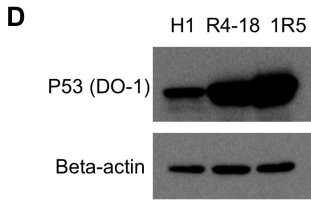
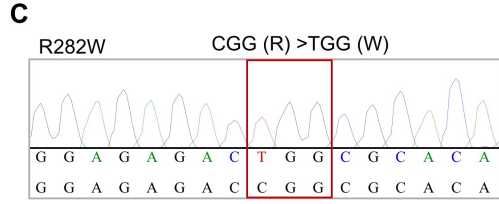
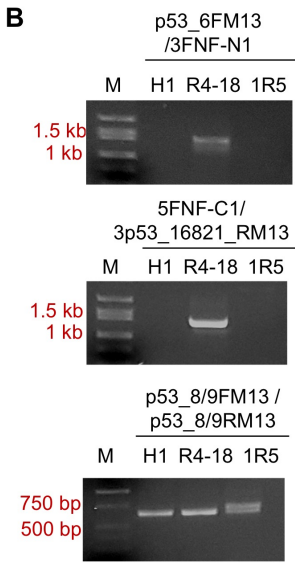
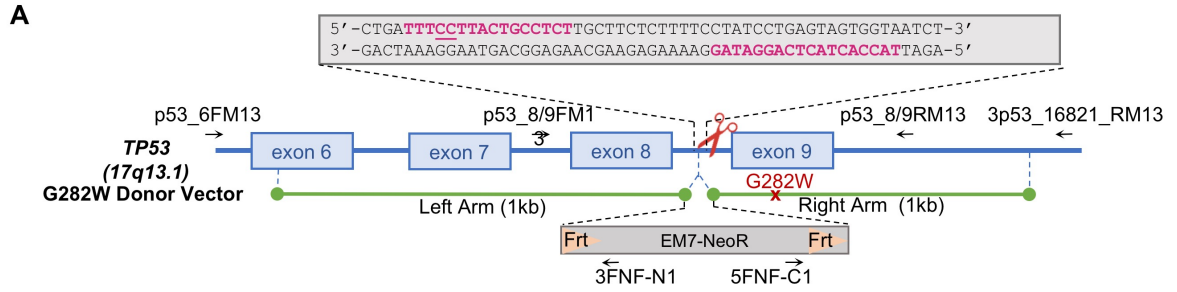


Figure 43. Establishment and characterization of the homozygous p53 R282W mutant human embryonic stem cell line H1-p53(R282W/R282W).

(A) Schematic diagram of the strategy for p53(R282W) generation. TALEN target sites are indicated in bold red. Start sites of the upstream and downstream homologous arms are underlined. (B) PCR of precise homologous recombination in *TP53* genome loci. (C) Sequences of the homozygous p53(R282W) mutation in H1-p53(R282W/R282W) cell line. (D) Immunoblotting of the p53(R282W) expression in cell line R4–18 and 1R5 (H1-p53(R282W/R282W)). (E) Cell morphology and AP staining of H1-p53(R282W/R282W) cell line. Scale bar, 50 μ m. (F) Immunofluorescence staining of pluripotency markers NANOG, OCT4, SSEA4 and TRA-1-81 in H1-p53(R282W/R282W) cell line. Scale bar, 50 μ m. (G) qRT-PCR assay for expression of endogenous pluripotency genes in H1-p53(R282W/R282W) cell line. (H) Karyotype analysis of H1-p53(R282W/R282W) cell line. (I) *In vitro* teratoma assay of H1-p53(R282W/R282W) cell line. Scale bar, 50 μ m. (J) Mycoplasma detection of H1-p53(R282W/R282W) cell line.

5.3 Establishment of a human embryonic stem cell line with homozygous *TP53* R248W mutant by TALEN mediated gene editing

We also generated a H1 hESC line harboring a homozygous *TP53* R248W mutation. The strategy of TALEN-mediated precise gene editing is illustrated in **Figure 44A**. The targeting plasmids contain a pair of TALEN plasmids targeting exon7 and intron 7 of *TP53*, respectively; and a pFNF donor vector carrying a Frt-EM7-NeoR-Frt (FNF) selection cassette flanked by 1 kb left and right homologous arms of the *TP53* genomic region. H1 hESCs were transduced with these plasmids and selected by G418. G418-resistant clones were confirmed by genomic PCR using two pairs of primers (p53_5FM13 and 3FNF-N1 for left arm, 5FNF-C1 and 3p53_16821 for right arm) (**Figure 44B**).

Clone P1–36 demonstrated accurate insertion of the FNF cassette with a *TP53* R248W mutation into the *TP53* genome targeting site. Unexpectedly, Sanger sequencing of endogenous *TP53* exon 7 (using the pair of primers p53_7FM13 and p53_7RM13) in the P1–36 line revealed the presence of a homozygous *TP53* R248W mutation in which the mutation was also detected in the un-inserted allele (**Figure 44C**, upper panel). The unique DNA sequence chromatogram of TGG in P1–36 ruled out the possibility of a mixed population in P1–36 (**Figure 44C**, upper panel). This additional *TP53* R248W mutation was probably created spontaneously during mutant donor vector-mediated homologous recombination. The FNF cassette in the P1–36 clone was subsequently removed by transfecting the line with Flp recombinase plasmid. The FNF removal clone 1P6 was identified by loss of genomic PCR products (**Figure 44B**, upper and middle panels). The

larger PCR band of the *TP53* exon 7 region of the FNF-removed clone 1P6 demonstrated the footprint of Frt, which was all that remained after excision from the FNF cassette-inserted allele (**Figure 44B**, arrow in lower panel). Sanger sequencing of endogenous *TP53* exon 7 of the 1P6 clone further confirmed the presence of the *TP53* R248W mutation in both alleles (**Figure 44C**, lower panel), consistent with the findings from the parental P1–36 clone. Immunoblotting revealed higher p53 protein levels in both P1–36 and 1P6 clones than those in parental H1 line (**Figure 44D**, higher panel), supporting the increased protein stability of mutp53. Although both P1–36 and 1P6 clones demonstrated homozygous *TP53* R248W mutation, higher p53 mRNA levels were measured in the 1P6 clone, explaining the higher p53 protein levels in the 1P6 clone compared to the P1–36 clone (**Figure 44D**, lower panel). We rename the 1P6 line to H1-p53(R248W/ R248W).

The H1-p53(R248W/R248W) line maintained a classical dome-shaped hESC morphology and exhibited positive alkaline phosphatase (AP) activity (**Figure 44E**). Immunofluorescent staining of the H1-p53(R248W/R248W) line demonstrated high expression of hESC pluripotency factors and hESC surface markers (Figure 33F). Although quantitative real-time PCR (qRT-PCR) showed lower mRNA levels of pluripotency genes in the H1-p53(R248W/R248W) line compared with the parental H1 line (**Figure 44G**), these cells functionally perform as PSCs, as demonstrated by their proliferation in hESC medium as well as in vivo three germ-line differentiation capacity (**Figure 44H**). Karyotype analysis confirmed the normal karyotype of the H1-p53(R248W/R248W) line (**Figure 44I**). Furthermore, PCR-

based mycoplasma detection assay demonstrated that the H1-p53(R248W/R248W) line is mycoplasma-free (**Figure 44J**). The short tandem repeat (STR) profile of H1-p53(R248W/R248W) line was identical to that of its parental H1 line (data not shown here).

In summary, the H1-p53(R248W/R248W) line is karyotypically normal and retains pluripotency. This line has great potential to offer insight into the role of p53(R248W) in embryogenesis and tumorigenesis.

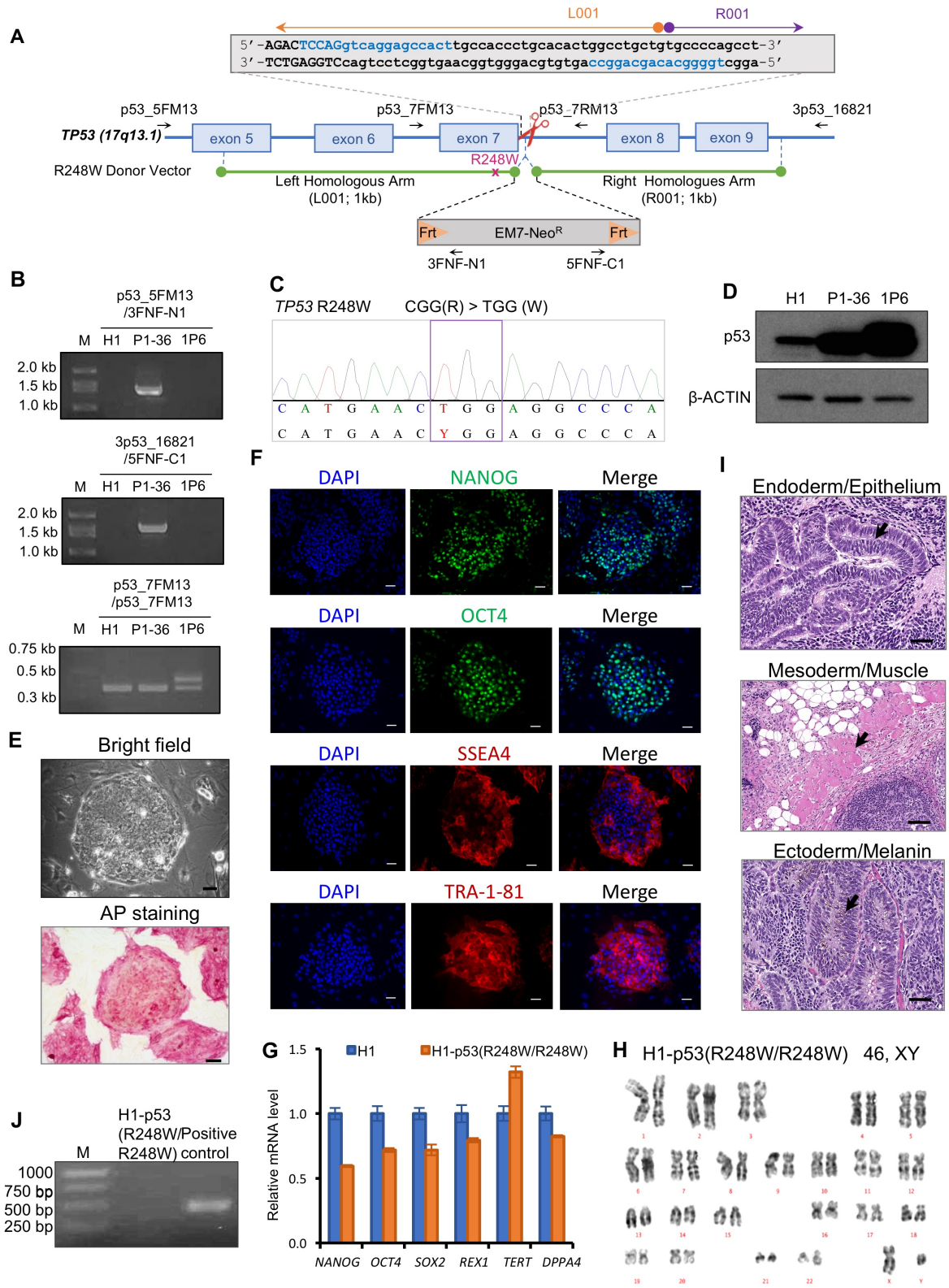


Figure 44 Generation and characterization of the homozygous p53 R248W mutant human embryonic stem cell line H1-p53(R248W/R248W).

(A) Schematic diagram of the strategy for p53(R248W) generation. TALEN target sites are indicated in bold blue. (B) PCR of precise homologous recombination in *TP53* genome loci. (C) Sequences of the homozygous p53(R248W) mutation in H1-p53(R248W/R248W) cell line. (D) Immunoblotting of the p53(R248W) expression in cell line P1-36 and 1P6 (H1-p53(R248W/R248W)). (E) Cell morphology and AP staining of H1-p53(R248W/R248W) cell line. Scale bar, 50 μ m. (F) Immunofluorescence staining of pluripotency markers NANOG, OCT4, SSEA4 and TRA-1-81 in H1-p53(R248W/R248W) cell line. Scale bar, 50 μ m. (G) qRT-PCR assay for expression of endogenous pluripotency genes in H1-p53(R248W/R248W) cell line. (H) Karyotype analysis of H1-p53(R248W/R248W) cell line. (I) *In vitro* teratoma assay of H1-p53(R248W/R248W) cell line. Scale bar, 50 μ m. (J) Mycoplasma detection of H1-p53(R248W/R248W) cell line.

5.5 Discussion

As mentioned in Chapter 1, patient-derived iPSCs have been used to model various diseases, such as long-QT syndrome (LQTS) (165, 166) [159,160], α 1 antitrypsin (AAT) deficiency (167, 243) [161,162], Diamond–Blackfan anemia (DBA) (244-246) [165–167] and familial Alzheimer’s disease (161) [168]. Successful cancer modeling has also been established using patient derived iPSCs (122, 168, 169). However, these disease models are generated from various patients who usually carry differences in the genetic background, and most current iPSC studies use unaffected iPSCs within the same family pedigree as controls, which are actually not the optimal controls. Recent advances in precise genome editing offers advantages in generating isogenic iPSC controls, which will be useful in revealing mutation/variant-associated disease phenotype.

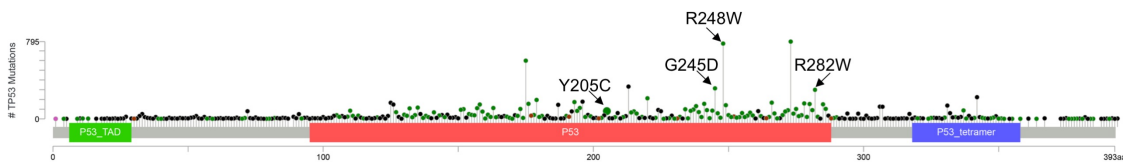


Figure 45. Mutation landscape of *TP53* in human cancers.

The mutation diagrams of human *TP53* were obtained from cBio Cancer Genomics Portal from 42199 tumor samples in 159 studies (<http://cbioportal.org>) (200) on 06/08/2019. Arrows indicate the hotspot mutation include in this study. Mutation types and corresponding color codes are as follows: Green: missense mutations. Black: truncating mutations (nonsense, nonstop, frameshift deletion or insertion, splice site variant). Brown: in-frame deletion, in-frame insertion. Pink: all other types of mutations.

In the present work, we attempted to correct mutant p53 in LFS patient derived iPSCs. On our hand correction of hotspot *TP53* mutation (G245D) in LFS iPSCs was unsuccessful. As shown in **Figure 45**, G245D mutation is one of the hotspot mutation in *TP53* across different human cancers. This mutation lies within the DNA binding domain of the p53 protein, result in decreased activation of *TP53* target genes (247, 248). This mutation also confers a gain-of-function, which can promote cancer growth and metastasis, for example by interacting with ZBP-89 (247) and inducing expression of FOXM1 and FOXO3 (249). One of the hypothesis for difficulty in correcting G245D mutation is that, in LFS patient iPSCs, the mutant p53 (G245D) can somehow inhibit WT p53 functions. Upon correction of mutant p53, WT p53 function is restored, promoting the process of apoptosis and cell cycle arrest. Therefore, the corrected clones could not survive. We also experienced difficulty in correcting mutant p53 (delG) in LFS breast cancer patient derived iPSCs (as described in Chapter 4). It is also possible that this mutant p53 (delG) can interfere with WT p53 functions, hijacking these LFS iPSCs to become addicted to this mutant p53 (delG), while correcting it results in cell death.

On the other hand, we were able to correct mutant p53 (Y205C) using TALENs mediated precise genome editing in another LFS iPSC line. Y205C mutation is not as prevalent as G245D mutation in human cancers, however, it is also identified as recurrent hotspot mutation (**Figure 45**). Successful correction of this mutation suggest that Y205C mutation might function in different pathway compared to G245D.

Although clinical history of this LFS patient carrying Y205C mutation was unable to be retrieved, this patient derived osteoblasts (from iPSCs) demonstrated *in vitro* oncogenic ability (data shown in chapter 3), suggesting this mutation is likely oncogenic. In addition, pan-cancer analysis found that *TP53* Y205C mutation is frequently mutated in small cell lung cancer, esophagogastric and colorectal cancer, also supporting the possible oncogenic role of this mutation. LFS iPSCs (Y205C) and isogenic control in this study will be useful recourse to explore oncogenic role of *TP53* Y205C mutation in different cancers, as mentioned above.

Missense substitutions at many “hotspot” sites confer novel cancer-promoting functions on mutant p53 and have been suggested to be attractive targets for cancer therapy. In the present work, we generated two H1 human embryonic stem cell lines carrying homozygous *TP53* R282W and R248W mutation respectively, using TALENs-mediated genome editing. The engineered cell lines demonstrate normal karyotype, maintain a pluripotent state, and are capable of generating a teratoma *in vivo* containing tissues from all three germ layers. The two hESC lines generated in this study can be used to study *TP53* mutation associated disease mechanism, and facilitate drug screening.

Chapter 6 Future Directions

Copyright information:

Contents of Chapter 6.2 and 6.3 are based my review article: Zhou R*, Xu A*, Gingold J, Strong LC, Zhao R, Lee DF. Li–Fraumeni Syndrome Disease Model: A Platform to Develop Precision Cancer Therapy Targeting Oncogenic p53. Trends Pharmacol. Sci. (2017), 10.1016/j.tips.2017.07.004. (*: First authors). I am the first author of the review. Permission to reuse the whole article for thesis was obtained from www.copyright.com with license number: 4598280693164.

6.1 Identification of osteosarcoma driver genes using LFS patient derived iPSCs-MSCs-OBs platform

In Chapter 3, we identified several candidate genes likely driving early osteosarcoma development, including *USP34*, *ANAPC1*, *ESPL1*, *MYLK*, *SLC35G2*, *FAM20A*, *SLC25A32*, *SYNE2*, *RPL8*, *FAM160A2*. Reported functions of these genes are summarized in **Table 13**.

Although the identified genes are involved in various important biological pathways, more validation still need to be done to reveal whether these mutated genes are true driver during osteosarcoma development or just a passenger. Since the identified candidates carry either truncating mutation or missense mutation that predicted to be damaging, we can use shRNA to knockdown expression of each gene and perform *in vitro* tumorigenic assay (soft agar) under iPSC-MSC-OB platform. It is anticipated that this quick *in vitro* screen using shRNA will help narrowing down candidates that are true drivers.

In Chapter 3, in addition to subcutaneous xenograft model, we also demonstrated using *in ovo* chick chorioallantoic membrane (CAM) assays to analyzing oncogenic ability of tumor cells. It is also critical, in the future, to use both *in vivo* and *in ovo* system to further validate the candidate genes' roles during initiation of osteosarcoma.

After confirming true driver genes using approaches described above, it would of great interest to explore the mechanism by which the driver gene exerts its function in osteosarcoma development. One approach will be modulating expression level (either knocking down or overexpressing) of validated driver genes in LFS OBs or OB-derived tumor cell lines and perform RNA-seq to examine the transcriptomic changes. After significant differentially expressed genes or pathways are identified, rescue assay can be performed under iPSC-MSC-OB platform. Further, drugs or compounds that specifically target the identified downstream targets or pathways can be tested to discover potential therapeutic strategies in treating osteosarcoma.

Candidate driver gene	Encoded Protein	Reported Functions
<i>USP34</i>	Ubiquitin specific processing protease 34 (deubiquitinase)	<ul style="list-style-type: none"> • Amplified during transformation and progression of follicular lymphoma (250) • Know-down of USP34 leads to degradation of axin and inhibition of β-catenin mediated transcription (251) • Stabilizing the E3 ligase RNF168 and maintaining genome stability (252)
<i>ANAPC1</i>	Anaphase promoting complex subunit 1	<ul style="list-style-type: none"> • Functions as a cell cycle-regulated E3 ligase which controls progression through mitosis and the G1 phase of the cell cycle (253) • Truncating mutation of <i>ANAPC1</i> is associated with high cancer-susceptibility (254)
<i>ESPL1</i>	Extra spindle pole bodies like 1 (separase)	<ul style="list-style-type: none"> • An enzyme functions during metaphase to anaphase transition which resolves sister chromatid cohesion (255) • Separase overexpression promotes aneuploidy and contribute to mammary tumor development (256, 257) • Loss of separase cooperates with the loss of p53 in the initiation and progression of T- and B-cell lymphoma, leukemia (258)
<i>MYLK</i>	Myosin light chain kinase (calcium/calmodulin dependent protein kinase)	<ul style="list-style-type: none"> • Facilitate myosin interaction with actin filaments to produce contractile activity (259) • Low expression of MYLK is associated with lung cancer and colon cancer (260, 261)
<i>SLC35G2 (TMEM22)</i>	Solute carrier family 35 member G2 (Transmembrane protein 22)	<ul style="list-style-type: none"> • Functions of TMEM22 largely remain unknown • Depletion of TMEM22 suppress growth of renal cell carcinoma (262)
<i>FAM20A</i>	Family with sequence similarity 20 proteins (secretory pathway pseudokinase)	<ul style="list-style-type: none"> • Mutations in <i>FAM20A</i> cause tooth enamel defects known as Amelogenesis Imperfecta (263) • FAM20A forms a functional complex with FAM20C and allosterically act as a pseudokinase to increase FAM20C activity towards secretory substrates which control enamel formation (264)

<i>SLC25A32</i>	Solute carrier family 25 member 32 (mitochondrial carrier family transport protein)	<ul style="list-style-type: none"> • SLC25A32 transports tetrahydrofolate (as well as FAD into mitochondria (265)) • SLC25A32 regulates mitochondrial one-carbon pathway in cancer cells (265)
<i>SYNE2</i>	Spectrin repeat containing nuclear envelope protein 2 (also known as nesprin-2)	<ul style="list-style-type: none"> • Involve in linking the nucleus to the cytoskeleton (266) • Nesprins (<i>SYNE1</i> and <i>SYNE2</i>) were identified as candidate cancer genes by high-throughput genome sequencing (267) • Identified as a recurrently mutated gene in head and neck squamous cell carcinoma (268) • Associated with p21 expression and clinical outcome of HBV-related HCC in a <i>TP53</i>-independent manner (269)
<i>RPL8</i>	Ribosomal protein L8	<ul style="list-style-type: none"> • Amplification of <i>RPL8</i> may be involved in pathogenesis of osteosarcoma (270) • Down-regulation of <i>RPL8</i> is associated poor response to chemotherapy in osteosarcoma patient (271) • Enriched ribosome pathway involving <i>RPL8</i>, may be associated with osteosarcoma (272)
<i>FAM160A2</i>	Family with sequence similarity 160 member A2 (also known as FHIP)	<ul style="list-style-type: none"> • <i>FAM160A2</i> is a component of the FTS/Hook/FHIP complex, which functions in regulating vesicle trafficking (273) • Recessive germline mutation in another family member <i>FAM160A2</i> is associated with familial NK/T cell lymphoma (274)

Table 13. Potential candidate genes driving LFS-associated osteosarcoma and their reported biological functions.

6.2 Intersection of the LFS iPSC model with new methodologies: organoids and organs-on-chip

Advances in 3D culture technology allow the generation of organoids from PSCs and adult stem cells (AdSCs). These 3D organoids better mimic the physiologic structure and function of organs than 2D culture and have been used to model normal development as well as human diseases (275, 276). Interestingly, the 3D organoid culture system has been extended to primary cancer culture in which cancer organoids can be generated from primary tumors including colon (277, 278) , pancreatic (279), and prostate cancers (280). Both normal and cancer organoids provide a unique platform for drug sensitivity and toxicity testing. Mature proximal tubule cells within iPSCs-derived kidney organoids undergo apoptosis after cisplatin treatment, indicating that kidney organoids could be used to test drug nephrotoxicity (281). Cystic fibrosis patient-derived rectal organoids have been used to characterize the response to cystic fibrosis transmembrane conductance regulator (CFTR)-modulating drugs, suggesting that organoids can be prospectively used to identify drug responders (282). A team from the Netherlands generated a living organoid biobank from colorectal cancer patients and demonstrated the feasibility of high-throughput drug screening while highlighting, as an example of potential personalized therapy, the sensitivity of one line to alterations in Wnt signaling (278).

Carcinogenesis and cancer progression can also be modeled using organoids. Introducing mutations of the tumor suppressors *APC*, *SMAD4*, and *TP53*, and the oncogene *KRAS*, into normal intestinal organoids led to malignant transformation

both *in vitro* and *in vivo* (283, 284). Neoplastic transformation was also observed when expressing mutant *KRAS* and/or *TP53* in normal PSC-derived pancreatic organoids (285) [215]. Knocking down *Tgfbr2* in *Tp53^{-/-} Cdh1^{-/-}* murine stomach organoids resulted in a metastatic phenotype *in vivo* (286). The classic ‘adenoma to carcinoma’ model has been recapitulated by sequentially creating cancer-driving mutations in human intestinal organoids (287).

These advances in 3D organoid systems lead us to postulate that integration of the LFS iPSC model with the organoid platform will provide additional opportunities for deciphering the pathogenesis of mutant p53 associated cancers and identifying potential druggable targets (**Figure 46**). One of the promising combinations will be using 3D cerebral organoids to study LFS-associated brain tumors. PSC-derived cerebral organoids can be grown in a spinning bioreactor system which enables rapid and abundant generation of a ‘mini-brain’ (288). Cerebral organoids have been utilized to model neurodevelopmental diseases such as microcephaly (288, 289) and lissencephaly (290), and have also been used to identify antiviral compounds against Zika virus (291). LFS iPSC-derived cerebral organoids hold potential in brain tumor modeling and may clarify the origins of GBM in affected patients.

Recently, researchers have developed organs-on-chip systems in an attempt to accurately mimic the cellular environment (292, 293). Organ-on-chip systems integrate cell culture with microfabrication and microfluidics technologies, and allow cells to be cultured in connected chambers. The term organs-on-chip was subsequently used to describe growth of multiple organs on a chip in which various

living human cells are cultured in a microenvironment designed to replicate the in vivo milieu (292). Organs-on-chip can represent key functional units of human organs or tissues. With the goal of mimicking the entire human body on a chip, this biomimetic system has great value in drug discovery and testing (294, 295). While many early organs-on-chip systems were developed from primary or transformed cell lines (296-301), newer systems incorporate iPSCs and relevant differentiated tissues into micro-fluidic devices (302, 303). Mathur *et al.* grew 3D cardiac tissue within a microfluidic device which mimics the blood flow and endothelial barrier. This human iPSC-based cardiac micro-physiology system proved particularly valuable in predicting drug-induced cardiotoxicity (302). In addition, functional differentiation of human pluripotent stem cells directly on microfluidic devices has recently been reported. Through optimal delivery of differentiation medium, Giovanni *et al.* (304) generated functional cardiomyocytes and hepatocytes that showed an expected response to defined drug treatments. We foresee that this powerful technique will provide invaluable information to clarify important missing pieces in the p53/LFS/cancer/ development puzzle.

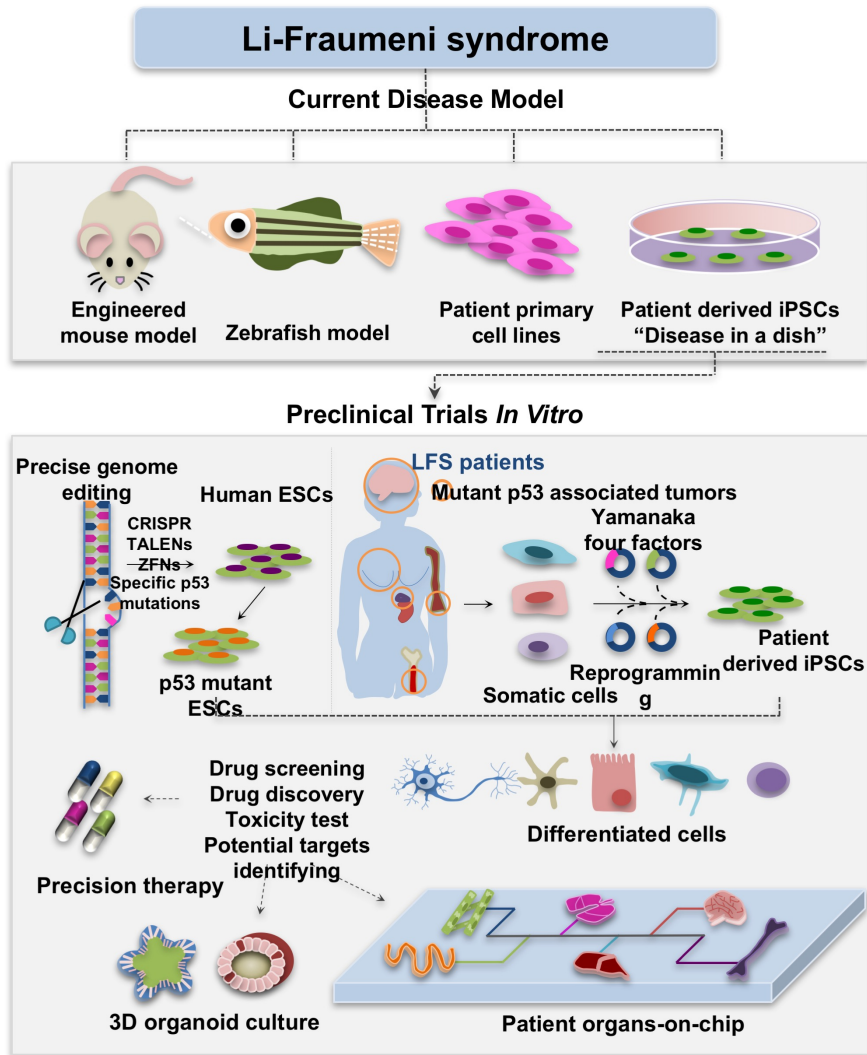


Figure 46. Application of LFS iPSC models to drug development for LFS and p53 mutation-associated tumors.

The LFS iPSC model overcomes the limitations of current LFS disease models such as those based on mice, zebrafish, or primary cell lines, and holds potential in modeling LFS-associated cancers and facilitating preclinical trials. Precise genome-editing techniques make it possible to expand the bank of PSCs with different p53 mutations, which provides a valuable resource for precision cancer medicine. Integration of 3D organoid and organs-on-chip systems with an LFS

iPSC disease model offers exciting opportunities for testing existing both WT and mutant p53-associated pathway related drugs and discovering new therapeutic compounds.

6.3 LFS iPSC Model: New Opportunities for Screening Compounds

Given its role as a tumor suppressor and its high rate of mutation in cancer, p53 poses an attractive target for cancer therapy. Many human tumors require loss of WT p53 or gain-of-function of mutant p53 to progress to a fully malignant phenotype. Thus, significant efforts have been devoted to p53-based drug development targeting both WT and mutant forms of p53. These strategies include (i) WT p53 activation, (ii) mutant p53 restoration, (iii) mutant p53 elimination, and (iv) p53 family inhibition, as summarized in **Table 14**.

WT p53 remains at relatively low intracellular levels predominantly due to ubiquitination by the E3 ligase MDM2 targeting it for rapid degradation (305). In many cancers the MDM2 proteins are dysregulated and exert an oncogenic function mainly by inhibiting p53 tumor-suppressor activity (306). As a result, considerable efforts have been made to develop compounds that interfere with the p53–MDM2 interaction, leading to the discovery of nutlin-3, RITA, and MI-219 (307-309). In addition, a new class of stapled peptides, designed to contain a hydrophobic binding interface that mimics the bound α -helical conformation of p53, have been shown to effectively block p53-MDM2 interactions (310-312). In addition to regulating WT p53, MDM2 can also regulate the degradation of mutant p53, and loss of MDM2 promotes tumor development in mutant p53 mice (313). This implies that drugs aimed at activating WT p53 by inhibiting MDM2 will also stabilize mutant p53 with adverse consequences.

Mutant p53 is also an attractive druggable target because mutant p53 protein is expressed at high levels in various tumor types but is generally only expressed at

very low levels in normal cells (314). To accomplish this, two strategies have been attempted: restoration of WT p53 transcriptional activity and depletion of mutant p53. The feasibility of restoration of WT activity in mutant protein stems from observations that loss of WT function introduced by some destabilizing mutations can be rescued by additional point mutations that stabilize the conformation of the p53 protein (315). As a result, a variety of compounds that might restore WT p53 function have been characterized, including NSC319726 (316), PhiKan083 (317), and WR-1065 (318). Depletion of oncogenic mutant p53 also turns out to be effective. Proper function of mutant p53 depends on interactions with the Hsp90 chaperone complex and HDAC6. The Hsp90/HDAC6 chaperone machine is significantly upregulated in tumors compared to normal tissues, and functions as a major determinant of mutant p53 stabilization (319). Inhibitors that target Hsp90 or HDAC6 both show positive results in depleting mutant p53 in preclinical trials (320, 321). Repression of the mevalonate pathway by statins, which inhibit HMG-CoA reductase, not only abrogates binding of multiple p53 mutants to DNAJA1 and the HSP40 complex but also increases mutant p53 degradation through interaction and ubiquitination by the co-chaperone C-terminus Hsp70/90 interacting protein (CHIP) E3 ubiquitin ligase (322).

Target	Compound	p53	Mechanism	Testing Stage	Reference
WT p53 Activation	RITA	WT	Inhibition of p53 binding	Preclinical	(307)
	nutlin-3	WT	Inhibition of p53-MDM2 interaction	Phase I	(308)
	MI-219	WT	Inhibition of p53-MDM2 interaction	Preclinical	(309)
	NSC319726	R175H	Restore WT structure and its transactivational function	Preclinical	(316)
Mutant p53 Restoration	PhiKan083	Y220C	Raise the melting temperature of mutant p53 and slow down its denaturation rate	Preclinical	(317)
	WR-1065	V272M	Restore the WT conformation of the temperature-sensitive p53 mutant V272M	Phase I	(318)
	Hsp90 inhibitors: 17-AAG	R175H, L194F, R273H, R280K,	Destroy the complex mutant p53/ HSP90 to release mutant p53 for its degradation	Phase I/II/III	(320)
Mutant p53 Elimination	HDAC inhibitors: SAHA	R175H, R280K, V247F/P223L	Inhibit HDAC6 and disrupt the HDAC6/ Hsp90/mutant p53 complex	Phase I/II	(321)
	HMG-CoA Reductase inhibitor: Statins	R156P, R175G, Y220C	Inhibit Mevalonate pathway and interfere HSP40/DNAJA1/ mutant p53 complex	Phase I/II/III	(322)
p53 family inhibition	RETRA	R273H, R248W, G266E, R280K	Increase the p73 levels and release p73 from mutant p53/p73 complex	Preclinical	(323)

Table 14. Compounds targeting WT and mutant p53.

Developments in iPSCs methodologies will likely improve drug discovery for p53-related therapies. Because LFS patient-derived iPSCs would provide a more reliable genetic back-ground for drug efficacy and toxicity screening, the failure rate of translation from animal models to humans can be reduced. Moreover, LFS iPSCs can be differentiated into multiple cell lineages, each of which can serve as a tumor model. As a result, a p53 drug screen can be narrowed down to one specific tumor type, increasing the fidelity of the system and the expected success rate. This approach has already shown promise for other genes. Engineered human embryonic stem cell (ESC)-derived neural progenitor cells (NPCs) and neural stem cells (NSCs) have been used to study and model diffuse intrinsic pontine gliomas (DIPGs) (170) and GBM (171), respectively. Both these studies identified novel potential drugs for brain tumors. As applications of iPSC models to cancer increase, the technology will likely gain increasing importance in developing and guiding cancer treatment (188, 324).

Reference

1. Li, F. P., and J. F. Fraumeni, Jr. 1969. Rhabdomyosarcoma in children: epidemiologic study and identification of a familial cancer syndrome. *Journal of the National Cancer Institute* 43: 1365-1373.
2. Li, F. P., and J. F. Fraumeni, Jr. 1969. Soft-tissue sarcomas, breast cancer, and other neoplasms. A familial syndrome? *Annals of internal medicine* 71: 747-752.
3. Li, F. P., J. F. Fraumeni, Jr., J. J. Mulvihill, W. A. Blattner, M. G. Dreyfus, M. A. Tucker, and R. W. Miller. 1988. A cancer family syndrome in twenty-four kindreds. *Cancer research* 48: 5358-5362.
4. Birch, J. M., A. L. Hartley, K. J. Tricker, J. Prosser, A. Condie, A. M. Kelsey, M. Harris, P. H. Jones, A. Binchy, D. Crowther, and et al. 1994. Prevalence and diversity of constitutional mutations in the p53 gene among 21 Li-Fraumeni families. *Cancer research* 54: 1298-1304.
5. Nichols, K. E., D. Malkin, J. E. Garber, J. F. Fraumeni, Jr., and F. P. Li. 2001. Germ-line p53 mutations predispose to a wide spectrum of early-onset cancers. *Cancer epidemiology, biomarkers & prevention : a publication of the American Association for Cancer Research, cosponsored by the American Society of Preventive Oncology* 10: 83-87.
6. Sorrell, A. D., C. R. Espenschied, J. O. Culver, and J. N. Weitzel. 2013. Tumor protein p53 (TP53) testing and Li-Fraumeni syndrome : current status of clinical applications and future directions. *Molecular diagnosis & therapy* 17: 31-47.

7. Chompret, A., L. Brugieres, M. Ronsin, M. Gardes, F. Dessarps-Freichey, A. Abel, D. Hua, L. Ligot, M. G. Dondon, B. Bressac-de Paillerets, T. Frebourg, J. Lemerle, C. Bonaiti-Pellie, and J. Feunteun. 2000. P53 germline mutations in childhood cancers and cancer risk for carrier individuals. *British journal of cancer* 82: 1932-1937.
8. Wu, C. C., S. Shete, C. I. Amos, and L. C. Strong. 2006. Joint effects of germ-line p53 mutation and sex on cancer risk in Li-Fraumeni syndrome. *Cancer research* 66: 8287-8292.
9. Hisada, M., J. E. Garber, C. Y. Fung, J. F. Fraumeni, Jr., and F. P. Li. 1998. Multiple primary cancers in families with Li-Fraumeni syndrome. *Journal of the National Cancer Institute* 90: 606-611.
10. Bougeard, G., M. Renaux-Petel, J. M. Flaman, C. Charbonnier, P. Fermeij, M. Belotti, M. Gauthier-Villars, D. Stoppa-Lyonnet, E. Consolino, L. Brugieres, O. Caron, P. R. Benusiglio, B. Bressac-de Paillerets, V. Bonadona, C. Bonaiti-Pellie, J. Tinat, S. Baert-Desurmont, and T. Frebourg. 2015. Revisiting Li-Fraumeni Syndrome From TP53 Mutation Carriers. *Journal of clinical oncology : official journal of the American Society of Clinical Oncology* 33: 2345-2352.
11. Zebisch, A., R. Lal, M. Muller, K. Lind, K. Kashofer, M. Girschikofsky, D. Fuchs, A. Wolfler, J. B. Geigl, and H. Sill. 2016. Acute myeloid leukemia with TP53 germ line mutations. *Blood* 128: 2270-2272.
12. Heymann, S., S. Delaloge, A. Rahal, O. Caron, T. Frebourg, L. Barreau, C. Pachet, M. C. Mathieu, H. Marsiglia, and C. Bourgier. 2010. Radio-induced

- malignancies after breast cancer postoperative radiotherapy in patients with Li-Fraumeni syndrome. *Radiat Oncol* 5: 104.
13. Limacher, J. M., T. Frebourg, S. Natarajan-Ame, and J. P. Bergerat. 2001. Two metachronous tumors in the radiotherapy fields of a patient with Li-Fraumeni syndrome. *Int J Cancer* 96: 238-242.
 14. Kemp, C. J., T. Wheldon, and A. Balmain. 1994. p53-deficient mice are extremely susceptible to radiation-induced tumorigenesis. *Nature genetics* 8: 66-69.
 15. Boyle, J. M., A. Spreadborough, M. J. Greaves, J. M. Birch, J. M. Varley, and D. Scott. 2001. The relationship between radiation-induced G(1)arrest and chromosome aberrations in Li-Fraumeni fibroblasts with or without germline TP53 mutations. *British journal of cancer* 85: 293-296.
 16. Villani, A., A. Shore, J. D. Wasserman, D. Stephens, R. H. Kim, H. Druker, B. Gallinger, A. Naumer, W. Kohlmann, A. Novokmet, U. Tabori, M. Tijerin, M. L. Greer, J. L. Finlay, J. D. Schiffman, and D. Malkin. 2016. Biochemical and imaging surveillance in germline TP53 mutation carriers with Li-Fraumeni syndrome: 11 year follow-up of a prospective observational study. *Lancet Oncol* 17: 1295-1305.
 17. Malkin, D., F. P. Li, L. C. Strong, J. F. Fraumeni, Jr., C. E. Nelson, D. H. Kim, J. Kassel, M. A. Gryka, F. Z. Bischoff, M. A. Tainsky, and et al. 1990. Germ line p53 mutations in a familial syndrome of breast cancer, sarcomas, and other neoplasms. *Science* 250: 1233-1238.

18. Srivastava, S., Z. Q. Zou, K. Pirollo, W. Blattner, and E. H. Chang. 1990. Germ-line transmission of a mutated p53 gene in a cancer-prone family with Li-Fraumeni syndrome. *Nature* 348: 747-749.
19. Varley, J. M. 2003. Germline TP53 mutations and Li-Fraumeni syndrome. *Human mutation* 21: 313-320.
20. Olivier, M., R. Eeles, M. Hollstein, M. A. Khan, C. C. Harris, and P. Hainaut. 2002. The IARC TP53 database: new online mutation analysis and recommendations to users. *Human mutation* 19: 607-614.
21. Frebourg, T., N. Barbier, Y. X. Yan, J. E. Garber, M. Dreyfus, J. Fraumeni, Jr., F. P. Li, and S. H. Friend. 1995. Germ-line p53 mutations in 15 families with Li-Fraumeni syndrome. *American journal of human genetics* 56: 608-615.
22. Varley, J. M., G. McGown, M. Thorncroft, M. F. Santibanez-Koref, A. M. Kelsey, K. J. Tricker, D. G. Evans, and J. M. Birch. 1997. Germ-line mutations of TP53 in Li-Fraumeni families: an extended study of 39 families. *Cancer research* 57: 3245-3252.
23. Shlien, A., U. Tabori, C. R. Marshall, M. Pienkowska, L. Feuk, A. Novokmet, S. Nanda, H. Druker, S. W. Scherer, and D. Malkin. 2008. Excessive genomic DNA copy number variation in the Li-Fraumeni cancer predisposition syndrome. *Proc Natl Acad Sci U S A* 105: 11264-11269.
24. Bougeard, G., L. Brugieres, A. Chompret, P. Gesta, F. Charbonnier, A. Valent, C. Martin, G. Raux, J. Feunteun, B. Bressac-de Paillerets, and T. Frebourg. 2003. Screening for TP53 rearrangements in families with the Li-

- Fraumeni syndrome reveals a complete deletion of the TP53 gene. *Oncogene* 22: 840-846.
25. Chompret, A., A. Abel, D. Stoppa-Lyonnet, L. Brugieres, S. Pages, J. Feunteun, and C. Bonaiti-Pellie. 2001. Sensitivity and predictive value of criteria for p53 germline mutation screening. *Journal of medical genetics* 38: 43-47.
 26. Bouaoun, L., D. Sonkin, M. Ardin, M. Hollstein, G. Byrnes, J. Zavadil, and M. Olivier. 2016. TP53 Variations in Human Cancers: New Lessons from the IARC TP53 Database and Genomics Data. *Human mutation* 37: 865-876.
 27. Vogelstein, B., D. Lane, and A. J. Levine. 2000. Surfing the p53 network. *Nature* 408: 307-310.
 28. Laptenko, O., and C. Prives. 2006. Transcriptional regulation by p53: one protein, many possibilities. *Cell death and differentiation* 13: 951-961.
 29. Biegging, K. T., S. S. Mello, and L. D. Attardi. 2014. Unravelling mechanisms of p53-mediated tumour suppression. *Nature reviews. Cancer* 14: 359-370.
 30. Matoba, S., J. G. Kang, W. D. Patino, A. Wragg, M. Boehm, O. Gavrilova, P. J. Hurley, F. Bunz, and P. M. Hwang. 2006. p53 regulates mitochondrial respiration. *Science* 312: 1650-1653.
 31. Bensaad, K., and K. H. Vousden. 2007. p53: new roles in metabolism. *Trends in cell biology* 17: 286-291.

32. O'Connor, J. C., D. M. Wallace, C. J. O'Brien, and T. G. Cotter. 2008. A novel antioxidant function for the tumor-suppressor gene p53 in the retinal ganglion cell. *Investigative ophthalmology & visual science* 49: 4237-4244.
33. Bensaad, K., and K. H. Vousden. 2005. Savior and slayer: the two faces of p53. *Nat Med* 11: 1278-1279.
34. Crichton, D., S. Wilkinson, J. O'Prey, N. Syed, P. Smith, P. R. Harrison, M. Gasco, O. Garrone, T. Crook, and K. M. Ryan. 2006. DRAM, a p53-induced modulator of autophagy, is critical for apoptosis. *Cell* 126: 121-134.
35. Tasdemir, E., M. C. Maiuri, L. Galluzzi, I. Vitale, M. Djavaheri-Mergny, M. D'Amelio, A. Criollo, E. Morselli, C. Zhu, F. Harper, U. Nannmark, C. Samara, P. Pinton, J. M. Vicencio, R. Carnuccio, U. M. Moll, F. Madeo, P. Paterlini-Brechot, R. Rizzuto, G. Szabadkai, G. Pierron, K. Blomgren, N. Tavernarakis, P. Codogno, F. Cecconi, and G. Kroemer. 2008. Regulation of autophagy by cytoplasmic p53. *Nature cell biology* 10: 676-687.
36. Roger, L., G. Gadea, and P. Roux. 2006. Control of cell migration: a tumour suppressor function for p53? *Biology of the cell* 98: 141-152.
37. Teodoro, J. G., A. E. Parker, X. Zhu, and M. R. Green. 2006. p53-mediated inhibition of angiogenesis through up-regulation of a collagen prolyl hydroxylase. *Science* 313: 968-971.
38. Wang, X., H. Y. Kua, Y. Hu, K. Guo, Q. Zeng, Q. Wu, H. H. Ng, G. Karsenty, B. de Crombrughe, J. Yeh, and B. Li. 2006. p53 functions as a negative regulator of osteoblastogenesis, osteoblast-dependent osteoclastogenesis, and bone remodeling. *The Journal of cell biology* 172: 115-125.

39. Liu, H., and B. Li. 2010. p53 control of bone remodeling. *Journal of cellular biochemistry* 111: 529-534.
40. Pant, V., A. Quintas-Cardama, and G. Lozano. 2012. The p53 pathway in hematopoiesis: lessons from mouse models, implications for humans. *Blood* 120: 5118-5127.
41. Yi, L., C. Lu, W. Hu, Y. Sun, and A. J. Levine. 2012. Multiple roles of p53-related pathways in somatic cell reprogramming and stem cell differentiation. *Cancer research* 72: 5635-5645.
42. Lee, D. F., J. Su, Y. S. Ang, X. Carvajal-Vergara, S. Mulero-Navarro, C. F. Pereira, J. Gingold, H. L. Wang, R. Zhao, A. Sevilla, H. Darr, A. J. Williamson, B. Chang, X. Niu, F. Aguilo, E. R. Flores, Y. P. Sher, M. C. Hung, A. D. Whetton, B. D. Gelb, K. A. Moore, H. W. Snoeck, A. Ma'ayan, C. Schaniel, and I. R. Lemischka. 2012. Regulation of embryonic and induced pluripotency by aurora kinase-p53 signaling. *Cell Stem Cell* 11: 179-194.
43. Zheng, H., H. Ying, H. Yan, A. C. Kimmelman, D. J. Hiller, A. J. Chen, S. R. Perry, G. Tonon, G. C. Chu, Z. Ding, J. M. Stommel, K. L. Dunn, R. Wiedemeyer, M. J. You, C. Brennan, Y. A. Wang, K. L. Ligon, W. H. Wong, L. Chin, and R. A. DePinho. 2008. p53 and Pten control neural and glioma stem/progenitor cell renewal and differentiation. *Nature* 455: 1129-1133.
44. Nagy, R., K. Sweet, and C. Eng. 2004. Highly penetrant hereditary cancer syndromes. *Oncogene* 23: 6445-6470.
45. He, Y., L. F. de Castro, M. H. Shin, W. Dubois, H. H. Yang, S. Jiang, P. J. Mishra, L. Ren, H. Gou, A. Lal, C. Khanna, G. Merlino, M. Lee, P. G. Robey,

- and J. Huang. 2015. p53 loss increases the osteogenic differentiation of bone marrow stromal cells. *Stem Cells* 33: 1304-1319.
46. Liu, H., D. Jia, A. Li, J. Chau, D. He, X. Ruan, F. Liu, J. Li, L. He, and B. Li. 2013. p53 regulates neural stem cell proliferation and differentiation via BMP-Smad1 signaling and Id1. *Stem cells and development* 22: 913-927.
47. McConnell, A. M., C. Yao, A. R. Yeckes, Y. Wang, A. S. Selvaggio, J. Tang, D. G. Kirsch, and B. R. Stripp. 2016. p53 Regulates Progenitor Cell Quiescence and Differentiation in the Airway. *Cell Rep* 17: 2173-2182.
48. Cottle, D. L., K. Kretzschmar, H. P. Gollnick, and S. R. Quist. 2016. p53 activity contributes to defective interfollicular epidermal differentiation in hyperproliferative murine skin. *The British journal of dermatology* 174: 204-208.
49. Wang, Q., Y. Zou, S. Nowotschin, S. Y. Kim, Q. V. Li, C. L. Soh, J. Su, C. Zhang, W. Shu, Q. Xi, D. Huangfu, A. K. Hadjantonakis, and J. Massague. 2017. The p53 Family Coordinates Wnt and Nodal Inputs in Mesendodermal Differentiation of Embryonic Stem Cells. *Cell Stem Cell* 20: 70-86.
50. Hong, H., K. Takahashi, T. Ichisaka, T. Aoi, O. Kanagawa, M. Nakagawa, K. Okita, and S. Yamanaka. 2009. Suppression of induced pluripotent stem cell generation by the p53-p21 pathway. *Nature* 460: 1132-1135.
51. Kawamura, T., J. Suzuki, Y. V. Wang, S. Menendez, L. B. Morera, A. Raya, G. M. Wahl, and J. C. Izpisua Belmonte. 2009. Linking the p53 tumour suppressor pathway to somatic cell reprogramming. *Nature* 460: 1140-1144.

52. Sarig, R., N. Rivlin, R. Brosh, C. Bornstein, I. Kamer, O. Ezra, A. Molchadsky, N. Goldfinger, O. Brenner, and V. Rotter. 2010. Mutant p53 facilitates somatic cell reprogramming and augments the malignant potential of reprogrammed cells. *The Journal of experimental medicine* 207: 2127-2140.
53. Vousden, K. H., and C. Prives. 2009. Blinded by the Light: The Growing Complexity of p53. *Cell* 137: 413-431.
54. Janicke, R. U., D. Sohn, and K. Schulze-Osthoff. 2008. The dark side of a tumor suppressor: anti-apoptotic p53. *Cell death and differentiation* 15: 959-976.
55. Kim, E., A. Giese, and W. Deppert. 2009. Wild-type p53 in cancer cells: when a guardian turns into a blackguard. *Biochemical pharmacology* 77: 11-20.
56. Martins, C. P., L. Brown-Swigart, and G. I. Evan. 2006. Modeling the therapeutic efficacy of p53 restoration in tumors. *Cell* 127: 1323-1334.
57. Ventura, A., D. G. Kirsch, M. E. McLaughlin, D. A. Tuveson, J. Grimm, L. Lintault, J. Newman, E. E. Reczek, R. Weissleder, and T. Jacks. 2007. Restoration of p53 function leads to tumour regression in vivo. *Nature* 445: 661-665.
58. Xue, W., L. Zender, C. Miething, R. A. Dickins, E. Hernando, V. Krizhanovsky, C. Cordon-Cardo, and S. W. Lowe. 2007. Senescence and tumour clearance is triggered by p53 restoration in murine liver carcinomas. *Nature* 445: 656-660.

59. Cheok, C. F., C. S. Verma, J. Baselga, and D. P. Lane. 2011. Translating p53 into the clinic. *Nature reviews. Clinical oncology* 8: 25-37.
60. Olivier, M., M. Hollstein, and P. Hainaut. 2010. TP53 mutations in human cancers: origins, consequences, and clinical use. *Cold Spring Harbor perspectives in biology* 2: a001008.
61. Kandoth, C., M. D. McLellan, F. Vandin, K. Ye, B. Niu, C. Lu, M. Xie, Q. Zhang, J. F. McMichael, M. A. Wyczalkowski, M. D. Leiserson, C. A. Miller, J. S. Welch, M. J. Walter, M. C. Wendl, T. J. Ley, R. K. Wilson, B. J. Raphael, and L. Ding. 2013. Mutational landscape and significance across 12 major cancer types. *Nature* 502: 333-339.
62. Hohenstein, P. 2004. Tumour suppressor genes--one hit can be enough. *PLoS Biol* 2: E40.
63. Petitjean, A., E. Mathe, S. Kato, C. Ishioka, S. V. Tavtigian, P. Hainaut, and M. Olivier. 2007. Impact of mutant p53 functional properties on TP53 mutation patterns and tumor phenotype: lessons from recent developments in the IARC TP53 database. *Human mutation* 28: 622-629.
64. Weisz, L., M. Oren, and V. Rotter. 2007. Transcription regulation by mutant p53. *Oncogene* 26: 2202-2211.
65. Song, H., M. Hollstein, and Y. Xu. 2007. p53 gain-of-function cancer mutants induce genetic instability by inactivating ATM. *Nature cell biology* 9: 573-580.
66. Caulin, C., T. Nguyen, G. A. Lang, T. M. Goepfert, B. R. Brinkley, W. W. Cai, G. Lozano, and D. R. Roop. 2007. An inducible mouse model for skin

- cancer reveals distinct roles for gain- and loss-of-function p53 mutations. *The Journal of clinical investigation* 117: 1893-1901.
67. Hingorani, S. R., L. Wang, A. S. Multani, C. Combs, T. B. Deramaudt, R. H. Hruban, A. K. Rustgi, S. Chang, and D. A. Tuveson. 2005. Trp53R172H and KrasG12D cooperate to promote chromosomal instability and widely metastatic pancreatic ductal adenocarcinoma in mice. *Cancer cell* 7: 469-483.
 68. Valenti, F., F. Ganci, G. Fontemaggi, A. Sacconi, S. Strano, G. Blandino, and S. Di Agostino. 2015. Gain of function mutant p53 proteins cooperate with E2F4 to transcriptionally downregulate RAD17 and BRCA1 gene expression. *Oncotarget* 6: 5547-5566.
 69. Samassekou, O., N. Bastien, D. Lichtensztejn, J. Yan, S. Mai, and R. Drouin. 2014. Different TP53 mutations are associated with specific chromosomal rearrangements, telomere length changes, and remodeling of the nuclear architecture of telomeres. *Genes, chromosomes & cancer* 53: 934-950.
 70. Matas, D., A. Sigal, P. Stambolsky, M. Milyavsky, L. Weisz, D. Schwartz, N. Goldfinger, and V. Rotter. 2001. Integrity of the N-terminal transcription domain of p53 is required for mutant p53 interference with drug-induced apoptosis. *The EMBO journal* 20: 4163-4172.
 71. Murphy, K. L., A. P. Dennis, and J. M. Rosen. 2000. A gain of function p53 mutant promotes both genomic instability and cell survival in a novel p53-null mammary epithelial cell model. *FASEB journal : official publication of*

- the Federation of American Societies for Experimental Biology* 14: 2291-2302.
72. Gaiddon, C., M. Lokshin, J. Ahn, T. Zhang, and C. Prives. 2001. A subset of tumor-derived mutant forms of p53 down-regulate p63 and p73 through a direct interaction with the p53 core domain. *Molecular and cellular biology* 21: 1874-1887.
 73. Huang, X., Y. Zhang, Y. Tang, N. Butler, J. Kim, F. Guessous, D. Schiff, J. Mandell, and R. Abounader. 2013. A novel PTEN/mutant p53/c-Myc/Bcl-XL axis mediates context-dependent oncogenic effects of PTEN with implications for cancer prognosis and therapy. *Neoplasia* 15: 952-965.
 74. Ali, A., A. S. Shah, and A. Ahmad. 2014. Gain-of-function of mutant p53: mutant p53 enhances cancer progression by inhibiting KLF17 expression in invasive breast carcinoma cells. *Cancer letters* 354: 87-96.
 75. Dong, P., M. Karaayvaz, N. Jia, M. Kaneuchi, J. Hamada, H. Watari, S. Sudo, J. Ju, and N. Sakuragi. 2013. Mutant p53 gain-of-function induces epithelial-mesenchymal transition through modulation of the miR-130b-ZEB1 axis. *Oncogene* 32: 3286-3295.
 76. Di Agostino, S., S. Strano, V. Emiliozzi, V. Zerbini, M. Mottolese, A. Sacchi, G. Blandino, and G. Piaggio. 2006. Gain of function of mutant p53: the mutant p53/NF-Y protein complex reveals an aberrant transcriptional mechanism of cell cycle regulation. *Cancer cell* 10: 191-202.

77. Atema, A., and P. Chene. 2002. The gain of function of the p53 mutant Asp281Gly is dependent on its ability to form tetramers. *Cancer letters* 185: 103-109.
78. Liu, K., S. Ling, and W. C. Lin. 2011. TopBP1 mediates mutant p53 gain of function through NF-Y and p63/p73. *Molecular and cellular biology* 31: 4464-4481.
79. El-Hizawi, S., J. P. Lagowski, M. Kulesz-Martin, and A. Albor. 2002. Induction of gene amplification as a gain-of-function phenotype of mutant p53 proteins. *Cancer research* 62: 3264-3270.
80. Scian, M. J., K. E. Stagliano, D. Deb, M. A. Ellis, E. H. Carchman, A. Das, K. Valerie, S. P. Deb, and S. Deb. 2004. Tumor-derived p53 mutants induce oncogenesis by transactivating growth-promoting genes. *Oncogene* 23: 4430-4443.
81. Marin, M. C., C. A. Jost, L. A. Brooks, M. S. Irwin, J. O'Nions, J. A. Tidy, N. James, J. M. McGregor, C. A. Harwood, I. G. Yulug, K. H. Vousden, M. J. Allday, B. Gusterson, S. Ikawa, P. W. Hinds, T. Crook, and W. G. Kaelin, Jr. 2000. A common polymorphism acts as an intragenic modifier of mutant p53 behaviour. *Nature genetics* 25: 47-54.
82. Muller, P. A., A. G. Trinidad, P. Timpson, J. P. Morton, S. Zanivan, P. V. van den Berghe, C. Nixon, S. A. Karim, P. T. Caswell, J. E. Noll, C. R. Coffill, D. P. Lane, O. J. Sansom, P. M. Neilsen, J. C. Norman, and K. H. Vousden. 2013. Mutant p53 enhances MET trafficking and signalling to drive cell scattering and invasion. *Oncogene* 32: 1252-1265.

83. Dong, P., Z. Xu, N. Jia, D. Li, and Y. Feng. 2009. Elevated expression of p53 gain-of-function mutation R175H in endometrial cancer cells can increase the invasive phenotypes by activation of the EGFR/PI3K/AKT pathway. *Molecular cancer* 8: 103.
84. Adorno, M., M. Cordenonsi, M. Montagner, S. Dupont, C. Wong, B. Hann, A. Solari, S. Bobisse, M. B. Rondina, V. Guzzardo, A. R. Parenti, A. Rosato, S. Bicciato, A. Balmain, and S. Piccolo. 2009. A Mutant-p53/Smad complex opposes p63 to empower TGFbeta-induced metastasis. *Cell* 137: 87-98.
85. Coffill, C. R., P. A. Muller, H. K. Oh, S. P. Neo, K. A. Hogue, C. F. Cheok, K. H. Vousden, D. P. Lane, W. P. Blackstock, and J. Gunaratne. 2012. Mutant p53 interactome identifies nardilysin as a p53R273H-specific binding partner that promotes invasion. *EMBO reports* 13: 638-644.
86. Muller, P. A., P. T. Caswell, B. Doyle, M. P. Iwanicki, E. H. Tan, S. Karim, N. Lukashchuk, D. A. Gillespie, R. L. Ludwig, P. Gosselin, A. Cromer, J. S. Brugge, O. J. Sansom, J. C. Norman, and K. H. Vousden. 2009. Mutant p53 drives invasion by promoting integrin recycling. *Cell* 139: 1327-1341.
87. Noll, J. E., J. Jeffery, F. Al-Ejeh, R. Kumar, K. K. Khanna, D. F. Callen, and P. M. Neilsen. 2012. Mutant p53 drives multinucleation and invasion through a process that is suppressed by ANKRD11. *Oncogene* 31: 2836-2848.
88. Yeudall, W. A., C. A. Vaughan, H. Miyazaki, M. Ramamoorthy, M. Y. Choi, C. G. Chapman, H. Wang, E. Black, A. A. Bulysheva, S. P. Deb, B. Windle,

- and S. Deb. 2012. Gain-of-function mutant p53 upregulates CXC chemokines and enhances cell migration. *Carcinogenesis* 33: 442-451.
89. Vaughan, C. A., S. Singh, B. Windle, H. M. Sankala, P. R. Graves, W. Andrew Yeudall, S. P. Deb, and S. Deb. 2012. p53 mutants induce transcription of NF-kappaB2 in H1299 cells through CBP and STAT binding on the NF-kappaB2 promoter and gain of function activity. *Archives of biochemistry and biophysics* 518: 79-88.
90. Ji, L., J. Xu, J. Liu, A. Amjad, K. Zhang, Q. Liu, L. Zhou, J. Xiao, and X. Li. 2015. Mutant p53 promotes tumor cell malignancy by both positive and negative regulation of the transforming growth factor beta (TGF-beta) pathway. *The Journal of biological chemistry* 290: 11729-11740.
91. Subramanian, M., P. Francis, S. Bilke, X. L. Li, T. Hara, X. Lu, M. F. Jones, R. L. Walker, Y. Zhu, M. Pineda, C. Lee, L. Varanasi, Y. Yang, L. A. Martinez, J. Luo, S. Ambs, S. Sharma, L. M. Wakefield, P. S. Meltzer, and A. Lal. 2015. A mutant p53/let-7i-axis-regulated gene network drives cell migration, invasion and metastasis. *Oncogene* 34: 1094-1104.
92. Pfister, N. T., V. Fomin, K. Regunath, J. Y. Zhou, W. Zhou, L. Silwal-Pandit, W. A. Freed-Pastor, O. Laptenko, S. P. Neo, J. Bargonetti, M. Hoque, B. Tian, J. Gunaratne, O. Engebraaten, J. L. Manley, A. L. Borresen-Dale, P. M. Neilsen, and C. Prives. 2015. Mutant p53 cooperates with the SWI/SNF chromatin remodeling complex to regulate VEGFR2 in breast cancer cells. *Genes & development* 29: 1298-1315.

93. Fontemaggi, G., S. Dell'Orso, D. Trisciuglio, T. Shay, E. Melucci, F. Fazi, I. Terrenato, M. Mottolese, P. Muti, E. Domany, D. Del Bufalo, S. Strano, and G. Blandino. 2009. The execution of the transcriptional axis mutant p53, E2F1 and ID4 promotes tumor neo-angiogenesis. *Nature structural & molecular biology* 16: 1086-1093.
94. Capponcelli, S., E. Pedrini, M. A. Cerone, V. Corti, S. Fontanesi, M. Alessio, A. Bachi, S. Soddu, D. Ribatti, P. Picci, L. J. Helman, G. Cantelli-Forti, and L. Sangiorgi. 2005. Evaluation of the molecular mechanisms involved in the gain of function of a Li-Fraumeni TP53 mutation. *Human mutation* 26: 94-103.
95. Khromova, N. V., P. B. Kopnin, E. V. Stepanova, L. S. Agapova, and B. P. Kopnin. 2009. p53 hot-spot mutants increase tumor vascularization via ROS-mediated activation of the HIF1/VEGF-A pathway. *Cancer letters* 276: 143-151.
96. Freed-Pastor, W. A., H. Mizuno, X. Zhao, A. Langerod, S. H. Moon, R. Rodriguez-Barrueco, A. Barsotti, A. Chicas, W. Li, A. Polotskaia, M. J. Bissell, T. F. Osborne, B. Tian, S. W. Lowe, J. M. Silva, A. L. Borresen-Dale, A. J. Levine, J. Bargonetti, and C. Prives. 2012. Mutant p53 disrupts mammary tissue architecture via the mevalonate pathway. *Cell* 148: 244-258.
97. Zhang, C., J. Liu, Y. Liang, R. Wu, Y. Zhao, X. Hong, M. Lin, H. Yu, L. Liu, A. J. Levine, W. Hu, and Z. Feng. 2013. Tumour-associated mutant p53 drives the Warburg effect. *Nature communications* 4: 2935.

98. Zhou, G., J. Wang, M. Zhao, T. X. Xie, N. Tanaka, D. Sano, A. A. Patel, A. M. Ward, V. C. Sandulache, S. A. Jasser, H. D. Skinner, A. L. Fitzgerald, A. A. Osman, Y. Wei, X. Xia, Z. Songyang, G. B. Mills, M. C. Hung, C. Caulin, J. Liang, and J. N. Myers. 2014. Gain-of-function mutant p53 promotes cell growth and cancer cell metabolism via inhibition of AMPK activation. *Molecular cell* 54: 960-974.
99. Li, X., J. B. Wu, L. W. Chung, and W. C. Huang. 2015. Anti-cancer efficacy of SREBP inhibitor, alone or in combination with docetaxel, in prostate cancer harboring p53 mutations. *Oncotarget* 6: 41018-41032.
100. Weisz, L., A. Damalas, M. Lontos, P. Karakaidos, G. Fontemaggi, R. Maor-Aloni, M. Kalis, M. Levrero, S. Strano, V. G. Gorgoulis, V. Rotter, G. Blandino, and M. Oren. 2007. Mutant p53 enhances nuclear factor kappaB activation by tumor necrosis factor alpha in cancer cells. *Cancer research* 67: 2396-2401.
101. Cooks, T., I. S. Pateras, O. Tarcic, H. Solomon, A. J. Schetter, S. Wilder, G. Lozano, E. Pikarsky, T. Forsheew, N. Rosenfeld, N. Harpaz, S. Itzkowitz, C. C. Harris, V. Rotter, V. G. Gorgoulis, and M. Oren. 2013. Mutant p53 prolongs NF-kappaB activation and promotes chronic inflammation and inflammation-associated colorectal cancer. *Cancer cell* 23: 634-646.
102. Di Minin, G., A. Bellazzo, M. Dal Ferro, G. Chiaruttini, S. Nuzzo, S. Bicciato, S. Piazza, D. Rami, R. Bulla, R. Sommaggio, A. Rosato, G. Del Sal, and L. Collavin. 2014. Mutant p53 reprograms TNF signaling in cancer cells

- through interaction with the tumor suppressor DAB2IP. *Molecular cell* 56: 617-629.
103. Ubertini, V., G. Norelli, D. D'Arcangelo, A. Gurtner, E. Cesareo, S. Baldari, M. P. Gentileschi, G. Piaggio, P. Nistico, S. Soddu, A. Facchiano, and G. Bossi. 2015. Mutant p53 gains new function in promoting inflammatory signals by repression of the secreted interleukin-1 receptor antagonist. *Oncogene* 34: 2493-2504.
 104. Freed-Pastor, W. A., and C. Prives. 2012. Mutant p53: one name, many proteins. *Genes & development* 26: 1268-1286.
 105. Muller, P. A., and K. H. Vousden. 2013. p53 mutations in cancer. *Nature cell biology* 15: 2-8.
 106. Sigal, A., and V. Rotter. 2000. Oncogenic mutations of the p53 tumor suppressor: the demons of the guardian of the genome. *Cancer research* 60: 6788-6793.
 107. Strano, S., S. Dell'Orso, A. M. Mongiovi, O. Monti, E. Lapi, S. Di Agostino, G. Fontemaggi, and G. Blandino. 2007. Mutant p53 proteins: between loss and gain of function. *Head & neck* 29: 488-496.
 108. Strano, S., S. Dell'Orso, S. Di Agostino, G. Fontemaggi, A. Sacchi, and G. Blandino. 2007. Mutant p53: an oncogenic transcription factor. *Oncogene* 26: 2212-2219.
 109. Brosh, R., and V. Rotter. 2009. When mutants gain new powers: news from the mutant p53 field. *Nature reviews. Cancer* 9: 701-713.

110. Muller, P. A., and K. H. Vousden. 2014. Mutant p53 in cancer: new functions and therapeutic opportunities. *Cancer cell* 25: 304-317.
111. Olivier, M., A. Petitjean, V. Marcel, A. Petre, M. Mounawar, A. Plymoth, C. C. de Fromental, and P. Hainaut. 2009. Recent advances in p53 research: an interdisciplinary perspective. *Cancer gene therapy* 16: 1-12.
112. Oren, M., and V. Rotter. 2010. Mutant p53 gain-of-function in cancer. *Cold Spring Harbor perspectives in biology* 2: a001107.
113. Lozano, G. 2007. The oncogenic roles of p53 mutants in mouse models. *Current opinion in genetics & development* 17: 66-70.
114. Peters, J. 2014. The role of genomic imprinting in biology and disease: an expanding view. *Nature reviews. Genetics* 15: 517-530.
115. Holm, T. M., L. Jackson-Grusby, T. Brambrink, Y. Yamada, W. M. Rideout, 3rd, and R. Jaenisch. 2005. Global loss of imprinting leads to widespread tumorigenesis in adult mice. *Cancer cell* 8: 275-285.
116. Murrell, A. 2006. Genomic imprinting and cancer: from primordial germ cells to somatic cells. *TheScientificWorldJournal* 6: 1888-1910.
117. Choufani, S., C. Shuman, and R. Weksberg. 2010. Beckwith-Wiedemann syndrome. *American journal of medical genetics. Part C, Seminars in medical genetics* 154C: 343-354.
118. Eggermann, T. 2010. Russell-Silver syndrome. *American journal of medical genetics. Part C, Seminars in medical genetics* 154C: 355-364.
119. Haley, V. L., D. J. Barnes, I. Sandovici, M. Constancia, C. F. Graham, F. Pezzella, C. Buhnemann, E. J. Carter, and A. B. Hassan. 2012. Igf2

- pathway dependency of the Trp53 developmental and tumour phenotypes. *EMBO molecular medicine* 4: 705-718.
120. Dugimont, T., C. Montpellier, E. Adriaenssens, S. Lottin, L. Dumont, V. lotsova, C. Lagrou, D. Stehelin, J. Coll, and J. J. Curgy. 1998. The H19 TATA-less promoter is efficiently repressed by wild-type tumor suppressor gene product p53. *Oncogene* 16: 2395-2401.
 121. Matouk, I. J., S. Mezan, A. Mizrahi, P. Ohana, R. Abu-Lail, Y. Fellig, N. Degroot, E. Galun, and A. Hochberg. 2010. The oncofetal H19 RNA connection: hypoxia, p53 and cancer. *Biochimica et biophysica acta* 1803: 443-451.
 122. Lee, D. F., J. Su, H. S. Kim, B. Chang, D. Papatsenko, R. Zhao, Y. Yuan, J. Gingold, W. Xia, H. Darr, R. Mirzayans, M. C. Hung, C. Schaniel, and I. R. Lemischka. 2015. Modeling familial cancer with induced pluripotent stem cells. *Cell* 161: 240-254.
 123. Stambolsky, P., Y. Tabach, G. Fontemaggi, L. Weisz, R. Maor-Aloni, Z. Siegfried, I. Shiff, I. Kogan, M. Shay, E. Kalo, G. Blandino, I. Simon, M. Oren, and V. Rotter. 2010. Modulation of the vitamin D3 response by cancer-associated mutant p53. *Cancer cell* 17: 273-285.
 124. Do, P. M., L. Varanasi, S. Fan, C. Li, I. Kubacka, V. Newman, K. Chauhan, S. R. Daniels, M. Bocchetta, M. R. Garrett, R. Li, and L. A. Martinez. 2012. Mutant p53 cooperates with ETS2 to promote etoposide resistance. *Genes & development* 26: 830-845.

125. Polotskaia, A., G. Xiao, K. Reynoso, C. Martin, W. G. Qiu, R. C. Hendrickson, and J. Bargonetti. 2015. Proteome-wide analysis of mutant p53 targets in breast cancer identifies new levels of gain-of-function that influence PARP, PCNA, and MCM4. *Proc Natl Acad Sci U S A* 112: E1220-1229.
126. Zhu, J., M. A. Sammons, G. Donahue, Z. Dou, M. Vedadi, M. Getlik, D. Barsyte-Lovejoy, R. Al-awar, B. W. Katona, A. Shilatifard, J. Huang, X. Hua, C. H. Arrowsmith, and S. L. Berger. 2015. Gain-of-function p53 mutants co-opt chromatin pathways to drive cancer growth. *Nature* 525: 206-211.
127. Strano, S., G. Fontemaggi, A. Costanzo, M. G. Rizzo, O. Monti, A. Baccarini, G. Del Sal, M. Levrero, A. Sacchi, M. Oren, and G. Blandino. 2002. Physical interaction with human tumor-derived p53 mutants inhibits p63 activities. *The Journal of biological chemistry* 277: 18817-18826.
128. Li, Y., and C. Prives. 2007. Are interactions with p63 and p73 involved in mutant p53 gain of oncogenic function? *Oncogene* 26: 2220-2225.
129. Weissmueller, S., E. Manchado, M. Saborowski, J. P. t. Morris, E. Wagenblast, C. A. Davis, S. H. Moon, N. T. Pfister, D. F. Tschaharganeh, T. Kitzing, D. Aust, E. K. Markert, J. Wu, S. M. Grimmond, C. Pilarsky, C. Prives, A. V. Biankin, and S. W. Lowe. 2014. Mutant p53 drives pancreatic cancer metastasis through cell-autonomous PDGF receptor beta signaling. *Cell* 157: 382-394.
130. Donehower, L. A., M. Harvey, B. L. Slagle, M. J. McArthur, C. A. Montgomery, Jr., J. S. Butel, and A. Bradley. 1992. Mice deficient for p53

- are developmentally normal but susceptible to spontaneous tumours. *Nature* 356: 215-221.
131. Jacks, T., L. Remington, B. O. Williams, E. M. Schmitt, S. Halachmi, R. T. Bronson, and R. A. Weinberg. 1994. Tumor spectrum analysis in p53-mutant mice. *Current biology : CB* 4: 1-7.
 132. Purdie, C. A., D. J. Harrison, A. Peter, L. Dobbie, S. White, S. E. Howie, D. M. Salter, C. C. Bird, A. H. Wyllie, M. L. Hooper, and et al. 1994. Tumour incidence, spectrum and ploidy in mice with a large deletion in the p53 gene. *Oncogene* 9: 603-609.
 133. Donehower, L. A. 1996. The p53-deficient mouse: a model for basic and applied cancer studies. *Seminars in cancer biology* 7: 269-278.
 134. Harvey, M., M. J. McArthur, C. A. Montgomery, Jr., J. S. Butel, A. Bradley, and L. A. Donehower. 1993. Spontaneous and carcinogen-induced tumorigenesis in p53-deficient mice. *Nature genetics* 5: 225-229.
 135. Liu, G., T. J. McDonnell, R. Montes de Oca Luna, M. Kapoor, B. Mims, A. K. El-Naggar, and G. Lozano. 2000. High metastatic potential in mice inheriting a targeted p53 missense mutation. *Proc Natl Acad Sci U S A* 97: 4174-4179.
 136. Lang, G. A., T. Iwakuma, Y. A. Suh, G. Liu, V. A. Rao, J. M. Parant, Y. A. Valentin-Vega, T. Terzian, L. C. Caldwell, L. C. Strong, A. K. El-Naggar, and G. Lozano. 2004. Gain of function of a p53 hot spot mutation in a mouse model of Li-Fraumeni syndrome. *Cell* 119: 861-872.

137. Olive, K. P., D. A. Tuveson, Z. C. Ruhe, B. Yin, N. A. Willis, R. T. Bronson, D. Crowley, and T. Jacks. 2004. Mutant p53 gain of function in two mouse models of Li-Fraumeni syndrome. *Cell* 119: 847-860.
138. Luo, J. L., Q. Yang, W. M. Tong, M. Hergenhahn, Z. Q. Wang, and M. Hollstein. 2001. Knock-in mice with a chimeric human/murine p53 gene develop normally and show wild-type p53 responses to DNA damaging agents: a new biomedical research tool. *Oncogene* 20: 320-328.
139. Liu, D. P., H. Song, and Y. Xu. 2010. A common gain of function of p53 cancer mutants in inducing genetic instability. *Oncogene* 29: 949-956.
140. Hanel, W., N. Marchenko, S. Xu, S. X. Yu, W. Weng, and U. Moll. 2013. Two hot spot mutant p53 mouse models display differential gain of function in tumorigenesis. *Cell death and differentiation* 20: 898-909.
141. Parant, J. M., S. A. George, J. A. Holden, and H. J. Yost. 2010. Genetic modeling of Li-Fraumeni syndrome in zebrafish. *Disease models & mechanisms* 3: 45-56.
142. Bischoff, F. Z., S. O. Yim, S. Pathak, G. Grant, M. J. Siciliano, B. C. Giovanella, L. C. Strong, and M. A. Tainsky. 1990. Spontaneous abnormalities in normal fibroblasts from patients with Li-Fraumeni cancer syndrome: aneuploidy and immortalization. *Cancer research* 50: 7979-7984.
143. Bischoff, F. Z., L. C. Strong, S. O. Yim, D. R. Pratt, M. J. Siciliano, B. C. Giovanella, and M. A. Tainsky. 1991. Tumorigenic transformation of spontaneously immortalized fibroblasts from patients with a familial cancer syndrome. *Oncogene* 6: 183-186.

144. Yin, Y., M. A. Tainsky, F. Z. Bischoff, L. C. Strong, and G. M. Wahl. 1992. Wild-type p53 restores cell cycle control and inhibits gene amplification in cells with mutant p53 alleles. *Cell* 70: 937-948.
145. Rogan, E. M., T. M. Bryan, B. Hukku, K. Maclean, A. C. Chang, E. L. Moy, A. Englezou, S. G. Warneford, L. Dalla-Pozza, and R. R. Reddel. 1995. Alterations in p53 and p16INK4 expression and telomere length during spontaneous immortalization of Li-Fraumeni syndrome fibroblasts. *Molecular and cellular biology* 15: 4745-4753.
146. Gollahon, L. S., E. Kraus, T. A. Wu, S. O. Yim, L. C. Strong, J. W. Shay, and M. A. Tainsky. 1998. Telomerase activity during spontaneous immortalization of Li-Fraumeni syndrome skin fibroblasts. *Oncogene* 17: 709-717.
147. Dameron, K. M., O. V. Volpert, M. A. Tainsky, and N. Bouck. 1994. Control of angiogenesis in fibroblasts by p53 regulation of thrombospondin-1. *Science* 265: 1582-1584.
148. Volpert, O. V., K. M. Dameron, and N. Bouck. 1997. Sequential development of an angiogenic phenotype by human fibroblasts progressing to tumorigenicity. *Oncogene* 14: 1495-1502.
149. Shay, J. W., G. Tomlinson, M. A. Piatyszek, and L. S. Gollahon. 1995. Spontaneous in vitro immortalization of breast epithelial cells from a patient with Li-Fraumeni syndrome. *Molecular and cellular biology* 15: 425-432.

150. Takahashi, K., K. Tanabe, M. Ohnuki, M. Narita, T. Ichisaka, K. Tomoda, and S. Yamanaka. 2007. Induction of pluripotent stem cells from adult human fibroblasts by defined factors. *Cell* 131: 861-872.
151. Yu, J., M. A. Vodyanik, K. Smuga-Otto, J. Antosiewicz-Bourget, J. L. Frane, S. Tian, J. Nie, G. A. Jonsdottir, V. Ruotti, R. Stewart, Slukvin, II, and J. A. Thomson. 2007. Induced pluripotent stem cell lines derived from human somatic cells. *Science* 318: 1917-1920.
152. Thomson, J. A., J. Itskovitz-Eldor, S. S. Shapiro, M. A. Waknitz, J. J. Swiergiel, V. S. Marshall, and J. M. Jones. 1998. Embryonic stem cell lines derived from human blastocysts. *Science* 282: 1145-1147.
153. Takahashi, K., and S. Yamanaka. 2006. Induction of pluripotent stem cells from mouse embryonic and adult fibroblast cultures by defined factors. *Cell* 126: 663-676.
154. Gonzalez, F., S. Boue, and J. C. Izpisua Belmonte. 2011. Methods for making induced pluripotent stem cells: reprogramming a la carte. *Nature reviews. Genetics* 12: 231-242.
155. Murry, C. E., and G. Keller. 2008. Differentiation of embryonic stem cells to clinically relevant populations: lessons from embryonic development. *Cell* 132: 661-680.
156. Lancaster, M. A., and J. A. Knoblich. 2014. Organogenesis in a dish: modeling development and disease using organoid technologies. *Science* 345: 1247125.

157. Yin, X., B. E. Mead, H. Safaee, R. Langer, J. M. Karp, and O. Levy. 2016. Engineering Stem Cell Organoids. *Cell Stem Cell* 18: 25-38.
158. Grskovic, M., A. Javaherian, B. Strulovici, and G. Q. Daley. 2011. Induced pluripotent stem cells--opportunities for disease modelling and drug discovery. *Nature reviews. Drug discovery* 10: 915-929.
159. Dimos, J. T., K. T. Rodolfa, K. K. Niakan, L. M. Weisenthal, H. Mitsumoto, W. Chung, G. F. Croft, G. Saphier, R. Leibel, R. Goland, H. Wichterle, C. E. Henderson, and K. Eggan. 2008. Induced pluripotent stem cells generated from patients with ALS can be differentiated into motor neurons. *Science* 321: 1218-1221.
160. Park, I. H., N. Arora, H. Huo, N. Maherali, T. Ahfeldt, A. Shimamura, M. W. Lensch, C. Cowan, K. Hochedlinger, and G. Q. Daley. 2008. Disease-specific induced pluripotent stem cells. *Cell* 134: 877-886.
161. Yagi, T., D. Ito, Y. Okada, W. Akamatsu, Y. Nihei, T. Yoshizaki, S. Yamanaka, H. Okano, and N. Suzuki. 2011. Modeling familial Alzheimer's disease with induced pluripotent stem cells. *Human molecular genetics* 20: 4530-4539.
162. Brennand, K. J., A. Simone, J. Jou, C. Gelboin-Burkhart, N. Tran, S. Sangar, Y. Li, Y. Mu, G. Chen, D. Yu, S. McCarthy, J. Sebat, and F. H. Gage. 2011. Modelling schizophrenia using human induced pluripotent stem cells. *Nature* 473: 221-225.
163. Carvajal-Vergara, X., A. Sevilla, S. L. D'Souza, Y. S. Ang, C. Schaniel, D. F. Lee, L. Yang, A. D. Kaplan, E. D. Adler, R. Rozov, Y. Ge, N. Cohen, L. J.

- Edelmann, B. Chang, A. Waghray, J. Su, S. Pardo, K. D. Lichtenbelt, M. Tartaglia, B. D. Gelb, and I. R. Lemischka. 2010. Patient-specific induced pluripotent stem-cell-derived models of LEOPARD syndrome. *Nature* 465: 808-812.
164. Pasca, S. P., T. Portmann, I. Voineagu, M. Yazawa, A. Shcheglovitov, A. M. Pasca, B. Cord, T. D. Palmer, S. Chikahisa, S. Nishino, J. A. Bernstein, J. Hallmayer, D. H. Geschwind, and R. E. Dolmetsch. 2011. Using iPSC-derived neurons to uncover cellular phenotypes associated with Timothy syndrome. *Nat Med* 17: 1657-1662.
165. Itzhaki, I., L. Maizels, I. Huber, L. Zwi-Dantsis, O. Caspi, A. Winterstern, O. Feldman, A. Gepstein, G. Arbel, H. Hammerman, M. Boulos, and L. Gepstein. 2011. Modelling the long QT syndrome with induced pluripotent stem cells. *Nature* 471: 225-229.
166. Moretti, A., M. Bellin, A. Welling, C. B. Jung, J. T. Lam, L. Bott-Flugel, T. Dorn, A. Goedel, C. Hohnke, F. Hofmann, M. Seyfarth, D. Sinnecker, A. Schomig, and K. L. Laugwitz. 2010. Patient-specific induced pluripotent stem-cell models for long-QT syndrome. *The New England journal of medicine* 363: 1397-1409.
167. Rashid, S. T., S. Corbineau, N. Hannan, S. J. Marciniak, E. Miranda, G. Alexander, I. Huang-Doran, J. Griffin, L. Ahrlund-Richter, J. Skepper, R. Semple, A. Weber, D. A. Lomas, and L. Vallier. 2010. Modeling inherited metabolic disorders of the liver using human induced pluripotent stem cells. *The Journal of clinical investigation* 120: 3127-3136.

168. Mulero-Navarro, S., A. Sevilla, A. C. Roman, D. F. Lee, S. L. D'Souza, S. Pardo, I. Riess, J. Su, N. Cohen, C. Schaniel, N. A. Rodriguez, A. Baccharini, B. D. Brown, H. Cave, A. Caye, M. Strullu, S. Yalcin, C. Y. Park, P. S. Dhandapany, G. Yongchao, L. Edelmann, S. Bahieg, P. Raynal, E. Flex, M. Tartaglia, K. A. Moore, I. R. Lemischka, and B. D. Gelb. 2015. Myeloid Dysregulation in a Human Induced Pluripotent Stem Cell Model of PTPN11-Associated Juvenile Myelomonocytic Leukemia. *Cell Rep* 13: 504-515.
169. Kotini, A. G., C. J. Chang, I. Boussaad, J. J. Delrow, E. K. Dolezal, A. B. Nagulapally, F. Perna, G. A. Fishbein, V. M. Klimek, R. D. Hawkins, D. Huangfu, C. E. Murry, T. Graubert, S. D. Nimer, and E. P. Papapetrou. 2015. Functional analysis of a chromosomal deletion associated with myelodysplastic syndromes using isogenic human induced pluripotent stem cells. *Nat Biotechnol* 33: 646-655.
170. Funato, K., T. Major, P. W. Lewis, C. D. Allis, and V. Tabar. 2014. Use of human embryonic stem cells to model pediatric gliomas with H3.3K27M histone mutation. *Science* 346: 1529-1533.
171. Duan, S., G. Yuan, X. Liu, R. Ren, J. Li, W. Zhang, J. Wu, X. Xu, L. Fu, Y. Li, J. Yang, W. Zhang, R. Bai, F. Yi, K. Suzuki, H. Gao, C. R. Esteban, C. Zhang, J. C. Izpisua Belmonte, Z. Chen, X. Wang, T. Jiang, J. Qu, F. Tang, and G. H. Liu. 2015. PTEN deficiency reprogrammes human neural stem cells towards a glioblastoma stem cell-like phenotype. *Nature communications* 6: 10068.

172. Roberts, A. E., J. E. Allanson, M. Tartaglia, and B. D. Gelb. 2013. Noonan syndrome. *Lancet* 381: 333-342.
173. Lindsley, R. C., and B. L. Ebert. 2013. Molecular pathophysiology of myelodysplastic syndromes. *Annu Rev Pathol* 8: 21-47.
174. Wu, G., A. Broniscer, T. A. McEachron, C. Lu, B. S. Paugh, J. Becksfort, C. Qu, L. Ding, R. Huether, M. Parker, J. Zhang, A. Gajjar, M. A. Dyer, C. G. Mullighan, R. J. Gilbertson, E. R. Mardis, R. K. Wilson, J. R. Downing, D. W. Ellison, J. Zhang, S. J. Baker, and P. St. Jude Children's Research Hospital-Washington University Pediatric Cancer Genome. 2012. Somatic histone H3 alterations in pediatric diffuse intrinsic pontine gliomas and non-brainstem glioblastomas. *Nature genetics* 44: 251-253.
175. Schwartzenuber, J., A. Korshunov, X. Y. Liu, D. T. Jones, E. Pfaff, K. Jacob, D. Sturm, A. M. Fontebasso, D. A. Quang, M. Tonjes, V. Hovestadt, S. Albrecht, M. Kool, A. Nantel, C. Konermann, A. Lindroth, N. Jager, T. Rausch, M. Ryzhova, J. O. Korbel, T. Hielscher, P. Hauser, M. Garami, A. Klekner, L. Bogner, M. Ebinger, M. U. Schuhmann, W. Scheurlen, A. Pekrun, M. C. Fruhwald, W. Roggendorf, C. Kramm, M. Durken, J. Atkinson, P. Lepage, A. Montpetit, M. Zakrzewska, K. Zakrzewski, P. P. Liberski, Z. Dong, P. Siegel, A. E. Kulozik, M. Zapatka, A. Guha, D. Malkin, J. Felsberg, G. Reifenberger, A. von Deimling, K. Ichimura, V. P. Collins, H. Witt, T. Milde, O. Witt, C. Zhang, P. Castelo-Branco, P. Lichter, D. Faury, U. Tabori, C. Plass, J. Majewski, S. M. Pfister, and N. Jabado. 2012. Driver mutations

- in histone H3.3 and chromatin remodelling genes in paediatric glioblastoma. *Nature* 482: 226-231.
176. Furnari, F. B., T. Fenton, R. M. Bachoo, A. Mukasa, J. M. Stommel, A. Stegh, W. C. Hahn, K. L. Ligon, D. N. Louis, C. Brennan, L. Chin, R. A. DePinho, and W. K. Cavenee. 2007. Malignant astrocytic glioma: genetics, biology, and paths to treatment. *Genes & development* 21: 2683-2710.
 177. Chin, L., J. N. Andersen, and P. A. Futreal. 2011. Cancer genomics: from discovery science to personalized medicine. *Nat Med* 17: 297-303.
 178. Zou, J., M. L. Maeder, P. Mali, S. M. Pruetz-Miller, S. Thibodeau-Beganny, B. K. Chou, G. Chen, Z. Ye, I. H. Park, G. Q. Daley, M. H. Porteus, J. K. Joung, and L. Cheng. 2009. Gene targeting of a disease-related gene in human induced pluripotent stem and embryonic stem cells. *Cell Stem Cell* 5: 97-110.
 179. Hockemeyer, D., F. Soldner, C. Beard, Q. Gao, M. Mitalipova, R. C. DeKolver, G. E. Katibah, R. Amora, E. A. Boydston, B. Zeitler, X. Meng, J. C. Miller, L. Zhang, E. J. Rebar, P. D. Gregory, F. D. Urnov, and R. Jaenisch. 2009. Efficient targeting of expressed and silent genes in human ESCs and iPSCs using zinc-finger nucleases. *Nat Biotechnol* 27: 851-857.
 180. Hockemeyer, D., and R. Jaenisch. 2016. Induced Pluripotent Stem Cells Meet Genome Editing. *Cell Stem Cell* 18: 573-586.
 181. Wang, Y., P. Liang, F. Lan, H. Wu, L. Lisowski, M. Gu, S. Hu, M. A. Kay, F. D. Urnov, R. Shinnawi, J. D. Gold, L. Gepstein, and J. C. Wu. 2014. Genome editing of isogenic human induced pluripotent stem cells

- recapitulates long QT phenotype for drug testing. *Journal of the American College of Cardiology* 64: 451-459.
182. Freedman, B. S., C. R. Brooks, A. Q. Lam, H. Fu, R. Morizane, V. Agrawal, A. F. Saad, M. K. Li, M. R. Hughes, R. V. Werff, D. T. Peters, J. Lu, A. Baccei, A. M. Siedlecki, M. T. Valerius, K. Musunuru, K. M. McNagny, T. I. Steinman, J. Zhou, P. H. Lerou, and J. V. Bonventre. 2015. Modelling kidney disease with CRISPR-mutant kidney organoids derived from human pluripotent epiblast spheroids. *Nature communications* 6: 8715.
 183. Sander, J. D., L. Cade, C. Khayter, D. Reyon, R. T. Peterson, J. K. Joung, and J. R. Yeh. 2011. Targeted gene disruption in somatic zebrafish cells using engineered TALENs. *Nat Biotechnol* 29: 697-698.
 184. Wang, K., M. Li, and H. Hakonarson. 2010. ANNOVAR: functional annotation of genetic variants from high-throughput sequencing data. *Nucleic Acids Res* 38: e164.
 185. Tan, C. M., E. Y. Chen, R. Dannenfelser, N. R. Clark, and A. Ma'ayan. 2013. Network2Canvas: network visualization on a canvas with enrichment analysis. *Bioinformatics* 29: 1872-1878.
 186. Diaz-Gay, M., M. Vila-Casadesus, S. Franch-Exposito, E. Hernandez-Illan, J. J. Lozano, and S. Castellvi-Bel. 2018. Mutational Signatures in Cancer (MuSiCa): a web application to implement mutational signatures analysis in cancer samples. *BMC Bioinformatics* 19: 224.
 187. Zhou, R., A. Xu, J. Gingold, L. C. Strong, R. Zhao, and D. F. Lee. 2017. Li-Fraumeni Syndrome Disease Model: A Platform to Develop Precision

- Cancer Therapy Targeting Oncogenic p53. *Trends Pharmacol Sci* 38: 908-927.
188. Gingold, J., R. Zhou, I. R. Lemischka, and D. F. Lee. 2016. Modeling Cancer with Pluripotent Stem Cells. *Trends Cancer* 2: 485-494.
189. Burridge, P. W., Y. F. Li, E. Matsa, H. Wu, S. G. Ong, A. Sharma, A. Holmstrom, A. C. Chang, M. J. Coronado, A. D. Ebert, J. W. Knowles, M. L. Telli, R. M. Witteles, H. M. Blau, D. Bernstein, R. B. Altman, and J. C. Wu. 2016. Human induced pluripotent stem cell-derived cardiomyocytes recapitulate the predilection of breast cancer patients to doxorubicin-induced cardiotoxicity. *Nat Med* 22: 547-556.
190. Mulero-Navarro, S., A. Sevilla, A. C. Roman, D. F. Lee, S. L. D'Souza, S. Pardo, I. Riess, J. Su, N. Cohen, C. Schaniel, N. A. Rodriguez, A. Baccharini, B. D. Brown, H. Cave, A. Caye, M. Strullu, S. Yalcin, C. Y. Park, P. S. Dhandapany, G. Yongchao, L. Edelmann, S. Bahieg, P. Raynal, E. Flex, M. Tartaglia, K. A. Moore, I. R. Lemischka, and B. D. Gelb. 2015. Myeloid Dysregulation in a Human Induced Pluripotent Stem Cell Model of PTPN11-Associated Juvenile Myelomonocytic Leukemia. *Cell Rep* 13: 504-515.
191. Zhou, R., A. Xu, J. Tu, M. Liu, J. A. Gingold, R. Zhao, and D. F. Lee. 2018. Modeling Osteosarcoma Using Li-Fraumeni Syndrome Patient-derived Induced Pluripotent Stem Cells. *J Vis Exp*.
192. Lian, Q., E. Lye, K. Suan Yeo, E. Khia Way Tan, M. Salto-Tellez, T. M. Liu, N. Palanisamy, R. M. El Oakley, E. H. Lee, B. Lim, and S. K. Lim. 2007.

- Derivation of clinically compliant MSCs from CD105+, CD24- differentiated human ESCs. *Stem Cells* 25: 425-436.
193. Kim, H., S. Yoo, R. Zhou, A. Xu, J. M. Bernitz, Y. Yuan, A. M. Gomes, M. G. Daniel, J. Su, E. G. Demicco, J. Zhu, K. A. Moore, D. F. Lee, I. R. Lemischka, and C. Schaniel. 2018. Oncogenic role of SFRP2 in p53-mutant osteosarcoma development via autocrine and paracrine mechanism. *Proc Natl Acad Sci U S A* 115: E11128-E11137.
194. Ribatti, D. 2016. The chick embryo chorioallantoic membrane (CAM). A multifaceted experimental model. *Mech Dev* 141: 70-77.
195. Fontenot, E., E. Rossi, R. Mumper, S. Snyder, S. Siamakpour-Reihani, P. Ma, E. Hilliard, B. Bone, D. Ketelsen, C. Santos, C. Patterson, and N. Klauber-DeMore. 2013. A novel monoclonal antibody to secreted frizzled-related protein 2 inhibits tumor growth. *Mol Cancer Ther* 12: 685-695.
196. Sys, G., M. Van Bockstal, R. Forsyth, M. Balke, B. Poffyn, D. Uyttendaele, M. Bracke, and O. De Wever. 2012. Tumor grafts derived from sarcoma patients retain tumor morphology, viability, and invasion potential and indicate disease outcomes in the chick chorioallantoic membrane model. *Cancer letters* 326: 69-78.
197. Zhang, D., Z. H. Pan, M. Awobuluyi, and S. A. Lipton. 2001. Structure and function of GABA(C) receptors: a comparison of native versus recombinant receptors. *Trends Pharmacol Sci* 22: 121-132.
198. Alexandrov, L. B., S. Nik-Zainal, D. C. Wedge, S. A. Aparicio, S. Behjati, A. V. Biankin, G. R. Bignell, N. Bolli, A. Borg, A. L. Borresen-Dale, S. Boyault,

- B. Burkhardt, A. P. Butler, C. Caldas, H. R. Davies, C. Desmedt, R. Eils, J. E. Eyfjord, J. A. Foekens, M. Greaves, F. Hosoda, B. Hutter, T. Ilcic, S. Imbeaud, M. Imielinski, N. Jager, D. T. Jones, D. Jones, S. Knappskog, M. Kool, S. R. Lakhani, C. Lopez-Otin, S. Martin, N. C. Munshi, H. Nakamura, P. A. Northcott, M. Pajic, E. Papaemmanuil, A. Paradiso, J. V. Pearson, X. S. Puente, K. Raine, M. Ramakrishna, A. L. Richardson, J. Richter, P. Rosenstiel, M. Schlesner, T. N. Schumacher, P. N. Span, J. W. Teague, Y. Totoki, A. N. Tutt, R. Valdes-Mas, M. M. van Buuren, L. van 't Veer, A. Vincent-Salomon, N. Waddell, L. R. Yates, I. Australian Pancreatic Cancer Genome, I. B. C. Consortium, I. M.-S. Consortium, I. PedBrain, J. Zucman-Rossi, P. A. Futreal, U. McDermott, P. Lichter, M. Meyerson, S. M. Grimmond, R. Siebert, E. Campo, T. Shibata, S. M. Pfister, P. J. Campbell, and M. R. Stratton. 2013. Signatures of mutational processes in human cancer. *Nature* 500: 415-421.
199. Moriarity, B. S., G. M. Otto, E. P. Rahrman, S. K. Rathe, N. K. Wolf, M. T. Weg, L. A. Manlove, R. S. LaRue, N. A. Temiz, S. D. Molyneux, K. Choi, K. J. Holly, A. L. Sarver, M. C. Scott, C. L. Forster, J. F. Modiano, C. Khanna, S. M. Hewitt, R. Khokha, Y. Yang, R. Gorlick, M. A. Dyer, and D. A. Largaespada. 2015. A Sleeping Beauty forward genetic screen identifies new genes and pathways driving osteosarcoma development and metastasis. *Nature genetics* 47: 615-624.
200. Cerami, E., J. Gao, U. Dogrusoz, B. E. Gross, S. O. Sumer, B. A. Aksoy, A. Jacobsen, C. J. Byrne, M. L. Heuer, E. Larsson, Y. Antipin, B. Reva, A. P.

- Goldberg, C. Sander, and N. Schultz. 2012. The cBio cancer genomics portal: an open platform for exploring multidimensional cancer genomics data. *Cancer Discov* 2: 401-404.
201. Tang, Z., C. Li, B. Kang, G. Gao, C. Li, and Z. Zhang. 2017. GEPIA: a web server for cancer and normal gene expression profiling and interactive analyses. *Nucleic Acids Res* 45: W98-W102.
202. Marsit, C. J., M. R. Karagas, A. Andrew, M. Liu, H. Danaee, A. R. Schned, H. H. Nelson, and K. T. Kelsey. 2005. Epigenetic inactivation of SFRP genes and TP53 alteration act jointly as markers of invasive bladder cancer. *Cancer research* 65: 7081-7085.
203. Xiao, Q., Y. Yang, X. Zhang, and Q. An. 2016. Enhanced Wnt signaling by methylation-mediated loss of SFRP2 promotes osteosarcoma cell invasion. *Tumour Biol* 37: 6315-6321.
204. Perry, J. A., A. Kiezun, P. Tonzi, E. M. Van Allen, S. L. Carter, S. C. Baca, G. S. Cowley, A. S. Bhatt, E. Rheinbay, C. S. Peadarallu, E. Helman, A. Taylor-Weiner, A. McKenna, D. S. DeLuca, M. S. Lawrence, L. Ambrogio, C. Sougnez, A. Sivachenko, L. D. Walensky, N. Wagle, J. Mora, C. de Torres, C. Lavarino, S. Dos Santos Aguiar, J. A. Yunes, S. R. Brandalise, G. E. Mercado-Celis, J. Melendez-Zajgla, R. Cardenas-Cardos, L. Velasco-Hidalgo, C. W. Roberts, L. A. Garraway, C. Rodriguez-Galindo, S. B. Gabriel, E. S. Lander, T. R. Golub, S. H. Orkin, G. Getz, and K. A. Janeway. 2014. Complementary genomic approaches highlight the PI3K/mTOR

- pathway as a common vulnerability in osteosarcoma. *Proc Natl Acad Sci U S A* 111: E5564-5573.
205. Nik-Zainal, S., L. B. Alexandrov, D. C. Wedge, P. Van Loo, C. D. Greenman, K. Raine, D. Jones, J. Hinton, J. Marshall, L. A. Stebbings, A. Menzies, S. Martin, K. Leung, L. Chen, C. Leroy, M. Ramakrishna, R. Rance, K. W. Lau, L. J. Mudie, I. Varela, D. J. McBride, G. R. Bignell, S. L. Cooke, A. Shlien, J. Gamble, I. Whitmore, M. Maddison, P. S. Tarpey, H. R. Davies, E. Papaemmanuil, P. J. Stephens, S. McLaren, A. P. Butler, J. W. Teague, G. Jonsson, J. E. Garber, D. Silver, P. Miron, A. Fatima, S. Boyault, A. Langerod, A. Tutt, J. W. Martens, S. A. Aparicio, A. Borg, A. V. Salomon, G. Thomas, A. L. Borresen-Dale, A. L. Richardson, M. S. Neuberger, P. A. Futreal, P. J. Campbell, M. R. Stratton, and C. Breast Cancer Working Group of the International Cancer Genome. 2012. Mutational processes molding the genomes of 21 breast cancers. *Cell* 149: 979-993.
206. Chen, X., A. Bahrami, A. Pappo, J. Easton, J. Dalton, E. Hedlund, D. Ellison, S. Shurtleff, G. Wu, L. Wei, M. Parker, M. Rusch, P. Nagahawatte, J. Wu, S. Mao, K. Boggs, H. Mulder, D. Yergeau, C. Lu, L. Ding, M. Edmonson, C. Qu, J. Wang, Y. Li, F. Navid, N. C. Daw, E. R. Mardis, R. K. Wilson, J. R. Downing, J. Zhang, M. A. Dyer, and P. St. Jude Children's Research Hospital-Washington University Pediatric Cancer Genome. 2014. Recurrent somatic structural variations contribute to tumorigenesis in pediatric osteosarcoma. *Cell Rep* 7: 104-112.

207. Hwang, S. J., G. Lozano, C. I. Amos, and L. C. Strong. 2003. Germline p53 mutations in a cohort with childhood sarcoma: sex differences in cancer risk. *American journal of human genetics* 72: 975-983.
208. Lammens, C. R., E. M. Bleiker, N. K. Aaronson, A. Wagner, R. H. Sijmons, M. G. Ausems, A. H. Vriends, M. W. Ruijs, T. A. van Os, L. Spruijt, E. B. Gomez Garcia, A. Cats, T. Nagtegaal, and S. Verhoef. 2010. Regular surveillance for Li-Fraumeni Syndrome: advice, adherence and perceived benefits. *Fam Cancer* 9: 647-654.
209. Masciari, S., D. A. Dillon, M. Rath, M. Robson, J. N. Weitzel, J. Balmana, S. B. Gruber, J. M. Ford, D. Euhus, A. Lebensohn, M. Telli, S. M. Pochebit, G. Lypas, and J. E. Garber. 2012. Breast cancer phenotype in women with TP53 germline mutations: a Li-Fraumeni syndrome consortium effort. *Breast Cancer Res Treat* 133: 1125-1130.
210. Olivier, M., D. E. Goldgar, N. Sodha, H. Ohgaki, P. Kleihues, P. Hainaut, and R. A. Eeles. 2003. Li-Fraumeni and related syndromes: correlation between tumor type, family structure, and TP53 genotype. *Cancer research* 63: 6643-6650.
211. Melhem-Bertrandt, A., J. Bojadzieva, K. J. Ready, E. Obeid, D. D. Liu, A. M. Gutierrez-Barrera, J. K. Litton, O. I. Olopade, G. N. Hortobagyi, L. C. Strong, and B. K. Arun. 2012. Early onset HER2-positive breast cancer is associated with germline TP53 mutations. *Cancer* 118: 908-913.
212. Wilson, J. R., A. C. Bateman, H. Hanson, Q. An, G. Evans, N. Rahman, J. L. Jones, and D. M. Eccles. 2010. A novel HER2-positive breast cancer

- phenotype arising from germline TP53 mutations. *Journal of medical genetics* 47: 771-774.
213. Javed, A., and A. Lteif. 2013. Development of the human breast. *Semin Plast Surg* 27: 5-12.
214. Polyak, K., and R. Kalluri. 2010. The role of the microenvironment in mammary gland development and cancer. *Cold Spring Harbor perspectives in biology* 2: a003244.
215. Visvader, J. E. 2009. Keeping abreast of the mammary epithelial hierarchy and breast tumorigenesis. *Genes & development* 23: 2563-2577.
216. Daniel, C. W., K. B. De Ome, J. T. Young, P. B. Blair, and L. J. Faulkin, Jr. 1968. The in vivo life span of normal and preneoplastic mouse mammary glands: a serial transplantation study. *Proc Natl Acad Sci U S A* 61: 53-60.
217. Hoshino, K., and W. U. Gardner. 1967. Transplantability and life span of mammary gland during serial transplantation in mice. *Nature* 213: 193-194.
218. Kordon, E. C., and G. H. Smith. 1998. An entire functional mammary gland may comprise the progeny from a single cell. *Development* 125: 1921-1930.
219. Davis, F. M., B. Lloyd-Lewis, O. B. Harris, S. Kozar, D. J. Winton, L. Muresan, and C. J. Watson. 2016. Single-cell lineage tracing in the mammary gland reveals stochastic clonal dispersion of stem/progenitor cell progeny. *Nature communications* 7: 13053.
220. Scheele, C. L., E. Hannezo, M. J. Muraro, A. Zomer, N. S. Langedijk, A. van Oudenaarden, B. D. Simons, and J. van Rheenen. 2017. Identity and

- dynamics of mammary stem cells during branching morphogenesis. *Nature* 542: 313-317.
221. Koren, S., L. Reavie, J. P. Couto, D. De Silva, M. B. Stadler, T. Roloff, A. Britschgi, T. Eichlisberger, H. Kohler, O. Aina, R. D. Cardiff, and M. Bentires-Alj. 2015. PIK3CA(H1047R) induces multipotency and multi-lineage mammary tumours. *Nature* 525: 114-118.
222. Li, Y., B. Welm, K. Podsypanina, S. Huang, M. Chamorro, X. Zhang, T. Rowlands, M. Egeblad, P. Cowin, Z. Werb, L. K. Tan, J. M. Rosen, and H. E. Varmus. 2003. Evidence that transgenes encoding components of the Wnt signaling pathway preferentially induce mammary cancers from progenitor cells. *Proc Natl Acad Sci U S A* 100: 15853-15858.
223. Lim, E., D. Wu, B. Pal, T. Bouras, M. L. Asselin-Labat, F. Vaillant, H. Yagita, G. J. Lindeman, G. K. Smyth, and J. E. Visvader. 2010. Transcriptome analyses of mouse and human mammary cell subpopulations reveal multiple conserved genes and pathways. *Breast Cancer Res* 12: R21.
224. Van Keymeulen, A., M. Y. Lee, M. Ousset, S. Brohee, S. Rorive, R. R. Girardi, A. Wuidart, G. Bouvencourt, C. Dubois, I. Salmon, C. Sotiriou, W. A. Phillips, and C. Blanpain. 2015. Reactivation of multipotency by oncogenic PIK3CA induces breast tumour heterogeneity. *Nature* 525: 119-123.
225. Wend, P., J. D. Holland, U. Ziebold, and W. Birchmeier. 2010. Wnt signaling in stem and cancer stem cells. *Semin Cell Dev Biol* 21: 855-863.

226. Qu, Y., B. Han, B. Gao, S. Bose, Y. Gong, K. Wawrowsky, A. E. Giuliano, D. Sareen, and X. Cui. 2017. Differentiation of Human Induced Pluripotent Stem Cells to Mammary-like Organoids. *Stem Cell Reports* 8: 205-215.
227. Schwartz, P. H., D. J. Brick, A. E. Stover, J. F. Loring, and F. J. Muller. 2008. Differentiation of neural lineage cells from human pluripotent stem cells. *Methods* 45: 142-158.
228. Tchieu, J., B. Zimmer, F. Fattahi, S. Amin, N. Zeltner, S. Chen, and L. Studer. 2017. A Modular Platform for Differentiation of Human PSCs into All Major Ectodermal Lineages. *Cell Stem Cell* 21: 399-410 e397.
229. Shackleton, M., E. Quintana, E. R. Fearon, and S. J. Morrison. 2009. Heterogeneity in cancer: cancer stem cells versus clonal evolution. *Cell* 138: 822-829.
230. Shah, M., and C. Allegrucci. 2013. Stem cell plasticity in development and cancer: epigenetic origin of cancer stem cells. *Subcell Biochem* 61: 545-565.
231. Visvader, J. E. 2011. Cells of origin in cancer. *Nature* 469: 314-322.
232. Visvader, J. E., and G. J. Lindeman. 2008. Cancer stem cells in solid tumours: accumulating evidence and unresolved questions. *Nature reviews. Cancer* 8: 755-768.
233. Shah, M., and C. Allegrucci. 2012. Keeping an open mind: highlights and controversies of the breast cancer stem cell theory. *Breast Cancer (Dove Med Press)* 4: 155-166.

234. Van Keymeulen, A., A. S. Rocha, M. Ousset, B. Beck, G. Bouvencourt, J. Rock, N. Sharma, S. Dekoninck, and C. Blanpain. 2011. Distinct stem cells contribute to mammary gland development and maintenance. *Nature* 479: 189-193.
235. Raouf, A., Y. Sun, S. Chatterjee, and P. Basak. 2012. The biology of human breast epithelial progenitors. *Semin Cell Dev Biol* 23: 606-612.
236. Molyneux, G., F. C. Geyer, F. A. Magnay, A. McCarthy, H. Kendrick, R. Natrajan, A. Mackay, A. Grigoriadis, A. Tutt, A. Ashworth, J. S. Reis-Filho, and M. J. Smalley. 2010. BRCA1 basal-like breast cancers originate from luminal epithelial progenitors and not from basal stem cells. *Cell Stem Cell* 7: 403-417.
237. Lim, E., F. Vaillant, D. Wu, N. C. Forrest, B. Pal, A. H. Hart, M. L. Asselin-Labat, D. E. Gyorki, T. Ward, A. Partanen, F. Feleppa, L. I. Huschtscha, H. J. Thorne, kConFab, S. B. Fox, M. Yan, J. D. French, M. A. Brown, G. K. Smyth, J. E. Visvader, and G. J. Lindeman. 2009. Aberrant luminal progenitors as the candidate target population for basal tumor development in BRCA1 mutation carriers. *Nat Med* 15: 907-913.
238. Proia, T. A., P. J. Keller, P. B. Gupta, I. Klebba, A. D. Jones, M. Sedic, H. Gilmore, N. Tung, S. P. Naber, S. Schnitt, E. S. Lander, and C. Kuperwasser. 2011. Genetic predisposition directs breast cancer phenotype by dictating progenitor cell fate. *Cell Stem Cell* 8: 149-163.
239. Goldman, O., S. Han, M. Sourisseau, N. Dziejcz, W. Hamou, B. Corneo, S. D'Souza, T. Sato, D. N. Kotton, K. D. Bissig, T. Kalir, A. Jacobs, T. Evans,

- M. J. Evans, and V. Gouon-Evans. 2013. KDR identifies a conserved human and murine hepatic progenitor and instructs early liver development. *Cell Stem Cell* 12: 748-760.
240. Hannan, N. R., C. P. Segeritz, T. Touboul, and L. Vallier. 2013. Production of hepatocyte-like cells from human pluripotent stem cells. *Nature protocols* 8: 430-437.
241. Si-Tayeb, K., F. K. Noto, M. Nagaoka, J. Li, M. A. Battle, C. Duris, P. E. North, S. Dalton, and S. A. Duncan. 2010. Highly efficient generation of human hepatocyte-like cells from induced pluripotent stem cells. *Hepatology* 51: 297-305.
242. Spence, J. R., C. N. Mayhew, S. A. Rankin, M. F. Kuhar, J. E. Vallance, K. Tolle, E. E. Hoskins, V. V. Kalinichenko, S. I. Wells, A. M. Zorn, N. F. Shroyer, and J. M. Wells. 2011. Directed differentiation of human pluripotent stem cells into intestinal tissue in vitro. *Nature* 470: 105-109.
243. Yusa, K., S. T. Rashid, H. Strick-Marchand, I. Varela, P. Q. Liu, D. E. Paschon, E. Miranda, A. Ordonez, N. R. Hannan, F. J. Rouhani, S. Darche, G. Alexander, S. J. Marciniak, N. Fusaki, M. Hasegawa, M. C. Holmes, J. P. Di Santo, D. A. Lomas, A. Bradley, and L. Vallier. 2011. Targeted gene correction of alpha1-antitrypsin deficiency in induced pluripotent stem cells. *Nature* 478: 391-394.
244. Garcon, L., J. Ge, S. H. Manjunath, J. A. Mills, M. Apicella, S. Parikh, L. M. Sullivan, G. M. Podsakoff, P. Gadue, D. L. French, P. J. Mason, M. Bessler, and M. J. Weiss. 2013. Ribosomal and hematopoietic defects in induced

- pluripotent stem cells derived from Diamond Blackfan anemia patients. *Blood* 122: 912-921.
245. Ge, J., M. Apicella, J. A. Mills, L. Garcon, D. L. French, M. J. Weiss, M. Bessler, and P. J. Mason. 2015. Dysregulation of the Transforming Growth Factor beta Pathway in Induced Pluripotent Stem Cells Generated from Patients with Diamond Blackfan Anemia. *PloS one* 10: e0134878.
246. Doulatov, S., L. T. Vo, E. R. Macari, L. Wahlster, M. A. Kinney, A. M. Taylor, J. Barragan, M. Gupta, K. McGrath, H. Y. Lee, J. M. Humphries, A. DeVine, A. Narla, B. P. Alter, A. H. Beggs, S. Agarwal, B. L. Ebert, H. T. Gazda, H. F. Lodish, C. A. Sieff, T. M. Schlaeger, L. I. Zon, and G. Q. Daley. 2017. Drug discovery for Diamond-Blackfan anemia using reprogrammed hematopoietic progenitors. *Science translational medicine* 9.
247. Zhang, C. Z., G. G. Chen, J. L. Merchant, and P. B. Lai. 2012. Interaction between ZBP-89 and p53 mutants and its contribution to effects of HDACi on hepatocellular carcinoma. *Cell Cycle* 11: 322-334.
248. Neskey, D. M., A. A. Osman, T. J. Ow, P. Katsonis, T. McDonald, S. C. Hicks, T. K. Hsu, C. R. Pickering, A. Ward, A. Patel, J. S. Yordy, H. D. Skinner, U. Giri, D. Sano, M. D. Story, B. M. Beadle, A. K. El-Naggar, M. S. Kies, W. N. William, C. Caulin, M. Frederick, M. Kimmel, J. N. Myers, and O. Lichtarge. 2015. Evolutionary Action Score of TP53 Identifies High-Risk Mutations Associated with Decreased Survival and Increased Distant Metastases in Head and Neck Cancer. *Cancer research* 75: 1527-1536.

249. Tanaka, N., M. Zhao, L. Tang, A. A. Patel, Q. Xi, H. T. Van, H. Takahashi, A. A. Osman, J. Zhang, J. Wang, J. N. Myers, and G. Zhou. 2018. Gain-of-function mutant p53 promotes the oncogenic potential of head and neck squamous cell carcinoma cells by targeting the transcription factors FOXO3a and FOXM1. *Oncogene* 37: 1279-1292.
250. Kwiecinska, A., K. Ichimura, M. Berglund, A. Dinets, L. Sulaiman, V. P. Collins, C. Larsson, A. Porwit, and S. B. Lagercrantz. 2014. Amplification of 2p as a genomic marker for transformation in lymphoma. *Genes, chromosomes & cancer* 53: 750-768.
251. Lui, T. T., C. Lacroix, S. M. Ahmed, S. J. Goldenberg, C. A. Leach, A. M. Daulat, and S. Angers. 2011. The ubiquitin-specific protease USP34 regulates axin stability and Wnt/beta-catenin signaling. *Molecular and cellular biology* 31: 2053-2065.
252. Sy, S. M., J. Jiang, W. S. O, Y. Deng, and M. S. Huen. 2013. The ubiquitin specific protease USP34 promotes ubiquitin signaling at DNA double-strand breaks. *Nucleic Acids Res* 41: 8572-8580.
253. Pines, J. 2011. Cubism and the cell cycle: the many faces of the APC/C. *Nature reviews. Molecular cell biology* 12: 427-438.
254. He, M. L., Y. Chen, Q. Chen, Y. He, J. Zhao, J. Wang, H. Yang, and H. F. Kung. 2011. Multiple gene dysfunctions lead to high cancer-susceptibility: evidences from a whole-exome sequencing study. *Am J Cancer Res* 1: 562-573.

255. Zhang, N., and D. Pati. 2017. Biology and insights into the role of cohesin protease separase in human malignancies. *Biol Rev Camb Philos Soc* 92: 2070-2083.
256. Zhang, N., G. Ge, R. Meyer, S. Sethi, D. Basu, S. Pradhan, Y. J. Zhao, X. N. Li, W. W. Cai, A. K. El-Naggar, V. Baladandayuthapani, F. S. Kittrell, P. H. Rao, D. Medina, and D. Pati. 2008. Overexpression of Separase induces aneuploidy and mammary tumorigenesis. *Proc Natl Acad Sci U S A* 105: 13033-13038.
257. Mukherjee, M., G. Ge, N. Zhang, D. G. Edwards, P. Sumazin, S. K. Sharan, P. H. Rao, D. Medina, and D. Pati. 2014. MMTV-Espl1 transgenic mice develop aneuploid, estrogen receptor alpha (ERalpha)-positive mammary adenocarcinomas. *Oncogene* 33: 5511-5522.
258. Mukherjee, M., G. Ge, N. Zhang, E. Huang, L. V. Nakamura, M. Minor, V. Fofanov, P. H. Rao, A. Herron, and D. Pati. 2011. Separase loss of function cooperates with the loss of p53 in the initiation and progression of T- and B-cell lymphoma, leukemia and aneuploidy in mice. *PLoS one* 6: e22167.
259. Somlyo, A. P., and A. V. Somlyo. 2003. Ca²⁺ sensitivity of smooth muscle and nonmuscle myosin II: modulated by G proteins, kinases, and myosin phosphatase. *Physiol Rev* 83: 1325-1358.
260. Tan, X., and M. Chen. 2014. MYLK and MYL9 expression in non-small cell lung cancer identified by bioinformatics analysis of public expression data. *Tumour Biol* 35: 12189-12200.

261. Lee, W. S., G. Seo, H. J. Shin, S. H. Yun, H. Yun, N. Choi, J. Lee, D. Son, J. Cho, J. Kim, Y. B. Cho, H. K. Chun, and W. Y. Lee. 2008. Identification of differentially expressed genes in microsatellite stable HNPCC and sporadic colon cancer. *J Surg Res* 144: 29-35.
262. Dobashi, S., T. Katagiri, E. Hirota, S. Ashida, Y. Daigo, T. Shuin, T. Fujioka, T. Miki, and Y. Nakamura. 2009. Involvement of TMEM22 overexpression in the growth of renal cell carcinoma cells. *Oncol Rep* 21: 305-312.
263. Cui, J., Q. Zhu, H. Zhang, M. A. Cianfrocco, A. E. Leschziner, J. E. Dixon, and J. Xiao. 2017. Structure of Fam20A reveals a pseudokinase featuring a unique disulfide pattern and inverted ATP-binding. *Elife* 6.
264. Cui, J., J. Xiao, V. S. Tagliabracci, J. Wen, M. Rahdar, and J. E. Dixon. 2015. A secretory kinase complex regulates extracellular protein phosphorylation. *Elife* 4: e06120.
265. Zheng, Y., T. Y. Lin, G. Lee, M. N. Paddock, J. Momb, Z. Cheng, Q. Li, D. L. Fei, B. D. Stein, S. Ramsamoj, G. Zhang, J. Blenis, and L. C. Cantley. 2018. Mitochondrial One-Carbon Pathway Supports Cytosolic Folate Integrity in Cancer Cells. *Cell* 175: 1546-1560 e1517.
266. Lombardi, M. L., D. E. Jaalouk, C. M. Shanahan, B. Burke, K. J. Roux, and J. Lammerding. 2011. The interaction between nesprins and sun proteins at the nuclear envelope is critical for force transmission between the nucleus and cytoskeleton. *The Journal of biological chemistry* 286: 26743-26753.

267. Sjoblom, T., S. Jones, L. D. Wood, D. W. Parsons, J. Lin, T. D. Barber, D. Mandelker, R. J. Leary, J. Ptak, N. Silliman, S. Szabo, P. Buckhaults, C. Farrell, P. Meeh, S. D. Markowitz, J. Willis, D. Dawson, J. K. Willson, A. F. Gazdar, J. Hartigan, L. Wu, C. Liu, G. Parmigiani, B. H. Park, K. E. Bachman, N. Papadopoulos, B. Vogelstein, K. W. Kinzler, and V. E. Velculescu. 2006. The consensus coding sequences of human breast and colorectal cancers. *Science* 314: 268-274.
268. Yachida, S., S. Jones, I. Bozic, T. Antal, R. Leary, B. Fu, M. Kamiyama, R. H. Hruban, J. R. Eshleman, M. A. Nowak, V. E. Velculescu, K. W. Kinzler, B. Vogelstein, and C. A. Iacobuzio-Donahue. 2010. Distant metastasis occurs late during the genetic evolution of pancreatic cancer. *Nature* 467: 1114-1117.
269. Han, C., X. Liao, W. Qin, L. Yu, X. Liu, G. Chen, Z. Liu, S. Lu, Z. Chen, H. Su, G. Zhu, Z. Lu, Z. Liu, X. Qin, Y. Gui, Z. Mo, L. Li, and T. Peng. 2016. EGFR and SYNE2 are associated with p21 expression and SYNE2 variants predict post-operative clinical outcomes in HBV-related hepatocellular carcinoma. *Scientific reports* 6: 31237.
270. Yang, J., and W. Zhang. 2013. New molecular insights into osteosarcoma targeted therapy. *Curr Opin Oncol* 25: 398-406.
271. Salas, S., P. Jezequel, L. Campion, J. L. Deville, F. Chibon, C. Bartoli, J. C. Gentet, C. Charbonnel, W. Gouraud, B. Voutsinos-Porche, A. Brouchet, F. Duffaud, D. Figarella-Branger, and C. Bouvier. 2009. Molecular characterization of the response to chemotherapy in conventional

- osteosarcomas: predictive value of HSD17B10 and IFITM2. *Int J Cancer* 125: 851-860.
272. Sun, L., J. Li, and B. Yan. 2015. Gene expression profiling analysis of osteosarcoma cell lines. *Mol Med Rep* 12: 4266-4272.
273. Xu, L., M. E. Sowa, J. Chen, X. Li, S. P. Gygi, and J. W. Harper. 2008. An FTS/Hook/p107(FHIP) complex interacts with and promotes endosomal clustering by the homotypic vacuolar protein sorting complex. *Mol Biol Cell* 19: 5059-5071.
274. Chan, J. Y., A. Y. J. Ng, C. L. Cheng, M. L. Nairismagi, B. Venkatesh, D. M. Z. Cheah, S. T. Li, S. H. Chan, J. Ngeow, Y. Laurensia, J. Q. Lim, J. W. L. Pang, S. Nagarajan, T. Song, B. Chia, J. Tan, D. Huang, Y. T. Goh, E. Poon, N. Somasundaram, M. Tao, R. H. H. Quek, M. Farid, C. C. Khor, J. X. Bei, S. Y. Tan, S. T. Lim, C. K. Ong, and T. Tang. 2018. Whole exome sequencing identifies recessive germline mutations in FAM160A1 in familial NK/T cell lymphoma. *Blood Cancer J* 8: 111.
275. Clevers, H. 2016. Modeling Development and Disease with Organoids. *Cell* 165: 1586-1597.
276. Huch, M., and B. K. Koo. 2015. Modeling mouse and human development using organoid cultures. *Development* 142: 3113-3125.
277. Sato, T., D. E. Stange, M. Ferrante, R. G. Vries, J. H. Van Es, S. Van den Brink, W. J. Van Houdt, A. Pronk, J. Van Gorp, P. D. Siersema, and H. Clevers. 2011. Long-term expansion of epithelial organoids from human

- colon, adenoma, adenocarcinoma, and Barrett's epithelium. *Gastroenterology* 141: 1762-1772.
278. van de Wetering, M., H. E. Francies, J. M. Francis, G. Bounova, F. Iorio, A. Pronk, W. van Houdt, J. van Gorp, A. Taylor-Weiner, L. Kester, A. McLaren-Douglas, J. Blokker, S. Jaksani, S. Bartfeld, R. Volckman, P. van Sluis, V. S. Li, S. Seepo, C. Sekhar Pedamallu, K. Cibulskis, S. L. Carter, A. McKenna, M. S. Lawrence, L. Lichtenstein, C. Stewart, J. Koster, R. Versteeg, A. van Oudenaarden, J. Saez-Rodriguez, R. G. Vries, G. Getz, L. Wessels, M. R. Stratton, U. McDermott, M. Meyerson, M. J. Garnett, and H. Clevers. 2015. Prospective derivation of a living organoid biobank of colorectal cancer patients. *Cell* 161: 933-945.
279. Boj, S. F., C. I. Hwang, L. A. Baker, Chio, Il, D. D. Engle, V. Corbo, M. Jager, M. Ponz-Sarvisé, H. Tiriác, M. S. Spector, A. Gracanin, T. Oni, K. H. Yu, R. van Boxtel, M. Huch, K. D. Rivera, J. P. Wilson, M. E. Feigin, D. Ohlund, A. Handly-Santana, C. M. Ardito-Abraham, M. Ludwig, E. Elyada, B. Alagesan, G. Biffi, G. N. Yordanov, B. Delcuze, B. Creighton, K. Wright, Y. Park, F. H. Morsink, I. Q. Molenaar, I. H. Borel Rinkes, E. Cuppen, Y. Hao, Y. Jin, I. J. Nijman, C. Iacobuzio-Donahue, S. D. Leach, D. J. Pappin, M. Hammell, D. S. Klimstra, O. Basturk, R. H. Hruban, G. J. Offerhaus, R. G. Vries, H. Clevers, and D. A. Tuveson. 2015. Organoid models of human and mouse ductal pancreatic cancer. *Cell* 160: 324-338.
280. Gao, D., I. Vela, A. Sboner, P. J. Iaquinta, W. R. Karthaus, A. Gopalan, C. Dowling, J. N. Wanjala, E. A. Undvall, V. K. Arora, J. Wongvipat, M. Kossai,

- S. Ramazanoglu, L. P. Barboza, W. Di, Z. Cao, Q. F. Zhang, I. Sirota, L. Ran, T. Y. MacDonald, H. Beltran, J. M. Mosquera, K. A. Touijer, P. T. Scardino, V. P. Laudone, K. R. Curtis, D. E. Rathkopf, M. J. Morris, D. C. Danila, S. F. Slovin, S. B. Solomon, J. A. Eastham, P. Chi, B. Carver, M. A. Rubin, H. I. Scher, H. Clevers, C. L. Sawyers, and Y. Chen. 2014. Organoid cultures derived from patients with advanced prostate cancer. *Cell* 159: 176-187.
281. Takasato, M., P. X. Er, H. S. Chiu, B. Maier, G. J. Baillie, C. Ferguson, R. G. Parton, E. J. Wolvetang, M. S. Roost, S. M. Chuva de Sousa Lopes, and M. H. Little. 2015. Kidney organoids from human iPS cells contain multiple lineages and model human nephrogenesis. *Nature* 526: 564-568.
282. Dekkers, J. F., G. Berkers, E. Kruisselbrink, A. Vonk, H. R. de Jonge, H. M. Janssens, I. Bronsveld, E. A. van de Graaf, E. E. Nieuwenhuis, R. H. Houwen, F. P. Vlegaar, J. C. Escher, Y. B. de Rijke, C. J. Majoor, H. G. Heijerman, K. M. de Winter-de Groot, H. Clevers, C. K. van der Ent, and J. M. Beekman. 2016. Characterizing responses to CFTR-modulating drugs using rectal organoids derived from subjects with cystic fibrosis. *Science translational medicine* 8: 344ra384.
283. Li, X., L. Nadauld, A. Ootani, D. C. Corney, R. K. Pai, O. Gevaert, M. A. Cantrell, P. G. Rack, J. T. Neal, C. W. Chan, T. Yeung, X. Gong, J. Yuan, J. Wilhelmy, S. Robine, L. D. Attardi, S. K. Plevritis, K. E. Hung, C. Z. Chen, H. P. Ji, and C. J. Kuo. 2014. Oncogenic transformation of diverse gastrointestinal tissues in primary organoid culture. *Nat Med* 20: 769-777.

284. Matano, M., S. Date, M. Shimokawa, A. Takano, M. Fujii, Y. Ohta, T. Watanabe, T. Kanai, and T. Sato. 2015. Modeling colorectal cancer using CRISPR-Cas9-mediated engineering of human intestinal organoids. *Nat Med* 21: 256-262.
285. Huang, L., A. Holtzinger, I. Jagan, M. BeGora, I. Lohse, N. Ngai, C. Nostro, R. Wang, L. B. Muthuswamy, H. C. Crawford, C. Arrowsmith, S. E. Kalloger, D. J. Renouf, A. A. Connor, S. Cleary, D. F. Schaeffer, M. Roehrl, M. S. Tsao, S. Gallinger, G. Keller, and S. K. Muthuswamy. 2015. Ductal pancreatic cancer modeling and drug screening using human pluripotent stem cell- and patient-derived tumor organoids. *Nat Med* 21: 1364-1371.
286. Nadauld, L. D., S. Garcia, G. Natsoulis, J. M. Bell, L. Miotke, E. S. Hopmans, H. Xu, R. K. Pai, C. Palm, J. F. Regan, H. Chen, P. Flaherty, A. Ootani, N. R. Zhang, J. M. Ford, C. J. Kuo, and H. P. Ji. 2014. Metastatic tumor evolution and organoid modeling implicate TGFBR2 as a cancer driver in diffuse gastric cancer. *Genome biology* 15: 428.
287. Drost, J., R. H. van Jaarsveld, B. Ponsioen, C. Kimberlin, R. van Boxtel, A. Buijs, N. Sachs, R. M. Overmeer, G. J. Offerhaus, H. Begthel, J. Korving, M. van de Wetering, G. Schwank, M. Logtenberg, E. Cuppen, H. J. Snippert, J. P. Medema, G. J. Kops, and H. Clevers. 2015. Sequential cancer mutations in cultured human intestinal stem cells. *Nature* 521: 43-47.
288. Lancaster, M. A., M. Renner, C. A. Martin, D. Wenzel, L. S. Bicknell, M. E. Hurles, T. Homfray, J. M. Penninger, A. P. Jackson, and J. A. Knoblich.

2013. Cerebral organoids model human brain development and microcephaly. *Nature* 501: 373-379.
289. Qian, X., H. N. Nguyen, M. M. Song, C. Hadiono, S. C. Ogden, C. Hammack, B. Yao, G. R. Hamersky, F. Jacob, C. Zhong, K. J. Yoon, W. Jeang, L. Lin, Y. Li, J. Thakor, D. A. Berg, C. Zhang, E. Kang, M. Chickering, D. Nauen, C. Y. Ho, Z. Wen, K. M. Christian, P. Y. Shi, B. J. Maher, H. Wu, P. Jin, H. Tang, H. Song, and G. L. Ming. 2016. Brain-Region-Specific Organoids Using Mini-bioreactors for Modeling ZIKV Exposure. *Cell* 165: 1238-1254.
290. Bershteyn, M., T. J. Nowakowski, A. A. Pollen, E. Di Lullo, A. Nene, A. Wynshaw-Boris, and A. R. Kriegstein. 2017. Human iPSC-Derived Cerebral Organoids Model Cellular Features of Lissencephaly and Reveal Prolonged Mitosis of Outer Radial Glia. *Cell Stem Cell*.
291. Xu, M., E. M. Lee, Z. Wen, Y. Cheng, W. K. Huang, X. Qian, J. Tcw, J. Kouznetsova, S. C. Ogden, C. Hammack, F. Jacob, H. N. Nguyen, M. Itkin, C. Hanna, P. Shinn, C. Allen, S. G. Michael, A. Simeonov, W. Huang, K. M. Christian, A. Goate, K. J. Brennand, R. Huang, M. Xia, G. L. Ming, W. Zheng, H. Song, and H. Tang. 2016. Identification of small-molecule inhibitors of Zika virus infection and induced neural cell death via a drug repurposing screen. *Nat Med* 22: 1101-1107.
292. Bhatia, S. N., and D. E. Ingber. 2014. Microfluidic organs-on-chips. *Nat Biotechnol* 32: 760-772.

293. Huh, D., H. J. Kim, J. P. Fraser, D. E. Shea, M. Khan, A. Bahinski, G. A. Hamilton, and D. E. Ingber. 2013. Microfabrication of human organs-on-chips. *Nature protocols* 8: 2135-2157.
294. Williamson, A., S. Singh, U. Fernekorn, and A. Schober. 2013. The future of the patient-specific Body-on-a-chip. *Lab on a chip* 13: 3471-3480.
295. Capulli, A. K., K. Tian, N. Mehandru, A. Bukhta, S. F. Choudhury, M. Suchyta, and K. K. Parker. 2014. Approaching the in vitro clinical trial: engineering organs on chips. *Lab on a chip* 14: 3181-3186.
296. Zervantonakis, I. K., C. R. Kothapalli, S. Chung, R. Sudo, and R. D. Kamm. 2011. Microfluidic devices for studying heterotypic cell-cell interactions and tissue specimen cultures under controlled microenvironments. *Biomicrofluidics* 5: 13406.
297. Zervantonakis, I. K., S. K. Hughes-Alford, J. L. Charest, J. S. Condeelis, F. B. Gertler, and R. D. Kamm. 2012. Three-dimensional microfluidic model for tumor cell intravasation and endothelial barrier function. *Proc Natl Acad Sci U S A* 109: 13515-13520.
298. Zheng, Y., J. Chen, M. Craven, N. W. Choi, S. Totorica, A. Diaz-Santana, P. Kermani, B. Hempstead, C. Fischbach-Teschl, J. A. Lopez, and A. D. Stroock. 2012. In vitro microvessels for the study of angiogenesis and thrombosis. *Proc Natl Acad Sci U S A* 109: 9342-9347.
299. Bischel, L. L., E. W. Young, B. R. Mader, and D. J. Beebe. 2013. Tubeless microfluidic angiogenesis assay with three-dimensional endothelial-lined microvessels. *Biomaterials* 34: 1471-1477.

300. Moya, M. L., Y. H. Hsu, A. P. Lee, C. C. Hughes, and S. C. George. 2013. In vitro perfused human capillary networks. *Tissue engineering. Part C, Methods* 19: 730-737.
301. Nguyen, D. H., S. C. Stapleton, M. T. Yang, S. S. Cha, C. K. Choi, P. A. Galie, and C. S. Chen. 2013. Biomimetic model to reconstitute angiogenic sprouting morphogenesis in vitro. *Proc Natl Acad Sci U S A* 110: 6712-6717.
302. Mathur, A., P. Loskill, K. Shao, N. Huebsch, S. Hong, S. G. Marcus, N. Marks, M. Mandegar, B. R. Conklin, L. P. Lee, and K. E. Healy. 2015. Human iPSC-based cardiac microphysiological system for drug screening applications. *Scientific reports* 5: 8883.
303. Palpant, N. J., L. Pabon, M. Roberts, B. Hadland, D. Jones, C. Jones, R. T. Moon, W. L. Ruzzo, I. Bernstein, Y. Zheng, and C. E. Murry. 2015. Inhibition of beta-catenin signaling respecifies anterior-like endothelium into beating human cardiomyocytes. *Development* 142: 3198-3209.
304. Giobbe, G. G., F. Michielin, C. Luni, S. Giulitti, S. Martewicz, S. Dupont, A. Floreani, and N. Elvassore. 2015. Functional differentiation of human pluripotent stem cells on a chip. *Nature methods* 12: 637-640.
305. Haupt, Y., R. Maya, A. Kazaz, and M. Oren. 1997. Mdm2 promotes the rapid degradation of p53. *Nature* 387: 296-299.
306. Wade, M., Y. C. Li, and G. M. Wahl. 2013. MDM2, MDMX and p53 in oncogenesis and cancer therapy. *Nature reviews. Cancer* 13: 83-96.
307. Issaeva, N., P. Bozko, M. Enge, M. Protopopova, L. G. Verhoef, M. Masucci, A. Pramanik, and G. Selivanova. 2004. Small molecule RITA binds to p53,

- blocks p53-HDM-2 interaction and activates p53 function in tumors. *Nat Med* 10: 1321-1328.
308. Vassilev, L. T., B. T. Vu, B. Graves, D. Carvajal, F. Podlaski, Z. Filipovic, N. Kong, U. Kammlott, C. Lukacs, C. Klein, N. Fotouhi, and E. A. Liu. 2004. In vivo activation of the p53 pathway by small-molecule antagonists of MDM2. *Science* 303: 844-848.
309. Shangary, S., D. Qin, D. McEachern, M. Liu, R. S. Miller, S. Qiu, Z. Nikolovska-Coleska, K. Ding, G. Wang, J. Chen, D. Bernard, J. Zhang, Y. Lu, Q. Gu, R. B. Shah, K. J. Pienta, X. Ling, S. Kang, M. Guo, Y. Sun, D. Yang, and S. Wang. 2008. Temporal activation of p53 by a specific MDM2 inhibitor is selectively toxic to tumors and leads to complete tumor growth inhibition. *Proc Natl Acad Sci U S A* 105: 3933-3938.
310. Chang, Y. S., B. Graves, V. Guerlavais, C. Tovar, K. Packman, K. H. To, K. A. Olson, K. Kesavan, P. Gangurde, A. Mukherjee, T. Baker, K. Darlak, C. Elkin, Z. Filipovic, F. Z. Qureshi, H. Cai, P. Berry, E. Feyfant, X. E. Shi, J. Horstick, D. A. Annis, A. M. Manning, N. Fotouhi, H. Nash, L. T. Vassilev, and T. K. Sawyer. 2013. Stapled alpha-helical peptide drug development: a potent dual inhibitor of MDM2 and MDMX for p53-dependent cancer therapy. *Proc Natl Acad Sci U S A* 110: E3445-3454.
311. Bernal, F., M. Wade, M. Godes, T. N. Davis, D. G. Whitehead, A. L. Kung, G. M. Wahl, and L. D. Walensky. 2010. A stapled p53 helix overcomes HDMX-mediated suppression of p53. *Cancer cell* 18: 411-422.

312. Bernal, F., A. F. Tyler, S. J. Korsmeyer, L. D. Walensky, and G. L. Verdine. 2007. Reactivation of the p53 tumor suppressor pathway by a stapled p53 peptide. *J Am Chem Soc* 129: 2456-2457.
313. Terzian, T., Y. A. Suh, T. Iwakuma, S. M. Post, M. Neumann, G. A. Lang, C. S. Van Pelt, and G. Lozano. 2008. The inherent instability of mutant p53 is alleviated by Mdm2 or p16INK4a loss. *Genes & development* 22: 1337-1344.
314. Goldstein, I., V. Marcel, M. Olivier, M. Oren, V. Rotter, and P. Hainaut. 2011. Understanding wild-type and mutant p53 activities in human cancer: new landmarks on the way to targeted therapies. *Cancer gene therapy* 18: 2-11.
315. Jin, K., L. Teng, Y. Shen, K. He, Z. Xu, and G. Li. 2010. Patient-derived human tumour tissue xenografts in immunodeficient mice: a systematic review. *Clin Transl Oncol* 12: 473-480.
316. Yu, X., A. Vazquez, A. J. Levine, and D. R. Carpizo. 2012. Allele-specific p53 mutant reactivation. *Cancer cell* 21: 614-625.
317. Boeckler, F. M., A. C. Joerger, G. Jaggi, T. J. Rutherford, D. B. Veprintsev, and A. R. Fersht. 2008. Targeted rescue of a destabilized mutant of p53 by an in silico screened drug. *Proc Natl Acad Sci U S A* 105: 10360-10365.
318. North, S., O. Pluquet, D. Maurici, F. El-Ghissassi, and P. Hainaut. 2002. Restoration of wild-type conformation and activity of a temperature-sensitive mutant of p53 (p53(V272M)) by the cytoprotective aminothiol WR1065 in the esophageal cancer cell line TE-1. *Molecular carcinogenesis* 33: 181-188.

319. Alexandrova, E. M., A. R. Yallowitz, D. Li, S. Xu, R. Schulz, D. A. Proia, G. Lozano, M. Dobbstein, and U. M. Moll. 2015. Improving survival by exploiting tumour dependence on stabilized mutant p53 for treatment. *Nature* 523: 352-356.
320. Li, D., N. D. Marchenko, R. Schulz, V. Fischer, T. Velasco-Hernandez, F. Talos, and U. M. Moll. 2011. Functional inactivation of endogenous MDM2 and CHIP by HSP90 causes aberrant stabilization of mutant p53 in human cancer cells. *Molecular cancer research : MCR* 9: 577-588.
321. Li, D., N. D. Marchenko, and U. M. Moll. 2011. SAHA shows preferential cytotoxicity in mutant p53 cancer cells by destabilizing mutant p53 through inhibition of the HDAC6-Hsp90 chaperone axis. *Cell death and differentiation* 18: 1904-1913.
322. Parrales, A., and T. Iwakuma. 2015. Targeting Oncogenic Mutant p53 for Cancer Therapy. *Frontiers in oncology* 5: 288.
323. Kravchenko, J. E., G. V. Ilyinskaya, P. G. Komarov, L. S. Agapova, D. V. Kochetkov, E. Strom, E. I. Frolova, I. Kovriga, A. V. Gudkov, E. Feinstein, and P. M. Chumakov. 2008. Small-molecule RETRA suppresses mutant p53-bearing cancer cells through a p73-dependent salvage pathway. *Proc Natl Acad Sci U S A* 105: 6302-6307.
324. Lin, Y. H., B. E. Jewell, J. Gingold, L. Lu, R. Zhao, L. L. Wang, and D. F. Lee. 2017. Osteosarcoma: Molecular Pathogenesis and iPSC Modeling. *Trends Mol Med* 23: 737-755.

Vita

Ruoji Zhou was born in Kunming, China on December 4, 1986, the daughter of Xiaoling Ma and Liming Zhou. After completing her education at The High School Affiliated to Yunnan Normal University, Kunming, China in 2005, she entered Sun Yat-sen University Zhongshan School of Medicine in Guangzhou, China. She received the degree Doctor of Medicine in clinical medicine in July 2010. For the next three year, she entered Fudan University Shanghai Medical School and studied at Department of Pathology in Shanghai Cancer Center as a graduate student. She received a degree of Master in Medicine in Oncology in July 2013. In August of 2013, she entered The University of Texas MD Anderson Cancer Center UTHHealth Graduate School of Biomedical Sciences.

Permanent address:

8100 Cambridge Street, APT 91,

Houston, Texas 77054